Topology Preserving Vascular Registration: Application to Percutaneous Coronary Intervention

Thomas Benseghir

Universite de Nice - Sophia Antipolis

ECOLE DOCTORALE STIC
SCIENCES ET TECHNOLOGIES DE L'INFORMATION ET DE LA COMMUNICATION

T H E S E

pour l'obtention du grade de

Docteur en Sciences

de l'université de Nice - Sophia Antipolis

Mention : Automatique Traitement du Signal et des Images

présentée et soutenue par

Thomas Benseghir

Topology Preserving Vascular Registration: Application to Percutaneous Coronary Intervention

Thèse dirigée par Grégoire Malandain

soutenue le 7 juillet 2015

Jury :

Reviewers :	Patrick Clarysse	-	CNRS (CREATIS)
	Pascal Fua	-	EPFL
Advisors :	Grégoire Malandain	-	INRIA (Morpheme)
	Régis Vaillant	-	GE Healthcare
Examinators :	Nassir Navab	-	TUM
President :	Xavier Pennec	-	INRIA (Asclepios)

Remerciements

Mes premiers remerciements vont naturellement à mes deux encadrants qui m'ont accompagné pendant la totalité de cette thèse. J'ai appris énormément de ces deux personnages exceptionnels et ne saurai leur rendre hommage à la hauteur de ce qu'ils m'ont apporté. Toi Grégoire et tes nombreuses maximes qui résonnent maintenant dans ma tête dès que j'écris quelque chose:

- "Il faut prendre le lecteur[1] par la main et le guider à travers un discours linéaire."

- "Ce qui se conçoit bien s'énonce clairement; et les mots pour le dire arrivent aisément."

Sans oublier bien-sûr ton goût pour l'excellence, aussi porté sur les cookies et les madeleines. Et toi Régis qui a su tempérer et canaliser mon énergie, toujours en me poussant à faire des choix pragmatiques et raisonnés. Tu as su m'ouvrir les portes de GE (au propre comme au figuré) et grâce à toi je me prépare à quelques belles années d'acronymes en tout genre. Je garde précieusement en mémoire ces réunions du lundi matin et ces ECM animés qui rythmaient mes semaines si bien remplies.

Alors que beaucoup voient la thèse comme un voyage, j'aime à la comparer à une grossesse. Et au delà de mes encadrants qui m'ont accompagné pendant mes nausées et mes envies de fraises, je remercie ceux qui ont aidé à l'accouchement. D'abord Patrick et Pascal pour leur travail profond de relecture grâce auquel j'ai pu améliorer la qualité de ce manuscrit. Plus largement, je remercie les membres du jury qui, grâce à leurs questions, ont ouvert de nombreuses perspectives à creuser dans de futurs travaux. Un remerciement tout particulier à Nassir qui a accepté d'assister à ma thèse à 5 heures du matin outre-atlantique, ainsi qu'à Xavier qui a présidé le jury et qui m'a permis de replacer mon travail dans un contexte plus large. Merci à vous d'avoir concrétiser l'aboutissement de ces années de recherche.

Rien de tout ceci n'aurait été possible sans ces nombreuses discussions au détour d'une machine à café, d'un bureau ou d'une salle de bloc. Au delà de l'intérêt scientifique, ces échanges ont aussi rendu cette "grossesse" bien plaisante. Merci d'abord à Aymeric, Ketan et nos deux Vincent pour leur pauses revigorantes à travers tout GE et leur soutien constant. A mon cher co-bureau Cyril et nos discussions souvent conclues par une friandise. Un merci sportif à François pour m'avoir aidé à trouver à la fois une place à GE et aussi la motivation de faire travailler mes jambes pour me vider la tête. Merci à Valérie pour avoir su croire en moi et de continuer à le faire. Un merci groupé pour toute l'équipe GE: Yves, Liliane, les Maximes (T. et C.), Dustin, Charlotte, les Laurences (G. et V.), Sophie, Pablo, Razvan, Giovani, Benjamin, Philippe, Isabelle, Kiem et tous les autres que j'oublie sûrement. J'ai aussi eu la chance de partager beaucoup de bons moments avec l'équipe ASCLEPIOS. Merci donc à mes chers co-bureaux temporaires Matthieu, Chloé, Nicolas, Krissy

[1] Fonctionne aussi avec le public et les membres du jury.

et Marine ; vous qui avez su m'accueillir avec tant de gentilesse. Une pensée particulière pour Isabelle qui s'est toujours pliée en quatre pour faciliter mes différents séjours et ma vie sur la côte d'azur. Lors d'une pause café, une soirée sushi ou un séminaire dans les montagnes, l'équipe a su me faire prendre le poids nécessaire à toute grossesse. Merci donc à Nicholas, Hervé (D. et L.), Xavier, Maxime, Marco, Alan, Hugo, Loïc (C. et L.F.), Hakim, Florian, Vikash, Mehdi, Bishesh, Rocio, Jan, Nina, Anant, Marc-Michel, Sophie, Thomas et Roch-Philippe.

Initialement prévue comme un partenariat GE / ASCLEPIOS, j'ai eu l'occasion de partager quelques bons moments avec l'équipe MORPHEME. Merci à Agustina, Marine, Gaël, Jane et à toute l'équipe MORPHEME, sage-femmes et maïeuticiens d'une semaine, pour leur aide pendant la dernière ligne droite. Grâce à vous tous, je me suis immédiatement senti à mon aise. J'ai particulièrement apprécié cette réunion d'équipe en bord de mer qu'il sera malheureusement difficile à instaurer côté GE... Durant cette thèse, j'ai beaucoup apprécié ces quelques voyages en conférences ou écoles d'été (souvent difficilement acceptés par mes proches comme périodes de "travail"). Parmis toutes ces rencontres, je fais un clin d'oeil barcelonais à Marta, Veronika, Oliver et Nazim.

Naturellement une thèse représente beaucoup d'investissement personnel et je remercie mes proches pour leur soutien et leur compréhension face à mon manque de temps. Merci à ma mère et ma grand mère qui m'ont appris le goût de l'effort et qui m'ont tout donné. Merci à Bernard, mon beau-papa, et Baptiste, mon frère, pour ces beaux moments remplis de jeux et discussions passionnées. Merci à Julien et Antoine pour notre trio inconditionnel, maintenant complété par nos trois drôles de dames. Un gros merci à ceux qui ont pu faire le déplacement à Nice et assister à mon réglage de climatisation : Mon père, Patrick et Andrée. Plus largement merci à toute ma famille pour leur compréhension et pour m'avoir laissé le temps de me concentrer sur cette fin de thèse. Merci à mes amis de longue date. Ceux qui ont su braver la distance et le manque de temps: Flore et banban, Thomas et la famille Guilment et bien sûr Cindy et Momo. Merci aussi à ma chère belle-maman Christine ainsi qu'à Philippe pour m'avoir toujours accueilli comme si j'étais de la famille. Un petit clin d'oeil sportif aux amis de l'escalade pour m'avoir accompagné dans la découverte de ce sport tellement prenant.

Enfin, je remercie ma plus belle aventure du quotidien... Celle par qui TOUS commencent et avec qui je finirai.

Acronyms

AVM ArterioVenous Malformations

CABG Coronary Artery Bypass Grafting

CT Computed Tomography

CTA Computed Tomography Angiography

CTO Chronic Total Occlusion

DICOM Digital Imaging and COmmunications in Medicine

DoF Degrees of Freedom

DRR Digitally Reconstructed Radiograph

DSA Digitally Subtracted Angiogram

ECG Electrocardiogram

EM Expectation Maximization

FFD Free Form Deformation

FFR Fractional Flow Reserve

GMM Gaussian Mixture Model

GT Ground-Truth

ICC Iterative Closest Curve

ICP Iterative Closest Point

LAD Left Anterior Descending

MI Mutual Information

MIP Maximum Intensity Projection

MPD Mean Projective Distance

MR Magnetic Resonance

NCC Normalized Cross Correlation

NMS Non-Maximum Suppression

PCI Percutaneous Coronary Intervention

PDF Probability Density Function

QCA Quantitative Coronary Analysis

RoI Region of Interest

SOD Source Object Distance

SSD Sum of Squared Difference

SVD Singular Value Decomposition

TACE Trans-Arterial Chemo-Embolization (also called Transcatheter Arterial ChemoEmbolization)

TP-ICC Tree-topology Preserving Iterative Closest Curve

TPS Thin Plate Spline

TRE Target Registration Error

WHO World Health Organization

Contents

Chapter 1

Introduction

This Ph.D. thesis takes root in the image-guided interventions field. In this vast domain, we will focus on the world of percutaneous procedures inside the arterial network. Imaging systems are used to help a physician, often called an interventionalist, in delivering therapeutic treatment through very specific tools inserted inside the patient. The technical challenge is to provide images adapted to the clinical task, which depends on the type of intervention performed. The work presented in this manuscript is focused on Percutaneous Coronary Intervention (PCI). Images (also called frames) acquired by the interventional guiding system show the tools navigated inside the patient's vasculature with respect to the anatomy. Their cadence can reach 30 frames per second with a spatial resolution of 0.2mm. Such performances fulfill most of the clinical expectations but interventionalists are now addressing more complex cases demanding new visualization capabilities. It is now very common that multiple images acquired on different types of equipments are available prior to the clinical procedure. Combining them with the frames guiding the intervention is seen as a potential way to propose a complete visualization of the information available along the procedure. Guiding images provided by the interventional system are projections of the patient anatomy onto a plane. They are produced by the attenuation of the X-ray beam by anatomical tissues and other objects in the field of view. In these images, vessels can be superimposed, which does not facilitate their interpretation. Additional difficulties arise with the presence of total occlusion of an artery branch.

Occluded portions are not visible in the live two dimensional (2D) modality because the lumen[1] X-ray absorption cannot be modified by the use of contrast agent. Fusing a pre-operative scanner acquisition with the live projective images could improve the intra-operative guidance. The Computed Tomography Angiography (CTA) scan allows to assess the patient's vasculature in three dimensions (3D). This type of acquisition is mostly performed for diagnostic purposes, helping to determine whether the patient needs a revascularization procedure or not. Interestingly, the reconstructed volume includes not only the lumen of the vessel, but also additional information such as the type of material constituting the vessel wall. A typical information available in this modality is the presence of calcification along the arteries, which is characteristic of the presence of a lesion and interacts with the therapy delivery. Moreover, for patient suffering from a complete occlusion, the occluded channel is formed of a specific material that can be seen in the CTA volume. Both types of information are crucial during the navigation phase of the

[1] The lumen is the inner region of the artery that is filled with blood.

intervention and the cardiologist could benefit from a fused visualization of these elements extracted from the pre-operative CTA and the live navigation images. This requires to bring them into the same referential. Description of this procedure and associated clinical needs is the main goal of Chapter 2.

These two acquisitions represent the patient at two different times (before and during the intervention) on two imaging systems without pre-defined link between them. Aligning two modalities representing the same reality is referred in the literature as the registration problem. To find the transformation between the 3D CTA and the 2D guiding image, 3D/2D registration algorithms generally optimize an objective function quantifying the distance between structures of interest. Most of the methods from the literature, classified in Chapter 3, involve a segmentation step to create a geometrical representation of the vasculature (feature). Feature-based algorithms rely on correspondences between segmented structures, called pairings. The success of a registration algorithm depends on the relevance of the pairings.

Building relevant pairings is one of the major axes of research regarding feature-based registration. By taking into account the nature of the segmented structures to be matched, several articles from the literature claim to increase accuracy and robustness of their algorithms. Prior knowledge on the vessels can be used to define local information, such as the tangent or local curvature, to improve the pairing procedure or to penalize non-coherent pairings between neighbors along the structure. However, most of the literature algorithms do not consider the vasculature globally. We deeply explain in Chapter 4 how features are extracted and which geometrical representation best fits for each modality. We then define a framework dedicated to the registration of curves that ensures to preserve the curvilinear structures along the iterations. This proposed framework extends the Iterative Closest Point (ICP) algorithm to curves.

The algorithm we propose, which is called the Iterative Closest Curve (ICC) algorithm, has a general formulation that can be applied to situations where the key features are curves. The ICC algorithm, which is the subject of Chapter 5, alternates two steps: building pairings between curves extracted from the two modalities; and finding the transformation that minimizes the Fréchet distance between paired curves. The Fréchet distance is a curve-to-curve distance based on a point pairing set between curves that preserves order along them (and thus the curve topology). By matching entire curves and optimizing the Fréchet distance, the ICC framework allows to take into account the curvilinear structure of the features in a global way. In a further step, we consider that the coronary arteries are arranged as a tree: vessels are "connected" to each other at bifurcations. This particular arrangement is composed of two types of connectivities defining the vasculature topology: connectivity along curves and connectivity at bifurcation points.

In Chapter 6, we create a tree pairing procedure preserving both types of connectivities. This constitutes a challenge because of the projective nature of the 2D modality. Actually, most of the tree matching methods from the literature assume that nodes of the tree (in our case bifurcations) can be identified in both modalities. This assumption is not satisfied in our 3D/2D application because of vessel

superimpositions in the 2D image. We thus define what is a pairing preserving the tree-topology in the 3D/2D case and consider a top-down approach to pair the 3D vasculature, starting from the root curve pairing and progressively continuing the recursion in the branches of the tree. A given tree pairing is evaluated using a score that takes into account the geometrical distances between paired curves but also their resemblances. Finding the best tree pairing is expressed as an optimization problem. It is solved by a divide-and-conquer algorithm avoiding the combinatorial explosion that would be induced by trying all possible tree-topology preserving pairings.

The tree pairing procedure can be easily introduced in the ICC framework, forming the Tree-topology Preserving ICC (TP-ICC). To evaluate this algorithm, we designed two error measures relative to each output expected from a registration algorithm: the resulting alignment and pairings. Particular efforts have been made in Chapter 7 to design measures that are intuitive, clinically relevant and based on a single ground-truth (which can be obtained without impacting the standard clinical procedure). The alignment error quantifies the distance between the 3D structure projection at the registered position and where it should be accordingly to the ground-truth. The quality of the pairings formed by the registration algorithm is assessed by the pairing error. These two measures demonstrate good correlation with visual assessment and are used in Chapter 8 to evaluate the proposed registration algorithm.

Chapter 2

Clinical Context

Contents

2.1 Pathologies and Treatments

According to the World Health Organization (WHO), the ischaemic heart disease is the number 1 cause of death both globally and for the high income countries (see Figure B.1 of Appendix B). Also known as coronary artery disease, it represents 13.2% of all deaths around the world. This Ph.D. thesis is made in the context of interventional cardiology, which is a key treatment option for coronary artery disease. In this section we shortly present the atherosclerosis pathology and its clinical consequences. We have focused our interest on coronary heart disease and the minimally invasive treatment that is at the center of this thesis.

2.1.1 Atherosclerosis, Stenosis and Occlusion

Atherosclerosis is the main syndrome responsible for cardiovascular diseases. It is characterized by a progressive deposit, called **plaque**, on the inner wall of arteries. This atheromatous plaque is composed of fat, cholesterol and calcium deposit. In a fist stage, the vessel wall enlarges to include the presence of plaque, while maintaining a normal cross section size. In a later stage, the plaque starts to progressively narrow the artery lumen[1] and can eventually impact the blood flow (see Figure 2.1).

[1] The lumen is the volume delimited by the artery walls where the blood can circulate.

Atherosclerosis is a chronic disease that remains asymptomatic for decades until this narrowing, also called stenosis, limits the blood supply to organs.

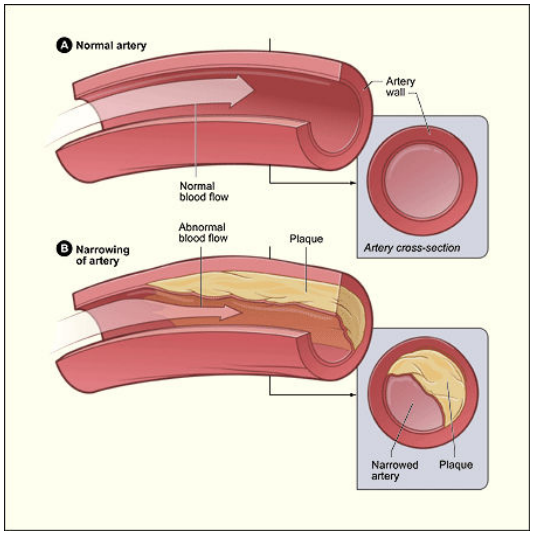

Figure 2.1: Atherosclerosis process illustrated by [National Heart, Lung, and Blood Institute, 2015b]. (Top) healthy vessel, (bottom) plaque deposit in an artery forming a stenosis that decreases the blood flow.

Depending on the anatomy impacted by the blood flow reduction, atherosclerosis can induce several different diseases. A complete blockage of cerebral vessels can induce death of neurons due to the lack of nutrients and oxygens contained in the blood. This phenomenon is known as a **stroke**. Like every organ, the heart has its own vascularization composed of the coronary arteries and the cardiac veins. Coronary arteries constitute the only blood supply of the myocardium (the heart muscle). A narrowing of these vessels, also called a stenosis, can create imbalance between demand and supply regarding oxygen and nutrients. It can induce chest pain, especially during activity and stress, when the demand is high, which stops at rest. These symptoms usually feel like a pressure or squeezing in the chest called **angina**.

Over time, plaque can harden and even rupture that causes a thrombus (or blood clot). If a thrombus completely blocks an artery, a whole part of the myocardium is cut off any supply and may lead to a heart attack. Non-irrigated cardiac cells will die eventually if the blood flow is not restored soon enough, creating scars in the muscle that can induce severe clinical complications. If the blockage occurs slowly, the heart muscle may develop small collateral vessels, or detours, in order to re-root the blood flow. These small created vessels may not be able to supply enough the heart muscle demands and thus angina symptoms can be felt.

A Chronic Total Occlusion (CTO) is a total blockage of a coronary artery that has been present at least for 3 months. If the blockage is present for less than 3 months it is called a total coronary occlusion. The CTO is generally formed of the

atheromatous plaque (as in the stenosis) and an old thrombus. Older occlusions have higher concentration of fibro-calcific material (also called hard plaque). However, dating a CTO is a challenging task. According to [Branislav, 2013], one third of the patients undergoing a stenosis diagnosis suffers from CTO. In case of CTO, multiple revascularization strategies can be used, all involving strong skills from the clinician.

2.1.2 Minimally Invasive Surgical Procedure

Well known risk factors of atherosclerosis are: lack of physical activities, smoking, unhealthy diet, high cholesterol level and diabetes. Playing on these causes constitutes the first treatment of atherosclerosis and can be achieved by a change of lifestyle or drugs. For more severe states, two medical procedures can be performed to treat consequences and re-vascularize properly the myocardium.

The older and less and less used approach is the Coronary Artery Bypass Grafting (CABG). It is an open-heart surgery where an artery or a vein from another area of the patient's body is taken and used to re-orient the flow. This bridge from the aorta or the left internal thoracic artery to a place distal to the occlusion, complements the restricted blood flow (see Figure 2.2b). It is still the most common open heart surgery in the US and involves an opening of chest bone to access the heart and stop it during the intervention. After this (ultra) invasive procedure, the patient typically spends 2 days in an intensive care unit and then around 5 days in a less intensive care area of the hospital. Full recovery is expected between 6 to 12 weeks after the intervention.

An alternative to open heart surgery is a minimally invasive treatment procedure that allows the patient to go home the day after the intervention and return to work after only one week. Actually, the patient generally remains awake during the intervention. This procedure is called angioplasty or Percutaneous Coronary Intervention (PCI) and involves the navigation of clinical tools inside the patient's vasculature. This minimally-invasive procedure is performed in a cardiac catheterization laboratory, also called a "cath-lab", where an X-ray system (presented in Figure 2.3) allows the cardiologist to visualize the tools inside the patient. This interventional system is at the center of this Ph.D. thesis and will be further described in Section 2.2.1.

The PCI treatment consists in opening narrowed or blocked coronary arteries from the inside under the X-ray guidance. A presentation of the overall procedure is provided in [National Heart, Lung, and Blood Institute, 2015a], which illustrates nicely the following steps. A needle is used to make a small hole in the blood vessel, usually the groin, to introduce a thin guide-wire into the artery. This guide-wire helps the clinician to position a tapered tube correctly, which is also called a sheath or introducer. A thin flexible tube, called a catheter, is then inserted in the femoral artery via the sheath. The catheter is then navigated through the patient's vasculature up to the aorta and the entry of coronary arteries, as illustrated in Figure 2.4a. A dedicated X-ray dye, called contrast medium, can be injected through the arteries via this catheter. Coronary arteries are usually not X-ray visible, but

(a) Typical vasculature

(b) Bypass graft

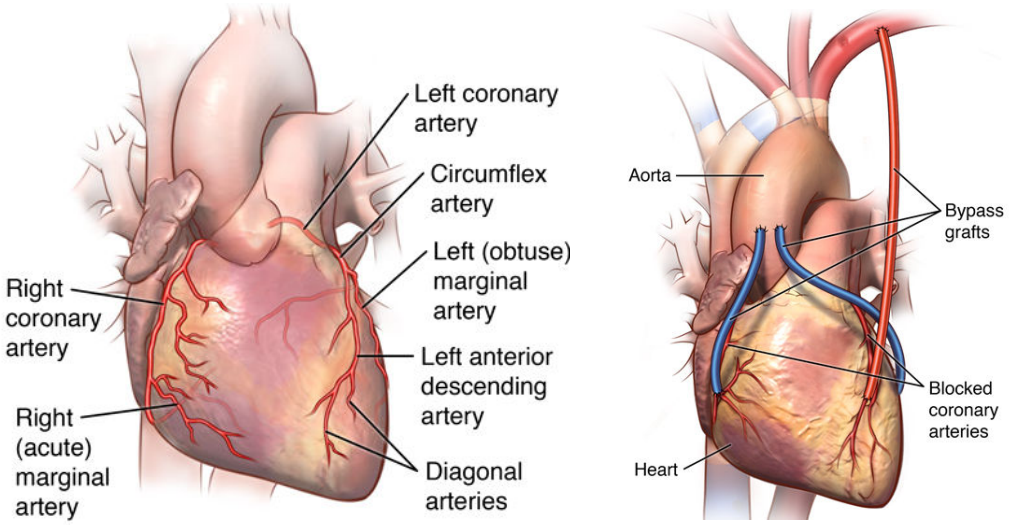

Figure 2.2: Illustration of Coronary Artery Bypass Graft (CABG) extracted from [Johns Hopkins Medicine, 2015a]. (a) shows typical healthy coronaries around the heart, (b) presents different bypass constructed using veins (in blue) and arteries (red).

Figure 2.3: Interventional system in the cath-lab. Interventional Guiding System, IGS-520 from GE Healthcare during a PCI intervention.

filling them with iodine contrast product allows to temporary visualize them until the contrast product is flushed. This procedure is called an **angiography** and allows the clinician to diagnose any blockage or narrowing along the arteries, as illustrated in Figure 2.4b.

(a) Catheterization (b) Angiography

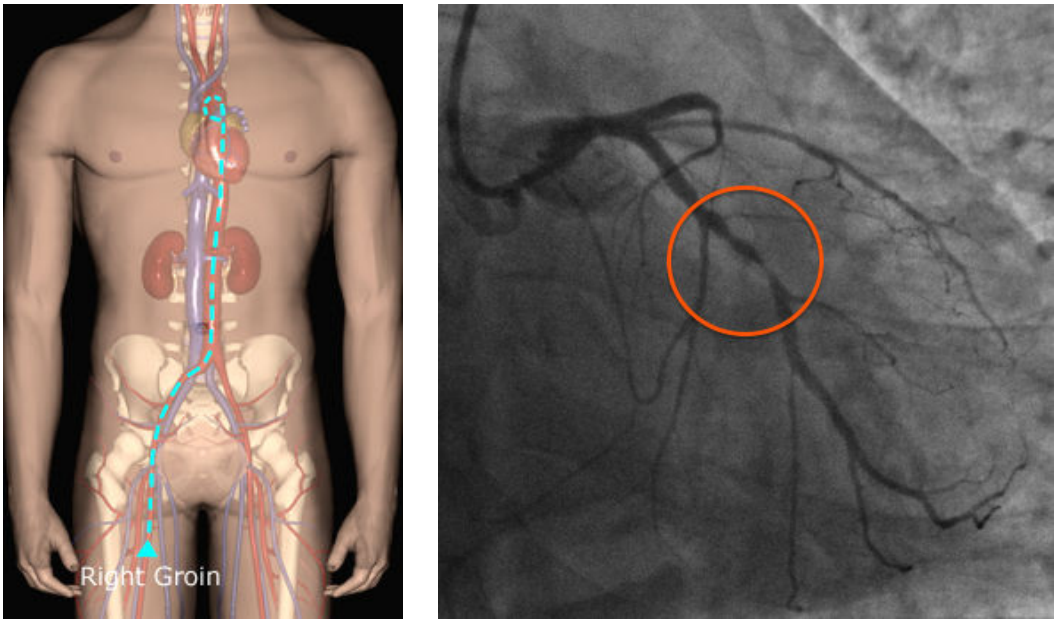

Figure 2.4: Illustration of the angiography procedure. (a) shows the path of the catheter from the groin to the aorta and (b) is the angiography obtained from an injected sequence recorded by an interventional system. The orange circle highlights a stenosis.

Until now the previously described angiography procedure serves a diagnostic purpose, but does not intend to cure the narrowing problem. To this aim, a guide wire is slided into the catheter to reach the stenosis or occlusion. Then, a balloon (with an elongated shape) is threaded over the guidewire up to the lesion. When its placement with respect to the lesion has been checked, by using the marker-balls at the balloon extremities, a pump is used for the inflation. The balloon is kept inflated to compress the plaque (see Figure 2.5a) during several seconds with a pressure depending on the type of balloon and the type of lesion[2]. After deflation the artery opening is controlled by an angiography and then the balloon is removed if the blood flow is correctly restored. Otherwise, this operation can be repeated. Balloon angioplasty is safer than the CABG, but arteries are more frequently re-narrowed over time.

The risks of re-stenosis can be greatly decreased by using a fine mesh tube of wire,

[2]The pressure applied to the balloon is counted as multiple of the atmosphere pressure (e.g. 10 atmospheres).

(a) Balloon angioplasty

(b) Stenting angioplasty

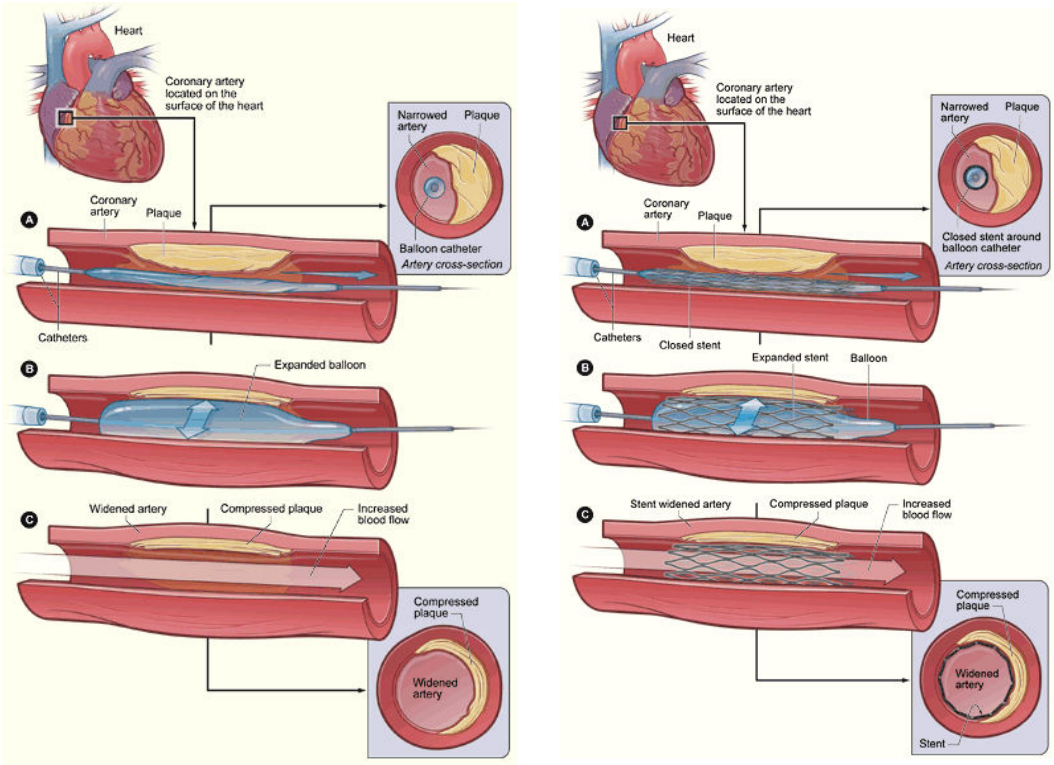

Figure 2.5: Illustration of an angioplasty procedure. (a) and (b) respectively illustrate the balloon angioplasty procedure and the stenting procedure.

called a **stent**, that prevents the artery walls to collapse again after the procedure (two examples are provided in Figure 2.6). The metal structure of the stent supports the artery walls and prevents the artery to be narrowed or blocked again. The stent is wrapped around the deflated balloon and when the balloon is inflated to compress the plaque, the stent expands and apposes the artery walls. After balloon deflation the stent remains in the artery as illustrated in Figure 2.5b. The correct deployment of the stent can be controled using elaborated techniques called "digital stent enhancement". It consists in combining images with a low contrast to noise ratio in order to boost the stent visibility in the image. If no further medical action is needed, the balloon and guide wire are removed, then the catheter is pulled back. Over time, cells in the artery grow to cover the stent mesh creating an inner layer identical to normal artery walls.

(a) Cypher stent [Cardiovascular News, 2004]

(b) Xience V [Diagnostic and Interventional Cardiology, 2014]

Figure 2.6: Example of stents.

The procedure usually takes from thirty minutes to three hours depending on the difficulty of the case. In case of complete blockage of the blood flow, which corresponds to a total occlusion, a "digging"-step that is also called crossing is necessary to go through the occlusion. When the guide-wire has dug its way through the entire occlusion, a balloon can then be introduced and the clinical procedure steps that follows are the same as in stenosis treatment. While the PCI technique to treat stenosis is well established by the community, optimal clinical approaches regarding Chronic Total Occlussion (CTO) procedures are still discussed. Several examples are:

- Antegrade approach: from the aorta, the guide-wire follows the blood flow and the occlusion is attacked from the anterior side. A schematic representation is provided in Figure 2.7.

- Parallel wire technique: two guide-wires are used to penetrate the occlusion. They are slided alternatively to dig a way through the occlusion.

- Retrograde approach: this technique takes advantage of the collateral vessels[3] to pass the occlusion from the posterior side.

Chronic Total Occlusion (CTO) treatment requires greater skills from the cardiologist and increases the procedure duration as well as the complication risks.

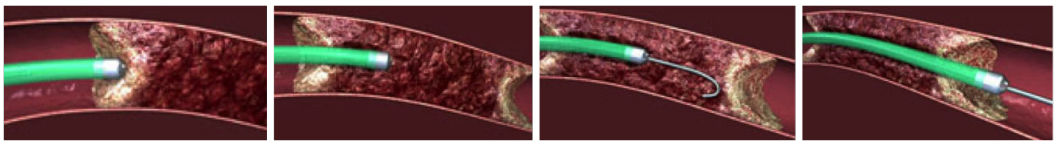

Figure 2.7: Digging through a CTO.

2.2 Angiography

The previous section was focused on the clinical side of the atherosclerosis pathology and treatment. In this section, we depict the Percutaneous Coronary Intervention (PCI) from the imaging point of view. Angiography can be used for diagnostic purposes in order to asses the size and length of a lesion. It is crucial to decide if a stenosis should be treated or not. Angiographic images are also involved during the navigation of the guide-wire in the patient's vasculature.

2.2.1 C-arm System

As it has been mentioned earlier, the C-arm system is the central element of an interventional room called a "cath-lab", which stands for catheterization laboratory. This system allows to visualize the patient's anatomy by the mean of X-rays to perform minimally invasive interventions. Interventional tools are navigated under live control of the imaging system, which provides real-time X-ray video when the clinician presses the X-ray pedal. The main components of the cath-lab are presented in Figure 2.8. The core of the cath-lab is the C-arm system, which acquires the X-ray images of the patient.

The denomination "C-arm" comes from the shape of the structure supporting the X-ray source and detector (see Figure 2.9). The X-ray tube generates a cone beam in the direction of the flat-panel detector. The beam direction is controlled by two perpendicular rotation axes, indicated in blue in Figure 2.9, that allow the system to image the anatomy in every possible angulation[4]. To image the anatomy of interest, translational degrees of freedom are necessary to position the patient correctly in the X-ray beam. The patient lies on his back on a table that is able to translate along three axes.

X-ray are produced by a beam of electrons traveling from the cathode to the anode inside the source part of the C-arm (also called the X-ray tube). X-photons

[3] Collateral vessels are "bridges" between the left and right coronary artery trees that are created to re-root the blood flow to non-irrigated myocardium regions.

[4] In practice collisions with the patient and the table limits the space of attainable positions.

Figure 2.8: Interventional Guiding System, IGS-520 from GE Healthcare, presenting main components of the cathlab: the C-arm system, the table and the large display monitor.

Figure 2.9: Interventional Guiding System, IGS-740 from GE Healthcare. The detector and X-ray source are linked by a C-shape structure. Blue arrows indicate the two rotational articulations of the system that allows to attain any possible angulation.

are produced in random directions at the surface of the anode, modeled by a point, called the X-ray source. All photons are absorbed by the tube except for a small opened window limiting the X-ray beam to a given solid angle in the space. Several metal filters are applied to the beam as well as a square shape collimator that cuts off the beam outside a given region of interest. X-rays are attenuated by the anatomy of the patient according to the Beer-Lambert law that is further detailed in Section 4.2.1. Remaining photons are caught by the detector and are transformed into an electric signal by a matrix of photo-diodes. Capacitors gather intensity created by these photo-diodes that is then converted into pixels intensity that will form the resulting image. Historically, fluorescent screens were used to convert X-ray photons, which have given the name of 'fluoroscopy' to the resulting image. The same principle is still used in several detectors, where a scintillator layer converts X-photons into visible photons.

This fluoroscopic image corresponds to the conic projection of the patient anatomy onto the image plane. The corresponding projective operator is a 3×4 matrix that allows to project a point in the three-dimensional (3D)-space of the interventional room into the 2D image plane. These matrices can be determined using a model of the C-arm system and the set of parameters describing the machine configuration during the acquisition. An alternative is to perform a calibration of the system geometry for many angulations. In both cases, the parameters needed to retrieve the system state are transfered simultaneously with the images. Multiple acquisition modes are available in an imaging system, resulting in different frame rates (up to 30 images per second), dose levels, post-processing and so on. These settings may depend on:

- The clinical application: C-arm systems are used to guide cerebral aneurysm treatment in neuroradiology, chemoembolization of liver tumors in interventional oncology or stent placement in Percutaneous Coronary Intervention (PCI).

- User preferences and patient's size: a compromise between image quality and radiation dose must be found, following the ALARA principle (As Low As Reasonably Achievable).

- The moment of the procedure: in PCI the expectations in terms of image quality are not constant at each step of the procedure. For example, a low-dose acquisition mode, is called **fluoro**, is generally used during the guide-wire navigation phase to limit the patient's exposure to radiations. On the contrary, diagnostic angiograms and controls of the stent deployment necessitates optimal image quality. This latter acquisition mode is called **record** or **cine**[5].

In this Ph.D. thesis, only cine angiography sequences, which were performed during the procedure, will be used. In the following, we will most of the time refer

[5]As indicated in the name "record", images acquired with this mode are always recorded and then transfered automatically using the DICOM standard.

to the X-ray images by the general term of **fluoroscopy**. This term is the mostly used in the image processing community and we decided to follow.

2.2.2 Angiography and Guidance

The C-arm system allows to visualize clinical tools inside the patient in real time, which opens the way to minimally invasive procedures. An example is provided in Figure 2.10a where the patient's heart is imaged. One would note that even if some anatomical parts are visible, both the heart and coronary arteries cannot be seen in the image. Actually, the X-ray image formation is based on the attenuation of the beam by the patient's anatomy. This property is often called "radio-opacity". Contrasts in the image are thus due to the difference between the attenuation coefficient of penetrated structures. The attenuation coefficient of the bones, which are composed of a dense arrangement of calcium, is much higher than soft tissues (such as muscles). Therefore, ribs can be well distinguished in the image. Actually, images presented here have been automatically processed by the system to make the bony structure less apparent since they are not important for the targeted clinical application. However the attenuations of fat, muscle tissues and blood are quite similar to each other and thus the coronary arteries cannot be distinguished in the image.

In order to visualize these structures of interest an iodine injection is performed into the patient's arteries via the catheter. Iodine, by nature, has much higher attenuation coefficient than the surrounding tissue. When it fills the vasculature, vessels becomes well contrasted in the projected image as shown in Figure 2.10b. For this reason the iodine product is also called **contrast medium**. The clinical exam that involves to inject contrast medium in order to reveal the vasculature is called an angiography. It allows to diagnose atherosclerosis and decide on the recommended type of treatment. This modality allows to assess the gravity of a stenosis by measuring the degree of occlusion (which can be done with a tool called Quantitative Coronary Analysis, or QCA). However, the distinction between soft tissues and calcified plaque cannot be made in the angiography contrary to the X-ray scanner imaging (see Section 2.3).

Besides this diagnostic application, contrast medium injections are also crucial during the navigation phase of the minimally invasive treatment. The guide-wire navigation down to the pathologic area is performed under X-ray guidance because its extremity is built of a material with a high radio-opacity. The guide-wire tip is well identified in fluoroscopic images (see Figure 2.11a) but an injection of contrast medium is necessary to visualize its position with respect to the vasculature (Figure 2.11b). Angiography is also often recorded after a stent implantation to assess if the blood flow has been correctly restored.

Angiography allows live guidance during the intervention. By visualizing the guide-wire with respect to the vasculature, the clinician is able to adapt his/her gesture to reach the pathology location. However, three major limitations due to the nature of this modality have been identified:

(a) Non-injected acquisition (b) Angiography acquisition

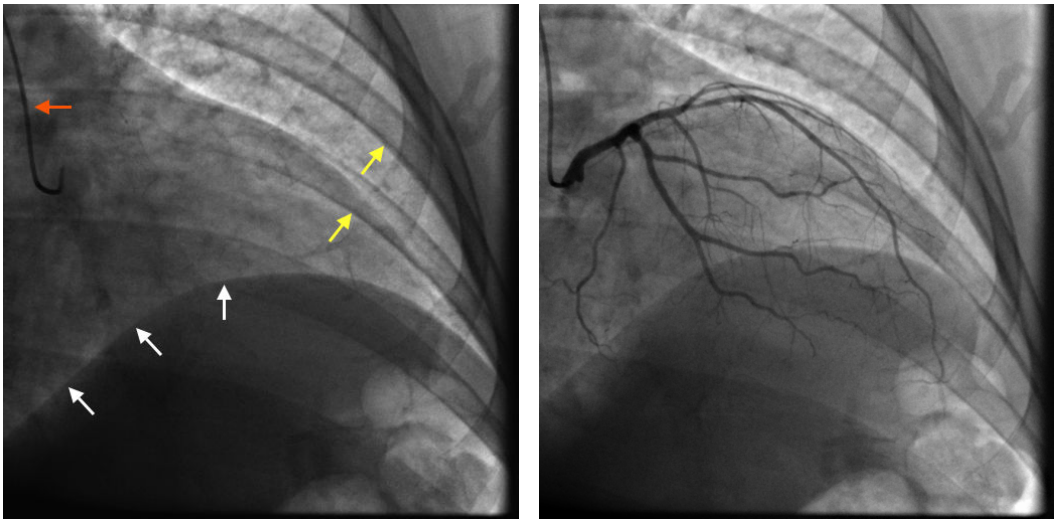

Figure 2.10: Fluoroscopic images with (b) and without (a) contrast medium injection. Arrows in (a) point out the injection catheter (orange), ribs (yellow) and the diaphragm boundary (white).

(a) Non-injected navigation phase (b) Injected navigation phase

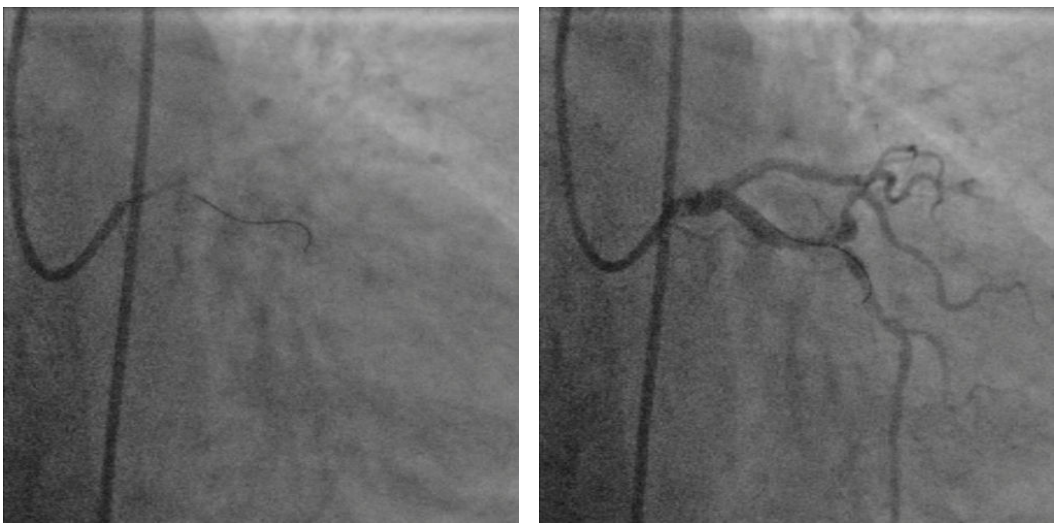

Figure 2.11: Guide-wire navigation in the coronary arteries under X-ray guidance (fluoro acquisition mode). (a) shows a non-injected image where the guide-wire tip is visible but not the arteries. (b) injected image where the position of the guide-wire with respect to the patient's vasculature can be seen.

- Because of the projective nature of the fluoroscopy, the angiogram may be difficult to interpret at some locations. Vasculature superimpositions shall be limited as much as possible around the vessel of interest since it leads to indetermination in guide-wire position. It is the physician that is in charge to place the C-arm to reach this desirable situation.

- A displacement along the projective direction cannot be well assessed in the projective image. Thus, the navigation inside a given vessel is facilitated if the projection axis is orthogonal to a plane containing the vessel. This lack of depth perception imposes the cardiologist to adapt the C-arm angulation to the step of the intervention and the coronary of interest.

- In case of total occlusion, contrast medium cannot fill the occluded vessel that remains invisible in the angiography (see Figure 2.12a). The navigation through the occlusion is performed without visualizing the vessel and is so called "blind"-navigation.

The two first problems often impose the clinician to change angulation of the system along the intervention. Some cardiologists prefer to deal with complicated clinical cases using two simultaneous different views of the patient anatomy by using a bi-plane system (as the one presented in Figure 2.13). However, this practice is quite marginal in the interventional cardiology community and is beyond the scope of this thesis.

(a) Before stenting angioplasty (b) After stenting angioplasty

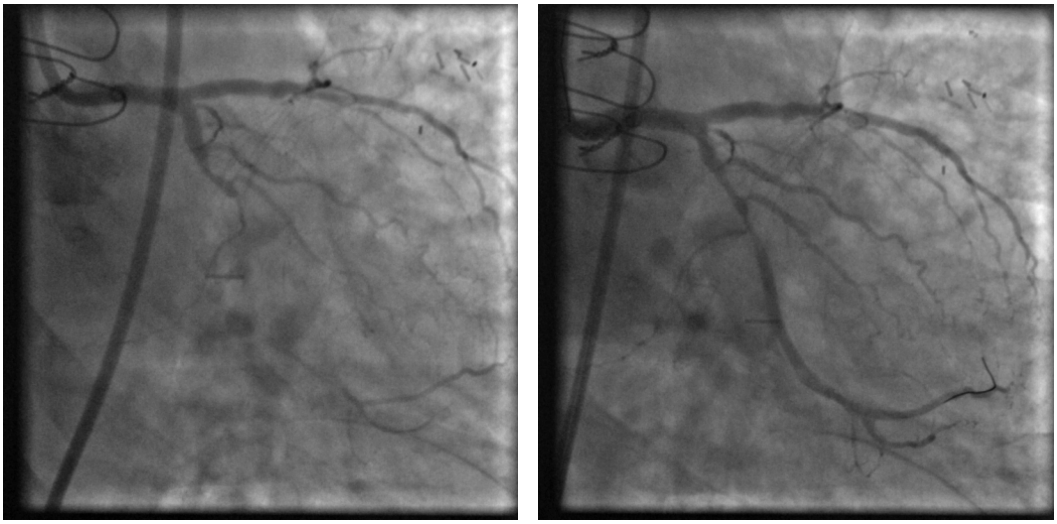

Figure 2.12: Chronic Total Occlusion (CTO) treatment by stenting angioplasty. In (a) despite the contrast medium injection the occluded part, visible in (b) after treatment, remains invisible in the angiography.

Figure 2.13: Example of bi-plane system: Innova IGS 630 from GE Healthcare. The secondary plane acquisition is provided by a ceiling mounted system.

2.3 Computed Tomography Angiography

The Computed Tomography Angiography (CTA) can complement the interventional angiography. It consists in a 3D reconstruction of the patient's anatomy by the mean of X-rays while contrast medium is injected intra-venously to reveal the vasculature. The fine resolution in terms of contrast is a strong advantage of the scanner and allows to see and quantify calcifications in the atheromatous plaque.

2.3.1 X-ray Scanner System

The Computed Tomography scanner, or CT-scan, is used to image the patient's anatomy in three dimensions. It produces a set of images called slices[6] that constitute a 3D matrix of voxels called a volume. A slice can be seen as the intersection between a plane and the patient anatomy. A scanner is composed of a table, where the patient is lying, and the imaging system with a cylindrical hole in its center (an example is provided in Figure 2.14). The imaging system is constituted of a ring structure on which is attached a generator producing X-rays inside the ring. On the other side, photons are received by a detector attached to the ring structure. The underlying physical principle is quite similar to the one involved in the C-arm system presented in Section 2.2.1. The X-ray beam is attenuated by the anatomy depending on the attenuation coefficient of the anatomy. But contrary to the interventional angiography procedure, the source and detector of the CT-scan are continuously rotating around the patient during the acquisition.

From this set of rotational X-ray projections a volume can be reconstructed using tomography theory. The CT-scan acquires a set of projections at different angulations that allows to reconstruct the imaged volume in 3D. Details on reconstruction

[6]The term slice refers to the intuitive analogy to virtually cutting a slice of the patient anatomy.

Figure 2.14: Revolution CT from GE Healthcare.

theory can be found in [Langet, 2013], even if the subject was about Cone-Beam CT reconstruction. Theoretical requirements to ensure an analytical solution of the reconstruction problem can also be found in the same Ph.D. thesis. This work highlights the importance of acquiring enough data (sub-sampling problem) from a static object (motion artifacts[7]) in order to produce a relevant reconstruction. In the case of heart anatomy reconstruction, the main issue is the motion induced by the beating heart. Historically, CT-scanners only acquired very few slices such as single slice CT, where the detector was composed of a 1D array of cells. To acquire the multiple slices composing the volume, the table where the patient is lying is translated during the acquisition.

In cardiac-CT, the main goal is to provide a static reconstruction of the anatomy of the heart and not a dynamic (3D+t) reconstruction of the moving heart. Electrocardiogram (ECG)-gated acquisitions allow to synchronize the X-ray measurements with the heart movement in order to limit artifacts due to motion. CT reconstructions of the heart are usually performed to represent the heart during the diastolic phase, when the myocardium is quite stable. Thanks to the ECG, X-ray are generated during diastole phase until enough data have been acquired to reconstruct the heart. This technique also limits the irradiation of the patient by avoiding X-ray emission during cardiac phases that are not used in the reconstruction (such as the systolic phase). Recent advances in CT technology allows to perform an acquisition of the whole heart in less than 0.3 seconds as in the revolution CT from GE Healthcare presented in Figure 2.14.

2.3.2 Pathology Diagnosis and Therapy Planning

Besides a slightly different technology, the underlying physical principal of the CT-scan imaging is the same as the interventional fluoroscopic system. It is based on the

[7]The term artifact denotes structures in the reconstructed volume that does not correspond to the patient anatomy but to errors in reconstruction.

X-ray attenuation of the anatomy and the resulting intensities of the reconstructed volume elements (called voxels) are linked to the X-ray attenuation coefficient. As mentioned in Section 2.2.2, vessels present quite similar X-ray transparency than muscle tissues, which make them hard to distinguish. To make them appear, a contrast medium similar to the one used intra-operatively is injected in the patient's vasculature. However, contrary to interventional angiography, the Computed Tomography Angiography (CTA) does not involve intra-arterial injection and thus avoid catheterization. The iodine contrast medium is injected intra-venously to be diluted in the patient's vasculature, revealing thus arteries and veins in the resulting reconstruction. This CTA exam allows to detect coronary artery blockage in a non-invasive way, contrary to the catheterization procedure depicted in Section 2.2.2 that is a minimally but still invasive procedure. It thus results into a faster and safer exam that can be handled by a nurse or a radiologist.

Even if the reconstructed volume allows to assess the patient's anatomy in 3D, vessels are curvilinear structures that are not best visualized by a slice scrolling. Actually, the vasculature mostly appears as white dots and small tubular sections in the standard axial, coronal and sagittal views (see Figure 2.15). Several workstations propose to fully take advantage of the reconstructed volume by providing software tools adapted to the vessel visualization. The *Volume Viewer* application presented in Figure 2.15 allows easier understanding of the anatomy. By automatically segmenting the coronary artery trees, the *Auto-Coronary-Analysis* tool (Volume Viewer from GE Healthcare) presents a 3D rendering of the coronary arteries that can be rotated to see the anatomy from different points of view. This rendering allows the clinician to find optimal angulations to visualize best some vessels of interest, which can be pushed to the interventional C-arm system in order to retrieve the same point of view during the intervention.

Besides this planning purpose, the cardiac CTA acquisition is mostly performed for the diagnosis of coronary artery disease. The interventional angiography, described in Section 2.2.2, allows to assess the significance of the stenosis based on the estimation of the diameter reduction of the artery at the lesion location. A decrease of less than 50% between the vessel diameter outside and inside the stenosis is usually declared as non-significant. When the lumen of the vessel is reduced by more than 70% (of the diameter) the artery becomes obstructed enough to decrease blood flow. A CTA acquisition can be performed to visualize calcifications in the atheromatous plaque. Calcifications are calcium deposit along artery walls that are important to be taken into account in the classification of a lesion. Degree of calcification of a lesion impacts several choices made during the stent placement such as the type of balloon used, the pressure applied and the time of inflation. Example of calcified arteries are presented in Figure 2.16 in a so called curve-view (provided by the Volume Viewer application). Calcifications appear as a white deposit along the vessel border.

The CTA modality is also of great interest in case of Chronic Total Occlusion (CTO) where the artery down the occlusion are not visible in interventional angiography. Two reasons allow the visualization of the occlusion in CTA:

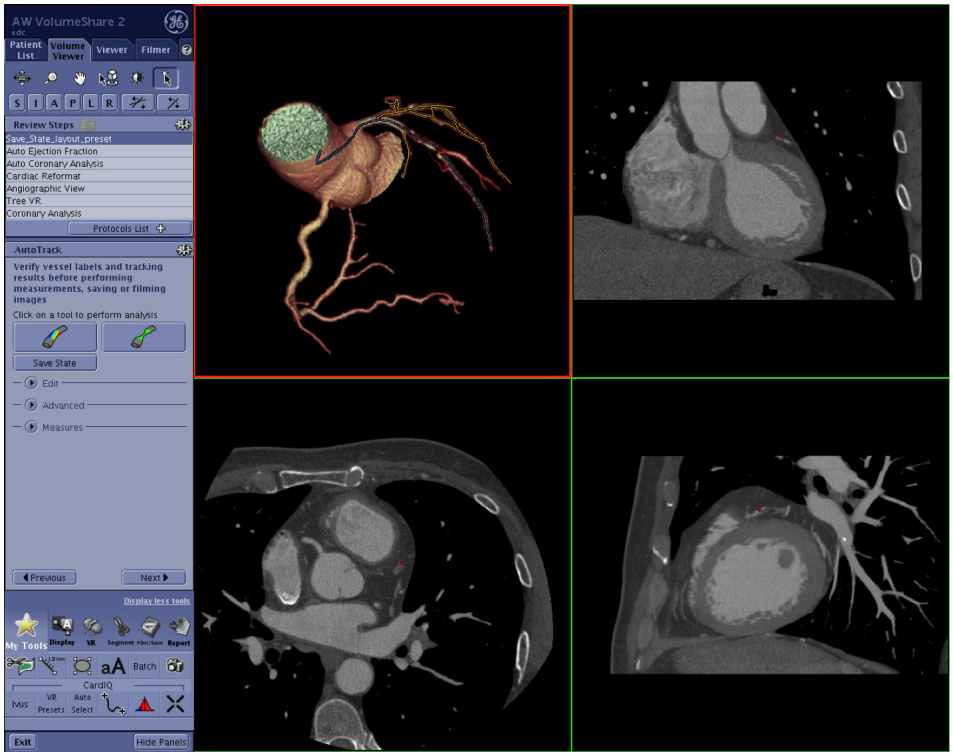

Figure 2.15: Volume Viewer from GE Healthcare interface on coronary visualization. In reading order: coronary volume rendering, coronal slice, axial slice and sagittal slice.

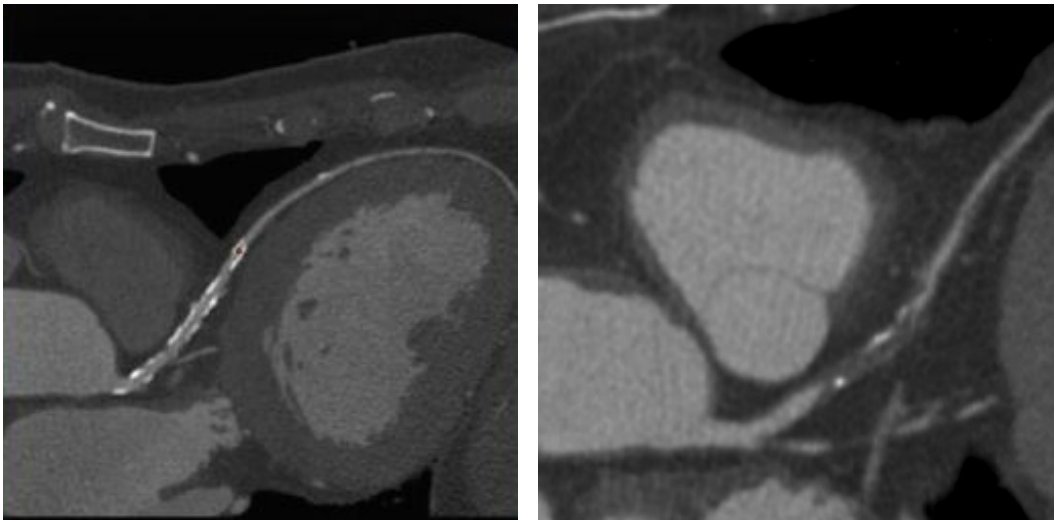

Figure 2.16: Curve-views of Left Anterior Descending (LAD) coronary arteries of two patients presenting calcified plaque. Calcifications are the hyper-intense signal at the border of the vessel.

- Intra-venous contrast product injection. Contrary to intra-arterial injection, the diluted intra-venous injection allows to visualize all the vasculature receiving flow. As highlighted in Section 2.1.1, collateral vessels can grow to irrigate parts of the myocardium that have been cut from the occlusion. In these vessels the flow is very limited and a sudden intra-arterial (retrograde) injection usually fails at showing vessels down the occlusion. However, in the case of intra-venous injection the whole vasculature receives a proportion of contrast medium for a while. Contrast medium has time to reach vessels down the occlusion by collaterals and contrasts the occluded vessel as shown in Figure 2.17.

- Better contrast sensitivity. The CTA modality allows to distinguish smaller contrast differences than the interventional modality and particularly the calcifications. If a stent has already been implanted in the patient's arteries, its location, deployment and interaction with the surrounding vessels are also visible in the reconstructed volume.

Therefore, this pre-operative CTA allows to characterize the composition of the occlusion as well as its length and tortuosity. Knowing the nature of the occlusion is very important during the crossing phase of minimally invasive CTO treatment.

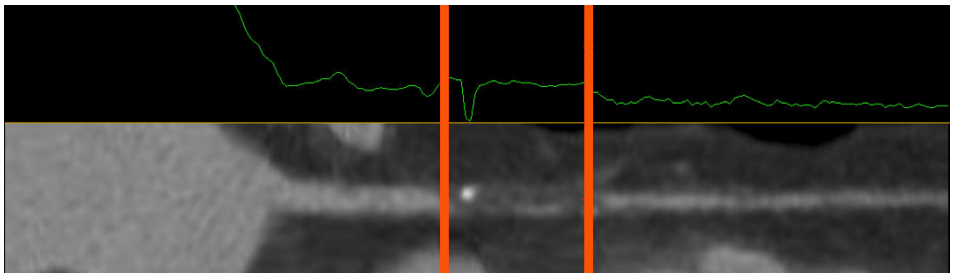

Figure 2.17: Lumen view of an occluded vessel (the occlusion is delimited by the orange lines). Calcifications in the plaque are visible as well as the length of the occlusion (between the two orange boundaries).

Reconstructing the coronary vasculature of the patient via CTA provides important inputs for the diagnosis of the pathology and the planning of an upcoming intervention. Dedicated visualization tools greatly facilitates these two goals by presenting the content of the reconstruction in a comprehensive manner[8].

2.4 Complementarity between Modalities

The previously described interventional angiography (Section 2.2) and cardiac CTA (Section 2.3) are showing great complementarity in the scope of atherosclerosis dis-

[8]Such tools necessitate a robust segmentation of the coronary arteries, which are depicted in Section 4.1

ease. At least, the following three points have been identified:

- **Easy depth perception versus superimposition and foreshortening**. The interventional angiography shows the vasculature of the patient projected into an image plane. By nature, this projected image lacks of depth perception and creates ambiguities at vessel superimposition. Bifurcations[9] often leads to such superimpositions and necessitates experience from the clinician to navigate though. In CTA all bifurcations are well defined and the 3D segmentation of the coronary tree allows to understand easily the patient anatomy.
- **Visible occlusion versus blind navigation**. In case of Chronic Total Occlusion (CTO), the 3D angiography allows to characterize the occlusion in terms of length and tortuosity. CTA also allows to assess the degree of calcification of an atheromatous plaque that is important to consider when treating both stenosis and total occlusion. All the previous types of information are not visible intra-operatively and the navigation in case of total occlusion must be achieved without seeing the surrounding vessel.
- **Static observation versus live guidance**. Surely the pre-operative CTA provides crucial information. However, the guidance of tools in the patient's vasculature must be controlled in real time. In the 2D live angiogram, the clinical tool position with respect to the current state of the vasculature allows the cardiologist to attain the pathology location.

The interventionalist could benefit from a fused visualization of CTA and live angiography and thus taking the best of the two modalities.

2.4.1 Clinical Application Propositions

In the CTO summit of 2015 [Escaned, 2015], several fusion applications have been raised to take advantage of the two complementary modalities. In case of total occlusion, the projection of the volume on top of the fluoroscopic image can give an idea on the progression of the guide-wire inside the occlusion. Figure 2.18 gives an idea on what could be a 2D roadmap application in case of occlusion. A variant of this 2D roadmap can be to only highlight calcifications, which may also be useful in the case of simpler lesion such as standard stenosis.

A 3D roadmap application can also be imagined, where the tip of the guide-wire is segmented and is shown in the 3D vessel of interest. Intra-operative presentation of the 3D roadmap can be of different natures:

- Adding a sort of progress bar on the lumen view of Figure 2.17.
- Adding guide-wire tip positioning in the curve-view of Figure 2.16.
- Providing a reconstruction of the guide-wire positioned in the 3D vasculature that is seen from an interesting point of view (that may be non-reachable by the system due to collisions).

[9] A bifurcation is the anatomical point where one vessel separates into two (or more) vessels.

(a) Fusion CTA angiogram (b) Guide-wire tip zoom

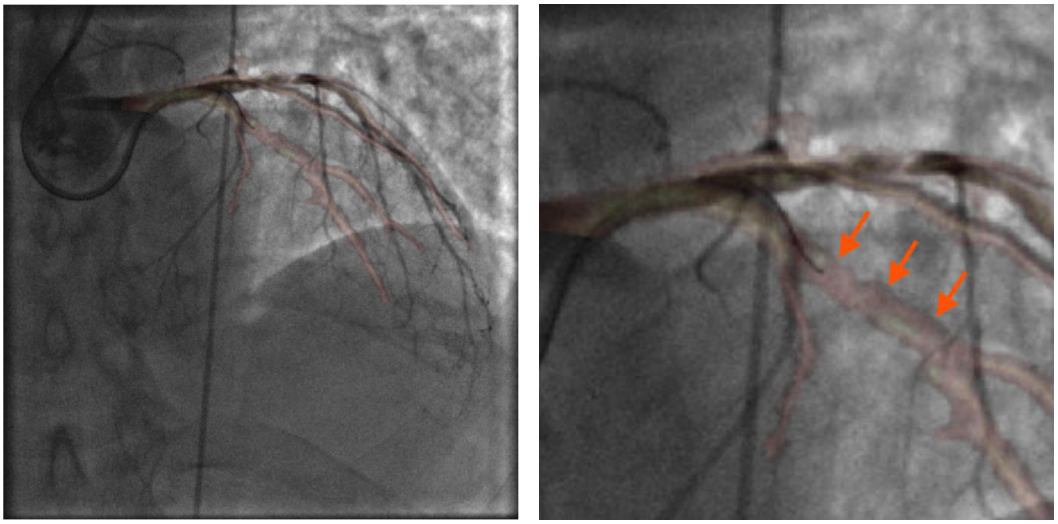

Figure 2.18: Example of 2D roadmap fusion during a CTO treatment while the guide-wire is entering the occlusion. The location of the occluded vessel (pointed by orange arrows) is visible thanks to the projection of the coronary tree extracted from the CTA.

Pre-operative CTA reconstruction can also be used to propose optimal angulations to the clinician during the procedure. Thanks to the 3D vasculature, one is able to predict superimposition of vessels that may occur and find system positioning that limits their number. If the guide-wire tip is localized (by segmentation) the system can also adopt automatically the angulation minimizing the projective foreshortening of the vessel currently navigated.

From a patient perspective, the fusion application could lead to multiple benefits:

- Fusion may facilitate the gesture of the clinician by increasing its confidence, which may lead to decrease the procedure duration. Faster procedures are synonymous of less X-ray exposure for the patient and thus less risks induced by radiations.

- After a recorded angiography sequence used to perform the registration, the cardiologist can benefit from the fusion application to save contrast medium injections. In fact, some small injections used to confirm the guide-wire position with respect to the vasculature could have been avoided if 3D registered vessels projection is available during the procedure. Saving contrast medium is of interest for the patient since a large amount of contrast material may induce complications after the procedure.

2.4.2 Registration Necessity

All applications of the previous Section 2.4.1 necessitate to bring the two different modalities into correspondence. Actually, both acquisitions represent the patient anatomy at two different states: before the intervention inside the X-ray scanner; and during the intervention imaged by the C-arm system. Each state refers to its own three-dimensional system of coordinates, denoted $\mathbb{S}_{pre}$ for the CT-scanner and $\mathbb{S}_{intra}$ for the C-arm system, and the relation between them is unknown. In order to fuse these two complementary modalities, a step of registration is necessary.

To be used in a 2D roadmap application, the registration algorithm should provide a transformation $\hat{T}$ from $\mathbb{S}_{pre}$ to $\mathbb{S}_{intra}$ that aligns correctly the pre-operative volume with the patient. This transformation must compensate the absence of geometrical pre-defined link between the two systems and the relative displacement of the patient. It may also compensate a temporal change such as the respiratory motion and the heart beat. For this role, the alignment is not expected to require more complex model than a standard rigid transformation. Finding this optimal transformation may be sufficient to propose a roadmap in the image plane. But correspondences between the two modalities must be provided to build a 3D application. Actually, for a given position of interest in the 2D vasculature we are looking for the corresponding vessel portion in 3D. Thus, in addition of a correct alignment, a registration algorithm must also provide relevant correspondences between the pre-operative and intra-operative acquisitions.

Chapter 3

State of the Art

Contents

3.1 Registration Problem Overview

The literature on medical image registration is quite huge and involves a wide variety of applications. Multiple reviews have been published on this topic, such as [Maintz and Viergever, 1998; Zitová and Flusser, 2003; Sotiras et al., 2013], which provide an interesting lecture grid to classify different registration algorithms. In this thesis, we will restrict the literature description to the 3D/2D registration case, which is a topic of its own, as shown in the review of [Markelj et al., 2012]. But before, we propose an overview of the registration problem and the key points of its resolution in order to familiarize the reader with the topic of registration in general and the major challenges to overcome.

In the example of our application, the 3D pre-operative Computed Tomography Angiography (CTA) and the 2D angiography performed during the intervention give complementary information that influences the therapy strategy. The interventionalist could benefit from a fused visualization of CTA and live angiography but it necessitates bringing them into the same referential. Actually, both modalities represent the patient anatomy at two different states: before the intervention inside the X-ray scanner; and during the intervention imaged by the C-arm system. Each state refers to its own three-dimensional system of coordinates and the relation between them is unknown. Integrating the pre-operative anatomical information into the

live guiding image to provide a guidance application necessitates to bring these two referential into correspondence.

This alignment is represented by a transformation that compensates the absence of geometrical pre-defined link between the two systems, the relative displacement of the patient between the two acquisitions and the change in anatomical states. Finding the optimal transformation that best aligns the pre-operative 3D anatomy with the 2D intra-operative one refers to the **registration problem**. It is generally expressed as solving the following equation:

$$\hat{T} = \underset{T \in \Omega}{\operatorname{argmin}} \mathcal{D}\left(T(\mathcal{Y}), \mathcal{X}\right) \tag{3.1}$$

where $\hat{T}$ is the sought transformation aligning the two complementary modalities $\mathcal{Y}$ and $\mathcal{X}$, Ω is the set of admissible transformations, and $\mathcal{D}$ is called the objective function and quantifies the distance or dissimilarity between structures.

As mentioned in different survey of medical image registration, such as [Maintz and Viergever, 1998; Zitová and Flusser, 2003; Markelj et al., 2012; Sotiras et al., 2013], choosing the objective function $\mathcal{D}$, the set of admissible transformations Ω and the minimization approach to compute Equation (3.1) constitute the major challenges of a registration problem. Moreover, to be used in a roadmap[1] application, a registration algorithm should provide correspondences between the two structures to be matched. Actually, for a given 2D position $x \in \mathcal{X}$ of interest to the clinician, a roadmap application should be able to provide the 3D corresponding point $y \in \mathcal{Y}$. Besides its importance regarding the clinical application, the notion of **pairing** is strongly related to the problem of registration.

Objective Function: The objective function $\mathcal{D}$ quantifies the quality of the alignment between the two structures to be matched $\mathcal{Y}$ and $\mathcal{X}$. Its definition is crucial since $\mathcal{D}$ constitutes the core of Equation (3.1) and thus determines the registration problem. It is assumed that the objective function reaches its minimum for a perfect alignment. Multiple properties are appreciated regarding an objective function such as a limited number of local minima (even the convexity), its linearity or the efficiency of its computation. Two types of objective function can be distinguished depending on the information representation. **Intensity-based objective function**, also called similarity measure in the literature, refers to a direct comparison of two images. In the case of CT-to-X-ray registration, since the physical principle of the two acquisitions is the same, efforts to bring the two modalities into comparable images are relatively low compared to MR-to-X-ray for example. This class of objective functions is usually preferred when structures to be matched are not sparse in the image or challenging to segment. They can involve direct pixel intensity comparison, estimations based on image gradients or enhanced version of the original image. **Feature based objective function** involves a sparse geometric representation of the information contained in both modalities to evaluate the quality of the registration. These approaches are independent of the type of modality

[1] A roadmap application has been defined in Section 2.4 regarding the 3D/2D case.

involved but strongly depend on the segmentation accuracy. The objective function corresponds to the distance between the two structures and depends on the feature representation. Features can be a set of non-connected points, curves composed of connected points or even more complex structures such as trees or graphs.

Admissible Transformations: The set of admissible transformations Ω constitute the set over which the optimization will be run. Its dimension is called the number of degrees of freedom (DoF) allowed by the transformation and corresponds to the minimal number of parameters necessary to define the transformation (for example a rigid transformation in the 3D space is a 6 DoF transformation). The more Degrees of Freedom are allowed in the registration, the better fit can be obtained during the registration. However, the difficulty to converge to the correct registration transformation during the optimization procedure is increased with the number of DoF. Usually registration algorithms progressively increase the number of DoF along the iterations, starting from a translation only (3 DoF or 2 DoF in the case of 3D/2D registration), then a rigid registration (6 DoF). Non-rigid registration algorithms can involve a global affine transformation (9 DoF) optimization, or more local deformation fields based on interpolation theory such as spline-based deformation field. When the number of DoF becomes large, as in Free Form Deformation (FFD) where a displacement vector is attached to every point of interest in the structure, a regularization term is often added to the objective function in order to keep a plausible deformation fields.

Optimization Procedure: The optimization procedure aims at finding the global optimum of the objective function $\mathcal{D}$ over the set of admissible transformations Ω. It can be based on an iterative best displacement in Ω such as the nearest neighbor or the downhill simplex method. Other optimization procedures are based on the gradient of function $\mathcal{D}$ such as the gradient descent or the Newton method. While the first type of methods is best suited when the local gradient estimation is not easily available, the latter is usually faster to converge toward the closest local minimum. A third type of methods relies on pairings between the two structures and generally consists in alternating the estimation of the pairing and the optimization of the transformation based on this pairing set. All these methods can be robustified by integrating them into a multiple initialization framework, where multiple starting positions are evaluated to run the registration.

Pairing Procedure: In this manuscript, we use equivalently the terms "pairings", "correspondences" and "matches" to refer to the association of two different modalities. The pairing procedure refers to the construction of a set of pairings that is crucial to build a roadmap application and is used in most of feature based registration methods. In clinical application of 3D/2D registration, providing the position in the 3D pre-operative modality that corresponds to the current location of the navigated tool in the 2D guiding image is called a roadmap application. Correspon-

dences between 3D and 2D locations are given by the pairing set resulting from a registration algorithm. Thus, the pairings between structures is of great importance in an interventional application scope even if it is rarely addressed in the literature on 3D/2D vascular registration.

The registration problem is sometimes solved in the literature following an extrinsic approach: using calibration tricks, synthetic markers or manual anatomical point-of-interest identification. These methods may have an impact on the clinical procedure and will not be considered in the scope of this state of the art. Our study is focused on approaches relying on the informative content extracted from both modalities that are qualified in [Markelj et al., 2012] as intrinsic methods. Intrinsic registration algorithms can be classified in two classes: **intensity-based** and **feature-based**. The first class of methods directly uses image contents to build the objective function to be optimized. Both modalities are thus considered as images (volume of voxels and grid of pixels) that will be compared with a similarity measure comparing their respective intensities. On the contrary, feature-based algorithms involve a sparse representation of the vasculature to be matched. Each modality is no more considered as a set of pixels (or voxels) but as a geometrical representation of the information contained in the image. Several intensity-based approaches use segmentation to restrict the computational time as well as focusing the objective function into informative parts. Such methods will not be classified as feature-based if no sparse geometric representation is involved. In the following sections we will be interested in both types of registration techniques, focusing our classification onto 3D/2D registration of vascular structures that only involves single plane acquisition.

3.2 Intensity-Based Methods

Intensity-based registration methods address the registration problem, expressed in Equation (3.1), by minimizing a dissimilarity criterion (or maximizing a similarity criterion) $\mathcal{D}$ based on voxels and pixels intensities. In the case of 3D/2D registration, comparing both modalities requires to bring them into the same dimensional space. As mentioned in [Markelj et al., 2012], one can either compare the volume projection into the image plane, or reconstruct a volume from the 2D modality. The latter is beyond the scope of this work since we expect single view acquisition that is not sufficient to provide a 3D reconstruction. Thus, in the following we will consider dissimilarity criterion between two images: $I_{\mathcal{Y}}$ related to the fluoroscopic image and $I_{\mathcal{X}}$ obtained from the projection of the 3D volume $V_{\mathcal{X}}$. We distinguish two classes of methods: "pure" intensity-based methods that use all pixels and voxels information to run the registration; and Region of Interest (RoI) focused intensity-based method that involve a step of segmentation to restrict pixels that will contribute to the similarity measure.

3.2.1 "Pure" Intensity-Based Methods

The Computed Tomography Angiography (CTA) volume and the fluoroscopic image are obtained from similar principles that involve X-ray attenuation. Their registration is referred as "quasi-intra-modal" in [Markelj et al., 2012] because one is able to obtain a relatively good simulated projective image from the 3D reconstructed volume. Casting rays from a source point into an image plane and simulating their X-ray attenuation inside the volume $V_{\mathcal{X}}$ creates an image $I_{\mathcal{X}}$ quite similar to what would be obtained in the corresponding intra-operative acquisition. This simulated image is called a DRR for Digitally Reconstructed Radiograph. Besides several neglected physical effects that contribute to the image formation, such as heel effect, scatter and truncation, the DRR image is directly comparable to the fluoroscopic image without additional treatment.

In [Metz et al., 2009], the Normalized Cross Correlation (NCC), which is based on a direct comparison of pixels intensities, is used as the similarity criterion $\mathcal{D}$. They use a gradient-based optimization technique that estimates the gradient of the NCC measure with respect to the 6 degrees of freedom of the sought rigid transformation. The similarity measure $\mathcal{D}$ is seen as a function mapping a 6 dimensional space (the set of rigid transformation) to a real value (the similarity). From a start point in this 6D space, given by initialization, the gradient descent method finds the closest local minimum by traveling in the direction pointed by the gradient of the similarity measure at the local position in the search space. Considering the application to 3D/2D coronary arteries registration, it has been highlighted in this work that static structures, such as ribs, can impact greatly the registration by creating several local minima in the function.

Obviously the NCC is not the only similarity measure that can be used to compare the DRR $I_{\mathcal{X}}$ and the reference fluoroscopic image $I_{\mathcal{Y}}$. In [Hipwell et al., 2003], a comparative study of several similarity measures (including the NCC) is performed in the context of 3D/2D cerebral vessel registration. All these measures were extracted from the work of [Penney et al., 1998] on 3D/2D spinal registration, where they are properly defined. Some of these measures are directly based on intensities of $I_{\mathcal{X}}$ and $I_{\mathcal{Y}}$ such as the normalized crossed correlation, the entropy of the difference image or the mutual information. Other refers to images gradient such as the gradient correlation or the gradient difference. Contrary to the previous CT-to-X-ray registration, the use of Magnetic Resonance (MR) scanner in this application involves completely different image formation principle than the X-ray modality. The authors of [Hipwell et al., 2003] made particular efforts to produce DRR from the MR angiography that looks like the 2D X-ray Digitally Subtracted Angiogram (DSA) of the brain vasculature. They finally concluded that gradient-based approaches perform best with subtracted modalities.

In the above references, a given pixel in the fluoroscopic image $I_{\mathcal{X}}$ corresponds to a unique pixel in the DRR image $I_{\mathcal{Y}}$. However this DRR pixel corresponds to the contribution of all voxels of the volume belonging to the projective ray. Thus correspondences between the two modalities are not one-to-one established but one

pixel in the image corresponds to multiple voxels in the volume. In the original work of [Kerrien et al., 1999], the standard DRR generation is replaced by a Maximum Intensity Projection (MIP). The MIP image is formed using the same ray casting principle as in the DRR, but only one voxel contributes to the intensity of a pixel in $I_{\mathcal{Y}}$: the one with the maximum intensity along the projective line. This MIP image is then compared to the acquired DSA of brain vasculature. After a step of in-plane alignment obtained by the optimization of the NCC with respect to the two translations parallel to the image plane, [Kerrien et al., 1999] assume that this initial pose, complemented with the alignment in rotation given by calibration, enables the use of local methods such as the optical flow. Computing the 2D optical flow is also justified by the resemblance between the MIP image and the 2D injected image. The use of the MIP is crucial because it allows to associate to each pixel of the MIP one unique voxel in the volume (which is the only one to contribute to the intensity). This property allows to retrieve a 3D transformation from the 2D/2D pairings given by the optical flow. So as [Metz et al., 2009], this paper highlighted the problem of computational time for image based methods that necessitate the projection of the volume. In [Kerrien et al., 1999], it is proposed to estimate new MIPs from a previous one, obtained at another volume position, by approximating a 3D transformation by a 2D one. Contrary to other previous approaches, authors of [Kerrien et al., 1999] use an exhaustive search strategy at different volume resolutions to explore the set of rigid transformations. However the computational time remains the main issue of all of the above methods.

3.2.2 RoI Intensity-Based Methods

The class of Region of Interest (RoI) intensity-based techniques contains a step of segmentation of at least one of the two modalities. Contrary to feature-based methods, which use sparse geometric representation to build matching between two structures, this segmentation is used to generate projective image $I_{\mathcal{Y}}$ only containing relevant information. Since only voxels/pixels of interest are considered, such methods are usually faster than their "pure" counterpart. As in pure intensity-based approaches the similarity measure between the two images $I_{\mathcal{X}}$ and $I_{\mathcal{Y}}$ is optimized to provide the registration position.

In the work of [Ruijters et al., 2009] a segmentation of the 3D coronary arteries is used to speed up the step of projection and focus the registration on vessel region. From the projection of the 3D segmentation, that corresponds to a binary image, is extracted a 2D distance map $I_{\mathcal{Y}}$ that will be compared to the vesselness image $I_{\mathcal{X}}$ computed from the fluoroscopic modality. The product between the distance image and the vesselness one is used as a similarity measure that is optimized using a Powell method inside a stochastic optimization approach. Starting from different samples spread in the space of admissible transformations, the Powell optimizer is launched. The objective function is evaluated at each convergence pose and the n best are kept. Random perturbations of the chosen poses create new starting position given to the Powell optimizer. This procedure limits the risk to fall into a

local minimum.

Few articles address the non-rigid registration problem in an intensity-based manner. To the best of our knowledge only [Gatta et al., 2011] addressed the problem of 3D/2D non-rigid registration of the vasculature. As in [Ruijters et al., 2009], the 3D CTA of the right coronary tree is automatically segmented to speed-up the projection step. But instead of computing a distance map from the 3D segmented projection, they compute the 2D vesselness on the 3D projected image. The deformation vector field is inferred in the 2D image by optimizing a similarity measure based on the difference between SIFT descriptors at each pixel. This method, called SIFTflow, provides a resulting 2D deformation field between the two images by minimizing the difference between images in the SIFT domain and two extra regularization terms. A comparison with another method, called the free form deformation, is provided in the same article, modeling the 2D deformation vector field using splines. The optimized objective function is composed of the normalized mutual information between the projected segmented 3D and the 2D vesselness images. Both methods were tested on a restricted database of right coronary arteries.

The two previous articles involved segmentation to restrict the number of pixels used in the projection and the similarity measure. However, no geometric representation of the vasculature was involved. Claiming for speeding up the projection of the vasculature, [Chan et al., 2004] assume that the 3D segmented vasculature can be represented by a set of 3D spheres. This original geometric representation is used to generate a 2D binary projection of the vasculature with low computational cost. However, this method is not classified in feature-based section because it only consider geometric representation as a trick to speed-up the projection and will not use it to build correspondences. Actually, the similarity measure is the sum of squared difference, computed between the projective binary image and the 2D DSA of the brain vasculature.

A similar approach is presented in [Turgeon et al., 2005] where the vasculature segmentation is projected into the image plane to produce a binary image. It is then compared to a binary segmentation of the 2D angiogram of the coronary arteries using the entropy correlation coefficient. The optimization of this similarity measure is performed using the Downhill simplex methods, considering two simultaneous orthogonal views to limit the number of local minima.

3.3 Feature-Based Methods

So as intensity-based methods, feature-based registration techniques solves Equation (3.1) by minimizing the distance $\mathcal{D}$ between two geometric representations of the structures of interest, called features. This objective function to optimize is generally based on underlying[2] pairings between the two sets of features. Pairings are of great importance because they open the way to roadmap application by providing

[2]The term underlying is used since some articles do not explicitly describe these pairings. However, correspondences exist implicitly because of the feature representation of the information.

correspondences between the planning modality and the live guiding image. In addition, this geometric representation allows to focus the registration on informative parts and generally results into faster algorithm by reducing drastically the amount of data. Structures can be of different nature such as a set of disconnected points, curves or even represented as hierarchically organized structures such as trees. Obtaining representative features in both modalities is a challenge of its own and will not be discussed here but in Section 4. State of the art methods often refers to model and data when one of the two features set is preferentially matched to the other. Regarding 3D/2D registration, the pre-operative 3D modality is usually considered as the model because it can be manually corrected to serve diagnostic purposes. In general, vessels are nicely modeled by their centerlines that can be represented by different types of features. In the following, articles from the literature are classified accordingly to their choice of features representing patient's vasculature.

3.3.1 Vasculature as a Set of Points

The simplest feature representing the vasculature is a set of points corresponding to the vessel centerlines location as it is represented in [Kita et al., 1998]. In this work, the registration is conducted using the Iterative Closest Point (ICP) algorithm applied to points constituting the skeleton of the segmented vessels in the MRA and in the DSA. Firstly introduce in [Besl and McKay, 1992], the ICP algorithm consists in the iteration of two steps: 1) pair each point of the model to its closest in the data; 2) estimate the transformation minimizing the distance between paired points. As in multiple articles from the literature, the work of [Kita et al., 1998] highlighted that the closest point pairing assumption made in the ICP framework can lead to incorrect pairings. Multiple refinements of the ICP algorithm have been provided in [Rusinkiewicz and Levoy, 2001] trying to solve the mispairing problem without changing the closest point assumption. These refinements include the selection of point of interest, the rejection of point pairs or the weighting of pairs. In order to avoid mispairing, [Kita et al., 1998] restricts the search zone in which closest point is sought. Each 3D point will be associated to a 2D region obtained via a growing procedure around its projection location as in a Voronoi diagram. It will then be paired to the closest point of the 2D structure inside the corresponding Voronoi region. This anisotropic search avoids bad pairings in case of missing vessel portion in the segmented structure. An adaptation of the transformation estimation to the case of 3D/2D point pairing is provided in the article.

Other, as [Sundar, 2006] and [Rivest-Henault et al., 2012], are also interested in optimizing the sum of closest point distance with respect to the set of rigid transformation. But in order to speed up the evaluation of this cost function, they compute a distance map relative to the 2D features. To each pixel in the image plane is associated a value corresponding to the distance to the closest centerline point in the 2D features. Its construction avoids looking for the closest point in the 2D structure for each 3D point by only getting the value of the distance map at the 3D point projection position. The underlying pairing set can be retrieved in the

same way using the chamfer matching, as presented in [Borgefors, 1988]. In [Sundar, 2006], this distance map is computed directly from the 2D segmented vessels, avoiding thus the step of centerline extraction, adding some modifications to behave like a real centerline distance map. Authors of [Sundar, 2006] evaluated three different optimizers (best-neighbor, Powell and gradient descent method) to optimize this objective function, while authors of [Rivest-Henault et al., 2012] provide a comparison between 9 different optimizers including the best-neighbor, the downhill simplex, the Powell and two global methods. Regarding the set of admissible transformations, [Sundar, 2006] consider rigid transformations and [Rivest-Henault et al., 2012] propose to add progressively more and more degrees of freedom. Starting from an inplane translation only optimization, an optimal rigid transformation then an optimal affine transformation is sought. Selecting the best optimizer generally leads to a compromise between accuracy, robustness and computational time. The latter has to remain low in order to be used in an interventional context. An interesting point to note in [Rivest-Henault et al., 2012] is the table presenting the objective function values with respect to the error computed using ground truth. It shows that smaller closest point pairing distance do not always correspond to lower error. Thus, even using the best possible optimizer the closest point pairing assumption may result into a wrong registered position.

In order the increase to robustness of algorithms based on distance map [Florin et al., 2005] use an optimization technique based on a Bayesian process and particle filtering. This method is based on the propagation of a set of particles representing different registration hypotheses (i.e. registration transformation). Each particle is associated to a weight related to its objective score. By using several particles one is able to estimate the density of probability on the space of admissible transformations. The probability associated to a given transformation corresponds to how likely this transformation is to be correct. Particles are then redistributed accordingly to this estimated Probability Density Function (PDF) and a random perturbation (corresponding to a random rigid displacement) is applied to each particle. A new PDF is then estimated from this new set of particles and the whole process is iterated. At convergence, the maximum of the final estimated PDF must correspond to the expected transformation to retrieve. A genetic algorithm is performed by running simultaneously different registration initiated at random initial solution and keeping the best one a posteriori. This method allows to be more robust to local minima but can easily become intractable as the number of particles increases.

Instead of investigating methods to optimize an objective function that is based on imperfect (because automatic) 2D segmentation, the original approach of [Groher et al., 2007] considers to update the 2D segmented features taking into account the current registration position. Starting from a regular 2D vessel centerlines segmentation, the sum of closest point distance is optimized using the downhill simplex method (as in [Rivest-Henault et al., 2012]). Given this registration position, they update the 2D vessel segmentation using the following assumption: The closer a pixel is to the projected 3D structure, the more likely it is to be a 2D vessel. A probabilistic formulation of the label attributed to 2D pixels takes into account both

the image information, which is given by a vessel enhancement technique, and the probability of pixel to be registered with a 3D feature, which is proportional to the distance to the projected 3D structure. From this 2D probability map are extracted new 2D vessel centerline features that are used to run the registration from the previous position. This whole procedure is set in an elegant Expectation Maximization (EM) framework where the E-step corresponds to the computation of the 2D vessel probability map and the M-step corresponds to the optimization of the objective function (sum of closest point distance). This nice framework allows one to replace the E-step by any probability estimation as well as replacing the M-step by any registration method.

Several articles faced the challenge of non-rigid registration using point set features representation. In [Metz et al., 2013] this problem has been addressed as temporal alignment of a patient specific coronary motion model obtained from the segmentation of a 3D+t CTA. The resulting transformation is composed of a time varying rigid transformation as well as a temporal alignment of the 3D+t acquisition that handle offset and scaling. It is expressed as a 3D+t/2D+t registration of the coronary arteries where the sum of closest point distance is optimized over a whole cardiac cycle. The considered distance is a sigmoid function of the standard closest point Euclidean distance. The sigmoid parameter controls the decreasing rate around segmented centerlines. By changing this parameter one is able to obtain either a distance map dispersed around centerline points (coarse) or on the contrary extremely localized around 2D features (fine). Thus a multi-resolution strategy is used in two steps of the optimization procedure. The first step considers in-plane translations optimization using grid search with progressively finer distance maps. The second part of the optimization iteratively updates both the time varying rigid-transformation and the temporal alignment parameters using a Powell optimizer. This article shows nice results, especially in the non-rigid case, but necessitates both a 3D+t CTA acquisition and a 2D+t acquisition where the coronary tree is fully injected during a whole cardiac cycle.

In its non-rigid registration section, the previously mentioned article [Rivest-Henault et al., 2012] proposes a method involving a 3D CTA and two dual X-ray projective views. The optimal 3D non-rigid transformation is retrieved after a step of reconstruction by standard triangulation. However, it has been highlighted that using the closest point assumption to build pairing between two views often leads to bad reconstruction. Their approach involves local vessel direction and thus will be deeper discussed in 3.3.3 since it no more involves simple set of points as features.

3.3.2 Vasculature as a Spatial Distribution

As it has been highlighted in several articles, including previously cited [Rivest-Henault et al., 2012] and [Kita et al., 1998], the closest point assumption often leads to non relevant pairings between features. Even if pairings between feature points are not explicitly mentioned, the articles referenced in 3.3.1 using a closest point distance map implicitly consider the closest point pairing assumption. While

pairing a point to its closest can be justified close to the registered position, it becomes less relevant as the initial pose estimate gets less precise. Since building correct correspondences from the beginning seems difficult, several authors relax the one-to-one correspondence in order to consider multiple pairing possibilities at the same time.

One example of such an approach can be found in [Granger and Pennec, 2002] where the one-to-one correspondence is relaxed to a soft assignment technique. In this paper, each point of one structure is paired to multiple points in the other where each possible pairing is weighted by normalized Gaussian weight. The weight of a matching is dependent on the Euclidean distance between matched points. Optimizing the transformation given this fuzzy pairing set is equivalent to optimize the sum of the Mahalanobis distance. It can be achieved by replacing binary weights $\{0; 1\}$ by real weights $[0; 1]$ in the least squares problem, which gives a similar direct formulation. A nice mathematical framework is provided in [Granger and Pennec, 2002], presenting this approach in an Expectation Maximization (EM) framework. Each 2D point in the segmented 2D feature is considered as a Gaussian centroid. A 2D probability map could have been deduced from this Gaussian mixture, which endorses multiplicity in the pairing contrary to a distance map. The E-step of this EM algorithm consists in projecting a 3D point from the model that is considered as an observation having a probability given by all close 2D Gaussian centroid contributing at this 2D location. This step corresponds to the weighted multiple pairings construction. The M-step consists in estimating the optimal transformation, given this set of weighted pairings, in the sense of sum of square Mahalanobis distance. The standard ICP algorithm can be seen as an EM-ICP algorithm where only the most likely pairing is kept for each point.

In this previous work, the 2D features are represented as a Gaussian Mixture Model (GMM) where all centerlines points are considered as a Gaussian centroid. The variance associated to each centroid is also discussed in [Granger and Pennec, 2002] proposing a deterministic annealing scheme. While a huge value of variance corresponds to a simple inertia center alignment, tiny value corresponds to the standard ICP algorithm. The deterministic annealing method starts from high value of variance (meaning high degree of multiplicity in pairings) and progressively decreases it until being equivalent to the ICP algorithm. By this mean EM approach can improve robustness while keeping the ICP accuracy at convergence. This approach has been applied to 3D/2D registration of the liver vasculature in the work of [Groher et al., 2009]. Contrary to the direct computation of the transformation described in [Granger and Pennec, 2002], a gradient descent optimization of the objective function is proposed in [Groher et al., 2009]. The retrieved non-rigid transformation is modeled by a set of 3D displacement vectors attached to each 3D feature points. Because of this high number of degrees of freedom, the registration becomes highly ill-posed and necessitates additional regularization terms in the objective function. A diffusion regularization term is used, as it is generally the case in non-rigid registration, to impose smoothness to the deformation vector field. It is based on the variations of the Thin Plate Spline (TPS) interpolation of the vector field: the more

variations in the interpolation, the less smooth the deformation vector field.

Instead of representing only the 2D features as a probability function and the other as observations, [Baka et al., 2014] consider both structures as probability of locations that evolves during iterations. They extend the work of [Jian and Vemuri, 2011] on 3D/3D Gaussian Mixture Model (GMM) registration to the 3D/2D registration of the coronary arteries. In GMM framework both point sets are considered as continuous Probability Density Functions (PDF) and the registration between them consists in maximizing their overlapping probability. This estimation is achieved by the L2 norm, or sum of squared difference, which is optimized using a gradient based optimizer. In the adaptation of [Baka et al., 2014] to the 3D/2D case, the 3D point set is projected before computing the corresponding 2D probability density function. This PDF will be compared to the GMM extracted from the 2D features with the objective function defined as the L2 norm. A progressive increase of the number of degrees of freedom is performed while the variance of Gaussian centroids is progressively decreased. Starting from a translation-only optimization, the final non-rigid registration transformation is parametrized using a statistical shape model. By using a population of segmented CTA, one is able to compute statistics on shapes that are formed of a point cloud. One is then able to define a mean shape as well as various main modes of variation defining a Gaussian distribution of shape around this mean shape. Details about this statistical shape model of coronary arteries are provided in [Baka et al., 2013]. This model is more restrictive than spline based deformation models, which is a strong advantage knowing that the 3D/2D registration is an ill-posed problem.

All previous methods shows that representing features by a probability function allows to increase the robustness of the registration with respect to the ICP approach. By relaxing the one-to-one pairing constraint imposed by the closest point pairing assumption, [Baka et al., 2014] were able to increase success rate while maintaining the ICP accuracy by progressively decreasing the fuzziness of the pairing during iterations. However, this article highlighted that relying only on Euclidean distance to assess the quality of a potential pairing often leads to registration problem. Several refinements of their method are developed such as taking into account the fact that features points belong to a vascular structure.

3.3.3 Vasculature as a Set of Local Vessel Portions

Several articles from the literature take advantage of their prior knowledge about the vascular structures to be matched. As it is assumed in the vesselness filter, used in the majority of articles to enhanced vessels in the image, vessels can be seen locally as linear contrasted structure. Thus the vasculature can be represented as a set of segmented centerline points, each one enriched by a vector representing the local vessel direction at this location. This vector locally tangent to the vessel centerline can be defined for both the 3D structure and the 2D structure at almost every location. Exceptions to this rule are bifurcation points or superimposition locations due to the projective modality.

In [Feldmar et al., 1997], the 3D feature is considered as a set of 6-dimensional points, containing the position and the tangent direction, that will be matched to a set of 4-dimensional points. The registration between 3D MRA and 2D DSA of brain vessels is addressed as an adaptation of the ICP algorithm to 6D/4D case. After a step of projection that maps a 3D point and its tangent direction to a 2D point and its tangent direction, a pairing is made between each 4D point resulting from the projection and its closest one, refering to a 4D Euclidean distance. Normalization factors between position difference and tangent difference inside the Euclidean distance were necessary to balance the implicit normalization of tangent vectors. Contrary to other mentioned articles, [Feldmar et al., 1997] propose a symmetric pairing construction where each point of the segmented MRA is matched to its closest in the segmented DSA and vice versa. This leads to a non-linear minimization problem to solve that is addressed by an extended Kalman filter (interested readers can find a description of this method in [Feldmar et al., 1995]). As shown in their results, by introducing the tangent information inside the ICP framework authors were able to build a more robust algorithm than the standard version of [Besl and McKay, 1992]. However, they insisted on the importance of removing wrong pairings, called outliers, to provide accurate and robust registration.

In their work described partially in 3.3.2, [Baka et al., 2014] also consider the tangent information in its EM-framework. Each point is represented by its position and by a normalized vector representing the vessel direction. The previous two 2D Probability Density Functions (PDF) are now 4D PDF defined by a Gaussian mixture of 4D centroids. As it has been stressed in [Feldmar et al., 1997], differences between positions and normalized direction should be taken into account. The covariance matrix associated to each centroid that controls the degree of fuzziness in the pairing, is represented by a bloc diagonal matrix. By doing so, position coordinates and tangent directions are considered independently, which allows to have different tolerances for positions and orientations. Introducing local vessel direction raises the problem of relative orientation. Actually, one direction vector and its opposite represent the same vessel orientation. To deal with this problem [Baka et al., 2014] duplicate every feature point: one with a given orientation and one with its opposite. To limit the overlap regarding orientations, the covariance matrix associated to the vessel orientation is designed such that differences higher than 90° are neglected.

In addition of the position distance and the orientation difference, the objective function used in [Baka et al., 2013] is also composed of a vesselness response term. The resulting correspondences are obtained by a closest point pairing procedure, using a dedicated measure combining the 2D Euclidean distance, the direction difference and the vesselness. The closest point assumption is made to build the set of point pairings but using a dedicated distance taking into account the position distance, the orientation difference and the confidence on the point extracted from the image (evaluated by the vesselness response). From this pairing set is computed an objective function constituted of the weighted sum of the previous distance. Weights are determined for each 3D point based on its proximity with respect to its neighbors

after projection. By this mean, 3D vessels contribute accordingly to their projected length and not their real length. This measure is extended to a complete cardiac cycle to run 3D/2D+t registration. The corresponding non-rigid registration over time problem is addressed as rigid registration over time coupled with the temporal alignment of a coronary arteries motion model learned from shape statistics on a database of several 3D+t CTA of the coronary arteries. The optimization with respect to this deformation model is done using a Matlab toolbox implementing the so-called "interior-reflective Newton method".

A more hybrid approach, between intensity- and feature-based technique, is developed in [Mitrović et al., 2013]. They consider the matching between segmented 3D centerlines from cerebral CTA and gradients extracted at each pixel of the DSA image. Each point from the 3D segmentation, including the position and local direction vector, is projected into the image plane. The authors consider the sum of scalar the product between the projected 3D local direction and the image gradient vectors in a small neighborhood around the projected 3D position. Since the local gradients estimate the direction locally perpendicular to the vessel, minimizing the sum of scalar products is equivalent to align vessel direction estimation in both modalities. This fast method has been applied to dual-plane acquisitions in neurology and even opens the way to 4D DSA.

3.3.4 Vasculature as a set of Curves

A natural way to represent the different vascular centerlines is a set of curves. A curve can be a set of ordered points, a continuous interpolation passing through them or a smooth approximation of them (e.g. Bezier curves). By representing vasculature that way, one is able introduce the notion of coherence along curves. In the work of [Groher et al., 2009], a refinement of the objective function described in 3.3.2 allows to avoid non-realistic deformations by the mean of a regularization term. Some remaining wrong vessel pairings can induce non-realistic changes in local vessel length. A length preservation constraint is thus added, which can be defined thanks to the curve representation of the 3D structure. This constraint is expressed as an extra cost inside the objective function that penalizes change of distance between a point and its two neighbors before and after the non-rigid deformation of the 3D features. The article presents examples of registration where the non-constrained version results in the collapsing of an entire vessel portion into a single location as well as a big elongation to compensate this collapse. Adding the constraint allows to solve this issue.

In the work of [Liu and Bullitt, 1998], both the 3D and the 2D structures are considered as a set of curves automatically extracted from each modality. They propose a registration algorithm based on a given set of corresponding curves manually paired by the user. Even given this pairing between curves, the standard closest point pairing often lead to non-relevant correspondences that can mislead the registration procedure (as highlighted in [Liu and Bullitt, 1998]). In order to limit error in pairings, a new point pairing strategy is developed, using the local vessel direction

to restrict the search zone for point pairing candidates. For each point along the projected 3D curve, a correspondent in the paired curve is search in the direction perpendicular to the local vessel direction. If no intersection can be found the point is not paired and if multiple intersections are found the closest one according to the 2D Euclidean distance is chosen. Given this freshly constructed point pairing set, the sum of squared Euclidean distance is optimized using a Newton approach. The time spent by the user to manually identify corresponding curves in the 3D and the 2D, for a MRA-to-DSA neurology application, has been evaluated to 5 minutes. This result is compared to the one hour spent by a clinician to manually define the rigid alignment of the volume that necessitates to tune the 6 Degrees of Freedom (DoF) of the transformation.

The proof of concept provided in [Duong et al., 2009] demonstrates the applicability of manual curve matching in the case of 3D/2D registration of coronary arteries. The registration is conducted by identifying corresponding vessels in both the CTA and the fluoroscopic image and then using the ICP framework on points constituting the curves. To speed up the algorithm, 2D distance maps are precomputed for each 2D vessel identified by the user to avoid the closest point search for all 3D projected points. The sum of closest point distance is optimized using the best-neighbor method to obtain the resulting rigid alignment. The presented results on 5 cases show the feasibility of such an approach even using a single vessel in the matching. This method has also been applied to images in which no contrast medium opacifies the 2D arteries by relying only on the guide-wire segmentation. This latter experiment opens the way to non-injected 3D/2D registration update if the initial pose estimate is close to the registered pose.

3.3.5 Vasculature as Trees and Graphs

All previous vascular structure representations involve several extracted features grouped in a set (a set of points or a set of curves) without connection between each other. The exception is the work of [Groher et al., 2009] where the vasculature is nicely represented by a graph structure. A graph is a mathematical representation made of nodes that are linked by edges. In [Groher et al., 2009], a node corresponds to a centerline points location and an edge represent the connectivity between points. A bifurcation, which corresponds to the separation of a vessel into multiple ones, is a node which have three (or more) departing edges. Besides the elegance of the notations, no advantage is taken from this representation in the registration algorithm.

The work of [Serradell et al., 2011] is going a step further by representing the segmented 3D vasculature by a tree. This tree structure is basically a graph, as in [Groher et al., 2009], but with no cycle[3]. In this structure one is able to define a hierarchy between nodes starting from the root until reaching leaves. In [Serradell et al., 2011], local vessel orientation is used in the matching, leading each node to

[3] A graph is containing a cycle if it exists a closed path in the graph that do not visit twice the same edge.

also carry a normalized tangent vector. The challenge of obtaining the same type of representation from the fluoroscopic image was not addressed in this article leading to the same representation as in [Feldmar et al., 1997]: a set of points containing both the position and the local vessel orientation. The retrieved deformation transformation is a sort of articulated deformation where the displacement of a node in the tree also impacts all its descendants (children, great children...). The displacement at each node is represented by a Gaussian distribution with a variance matrix depending on all ancestors variance matrices. Building optimal correspondences is seen as an optimal assignment problem between projected nodes into the image plane and 2D segmented points both enriched by their respective local vessel direction estimation. The cost associated to an assignment, or pairing, is given by the weighted sum of the orientation difference and the Mahalanobis distance between 2D positions that refers to the covariance matrix associated to the 3D point displacement. The optimal matching is then obtained using the Hungarian algorithm that aims at assigning a 2D different corresponding point to each 3D node with the minimal overall cost. Given this assignment, the 3D transformation modeled by Gaussian centroids associated to each node in the tree is optimized using a Kalman filter. One should note that in this case the alternative computation of pairings and optimal transformation computation was used to the purpose of non-rigid reconstruction algorithm. Starting from a 3D CTA the goal was to obtain a 3D+t CTA based on 2D+t injected fluoroscopic acquisition.

Other articles, such as [Smeets and Bruyninckx, 2010] and [Serradell et al., 2015], describe tree matching and graph matching algorithm but are restricted to 3D/3D and 2D/2D vessel registration. They are both based on bifurcation matching, assuming that corresponding bifurcations can be well identified in both modalities. In the case of 3D/2D registration, the projective nature of the 2D image creates superimposition and vessel foreshortening which highly complicate the precise localization of bifurcations.

3.4 Thesis Point of View

By using all available information in both modalities, as in [Metz et al., 2009], intensity-based registration methods seems attractive at first sight. However, in the case of vessel registration, the reliable information is sparse in space. Intensity-based registration techniques often involve an enhanced version of the image or a segmented version of the volume but so far without representing it as a geometrical structure. A representative work applied to our domain of interventional cardiology can be found in [Gatta et al., 2011]. In this class of methods, obtaining correspondences between the two modalities are not straightforward since a pixel in the image plane gets the contribution of all the voxels along its back-projected line. Non-rigid registration becomes easily intractable and has only been addressed in 2D. Moreover, the clinical relevance of the resulting transformation can be challenged. Therefore, the majority of the state of the art articles on 3D/2D vessel registration are based

on features extracted from each modality.

In feature-based registration, we have highlighted that the correspondences between structures are crucial to the accuracy and robustness of an algorithm. Representing the vascular structure as a set of unstructured centerline points seems to lead to non-relevant pairings even refining them with robust optimizers as it is shown in [Rivest-Henault et al., 2012]. Robustness can be increased via a probabilistic framework, by relaxing the one-to-one pairing constraint. In [Baka et al., 2014], the coronary arteries registration is addressed as an expectation maximization problem where both structures are considered as probability density functions. Introducing information on the structures involved allows to overcome some of these difficulties. By adding the local vessel direction at each centerline point, [Feldmar et al., 1997] limits the number of irrelevant pairings. Some articles also penalize wrong pairing by adding a cost function depending on the distance between points paired to 3D points that are close to each other. Matching trees (3D) or graphs (2D) has been applied to coronary arteries registration in [Serradell et al., 2011], considering the vascular structure as a whole. However, to the best of our knowledge, none of the articles mentioned in this chapter ensure coherence of the pairings in the 3D/2D case, along the iterations or at convergence.

The goal of this thesis is to demonstrate the interest of taking into account the topology of the structures to be matched in a registration procedure. Since vessels can be accurately represented by their centerline curves, ensuring that the connectivity between points along curves is maintained during the registration constitutes the first step toward topology preservation. Moreover, the order between points along vessels as well as the connectivity between vessels at bifurcation locations are of great interest to build relevant pairings and therefore accurate and robust registration algorithm. To this aim, we developed a registration framework designed for the registration of curves, which preserves the curvilinear structure of the data. The particular nature of the tree-topology, which mixes connectivity along curves and connectivity at bifurcations, encourages us to develop a pairing procedure matching a tree to a graph. We keep believing the principle: “Why penalizing non-coherent behavior, when you can impose coherence by the framework you use ?”.

Chapter 4

Sparse Geometrical Representation of the Vasculature

Contents

The work presented in this manuscript can be classified as a feature-based approach according to Chapter 3. Structures to be matched are sparsely represented by geometrical objects, also called features. The word "sparse" in the title refers to the fact that simple geometrical features can represent accurately vessel in a sparse way, contrary to the 3D voxels array representation considered in intensity-based registration. The type of features, as well as the way they are obtained, are of great importance to the understanding of the proposed method. Since topology preservation constitutes the core of our contributions, we gave particular importance to the description of the geometrical structures used to represent the anatomical information. Trees and graphs structures are often involved along the manuscript and the reader may refer to [Diestel, 2012] for a deep description of these mathematical objects.

4.1 Model: 3D Coronary Vessel Tree

In this section we describe how a Computed Tomography Angiography (CTA) can be sparsely represented by a geometrical structure. The term "model" is used in contrast to the term "data" which denotes the segmented 2D structure. These two terms come from the registration community where they are often used to refer to model-to-data registration. It means that one of the two structures to be registered can be used as a reference to be matched to the other. In our case the 3D CTA serves a diagnostic purpose and is also used to plan the intervention. Consequently,

the vessel segmentation[1] procedure depicted in the following Section 4.1.1 would be manually corrected by the clinician in case of imperfections in the results. This is why the 3D modality will be called the model but must not be confused with a simplification of the patient anatomy or a result of statistics on several patients. The work described in this section essentially comes from a GE Healthcare product called *Auto-Coronary-Analysis* and is not a contribution of this thesis. Only the tree structure representation described in the second part of Section 4.1.2 can be attributed to the author.

4.1.1 Vessel Segmentation

Starting from a multi-slice Computed Tomography Angiography (CTA), represented in Figure 4.1a, a segmentation of the heart and the coronary arteries, as the one presented in Figure 4.1b is first performed. This step removes bones, soft tissues and peripheral injected anatomies from the CTA volume. The segmentation is obtained using two thresholds that isolates a range of high intensities corresponding to the contrast medium. Concentration of the intravenous injected product is well established in protocols and thus reconstructed intensities of the lumen and heart chamber can be inferred quite precisely.

(a) CTA slices

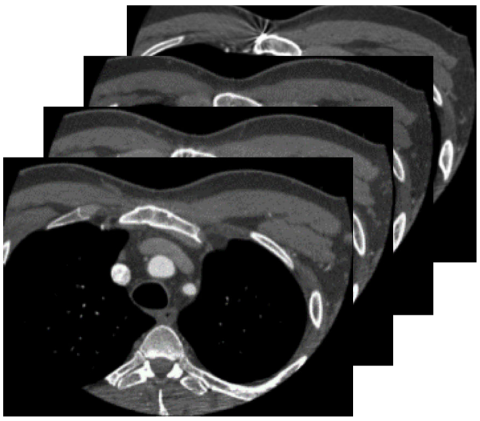

(b) Heart and Coronaries

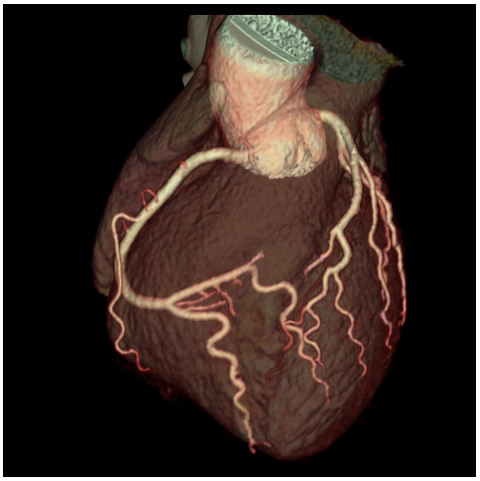

Figure 4.1: Input 3D Computed Tomography Angiography image (a) and the intensity-based segmentation of the heart including the surrounding coronary arteries (b).

To obtain a segmentation of the coronary arteries, a region growing algorithm is used based on the intensities. Starting from seed points, region growing algorithms progressively extends segmented regions to neighbors depending on some criterion

[1] In the following the term segmentation alone refers to the result of the segmentation procedure, which is a set of voxels identified in the volume.

(in our case voxel intensities). The step of seeds selection in the segmentation algorithm is crucial to obtain a precise segmentation of the coronary arteries without background[2] structures. A Hessian based technique, similar to the one presented in the upcoming Section 4.2.1, is used to enhance 3D tubular structures. Points in the volume presenting the highest response to this 3D vessel enhancement filter are chosen to be seed points. The resulting segmentation obtained by region growing is a set of voxels forming a unique connected component, presented to the clinician in a volume rendering way shown in Figure 4.2.

Figure 4.2: Volume rendering of a segmented coronary tree of the same patient seen from two different angulations.

This 3D segmentation allows an easier understanding of the patient's anatomy but is not the privileged view used for diagnosis. To build relevant visualization tools, it is necessary to extract vessel centerlines starting from the aorta and ending at extremity of segmentation. While the aorta can be easily identified by using a priori information regarding its size and position in the volume, the segmentation extremities are found by computing a distance map in the segmented coronary tree. This map assigns to each pixel in the segmented volume its geodesic distance to the aorta in the segmentation (this map can be easily built using a region growing algorithm). Centerline extremities are defined as local maxima of the distance map.

Knowing the starting point (aorta) and the ending point (an extremity), the centerline curve is extracted by computing the shortest path in the segmentation between these points. The shortest path is determined using length costs that depends on geodesic distance along the segmentation (using the distance map) and the voxel intensity in the volume. The latter allows to favor the center of the lumen which is expected to be brighter than the vessel walls. An example of centerline is presented in Figure 4.3a and supports several visual modes well suited for diagnosis. The curved view presented in Figure 4.3b shows the whole vessel into a single image

[2]In a segmentation context, the background is defined as structures that are not targeted to be segmented. In our case all voxels that do not belong to the coronary arteries.

which is a visual representation of the entire vessel without much distortions. The oblique view is designed to simulate navigation in the volume by presenting images extracted from the CTA volume in planes that are perpendicular to the local centerline direction. Finally the lumen view of Figure 4.4 shows the lumen and vessel walls, as well as the evolution of the measured diameter of the vessel to identify stenosis.

(a) Centerline extraction (b) Curved view (c) Oblique view

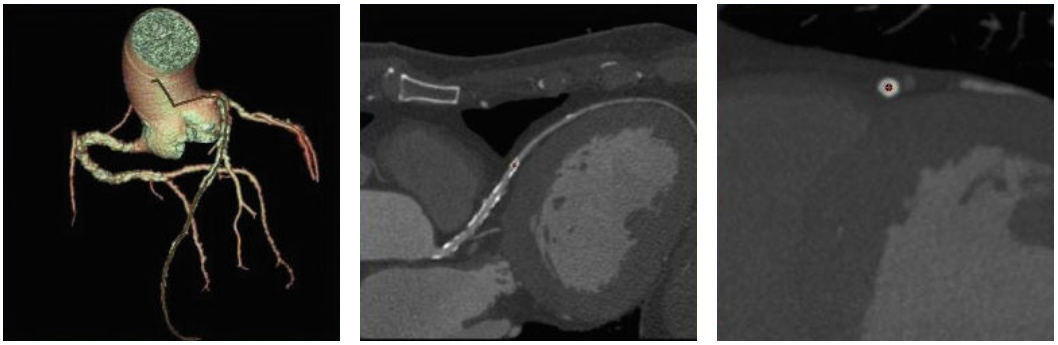

Figure 4.3: Extracted vessel centerline joining the aorta to a segmentation extremity (a) and two views build upon this centerline: the curved view (b) presenting a plane containing the whole vessel and the oblique view (c) that shows a plane orthogonal to the local vessel direction.

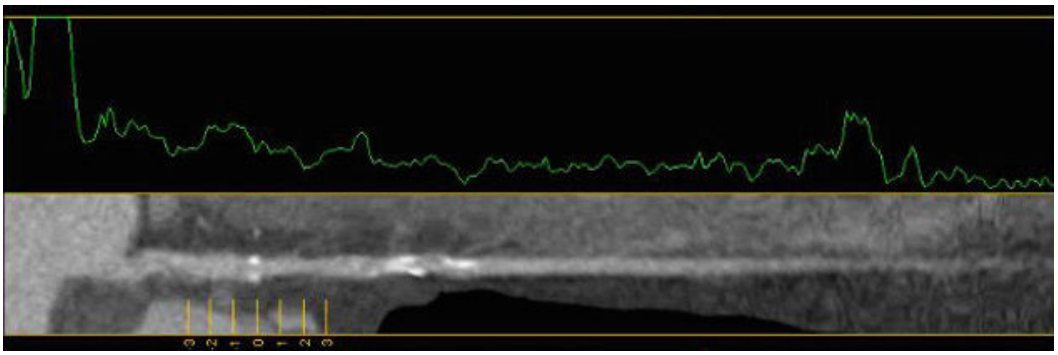

Figure 4.4: Lumen view presenting the evolution of the vessel diameter from the aorta to the extremity (top) and an image presenting the vessel and local neighborhood as if it was deployed to be a straight line (bottom).

At the end of this procedure, a segmentation of the volume (connected component of voxels) and multiple centerlines from the aorta to extremities are available. While the segmented volume can allow rendering into the fusion application, the centerline representation will be used to build features that will be matched during the registration algorithm.

4.1.2 Geometrical Representation of the 3D Vasculature

At this stage, the patient's coronary arteries are represented as multiple 3D centerline curves C_k modeled by polygonal curves:

$$C_k = \Big[C_k[1], C_k[2] \dots C_k[\#]\Big] \quad \text{s.t. } \forall i,\ C_k[i] \in \mathbb{R}^3 \tag{4.1}$$

where $C_k[\#]$ denotes the last point of curve C_k. A polygonal curve is defined as an ordered set of points that are pairwise interpolated by a straight line. A curve C_k is defined by:

$$P \in C_k \iff \begin{cases} \exists\ i \in \mathbb{N} \\ \exists\ \alpha \in [0;1] \end{cases} \text{s.t. } P = \alpha \cdot C_k[i] + (1-\alpha) \cdot C_k[i+1] \tag{4.2}$$

By design of the segmentation algorithm, curves provided as output start from the main branch entry at the level of the aorta, denoted A, such that:

$$\forall k,\ C_k[1] = A \tag{4.3}$$

Each curve ends at an extremity that is defined as the most distal points in the tree segmentation. Such a representation is well adapted to the diagnostic task because the clinician can follow any entire vessel and detect a potential stenosis. However, it also introduces redundancy at proximal regions: two different vessels will at least share the main branch as common part. To get rid of this redundancy we worked on representing the 3D model as a tree. A tree $(\mathbf{E}, \mathbf{N})$ is composed of a set of nodes $\mathbf{N}$ pairwise connected by links called edges in the set of edges $\mathbf{E}$. It differs from a graph, because a tree must not contain any cycle in its structure. The 3D vasculature can be represented as this tree structure $\mathcal{Y}$ where edges correspond to artery centerlines linking consecutive nodes and nodes are either anatomical vessel bifurcations[3] or an extremity of the segmentation.

To represent the whole structure, we introduced extra nodes at the segmentation extremities, which do not have any true anatomical meaning. In the scope of this work we will make the distinction between anatomical bifurcations, denoted by $\mathbf{B}$, and extremities also called leaf nodes, denoted by $\mathbf{L}$. Thus the 3D vasculature $\mathcal{Y}$ can be represented by a tree structure, adding a distinction between real bifurcations and extremities:

$$\mathcal{Y} = \big(\mathbf{E}, \{\mathbf{B}, \mathbf{L}\}\big) \tag{4.4}$$

One is able to define a hierarchy between nodes and edges by designating a node (or an edge) as the root. Starting from the root, each connected nodes and edges are called children and so recursively until extremities, also called leaves, are reached. It should be noted that the structure formed of a node or a branch extracted from a tree with all its descendants is also a tree. This property is important for defining recursive algorithms along the tree. This choice of feature to represent the 3D vasculature endorses both types of connectivities that exists in the vasculature:

[3] A vessel bifurcation is the anatomical part where one vessel branch splits into two vessel branches.

- **Connectivity along curves**: two consecutive points that belong to the same curve are connected.
- **Connectivity at bifurcation points**: two curves (or edges) sharing a common bifurcation (or node) and thus a common point at their respective extremities are connected too.

To obtain this topologically coherent representation of the vasculature from the set of redundant curves, a tree extraction step is necessary. We first need to define the distance between a point Z and a vascular tree $\mathcal{Y}$:

$$d\left(Z, \mathcal{Y}\right) = \underset{Y \in \mathcal{Y}}{\operatorname{argmin}} \left\| Z - Y \right\| \tag{4.5}$$

The tree extraction procedure starts by taking a curve C_1 from the set of segmented curves to build a trivial tree. This trivial tree is composed of only one edge $E_1 = C_1$ that joins two extremity nodes (or leaves) $L_1 = C_1[1]$ et $L_1' = C_1[\#]$. The resulting tree $\mathcal{Y}$ is progressively built by integrating curves to its structure until no more curves are available. An other curve C_2 is thus taken from the set of segmented centerlines to enrich the tree $\mathcal{Y}$.

We compute what we called the proximal intersection, denoted $C_2 \cap \mathcal{Y}$, between the curve C_2 and the tree $\mathcal{Y}$:

$$C_2 \cap \mathcal{Y} = C[1 \dots K] \tag{4.6}$$

where K is defined by:

$$\begin{cases} d\left(C[k], \mathcal{Y}\right) \leq \Delta \ , \ \forall k \in [1 \dots K] \\ d\left(C[K+1], \mathcal{Y}\right) > \Delta \end{cases} \tag{4.7}$$

This proximal intersection is designed to identify the common part between a curve and the tree being built, while ignoring eventual distal (fake) intersection if vessels gets too close to each other. The parameter Δ refers to a threshold on the distance that in our case is set to the radius estimation at point $C[i']$. Therefore the subcurve $C_2 \cap \mathcal{Y}$ correspond to the part of C_2 already present in the tree $\mathcal{Y}$ because of redundancy.

The non-shared part is defined by:

$$(C_2 \cap \mathcal{Y})^c = C_2[K+1 \dots \#] \tag{4.8}$$

where K is defined in Equation (4.7) and $\#$ denotes the position of the ending point of C_2. This part that is non-redundant with the tree is added by:

- Creating a bifurcation node $B_2 = (C_2 \cap \mathcal{Y})[\#]$ at the location of the last shared point between C_2 and $\mathcal{Y}$. This action generally results into a cut of an already existing edge in the tree.
- Adding an edge in the graph between B_2 and $L_2 = C_2[\#]$ composed of the non-shared part $(C_2 \cap \mathcal{Y})^c$.

By iterating this procedure over the whole set of overlapping curves, we build a tree structure as defined in Equation (4.4). A representation of the resulting vascular tree structure is provided in Figure 4.5.

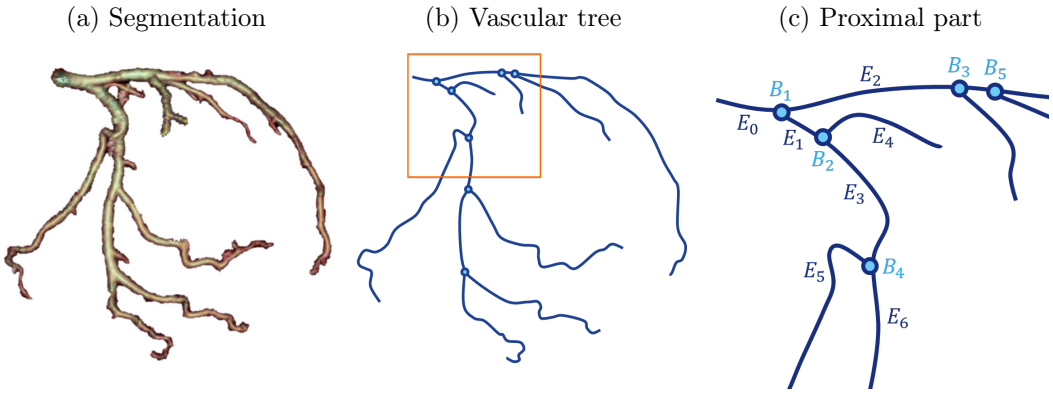

Figure 4.5: Vascular tree representing the coronary arteries. (a) segmentation of the arteries, (b) sparse tree representation with proximal part squared in orange, (c) zoom on the proximal part of the tree structure.

In this particular structure, we identified several parts deserving anatomically denomination:

- **Main Bifurcation**: is the first anatomical bifurcation (in the direction of blood flow) in the coronary tree, starting from the aorta. In Figure 4.5c it corresponds to the bifurcation node B_1. In the tree structure representation, we also call it root bifurcation node.

- **Main Branch**: is the vessel portion that starts from the aorta and ends at the main bifurcation In Figure 4.5c it corresponds to the centerline E_0. In the tree structure representation we call it the root edge.

4.2 Data: 2D Projected Vasculature

This section describes how the fluoroscopic image obtained from the X-ray C-arm system is transformed into a sparse geometrical representation of coronary arteries. Contrary to the 3D pre-operative modality, the fluoroscopic image must be processed quickly and without user interaction to be compatible with the interventional application. The resulting segmented feature will thus be more subject to noise and fake detection than its pre-operative counterpart. It is therefore denoted "data" in contrast to the 3D model. Contrary to the 3D segmentation tool that was already available as a product (Auto-Coronary-Analysis, GE Healthcare), the extraction of the 2D vasculature was developped during this thesis. However, the vessel segmentation is not the core of this Ph.D. The following section should thus

be considered as a perfectible way to extract the 2D vasculature from a projective X-ray image in order to perform feature based registration.

An overview of the literature can be found in [Zhang, 2010] on the topic of 2D coronary arteries segmentation and in [Kirbas and Quek, 2003] for a review on larger fields of applications. The method we propose consists in three consecutive steps: enhancing vessels in the image, segmenting vessel centerlines and finally building up a vascular graph representing the vasculature. While the two first steps are widely used in the different approaches described in [Zhang, 2010], very few methods take into account the topological consistency in their modeling of the vasculature. We should mention the exception of [Türetken et al., 2013] that consider the construction of a graph from linear structures as an optimization of an objective function. This original work extends the approach of [Türetken et al., 2012] that solved efficiently the extraction problem using a quadratic mixed integer program formulation.

The three steps of our method are applied to a single image extracted from an image sequence recorded during the intervention. The image is chosen manually to be the "most" injected frame in the sequence, taken at a phase of the cardiac cycle corresponding to the CT acquisition. Automatizing this manual step has been addressed in [Chen et al., 2011; Matern et al., 2012], which allows us to consider the processing of a single image. Adding temporal consistency in the segmentation of linear structure along time has been tackled in [Glowacki et al., 2014] and may inspire some future work on 2D vasculature extraction.

4.2.1 Vessel Enhancement

The goal of the vessel enhancement procedure is to boost the vessel response in the fluoroscopic image. An expected result is shown in Figure 4.6 where a vessel pixel in the image should have a high response (high intensity). This step is necessary because it greatly facilitates the segmentation of the coronary arteries. Actually, the large disparity between pixel intensities along vessels forbids the use of segmentation techniques simply based on pixel intensities. This disparity is a consequence of the image acquisition process that involves X-rays propagation through the patient's anatomy. The image formation principle is more detailed in Appendix C, where an overview of vessel enhancement acquisitions are provided for peripheral anatomies. Unfortunately, these techniques of vessel enhancement suffers from disturbing artifacts in case of movements and are not applicable to the imaging of the heart anatomy.

To enhance vessels in a cardiac application, articles from the literature often estimate the background image of the anatomy by morphological operators. Injections of contrast medium inside the arteries make them appear as dark contrasted structures in the image that have a bounded radius. We estimate the background image by a morphological closing[4] to remove from the image contrasted structures whose size is below the vessel diameter (including the vessels). Obviously this estimation

[4]This morphological operator applied to a gray-scale image is composed of a dilatation followed by an erosion.

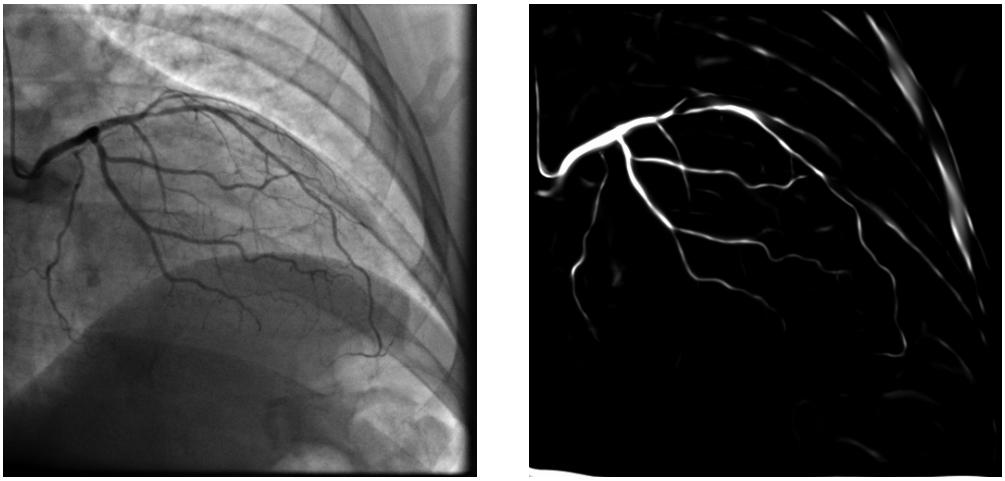

Figure 4.6: Goal of the vessel enhancement procedure: left) native image, right) resulting enhanced image.

produces a background image more approximative than the mask image acquired in peripheral clinical applications (see Appendix C) but still allows to obtain an estimation of the contrast image as presented in Figure 4.7. Even if this type of techniques helps to get rid of the majority of the background content, multiple negative contrasted structures of a size compatible with coronary arteries radius remain (such as ribs boundaries and pulmonary structures). To further enhance vessels in the background divided image I_{BD} the most used technique is the one described in [Frangi et al., 1998].

This Hessian based filtering technique assumes that vessels are locally linear tubular structures. The Hessian matrix represents the second order derivative and is defined at every pixel p in the 2D image I as:

$$H[x] = \begin{pmatrix} \frac{\partial^2 I}{\partial^2 u}[x] & \frac{\partial^2 I}{\partial u \partial v}[x] \\ \frac{\partial^2 I}{\partial v \partial u}[x] & \frac{\partial^2 I}{\partial^2 v}[x] \end{pmatrix} \tag{4.9}$$

where u and v represent respectively the horizontal direction and the vertical direction in the image plane. An eigenvalue decomposition is performed on each matrix $H[x]$ giving two eigenvalues $(\lambda_1[x], \lambda_2[x])$ and their corresponding eigenvectors $(\overrightarrow{a_1}[x], \overrightarrow{a_2}[x])$. Without lack of generality it can be assumed that $|\lambda_2[x]| > |\lambda_1[x]|$. If the pixel x belongs to a vessel the vector $\overrightarrow{a_2}[x]$, that corresponds to the highest eigenvalue, is perpendicular to the local vessel direction while $\overrightarrow{a_1}[x]$ is tangent to the vessel (see Figure 4.8). An intuitive representation is proposed in [Frangi et al., 1998] to figure this decomposition as a local ellipse representing the second order local behavior of the image I around pixel x. The study of the eigenvalues can thus be used to characterize the local structure in which belongs the pixel x. The different possible 2D structures are shown in Table 4.1.

Since we are interested in highlighting vessels we select pixels such that the ratio

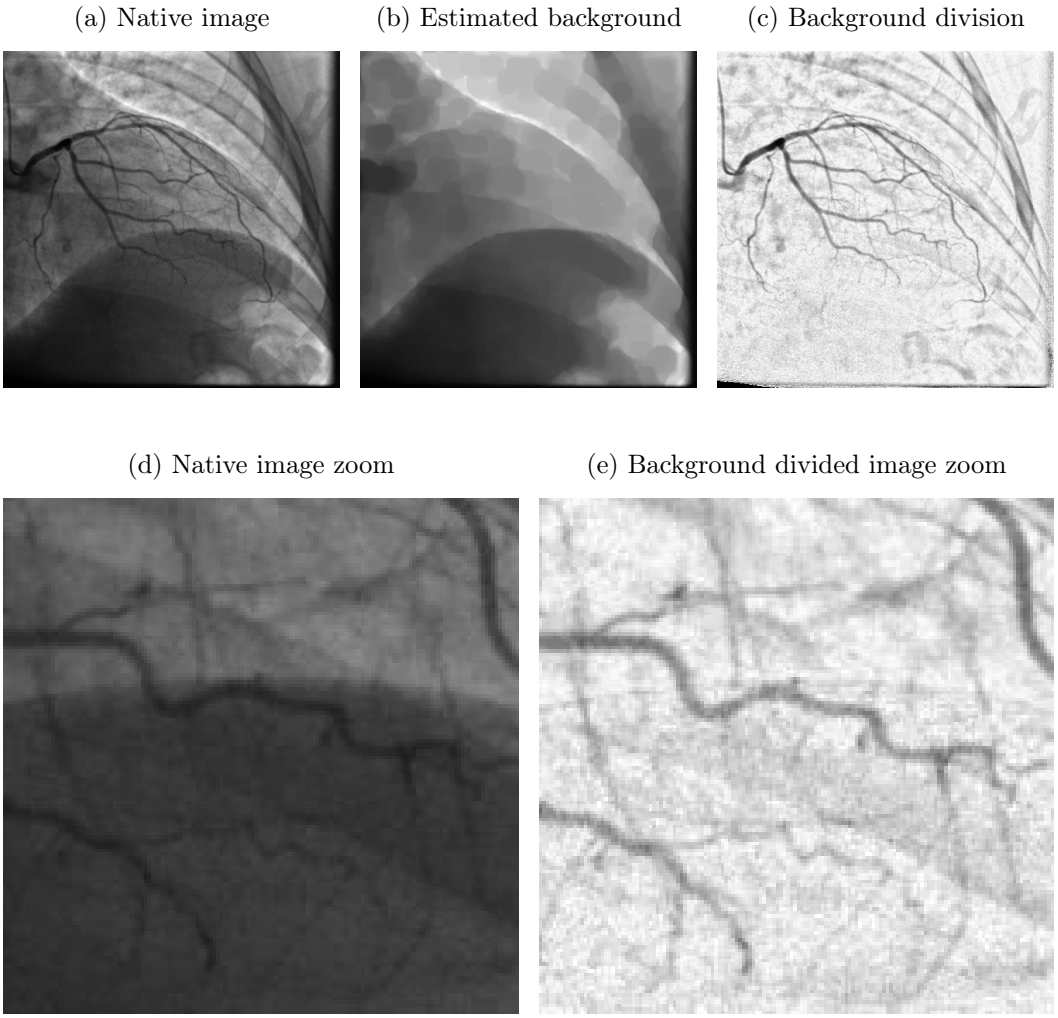

Figure 4.7: Estimation of the vessel contrast image using morphological operators. (a) native injected image, (b) estimation of the background image using a morphological closing, (c) resulting background divided image estimating the contrast created by a vessel, (d) zoom on a vessel superimposed to the diaphragm in the native image, (e) zoom on the same part in the background divided image.

(a) Vessel eigenvectors (b) Bifurcation eigenvectors

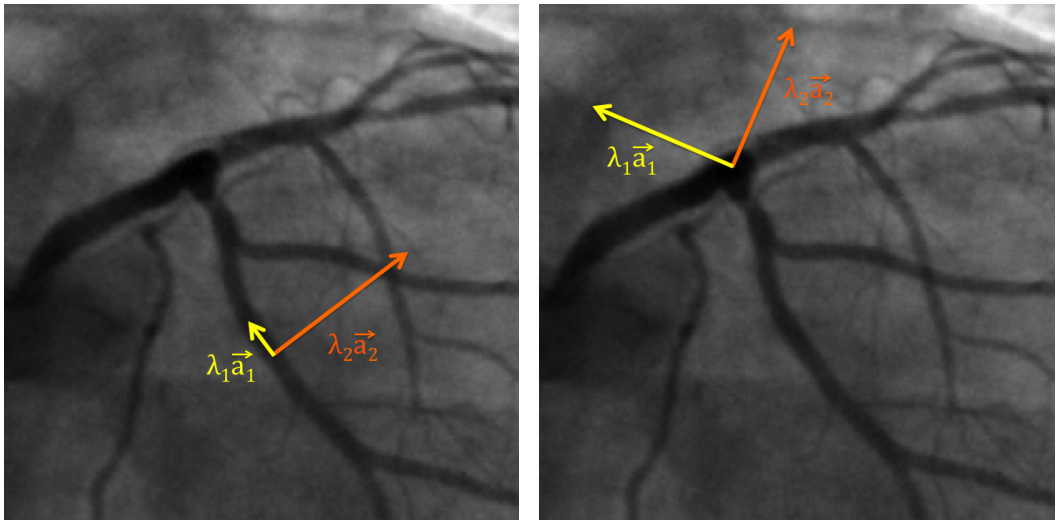

Figure 4.8: Eigenvectors meaning on a vascular image. The eigenvalue decomposition of the Hessian matrix has been performed along a vessel centerline (a) and at the center of a bifucation (b). The normalized eigenvectors are multiplied by their respective eigenvalues and plotted at the location where the Hessian matrix has been computed.

Table 4.1: Possible local patterns in a 2D image function of eigenvalues.

$\|\lambda_1[x]\|$	$\|\lambda_2[x]\|$	**Pattern around pixel** x
Low	Low	non contrasted structure with no particular orientation (noise)
Low	High	elongated contrasted structure (tube)
High	High	isotropic high contrasted structure (blob)

$r[x]$:

$$r[x] = \frac{|\lambda_1[x]|}{|\lambda_2[x]|} \tag{4.10}$$

is small, meaning that x lies in an elongated structure. Moreover, the relative norm of the eigenvalues at different locations in a given image increases with the contrast created by the local structure:

$$s[x] = \sqrt{\lambda_1[x]^2 + \lambda_2[x]^2} \tag{4.11}$$

and the more likely x belongs to a vessel. The vesselness criterion V, extracted from

[Frangi et al., 1998], is based on previous equations (4.10) and (4.11):

$$V[x] = \begin{cases} 0 & \text{if } \lambda_2[x] < 0 \\ \exp\left(-\frac{r[x]^2}{2b^2}\right) \cdot \exp\left(-\frac{s[x]^2}{2c^2}\right) & \text{elsewhere} \end{cases} \tag{4.12}$$

where b and c are two normalization factors and the condition on $\lambda_2[x]$ takes into account the fact that vessels are negative contrasted structures (dark structures on bright background).

This measure, based on the Hessian matrix, quantifies how likely a pixel is to belong to a vessel centerline. The derivative operator used to compute the $H[x]$ corresponds to a Gaussian derivative estimator, which is defined by a scale parameter σ controlling the width of the kernel used to estimate the derivative. Thus, the resulting vesselness response $V(\sigma)[x]$ at a pixel x depends on this scale parameter. Moreover, if x lies in a vessel center then the vesselness will be maximum for a value of σ corresponding to the local radius of the vessel. Since the projected coronary arteries present a full range of possible radii, [Frangi et al., 1998] computes the vesselness measure at different scales and mixes them into a single response:

$$\mathcal{V}[x] = \max_{\sigma_{min}<\sigma<\sigma_{max}} V(\sigma)[x] \tag{4.13}$$

where in practice σ takes discrete values, starting from $\sigma = \sigma_{min}$ and each time doubles the value of σ until σ_{max} is reached. The two extreme values of σ are determined by the expected apparent sizes of the arteries[5]. Vesselness at three different scales are provided in Figure 4.9, each scale favoring a particular range of vessel radii. A comparison between the Frangi vesselness map with and without background division is provided in Figure 4.10. One will note that the response induced by the ribs in the top-left region has been strongly attenuated by the background division step. However, vesselness response around bifurcations remains quite low. This behavior is well know by the vessel detection community and comes from the fact that the vesselness filter enhances locally linear structures[6].

4.2.2 Centerline Extraction

Now that we have obtained a vesselness image giving a likelihood of a pixel to belong to a vessel, we propose a geometric representation of the vessel structure. Registration methods based on this representation are called feature-based methods and have multiple advantages regarding our applications (detailed in Section 3.3). Based on observations, vessels can be well approximated by tubular structures as modeled in the vesselness approach. A tubular structure is formed by a curve called a centerline, usually modeled as an ordered set of points, and radii associated to

[5]The apparent size is calculated by multiplying the expected radii of the coronary arteries to be detected by a scaling factor induced by the cone-beam X-ray projection.

[6]Bifurcations are more isotropic structures and are often classified in Table 4.1 as blobs.

(a) Fine scale response (b) Middle scale response (c) Coarse scale response

Figure 4.9: Frangi Vesselness map at three different scales (from fine to coarse).

(a) Vesselness (with background division) (b) Vesselness (no background division)

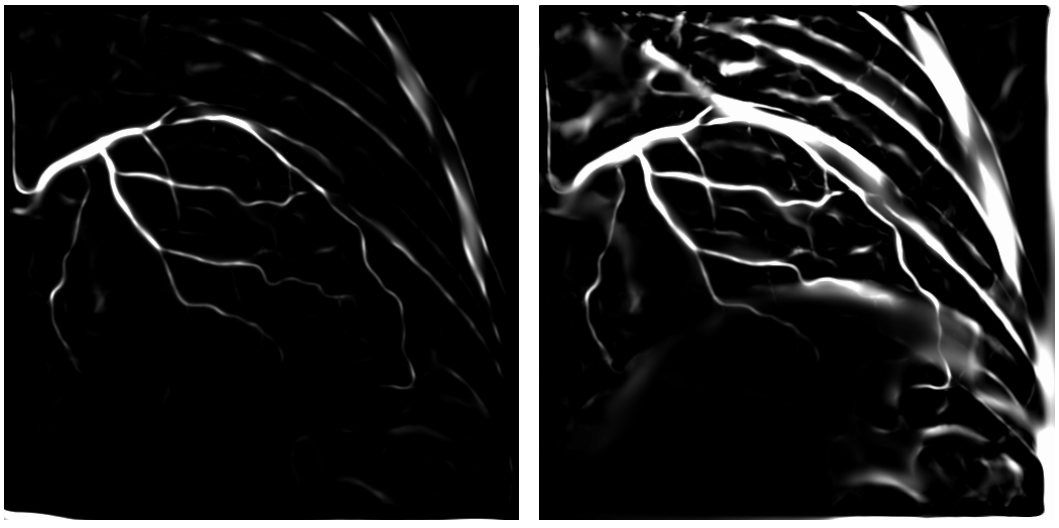

Figure 4.10: Comparison between vesselness maps obtain with and without previous background division (window-width and window-level of both images have been automatically set on the region of interest of Figure 4.7d and 4.7e)

each point of the centerline. The majority of the literature only uses the centerline information and does not make use of the radius information. The first step to the sparse geometrical representation of the 2D vasculature is the vessel centerline extraction from the enhanced image.

Given a vessel of radius R, the work of [Frangi et al., 1998] shows that the maximum vesselness response is obtained at a scale $\sigma = R$ corresponding to the size of the Gaussian derivative. It can be shown that this response is higher at the center of the vessel than at its borders. Given a pixel x, its corresponding normalized eigenvector $\overrightarrow{a_2}[x]$ extracted from the Hessian matrix $H[x]$ define a line perpendicular to the local vessel direction. Thus, if a pixel x lies on the centerline then it must be a local maximum of vesselness map in the direction defined by $\overrightarrow{a_2}[x]$. In other words, its two neighbors $x+\overrightarrow{a_2}[x]$ and $x-\overrightarrow{a_2}[x]$ must have lower vesselness response, which can be written as:

$$\begin{cases} \mathcal{V}[x] > \mathcal{V}\big[x - \overrightarrow{a_2}[x]\big] \\ \mathcal{V}[x] > \mathcal{V}\big[x + \overrightarrow{a_2}[x]\big] \end{cases} \tag{4.14}$$

To extract centerlines we run a Non-Maximum Suppression (NMS) algorithm that sets to 0 every pixel that does not satisfy the condition of Equation (4.14). It leads to a skeletonized vesselmap presented in Figure 4.11 where only the pixels at the vessel center remains. One should note that the resulting image is non-binary and still presents different intensities. In order to select the vessel centerlines a binarization step is still mandatory.

(a) NMS (b) NMS zoom

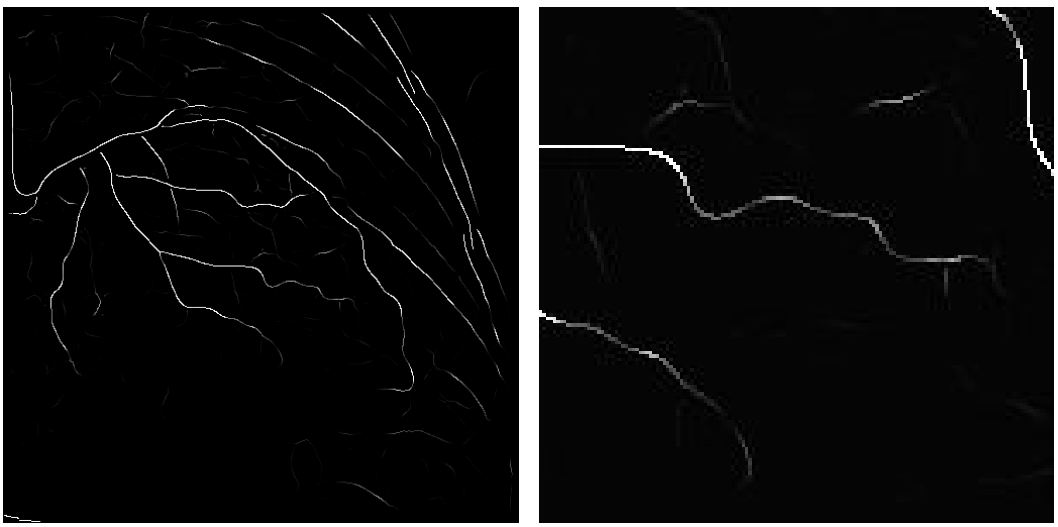

Figure 4.11: Non-Maximum Suppression (NMS) applied to the vesselness map. A zoom on the middle part allows to see the one pixel width response.

Even if the NMS image of Figure 4.11a looks quite clean in terms of background structure, a naive thresholding (keeping all pixels having a non-zero response) pro-

vided in Figure 4.12a reveals that many parasite structures remains in the NMS image. To keep only high responding structures, while allowing some lower responses in order to be robust to low vesselness at bifurcation locations, we propose to use the hysteresis thresholding method. Its principle is simple and is based on two thresholds T_{high} and T_{low} such that $T_{high} > T_{low}$. All pixels with a response in the NMS above T_{high} are classified as centerline pixels and those below T_{low} are considered as background pixels. A pixel between the two thresholds is considered as a centerline pixel if it is connected[7] to at least one pixel that is a centerline pixel. One should note that the previous condition can be satisfied even if no pixel in the neighborhood is above T_{high}, but if one has been declared a centerline pixel because it was itself in the neighborhood of a centerline pixel. This recursive propagation can be performed efficiently and finally results into a binary image. A set of curves in 2D, each constituted as a set of ordered points, can then be extracted from the binary image using the same connectivity relationship between pixels. The result of the hysteresis thresholding is presented in Figure 4.12 as well as the extracted geometric centerlines on top of the native image.

(a) Naive thresholding (b) Hysteresis thresholding

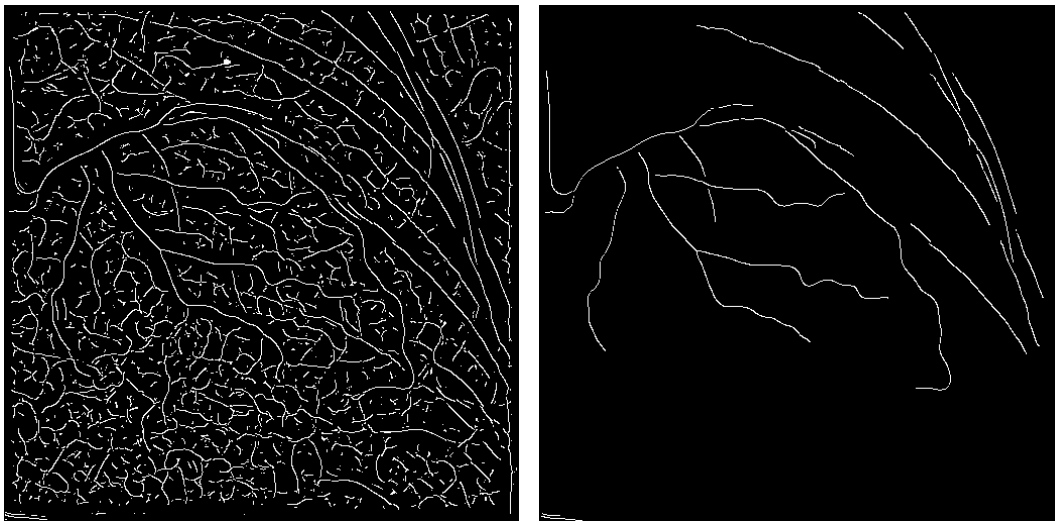

Figure 4.12: Thresholding of the NMS image to obtain vessel centerlines. (a) presents all non-zero pixel in the image, (b) is the result of the hysteresis thresholding.

At this stage we were able to obtain a set of centerlines, where each one can be

[7] Here we consider the 8-connectivity meaning that a pixel is connected to each direct neighbors and diagonal ones.

modeled as a polygonal curve[8] c in the 2D space:

$$c = \Big[c[1], c[2] \dots c[\#]\Big] \quad \text{s.t. } \forall i,\ c[i] \in \mathbb{R}^2 \tag{4.15}$$

Similarly to the 3D, the notation $c[\#]$ stands for the last point of the curve c. This set of centerline curves seems to correctly represent the 2D vasculature, but if we take a closer look (see Figure 4.13a for an example) multiple vessel portions appear to be missing especially at bifurcation location. This is explained by the vessel enhancement technique based on the analysis of the Hessian matrix, described in 4.2.1, which enhances locally linear contrasted structures in the image. However, at bifurcation locations a vessel is no more nicely represented by a linear structure and the vesselness response of pixels around bifurcation drastically falls.

4.2.3 Vascular Graph Extraction

In the previous section, we identified two types of holes in the vessel structures:

- **Cut vessel**: This type of missing connections are illustrated in Figure 4.13a inside orange circles. They correspond to multiples centerlines that should be connected into a unique one to properly describe the local anatomy.
- **Missing bifurcation**: The most frequent hole in the structure occurs at bifurcation location. Examples are circled in yellow in Figure 4.13a.

We designed a centerline reconnection algorithm that fills both types of holes in the 2D structure. It is composed of a first step that consists in joining centerlines that seem to correspond to the same vessel (cut vessel) and a second one addressing the problem of filling holes at bifurcation locations.

Regarding the first step, let us consider two centerline curves c_1 and c_2 as in Figure 4.13c. We denote by $a = c_1[\#]$ and $b = c_2[1]$ their two closest extremities without loss of generality. In order to decide whether c_1 and c_2 should be connected between these extremity points, we first check if these extremities are not too far from each other. Since the cut centerline problem often occurs because of the presence of another vessel in the same location, we do not expect the distance $\|b - a\|$ to be higher than the diameter of the biggest detected vessel. This condition is represented in Figure 4.14 and can be written as:

$$\big\|b - a\big\| < 2\sigma_{max} \tag{4.16}$$

where σ_{max} is the highest scale of the Frangi vesselness introduced in Equation (4.13). We also expect that the curves c_1 and c_2 are pointing to one another. To quantify this, we introduce the tangent vector $\overrightarrow{t_b}$ at a curve extremity b. A simple estimation of this vector can be defined by the two first points in the curve:

$$\overrightarrow{t_b} = \overrightarrow{tan}\big(c_2[1]\big) = \overrightarrow{c_2[2]c_2[1]} \tag{4.17}$$

[8] A polygonal curve is composed of ordered points that are pairwise connected by a straight line. Proper definition is provided in Equation (4.2)

(a) Segmented centerlines

(b) Zoom on proximal part

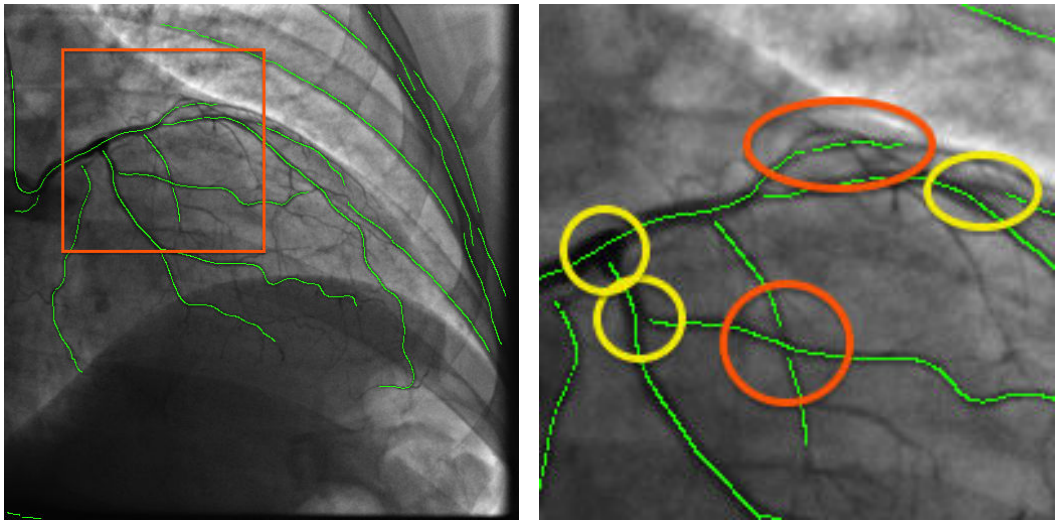

(c) Cut vessel

(d) Missing bifurcation

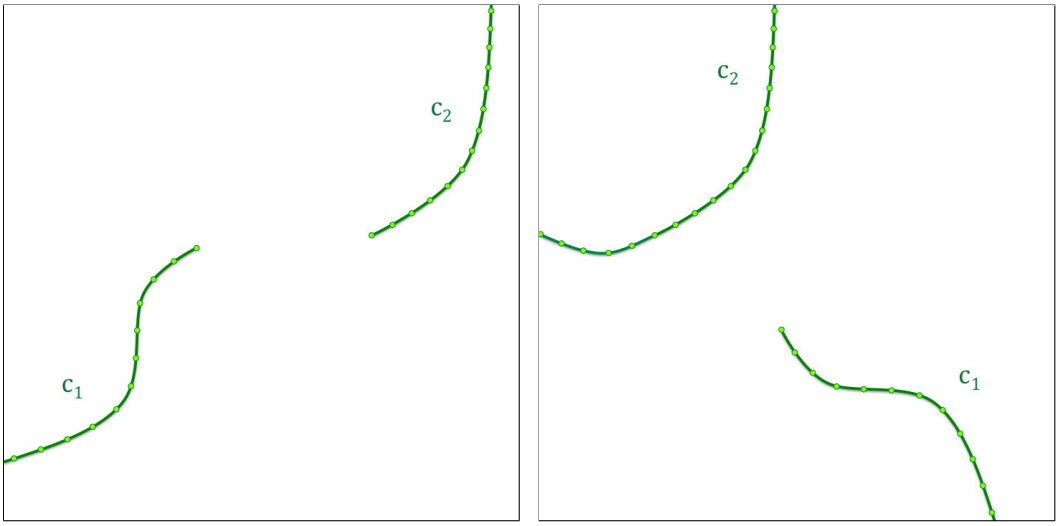

Figure 4.13: Segmented centerlines before the reconnection procedure on the whole image (a). (b) is a zoom in the orange region of (a), showing two types of segmentation problems: a single vessel cut in multiple centerlines (examples are circled in orange) and missing connections at bifurcations (examples are circled in yellow). A diagram representation of each type of problem is provided in (c) and (d).

The tangent t_a at the other extremity a can be defined similarly; both are represented in Figure 4.14. In practice, more robust tangent estimators $\overrightarrow{tan}(.)$ are preferred to face noise and involve to consider more than two points to compute the extremity tangent[9]. Tangent vectors $\overrightarrow{t_a}$ and $\overrightarrow{t_b}$ should satisfy:

$$\overrightarrow{t_a} \cdot \overrightarrow{t_b} < 0 \tag{4.18}$$

to be considered as candidates for reconnection.

These two previous conditions limit the number of couples of extremities to test before estimating if the two curves correspond to the same underlying vessel. We thus test an additional condition, if the two previous ones are satisfied, that checks if one extremity point is in the prolongation of the other curve and vice versa. We consider to extrapolate of the vessel along its extremity tangent, which corresponds to a linear extrapolation in the direction of the tangent vector. We define the linear extrapolation of c_1 at the location b, denoted a' by:

$$a' = a + \left\|b - a\right\| \cdot \overrightarrow{t_a} \tag{4.19}$$

as well as the extrapolation of c_2 at the location a, denoted b':

$$b' = b + \left\|b - a\right\| \cdot \overrightarrow{t_b} \tag{4.20}$$

The centerlines c_1 and c_2 constitute good candidates for pairing if the two following extrapolation errors ε_1 and ε_2 are under a certain threshold:

$$\begin{cases} \varepsilon_1 = \left\|b - a'\right\| < \sigma_{min} \\ \varepsilon_2 = \left\|a - b'\right\| < \sigma_{min} \end{cases} \tag{4.21}$$

Here again the distance threshold is defined accordingly to the scales used in the Frangi vesselness, considering that vessel extrapolation must be as precise as the smallest vessel sought. If the couple (c_1, c_2) satisfies all equations (4.16), (4.18) and (4.21), then c_2 is said to be a candidate for reconnection with c_1. If a curve c_1 can find multiple curves to be prolonged with, the one with the lowest sum of extrapolation errors $\varepsilon_1 + \varepsilon_2$ is chosen. The two curves c_1 and c_2 are then joined into a new one c such that:

$$c = \Big[c_1[1], c_1[2] \dots c_1[\#], c_2[1], c_2[2] \dots c_2[\#]\Big] \tag{4.22}$$

The resulting reconnected centerline is then re-sampled uniformly at 1 pixel distance, to fill the empty part between $c_1[\#]$ and $c_2[1]$, and smoothed[10] in this added portion.

Now that cut centerlines are joined, we still need to solve the problem occurring at bifurcation locations, which is illustrated in Figure 4.13d. Again we consider a

[9] In this thesis we computed the tangent using Equation (4.17) but after a smoothing of all detected curves.

[10] Smoothing of a polygonal curve can consist in replacing each point by the barycenter of its neighbors.

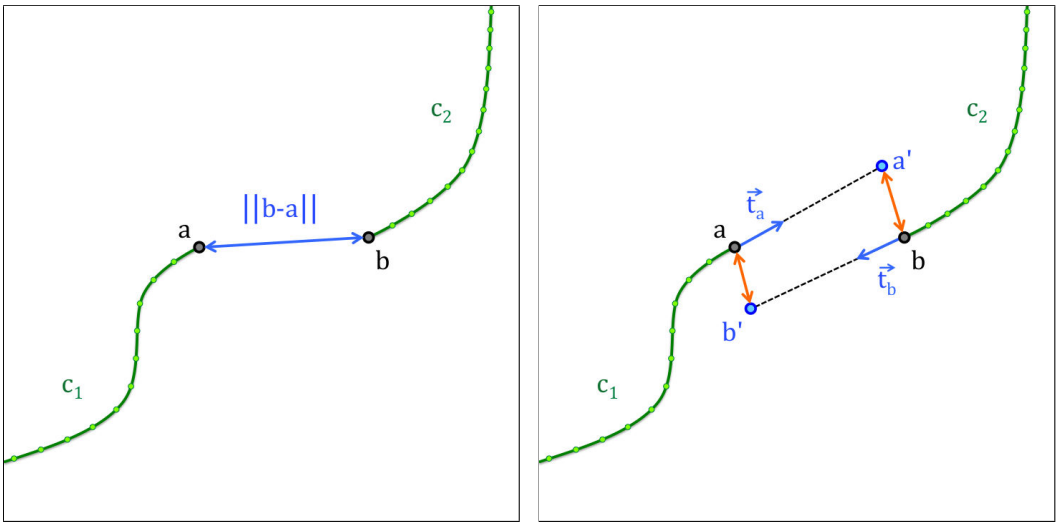

Figure 4.14: Cut vessel reconnection procedure. The left diagram illustrates the distance between the two centerlines extremities considered for the reconnection. On the right, the linear extrapolation of the extremities of each vessel following the direction of tangent vectors (in blue) are denoted a' and b'. The extrapolation errors involved in Equation (4.21) are represented as orange arrows.

curve c_1 and its extremity $a = c_1[\#]$ around which we are looking for a potential bifurcation reconnection. We assume that it is relevant to reconnect the curve c_1 to a curve c_2 if at least one point of c_2 is in the "field-of-view" of the extremity of c_1, represented in orange in Figure 4.15. A point p in the image plane belongs to the 2D field-of-view neighborhood of a, denoted $\mathcal{N}(a)$, if:

$$p \in \mathcal{N}(a) \Leftrightarrow \begin{cases} \|p - a\| < 2\sigma_{max} \\ \text{angle}\left(\overrightarrow{t_a}, \overrightarrow{ap}\right) < \Theta_{max} \end{cases} \tag{4.23}$$

where σ_{max} denotes the coarsest scale used in the vesselness map, the angle(.,.) function computes the angle between two vectors, $\overrightarrow{ap}$ is the vector defined by the two points a and p, and Θ_{max} controls the angular opening. A curve c_2 is said to belong to this neighborhood if at least one of its points is inside $\mathcal{N}(a)$. If multiple 2D curves belong to $\mathcal{N}(a)$, the curve c_1 will be extended to the closest one.

The result of the whole reconnection algorithm, composed of the cut vessel reconnection step then the bifurcation prolongation step, is presented in Figure 4.16.

Looking at Figure 4.16, representing the 2D vascular structure as a set of (disconnected) curves does not represent all types connectivity visible in the projected vasculature: clearly centerlines curves look connected at bifurcation points. However, extracting a tree as it can be done for the 3D vasculature (see 4.1.2 for more details) cannot be achieved because of vessels superimposition that creates loops[11].

[11] See Section 4.1.2 for a definition of a loop.

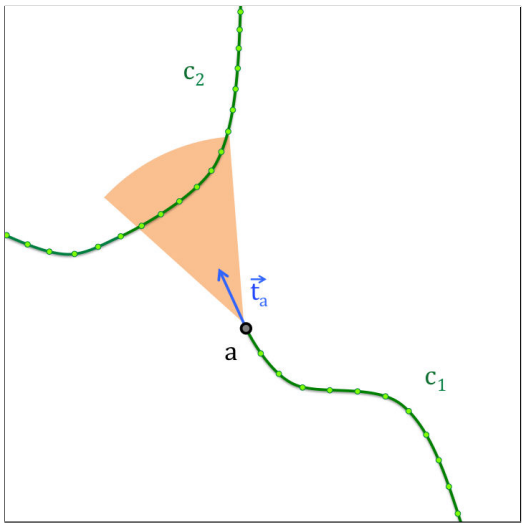

Figure 4.15: Bifurcation missing reconnection procedure. The conic search zone neighborhood is presented in orange based on the extremity tangent vector represented in blue.

(a) Reconnected centerlines (b) Reconnected centerlines zoom

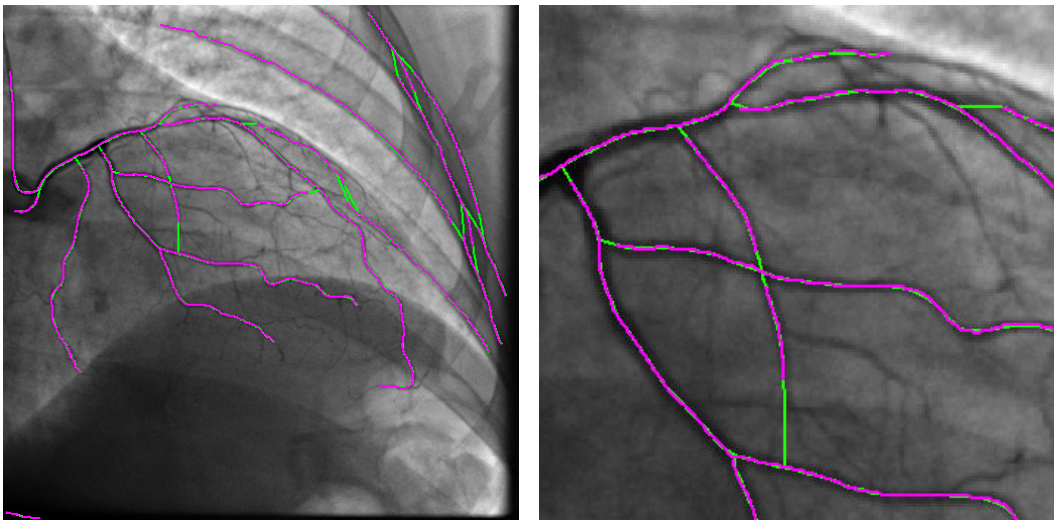

Figure 4.16: Segmented centerlines (in purple) and the extracted graph (in green) after reconnection and smoothing. (a) is the result of the centerline reconnection algorithm and (b) a zoom on the same region of interest as Figure 4.13a

Even if the hierarchy between centerlines cannot be retrieved, the 2D vasculature can be well represented by a graph in the image plane. A graph $\mathcal{X} = (\mathbf{e}, \mathbf{n})$ is composed of a set of nodes $\mathbf{n}$ pairwise connected by links called edges in the set of edges $\mathbf{e}$. The segmented vasculature can be seen as a graph where edges are segmented centerline curves joined by nodes that correspond either to a bifurcation between different curves or to an end of segmentation. Thus a node $n \in \mathbf{n}$ is a point in the image plane (i.e. $n \in \mathbb{R}^2$) and an edge $e \in \mathbf{e}$ is a centerline curve represented by a polygonal curve as defined in Equation (4.15). The resulting sparse geometrical representation of the fluoroscopic image is presented in Figure 4.17. Contrary to a set of non-connected curves, this graph representation supports the two connectivity types present in the vascular structure (as it was already mentioned in Section 4.1.2).

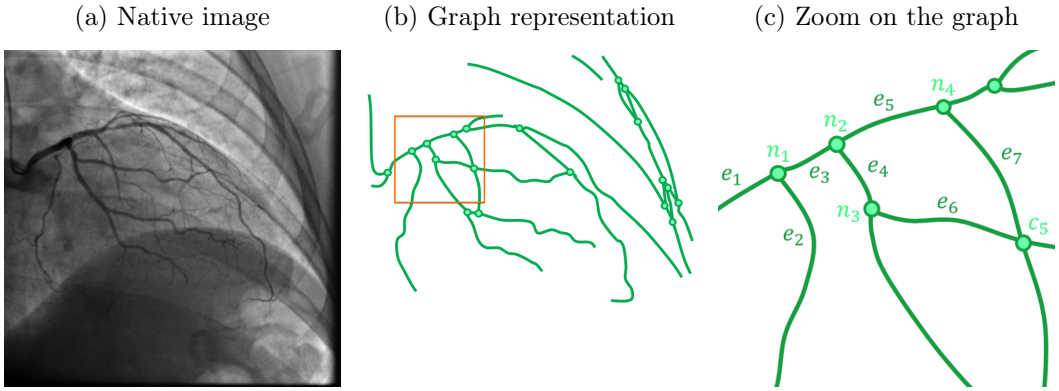

Figure 4.17: Graph representation of the 2D vasculature. (a) native image, (b) extracted graph representation only showing bifurcation nodes and not extremity ones, (c) zoom on the orange region of (b) presenting nodes n_i and edges e_j.

4.3 Discussion

In the two previous sections we have described two feature representations of the structures to be matched that fit well to the particular topology of the vasculature. In one hand, the 3D vessel tree extracted from the CTA scan is referred as the model because it is verified and corrected by the clinicians who use it in a diagnostic and planning purpose. In the other hand, the 2D vascular graph is automatically extracted from the 2D image and is subject to imperfections. The main problem of the extracted 2D features is fake detection as it is illustrated in Figure 4.18. In this thesis we are interested in preserving the topology along the registration procedure, which necessitates a correct representation of the vasculature. Mis-detection of vessels in the image plane can dramatically impact the topology of the resulting detected graph. We thus prefer an over-segmentation of the structures, even at the cost of several fake branches and nodes in the graph, rather than an under-

segmentation that would lead to missing important vessels.

(a) Image 1 (b) Image 2

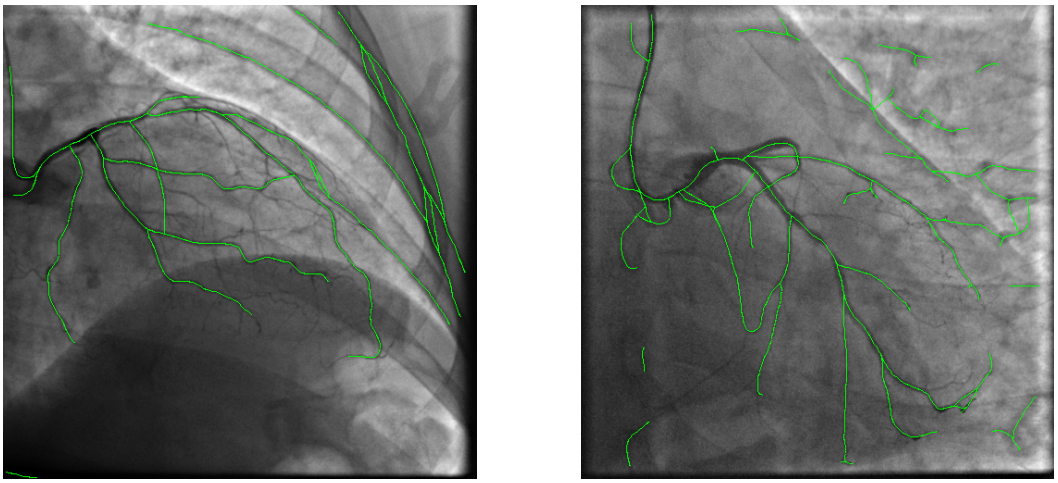

Figure 4.18: Imperfections of the automatically extracted vascular graph. (a) fake detections of the ribs as vascular structures, (b) fake detections of pulmonary structures as vessels.

In addition, the model and the data present multiple differences induced by their dimensionality difference (2D and 3D). The projective nature of the 2D image induces vessel superimpositions, especially around bifurcation location. Actually, one cannot precisely locate anatomical bifurcations in 2D and cannot even expect a one-to-one correspondence between bifurcations in 3D and bifurcation in 2D. For example, bifurcations B_1, B_2 and B_4 of Figure 4.19b are superimposed in the location detected in the vascular graph as the node n_1 in Figure 4.19c. Moreover, as it has been highlighted in Section 2.4, the CTA modality may show occluded vessels that are not visible (and thus non-segmentable) in the 2D image as in Figure 4.20b. The intra-arterial interventional injection allows to segment the vasculature more distally than the intra-venous CTA injection as shown in Figure 4.20b in numerous vessels.

To visually evaluate the results of this procedure, we provide in Figure 4.21 a representative overview of the automatic graph extraction from fluoroscopic images. Detected structures on the whole database, presented in Appendix D and including cases chosen in Figure 4.21, were obtained using the same set of parameters for the image filtering, segmentation and graph extraction. One will note different levels of false detection depending on the vessel contrast observed in the image (depending on the patient thickness and on the vessel filling by the contrast medium). However, we achieved a segmentation of the 2D vasculature that includes most of the connexions between centerlines.

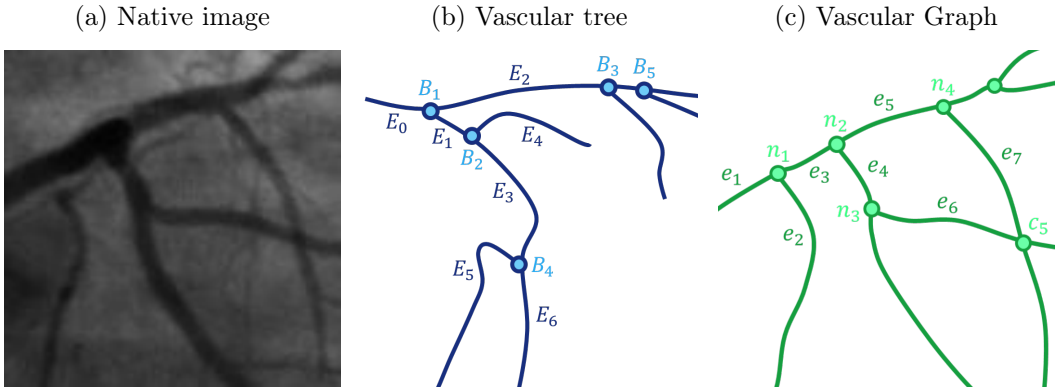

Figure 4.19: Superimposition of multiple bifurcations in the projective image: bifurcation nodes B_1, B_2 and B_4 are all projected onto the same node n_1. (a) zoom on the proximal part of the fluoroscopic image, (b) annotated proximal 3D tree structure part, (c) annotated proximal 2D graph structure part.

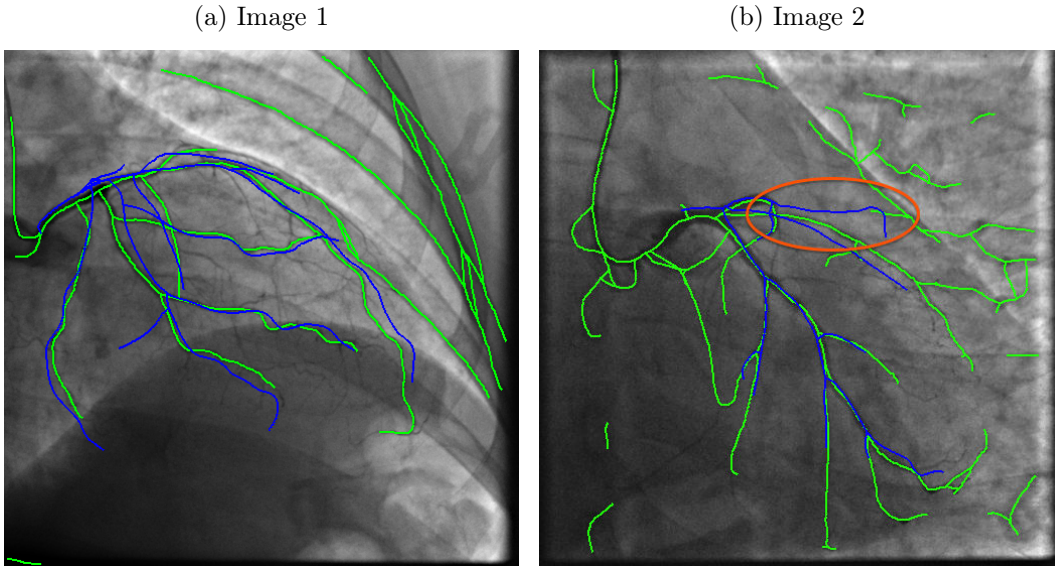

Figure 4.20: Differences regarding centerlines segmentation. In blue: projection of the 3D vascular tree at the correct registered pose, in green: 2D segmented centerlines. (a) example of 2D vessels segmented deeper in the distality that their 3D counterpart, (b) example of an occluded vessel (in the orange region) that is present in the 3D but invisible in the 2D.

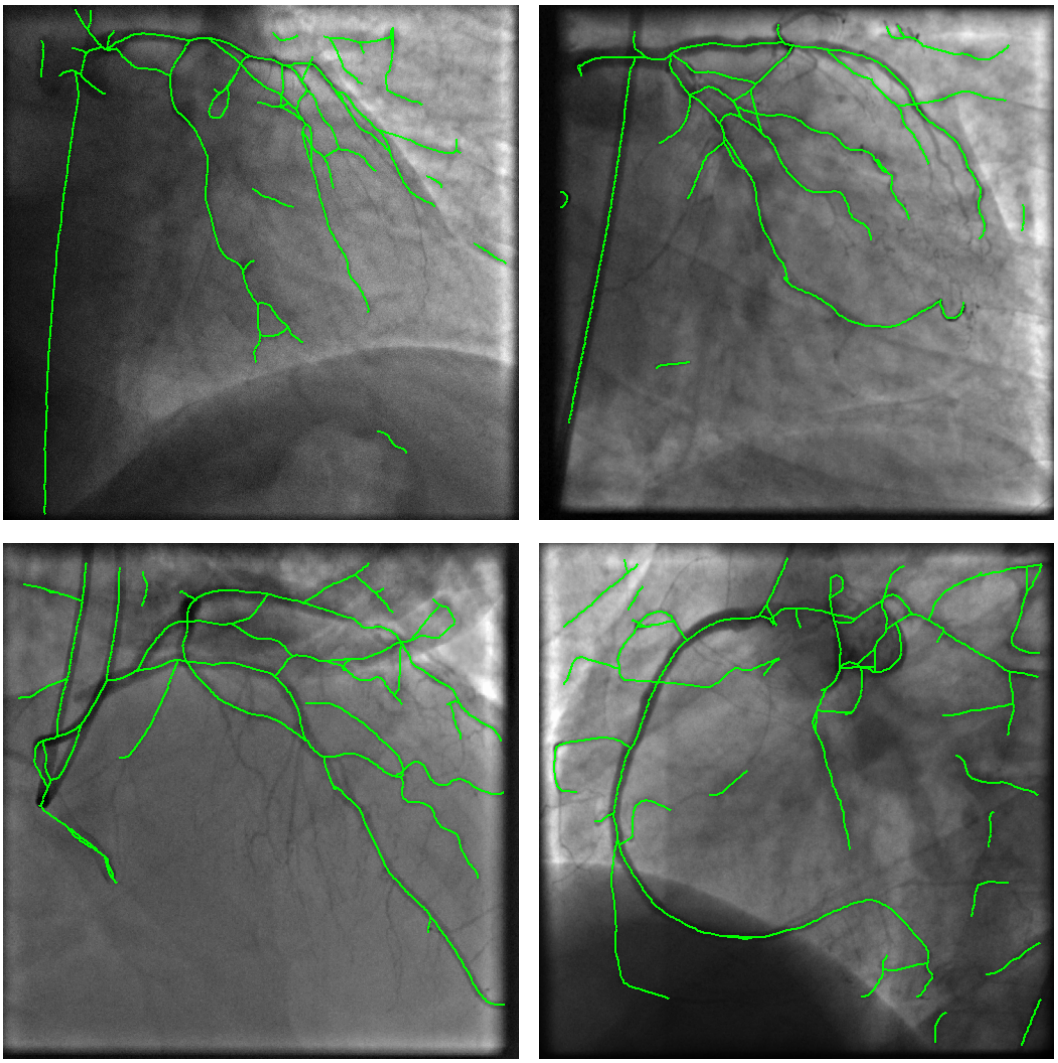

Figure 4.21: Fully automated vascular graph extraction from different angiographic images of the database.

Chapter 5

The Iterative Closest Curve Framework

Contents

In the literature on 3D/2D vessel registration (Section 3.3), the majority of feature-based algorithms highlighted the importance of rejecting wrong pairings between the 3D and the 2D structure. From the well known Iterative Closest Point (ICP) algorithm introduced in [Besl and McKay, 1992], multiple efforts have been made to deal with the problem of pairings induced by the closest point assumption (illustrated in Figure 5.3). Multiple refinements of the ICP algorithm have been provided in [Rusinkiewicz and Levoy, 2001], such as points of interest selection or pairing rejection, trying to solve the mispairing problem without changing the closest point assumption. By relaxing the one-to-one pairing constraint, Expectation Maximization (EM) based approaches, such as [Granger and Pennec, 2002; Groher et al., 2009; Baka et al., 2014], increased the capture range of the ICP algorithm. However at convergence, these approaches behave like the ICP and thus can lead to pairing inconsistencies. In order to build better pairings, [Feldmar et al., 1997; Mitrović et al., 2013; Baka et al., 2013, 2014] used prior knowledge on vascular structure to be matched by adding the local vessel direction estimation at each feature point. The lack of coherence regarding the pairings along vessels has been

addressed in [Groher et al., 2009] by adding a penalization term into the optimized cost function.

Instead of penalizing incoherence we propose here to impose coherence along the pairings by matching entire 3D curves to curves extracted from the 2D graph. We got inspired from the work of [Liu and Bullitt, 1998] and [Duong et al., 2009] that consider the registration problem as an alignment between curves. Its applicability to coronary arteries registration has been shown in [Duong et al., 2009]. However both techniques rely on manual correspondences between curves of the two modalities that strongly limit their use in an interventional framework. In this chapter, we define a framework to register two structures composed of curves that addresses the matching and alignment problem. It is called Iterative Closest Curve (ICC) because it is based on the same idea as the ICP algorithm, replacing points to be matched by curves.

5.1 General Principle

The registration problem consists in best aligning the model $\mathcal{Y}$ with the data $\mathcal{X}$ by finding the optimal transformation $\hat{T}$ in a set Ω of admissible ones. Feature-based registration algorithms usually require solving the following equation:

$$\hat{T} = \underset{T \in \Omega}{\operatorname{argmin}} \, \mathcal{D}\left(T(\mathcal{Y}), \mathcal{X}\right) \tag{5.1}$$

where the distance $\mathcal{D}$ is based on set of correspondences between $\mathcal{Y}$ and $\mathcal{X}$. These pairings may be explicitly defined and used to determine the transformation, or may be implicitly present as a consequence of the transformation. The purpose of the ICC-framework is to solve this registration problem using the prior knowledge that both structures are composed of curves. We extend the Iterative Closest Point (ICP) method, introduced in [Besl and McKay, 1992], by matching curves instead of points. The ICC algorithm involves a curve-to-curve distance called the Fréchet distance. It is based on a point pairing set between curves that preserves order along them. As a consequence, the proposed procedure preserves the curve topology of structures to be matched. This section is dedicated to the general principle of the ICC algorithm. We focus our effort on defining a framework that can be applied to every matching and registration problems where curves can be extracted from both datasets.

5.1.1 The Fréchet Distance

In order to match and align curves, one needs to define a curve-to-curve distance. This distance will constitute the core of the ICC algorithm and thus must be defined precisely. Measuring the distance between two polygonal curves[1] has been addressed in [Alt and Godau, 1992], where the two curves are treated similarly. In model-to-data registration, the model is matched to the data and not the other way around.

[1] Polygonal curves have been defined in Equation (4.2).

We provide in the following non-symmetric versions of distances between the model curve c_M and the data curve c_D, respectively defined as $c_M = \left[c_M[1] \dots c_M[\#]\right]$ and $c_D = \left[c_D[1] \dots c_D[\#]\right]$.

The first distance presented in [Alt and Godau, 1992] is the Hausdorff distance that considers the two curves as sets of points without any particular connexion between them:

$$\mathcal{H}(c_M, c_D) = \max_i \left\{ \min_j \left\| c_M[i] - c_D[j] \right\| \right\} \tag{5.2}$$

An intuitive interpretation of this measure is that each point of the model curve c_M is associated to its closest in the data curve c_D and the Hausdorff distance is the maximum distance between paired points. This distance is based on a closest point pairing set between c_M and c_D, denoted $\pi_{\mathcal{H}}$, defined by:

$$\pi_{\mathcal{H}} = \left\{ \left(c_M[i] \ , \ \operatorname*{argmin}_{x \in c_D} \left\| c_M[i] - x \right\| \right) \right\} \tag{5.3}$$

where each point $c_M[i]$ of c_M is paired to its closest in c_D. Given this pairing, Equation (5.2) can be rewritten:

$$\mathcal{H}(c_M, c_D) = \max_{(y,x) \in \pi_{\mathcal{H}}} \left\| y - x \right\| \tag{5.4}$$

By definition, the Hausdorff distance treats curves as two sets of points without any particular connectivity between them. It has been stressed in the literature (see Section 3.3.3) that the closest point pairing procedure between sets, without any further constraint, often leads to non-relevant pairings. In fact, this observation has been made also for curves in [Alt and Godau, 1992], especially for tortuous ones. Instead of the Hausdorff distance, Alt and Godau [1992] consider a distance built on pairings that ensure point order preservation along both curves. This distance is called the Fréchet distance and is often explained in the following way: a man and his dog are walking; one is following the curve c_M and the other c_D; both are able to control their speed but none is able to backtrack; the Fréchet distance represents the length of the smallest leash that is necessary to join the man and his dog during the entire walk. The continuous version of this Fréchet distance is provided in [Alt and Godau, 1992] and involves two reparametrization functions that model the man and the dog speeds along their walk. It has been shown in [Eiter and Mannila, 1994] that the discrete version of the Fréchet distance, denoted $\mathcal{F}$, is a close upper bound of the continuous one in the case of polygonal curves.

The discrete Fréchet distance is based on the concept of order preserving point pairing set. A point pairing set π between c_M and c_D is said to preserve the order along both curves if it satisfies:

$$\begin{cases} \forall \left(c_M\left[i\right], c_D\left[j\right] \right) \in \pi \\ \forall \left(c_M\left[i'\right], c_D\left[j'\right] \right) \in \pi \end{cases} \quad i < i' \iff j < j' \tag{5.5}$$

We recall that we consider non-symmetrical model-to-data distances and thus we expect that a pairing set π provides correspondences between **all** points constituting

the model curves c_M but not necessarily all points in the data curve. In addition of Equation (5.5), an admissible pairing set should therefore satisfy:

$$\forall c_M[i] \in c_M \ , \ \exists (y, x) \in \pi \quad \text{s.t.} \quad c_M[i] = y \tag{5.6}$$

The discrete Fréchet distance can now be defined by:

$$\mathcal{F}(c_M, c_D) = \min_{\pi} \left\{ \max_{(y,x)\in\pi} \|y - x\| \right\} \tag{5.7}$$

where π describes all admissible order preserving pairings between c_M and c_D. Here the different possibilities of π describe all possible walks of the man and his dog, this time both can only take a finite number of positions. The maximum operator computes the length of the leash necessary to have the walk defined by the pairing set π and the minimum operator choses the best walk among all based on the leash length. An example of the pairings created by the Hausdorff distance and the Fréchet distance is provided in Figure 5.1.

(a) Hausdorff distance (b) Fréchet distance

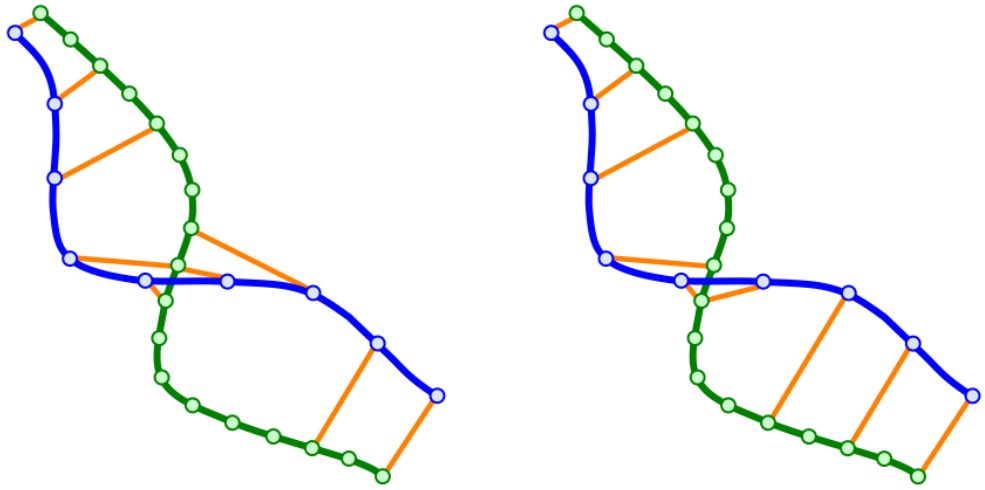

Figure 5.1: Difference between the pairings created by the Hausdorff distance (a) and the Fréchet distance (b). The model-to-data distance is computed from the projected 3D curve (in blue) and the 2D curve (green). Pairings between points, used to compute the two distances, are presented in orange. By following the point pairings from the top left to the bottom right, the reader will see that the pairing induced by the Hausdorff distance present a portion of backtracking, which is not the case of the Fréchet pairing.

A summation variant of the discrete Fréchet distance is also provided in [Eiter and Mannila, 1994], replacing the maximum operator by a sum. The sum version

is usually preferred when the pairing set is of interest to the application[2]. Since pairings are crucial in our application, we will use the summation definition of the Fréchet distance in a squared version, replacing Equation (5.7) by:

$$\mathcal{F}(c_M, c_D) = \min_{\pi} \left\{ \sum_{(y,x)\in\pi} \|y - x\|^2 \right\} \tag{5.8}$$

The pairing set realizing the minimum is called the Fréchet pairing and is denoted $\pi_{\mathcal{F}}$:

$$\pi_{\mathcal{F}}(c_M, c_D) = \operatorname*{argmin}_{\pi} \left\{ \sum_{(y,x)\in\pi} \|y - x\|^2 \right\} \tag{5.9}$$

One should note that if the square does not change the optimal pairing with respect to the simple sum version, this formulation will allow us to use least squares optimization procedures in the following sections. Regarding the implementation of this distance, efficient methods exist in the literature to find the optimal pairing, mostly involving dynamic programming. They are usually based on a 2D representation of pairings between two curves, called the "free space", where a point in this space represents a possible point pairing between curves. A cost is associated to each pairing (the Euclidean distance between paired points) and the resulting Fréchet pairing is given by the optimal walk in this space that satisfies constraints to preserve order along curves.

Unfortunately, computing the exact Fréchet distance $\mathcal{F}$ of Equation (5.8) is usually greedy in terms of computational time, especially when the number of points defining polygonal curves increases. We considered the implementation of an upper bound of this distance using Algorithm 1. It consists in traveling along the model curve c_M and assigning to each point its closest in the part of the data curve c_D that will not induce backtracking. First, it is assumed that c_M and c_D are indexed in the same order[3], meaning that the route from $c_M[1]$ to $c_M[\#]$ corresponds to the route from $c_D[1]$ to $c_D[\#]$. Then, we search the closest point of $c_M[1]$ in the entire curve c_D and denote j_1 the index in c_D such that:

$$j_1 = \operatorname*{argmin}_{j} \left\| c_M[1] - c_D[j] \right\| \tag{5.10}$$

Knowing this pairing $(c_M[1], c_D[j_1])$, we continue the procedure with the point $c_M[2]$. Once again the closest point of $c_M[2]$ is searched, but in a part of c_D that will not induce backtracking. The general formulation of the index forming the pairing induced by the approximated Fréchet distance is:

$$j_{i+1} = \operatorname*{argmin}_{j>j_i} \left\| c_M[i+1] - c_D[j] \right\| \tag{5.11}$$

[2]If every point of the model contributes to the quantity that is minimized then all pairings will be optimized, contrary to the max version, which will only be sensitive to the worst pairing between the two curves.

[3]In practice if one does not know the respective orientation of curves, he or she can try both possibilities and chose the one with the lowest Fréchet distance.

This faster estimation of the Fréchet distance has been implemented and tested on various vessels extracted from clinical cases. We visually assessed that there was no significant difference between the Fréchet pairing created by the exact and the approximated Fréchet distance. This confirms that the proposed approximation can be used to determine the point pairing set, and thus the estimated Fréchet distance, in our clinical application.

Because of the model-to-data nature of our problem, we consider a non-symmetrical Fréchet distance that computes the distance from the model curve to the data curve. As illustrated in Figure 5.2a, a non-negligible data curve portion may be "jumped" by the pairings induced by the Fréchet distance (the dorsal-fin shape portion in the example). To limit this phenomenon, we introduce a search zone parameter Δ_J. It corresponds to the maximal length of the gap (along the data curve) between data points paired to two consecutive points along the model curve. Reducing the search zone also leads to further decrease the computational complexity of Equation (5.11) that becomes:

$$j_{i+1} = \underset{j \in [j_i \dots j_i + \Delta_J]}{\operatorname{argmin}} \left\| c_M[i+1] - c_D[j] \right\| \tag{5.12}$$

The effect of Δ_J on a toy example is presented in Figure 5.2b.

(a) Without limited search zone (b) With limited search zone

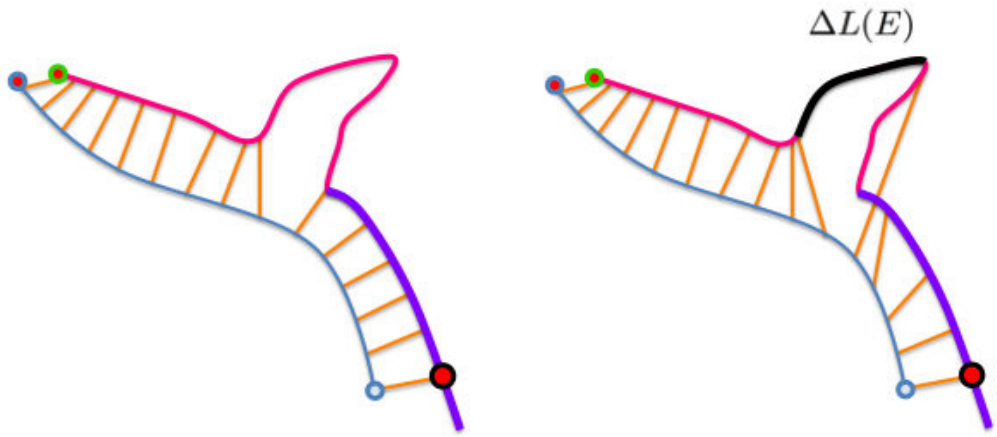

Figure 5.2: Illustration of the impact of a limited search zone on the Fréchet pairings between the projected 3D curve (in blue) and the 2D curve (in purple and pink). (a) Fréchet pairings presenting a long jump in the absence of search zone; (b) Fréchet pairings obtained by Algorithm 1 with a search zone limit represented in black.

To summarize, the Fréchet distance gives both a quantification of the distance between curves and a point pairing set that preserves point order along them. Since

Algorithm 1 Fréchet distance and Fréchet pairing computation

INPUT: c_M : model curve,
INPUT: c_D : data curve,
INPUT: Δ_J : search zone parameter
OUTPUT: $\mathcal{F}$: Fréchet distance between c_M and c_D,
OUTPUT: $\pi_{\mathcal{F}}$: Fréchet pairings realizing the Fréchet distance

1: **function** FRECHET(c_M,c_D)
2: $\mathcal{F} \leftarrow 0$
3: $\pi_{\mathcal{F}} \leftarrow \emptyset$
4: $j_{prec} \leftarrow 1$
5: **for all** $i_{curr} \in \left[1 \dots \text{card}(c_M)\right]$ **do**
6: $d_{min} \leftarrow +\infty$
7: **for all** $j \in \left[j_{prec} \dots j_{prec} + \Delta_J\right]$ **do**
8: **if** $\|c_M[i_{curr}] - c_D[j]\| < d_{min}$ **then**
9: $d_{min} \leftarrow \left\|c_M[i_{curr}] - c_D[j]\right\|$
10: $j_{curr} \leftarrow j$
11: **end if**
12: **end for**
13: $\mathcal{F} \leftarrow \mathcal{F} + {d_{min}}^2$
14: $\pi_{\mathcal{F}} \leftarrow \pi_{\mathcal{F}} \cup \left\{\left(c_M[i_{curr}], c_D[j_{curr}]\right)\right\}$
15: **end for**
16: **return** $\mathcal{F}$ and $\pi_{\mathcal{F}}$
17: **end function**

this measure takes into account the curve topology, it will be at the center of the ICC-framework.

5.1.2 The Iterative Closest Point Algorithm

The Iterative Closest Point (ICP) algorithm is a general feature-based registration algorithm that minimizes Equation (5.1) where the distance $\mathcal{D}$ between the model $\mathcal{Y}$ and the data $\mathcal{X}$ is the sum of closest point distance. The ICP registration problem can be written:

$$\begin{cases} \hat{T} = \underset{T \in \Omega}{\operatorname{argmin}} \sum_{Y \in \mathcal{Y}} \left\| \text{Closest}_{\mathcal{X}}\big(T(Y)\big) - T(Y) \right\|^2 \\ \text{Closest}_{\mathcal{X}}\big(T(Y)\big) = \underset{x \in \mathcal{X}}{\operatorname{argmin}} \left\| x - T(Y) \right\|^2 \end{cases} \tag{5.13}$$

where Ω denotes the set of admissible transformations. Solving at the same time the transformation optimization (first part of Equation (5.13)) and the closest point correspondences between the model and the data (second part of Equation (5.13)) is a challenging task.

Thus, Besl and McKay [1992] propose to alternate the pairing set construction and the transformation optimization in a recursive procedure that can be written:

$$\begin{cases} \pi_i = \bigcup_{Y \in \mathcal{Y}} \Big(Y, \text{Closest}_{\mathcal{X}}\big(T_{i-1}(Y)\big) \Big) \\ T_i = \underset{T \in \Omega}{\operatorname{argmin}} \sum_{(Y,x) \in \pi_i} \left\| x - T(Y) \right\|^2 \end{cases} \tag{5.14}$$

where π_i is the point pairing set established using the closest point assumption at the given transformation T_{i-1} and T_i is the optimal transformation minimizing the least squares criterion with the given correspondences π_i. This process is initiated by a transformation T_0 that constitutes the initial pose estimation. The ICP algorithm can be written in the following 3-steps form:

1. At a given transformation T_{i-1}, compute the closest point pairings between each point of the model $\mathcal{Y}$ transformed by T_{i-1} to its closest in the data $\mathcal{X}$. This pairing set π_i is computed using the first line of Equation (5.14) where the closest point pairing can be computed by an exhaustive search in the data $\mathcal{X}$ for each point in the model $\mathcal{Y}$.

2. At a given point pairing set π_i, compute the optimal transformation T_i that minimizes the sum of squared distances between corresponding points. Depending on the set of admissible transformations Ω, several methods can be used to solve the second step of Equation (5.14). In [Besl and McKay, 1992], a direct method is provided to compute the optimal rigid transformation aligning two sets of paired points.

3. Return to step 1 until convergence, where convergence means that two consecutive estimations of the transformation T_{i-1} and T_i are close enough to each other to be considered as equivalent. If the transformation T_{i-1} is invertible, one can compute the incremental transformation ${T_{i-1}}^{-1} \circ T_i$ and evaluate the distance to identity. In practice, the transformation computed in step 2 is applied to the model $\mathcal{Y}$ such that this transformation corresponds in fact to an incremental transformation.

A proof of convergence of this procedure is given in [Besl and McKay, 1992], based on the fact that steps 1 and 2 decrease each time the same distance criterion, which is lower bounded.

This algorithm has been used in a wide variety of domains because of its applicability to any kind of features (geometric representations can generally be sampled as a point set). However, it has been criticized in the literature suffering from low capture range[4] often attributed to the closest point correspondences built during the pairing phase. In our application this leads to pairing "jumps" along vessels that are illustrated in Figure 5.3 where several vessels are partly paired to two different and quite distant vessels. For these reasons, the ICP algorithm often converges to a wrong registration position (see Figure 5.4 for an example).

(a) ICP pairings (b) Pairing jumps along vessels

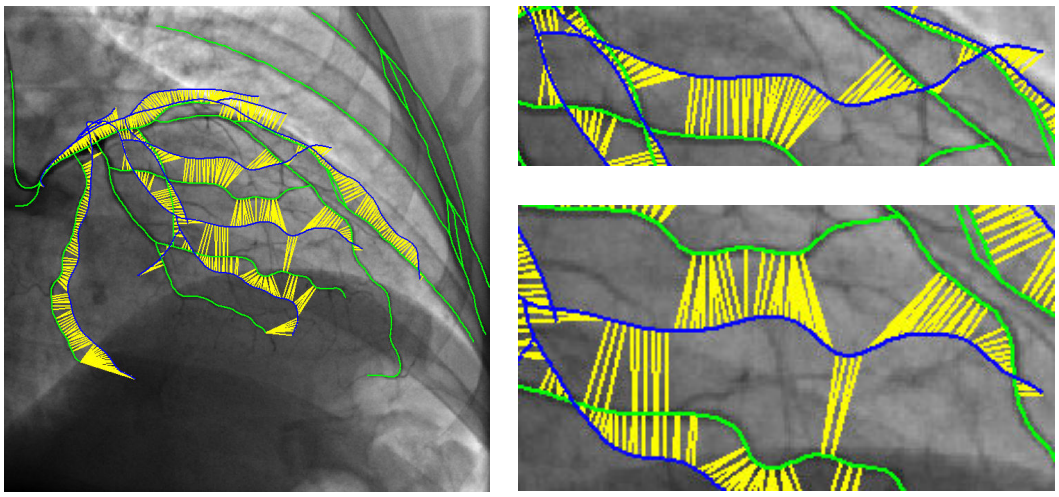

Figure 5.3: Closest point pairings (yellow) between the 3D projected model structure (blue) and the 2D data structure (green). (a) closest point pairings at the initial pose given by calibration, (b) illustration of pairing jumps along two vessels of the 3D structure.

Multiple refinements of this ICP algorithm have been developed since 1992 to improve the method behavior. A representative panel is provided in [Rusinkiewicz

[4]Capture range of a registration algorithm is defined as the robustness of an algorithm with respect to the amplitude of the displacement to compensate.

(a) ICP registered position (b) Correct Registration

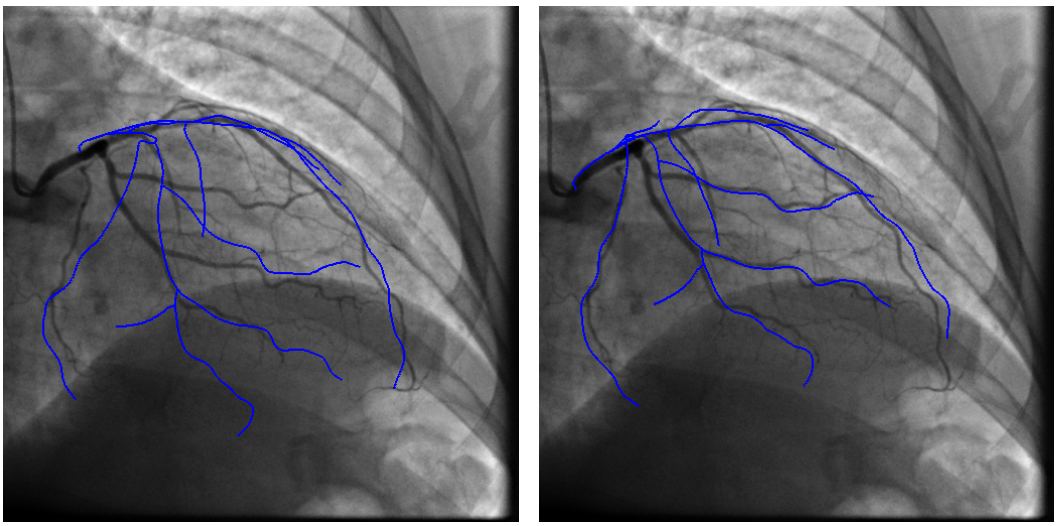

Figure 5.4: Registered position at convergence of the ICP algorithm compared to the correct pose.

and Levoy, 2001] that presents efficient variants impacting every stage of the ICP algorithm. Regarding modifications of the point pairing procedure, closest points can be searched in particular directions such as directions orthogonal to the local vessel tangent. Different metrics can also be used to determine the closest point pairing instead of the Euclidean norm. Distances involving local tangent information or image intensity can be used to build more relevant pairings. ICP variants also impact the way the optimal transformation is computed at a given pairing set. A weight can be associated to each point pairing, which is then introduced in the second line of Equation (5.14) to build a weighted least squares optimization problem. A weight represents the confidence relative to a given correspondence and can depend on the distance between paired points or the compatibility of tangent directions. Zero-weights can also be introduced to reject some pairings from the transformation computation. Outlier rejection methods are usually applied, considering each pairing as a part of the population from which is studied the distance distribution.

All of the previous refinements address the problem of wrong pairings, induced by the closest point assumption, via a rejection strategy. These approaches are efficient under two conditions:

- Enough correct correspondences are made by the pairing algorithm to lead the transformation in the correct direction.
- Wrong pairings are (easily) identifiable from the correct ones using some outlier detection technique.

In the clinical case presented in Figure 5.3, less than 40% of the pairings made by the

ICP are correct (according to the pairing error that will be defined in Section 7.3). Moreover, distinguishing correct from wrong pairings (at the level of point) in Figure 5.3b is quite challenging even for the human eye. In fact in each of these vessels, half of the pairings are wrong. Therefore, we worked on a completely different approach. Instead of limiting the impact of bad correspondences in the transformation computation step, we focus our efforts on building more relevant pairings. To this aim, we developed a registration algorithm that imposes pairing coherence along curves composing the features to be matched.

5.1.3 The Iterative Closest Curve Algorithm

As it was mentioned earlier, the Iterative Closest Curve (ICC) framework extends the principle of the ICP algorithm to the registration of curves. It should be stressed that the proposed approach is applicable to any registration problem as far as one is able to build a set of curves from the model $\mathcal{Y}$ that will be matched to curves extracted from the data $\mathcal{X}$. Similarly to the ICP, we aim at solving Equation (5.1). But this time the distance $\mathcal{D}$ between the model $\mathcal{Y}$ and the data $\mathcal{X}$ is based on a curve-to-curve distance that conducts to the following formulation of the ICC problem:

$$\begin{cases} \hat{T} = \underset{T\in\Omega}{\operatorname{argmin}} \sum\limits_{C\subset\mathcal{Y}} \mathcal{F}\Big(T(C), \operatorname{Closest}_{\mathcal{X}}\big(T(C)\big)\Big) \\ \operatorname{Closest}_{\mathcal{X}}\big(T(C)\big) = \underset{c\subset\mathcal{X}}{\operatorname{argmin}}\, \mathcal{F}\big(T(C), c\big) \end{cases} \tag{5.15}$$

where Ω is the set of admissible transformations, $\mathcal{F}$ is the Fréchet distance defined in (5.8) and $C \subset \mathcal{Y}$ (respectively $c \subset \mathcal{X}$) denotes a curve extracted from the model (respectively the data).

Naturally, we propose an alternating optimization procedure:

$$\begin{cases} \Pi_i = \bigcup\limits_{C\subset\mathcal{Y}} \Big(C, \operatorname{Closest}_{\mathcal{X}}\big(T_{i-1}(C)\big)\Big) \\ T_i = \underset{T\in\Omega}{\operatorname{argmin}} \sum\limits_{(C,c)\in\Pi_i} \mathcal{F}\big(T(C), c\big) \end{cases} \tag{5.16}$$

Besides the resemblance with the ICP formulation of Equation (5.13), the reader should note the following major differences:

- The pairing set Π_i is formed of correspondences between **curves** extracted from the model and the data and not points.
- The closest operator refers to the matching of curves based on the Fréchet distance.
- The transformation estimation step minimizes the distance between paired curves.

The curve pairing set Π_i is built by associating each curve C, extracted from the model, with its closest curve in the data (with respect to the Fréchet distance) at the

current transformation T_{i-1}. If both the model and the data are expressed as sets of curves that can be matched to each others, one can apply an exhaustive search on each possible pair between a given model curve and curves from the data and then choose the one with the lowest Fréchet distance. In Section 5.2.1, we provide an example on how to select curves to be matched when both structures are more sophisticated.

The second step of the ICC procedure consists in finding the optimal transformation T_i that minimizes the sum of Fréchet distances between paired curves in Π_i. Using the definition of the Fréchet distance given in Equation (5.8), the transformation part of Equation (5.16) becomes:

$$T_i = \underset{T\in\Omega}{\operatorname{argmin}} \sum_{(C,c)\in\Pi_i} \min_{\pi} \left\{ \sum_{(Y,x)\in\pi} \left\| T(Y) - x \right\|^2 \right\} \tag{5.17}$$

where π describes all possible point pairing sets between C and c that preserves point order along curves. This equation can be re-written:

$$\begin{cases} T_i = \underset{T\in\Omega}{\operatorname{argmin}} \sum_{(C,c)\in\Pi_i} \sum_{Y\in C} \left\| \text{Closest}_c\big(T(Y)\big) - T(Y) \right\|^2 \\ \text{Closest}_c\big(T(Y)\big) = x \in c \;\text{ s.t. }\; \big(T(Y), x\big) \in \pi_{\mathcal{F}}\big(T(C), c\big) \end{cases} \tag{5.18}$$

One would have noticed the same formulation as the ICP problem of Equation (5.13), where the summation over the whole model $\mathcal{Y}$ is expressed as a double sum visiting all curves and all points of each curve. But in the previous Equation (5.18) the closest point pairing is replaced by the Fréchet pairing between given paired curves. As for the ICP problem, the optimal pairings induced by the Fréchet distance depend on the optimal transformation and vice-versa. We thus consider an alternating procedure that will iteratively update the Fréchet pairings and the optimal transformation:

$$\begin{cases} \pi_j = \bigcup_{(C,c)\in\Pi_i} \pi_{\mathcal{F}}\big({T'}_{j-1}(C), c\big) \\ {T'}_j = \underset{T\in\Omega}{\operatorname{argmin}} \sum_{(Y,x)\in\pi_j} \left\| x - T(Y) \right\|^2 \end{cases} \tag{5.19}$$

The second step of the ICC procedure (Equation (5.16)) consists itself in an iterative procedure alternating the Fréchet pairings construction and least squares transformation optimization. It is similar to an ICP algorithm where the closest point pairing is replaced by the Fréchet pairing, which ensures that curves are still matched to curves and points along them are paired accordingly to their topology.

The ICC algorithm can be summarized as follow by integrating the Equation (5.19) procedure into the second step of Equation (5.16):

1. For a given transformation T_{i-1}, compute the closest curve pairing set Π_i given by the first part of Equation (5.16).

2. Given the curve pairing set Π_i, compute the transformation T_i that minimizes the Fréchet distance between paired curves by iterating the following procedure until convergence:

   a. For a given transformation T'_{j-1}, starting with $T'_0 = T_{i-1}$, compute the point pairing sets induced by the Fréchet distance between paired curves in Π_i. The union of these point pairing sets forming π_j.

   b. Given the point pairing set π_j, compute the transformation T'_j minimizing the sum of squared distance between paired points. This step is exactly equivalent to step-2 of the ICP algorithm presented in Section 5.1.2.

   c. Return to step-a until convergence of T'_j (as discussed in Section 5.1.2).

3. Return to step-1 until convergence of T_i.

More intuitively, steps-1,2,3 refer to the problem of alignment at the level of curves, and steps-a,b,c refine the underlying point pairing set that preserves the curve topology.

5.1.4 Framework Discussion

In this Section 5.1, we provided to the reader a general algorithm for registering two structures in which working at the level of curves makes more sense that considering points separately. The Iterative Closest Curve (ICC) algorithm is based on the Fréchet distance, which computes the best point pairing set between two curves while preserving order along them. Regarding the objective function optimized in Equation (5.1), the Iterative Closest Point (ICP) and the ICC method refer to the same formulation:

$$\mathcal{D}\left(T\left(\mathcal{Y}\right), \mathcal{X}\right) = \sum_{(Y,x)\in\pi} \left\|x - T(Y)\right\|^2 \tag{5.20}$$

The difference lies in the way the point pairing set π is defined and more important, the constraints that this pairing set must satisfy. In the ICP approach, the point pairing set π is unconstrained and each point of the model is matched to its closest in the data independently (without taking into account coherence along structures). On the contrary, the ICC approach imposes to π coherence constraints along curves. First, the points of the model that belong to the same curve must be matched to points that belong to the same data curve. Moreover, the order along curves must be preserved during the pairing procedure, which means that the curve topology of both structures is taken into account.

5.2 Application to 3D/2D Vasculature Registration

Before being able to apply the ICC framework to the 3D/2D registration of vascular structures several implementation choices shall be discussed. In the ICC registration problem, in Equation (5.15), the Fréchet distance is computed between each

curve $C \subset \mathcal{Y}$ and its closest among curves $c \subset \mathcal{X}$. If the model and the data are already expressed as set of curves that can be directly matched to each other, then a simple exhaustive search can be performed. But in general both structures are more sophisticated and a choice will be made on the curves to consider during the matching. In the following Section 5.2, we present implementation choices for the registration of the model represented as a 3D vascular tree and the data represented as a 2D vascular graph (as presented in Chapter 4). These choices mostly impact the pairing procedure. Regarding the transformation computation at a given point pairing set (second parts of Equation (5.19) and (5.14)), the reader can have a precise idea on how to compute it by referring to [Besl and McKay, 1992] if the model and the data belong to the same space. However in the case of 3D/2D registration, a projective operator is mandatory to bring the two modalities into the same space, which complexifies a little the computation of the optimal transformation.

5.2.1 Choice of Curves to be Matched

Curves are the very essence of the Iterative Closest Curve (ICC) algorithm and their selection is of great importance. In our vascular application, structures to be matched are represented by a tree and a graph (as presented in chapter 4). These types of features correspond well to the nature of the vasculature where vessel centerlines are connected to each other at bifurcations nodes. In order to apply the ICC algorithm, one has to extract meaningful curves from these features. Moreover, the number of curve pairings to evaluate must remain manageable since computational time is restricted for an intra-operative application. Our choice is also guided by the model-to-data nature of our problem as well as the expected differences between the two modalities depicted in Section 4.3.

We recall that in model-to-data registration, the matching is usually made in a non-symmetrical way by looking for correspondents of parts of the model in the data and not the other way around. Let us first focus on the extraction of meaningful curves from the model $\mathcal{Y}$ denoted $\mathcal{C}_\mathcal{Y}$. Since the model is composed of several centerline edges $E \in \mathbf{E}$ linked to each other via bifurcation nodes $B \in \mathbf{B}$, what may be the first choice that comes to mind is to considering the matching of curves E independently. However, the main goal of the ICC algorithm is to impose topological consistency regarding the pairings and thus avoid "jumps" induced by the Iterative Closest Point (ICP) pairing procedure (as shown in Figure 5.3). Considering the matching of edges independently does not solve this problem but lets it only occurs at bifurcation locations.

Inspired from [Duong et al., 2009], we chose to register vessel centerlines extracted from the main bifurcation to a segmentation extremity (leaf of the tree) in order to avoid potential incoherence at bifurcation nodes. This set of curves $\mathcal{C}_\mathcal{Y}$ is similar to the initial representation of the 3D model in early Section 4.1.2 and can be easily extracted from the tree representation by starting from each leaf of the tree and computing the union of all ascendant edges up to the main bifurcation. By design of the tree representation, ascendant edges are pairwise connected where the

connexion between edges E and E', denoted $E \leftrightarrow E'$, is defined by:

$$E \leftrightarrow E' \iff \exists B \in \mathbf{B}, \begin{cases} E[1] = B \text{ or } E[\#] = B \\ E'[1] = B \text{ or } E'[\#] = B \end{cases} \tag{5.21}$$

The union of two connected edges E and E' in the tree, denoted $[E \cup E']$, forms a centerline curve. It is defined by the following equation assuming, without loss of generality that $E[\#] = B = E'[1]$:

$$\left[E \cup E'\right] = \left[E[1] \dots E[\#], E'[1] \dots E'[\#]\right] \tag{5.22}$$

Using the previous definition of the union, one is able to build the set $\mathcal{C}_\mathcal{Y}$ of curves to be matched that satisfies:

$$\forall C \in \mathcal{C}_\mathcal{Y},\ C[1] = B_0 \tag{5.23}$$

where B_0 is the main bifurcation of the tree. Therefore the final extremity of each curve C, denoted $C[\#]$, is a leaf node $L \in \mathbf{L}$ of the tree (an extremity of segmentation).

Now that model curves to be matched have been identified, we want to extract curves from the data that are candidates for matching. Yet, building a priori meaningful curves from the data is a much more challenging task than it was for the model. First, it has been highlighted in Section 4.3 that the data $\mathcal{X}$ suffers from imperfections such as fake detections. This can induce many extremity nodes in the graph and thus many potential vessels from root to extremities. In addition, assuming that one is able to identify the main bifurcation (manually or automatically), contrary to the tree $\mathcal{Y}$ there is usually not a unique path along the graph that links two particular points. In this context, the number of 2D vessels to be matched can easily explode and become intractable in practice. We thus extract dynamically from $\mathcal{X}$ a set of candidate curves, denoted $\Gamma(C)$, for the matching with a given model curve C.

This set $\Gamma(C)$ is composed of curves that correspond to paths along the graph. A path p in the vascular graph $\mathcal{X}$ is defined as a curve composed of a set of edges (thus an edge cannot be taken twice) pairwise connected, starting at a point in the first edge and ending at the last one. Extremities of this curve are not necessarily nodes in the graph:

- The main bifurcation may not be precisely identified in 2D since it often leads to superimposition of vessels, which makes it complicated to detect (as shown in Figure 4.19a).
- The 3D vessel distality corresponds to the end of the segmentation that have no anatomical interpretation. As shown in Figure 4.20, end of segmentation may occur at quite different anatomical positions between the 3D and the 2D.

For these two reasons, one cannot expect a path $p \in \Gamma(C)$ to start and end only at nodes but also at points along edges.

To properly define a path in a vascular graph we first have to define the connectivity between edges in the graph as in the tree definition. Edges e and e' of the set $\mathbf{e}$ of edges in the graph are connected, denoted $e \leftrightarrow e'$, if:

$$e \leftrightarrow e' \iff \exists n \in \mathbf{n}, \begin{cases} e[1] = n \text{ or } e[\#] = n \\ e'[1] = n \text{ or } e'[\#] = n \end{cases} \tag{5.24}$$

where $\mathbf{n}$ is the set of nodes in $\mathcal{X}$. The union of two connected edges e and e' in the graph, denoted $[e \cup e']$, forms a centerline curve. It is defined similarly to Equation (5.22), (assuming without loss of generality that $e[\#] = n = e'[1]$):

$$\left[e \cup e'\right] = \left[e[1] \dots e[\#], e'[1] \dots e'[\#]\right] \tag{5.25}$$

Defining a path in the graph also involves the notion of **sub-curve**. A curve c' is said to be a sub-curve of c, denoted $c' \subset c$, if the following relation is satisfied:

$$c' \subset c \iff \exists i_1, \exists i_2 \text{ s.t. } c' = \left[c[i_1] \dots c[i_2]\right] \tag{5.26}$$

The 2D vessel corresponding to a 3D curve going from the main bifurcation to an extremity is expected to be a path p in the graph, denoted $p \sqsubset \mathcal{X}$ and defined by:

$$p \sqsubset \mathcal{X} \iff \exists e_1 \in \mathbf{e}, \exists e_2 \in \mathbf{e} \dots \text{ s.t. } \begin{cases} p \subset [e_1 \cup e_2 \cup \dots] \\ \forall k, e_k \leftrightarrow e_{k+1} \end{cases} \tag{5.27}$$

More intuitively, a path is a set of points in the graph that are pairwise connected, considering the two types of connectivities in the graph (along curves and at bifurcation points), without redundancy. The resulting curve matching will thus be formed of correspondences between model curves extracted from the main bifurcation to an extremity and a curve that belongs to a set of paths in the graph extracted dynamically for each model curve. The following section depicts how this set of candidates is extracted for each model curve.

5.2.2 Candidates Selection

In the ICC algorithm, each curve extracted from the model is paired to its closest in the data based on the Fréchet distance. The proposed implementation of the ICC algorithm involves the matching of a set of curves $\mathcal{C}_\mathcal{Y}$, a priori extracted from the model, to paths extracted dynamically from the data. In order to control the computational complexity, extracting a limited set of pairing candidates is mandatory. For a given curve C extracted from the model, we want to build a set of paths extracted from the graph $\mathcal{X}$, denoted $\Gamma(C)$. Here curves from the model and data belong to two different spaces (3D and 2D). In order to bring them into the same coordinate space, a projective operator $P : \mathbb{R}^3 \to \mathbb{R}^2$ is given by calibration of the C-arm system (providing the 2D acquisition) and allows to project 3D object onto the 2D space.

To build the set of candidates we assume that the main bifurcation point pairing (B, b) is given as initialization and thus we denote the set of resulting candidates

$\Gamma(C \mid (B, b))$. It makes correspondences between the 3D main bifurcation corresponding to the beginning of the curve to match $B = C[1]$ and a 2D point b in the graph $\mathcal{X}$. This pairing is justified by our application to coronary arteries registration (see the end of this section for more details). If this assumption cannot be made in the reader's scope, one can extend the following approach as discussed in the end of this section. Thus, the first condition imposed to a path p in the graph $\mathcal{X}$ to be a candidate is:

$$p[1] = b \tag{5.28}$$

It is assumed that a relevant pairing candidate p for the curve C must have its extremities close to the projected extremities of C. Thus in addition of Equation (5.28), we expect the extremity point $p[\#]$ of the candidate path to belong to the 2D neighborhood of the projected extremity $P(C[\#])$:

$$p[\#] \in \mathcal{N}\big(P(C[\#]), r(C)\big) \tag{5.29}$$

where $\mathcal{N}\big(P(C[\#]), r(C)\big)$ is a disc centered in $P(C[\#])$ of radius $r(C)$. Obviously, the size $r(C)$ of this neighborhood depends on the amount of misalignment to compensate during the registration procedure. If we consider the point pairing (B, b) as an anchor for the 3D registration transformation to retrieve, the more the extremity $C[\#]$ is distant from the main bifurcation B the bigger its potential displacement and thus the wider the neighborhood search zone. The size $r(C)$ of the neighborhood depends on the Euclidean distance between the bifurcation B and the other extremity of the curve C:

$$r(C) \propto \big\|C[1] - C[\#]\big\| \tag{5.30}$$

where $C[1] = B$ and the proportional coefficient will be discussed at the end of this section. The set of pairing candidates $\Gamma(C)$ is defined by:

$$p \in \Gamma\big(C \mid (B, b)\big) \Leftrightarrow \begin{cases} p \sqsubset \mathcal{X} \\ p[1] = b \\ p[\#] \in \mathcal{N}\big(P(C[\#]), r(C)\big) \end{cases} \tag{5.31}$$

where the first condition imposes p to be a path in the graph, referring to Equation (5.27).

Building this set of candidates for a given curve C extracted from the model can be done in the following way. First, the curve C is projected onto the image plane where the 2D data graph has been extracted (blue curve in Figure 5.5a). Then, the search zone that corresponds to the neighborhood of the projected extremity $P(C[\#])$ is computed. A path p should end in this zone to be considered as a candidate (see Figure 5.5a for an example). Edges in the graph $\mathcal{X}$ that have at least one point that belongs to the search zone are then identified. For each of these edges, several paths can be built starting at point b and ending along this edge. In order to limit the number of possible paths, which can become easily large[5], we

[5] One can have an example by counting the number of paths linking the red dot to one purple line in Figure 5.5b in the whole graph.

select only one path for each edge. This candidate, corresponding to a given edge e in the search zone, is chosen by computing the shortest path in the graph linking the point b paired to the main bifurcation (red dot) to the edge e. This shortest path is computed using the Dijkstra's algorithm, considering the length of a 2D curve as the weight of an edge. A resulting candidate is composed of the union of an edge in the search zone (purple parts in Figure 5.6) and the shortest path linking it to the bifurcation paired point b (pink parts in Figure 5.6).

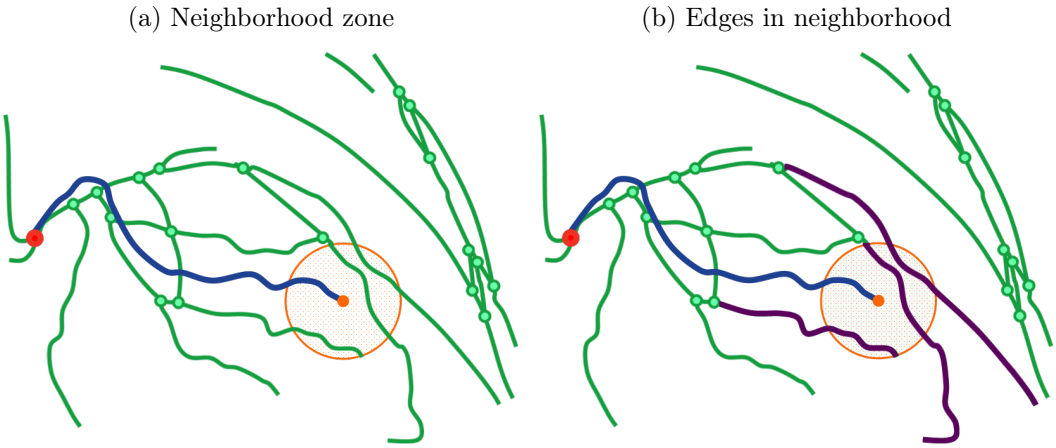

Figure 5.5: Search zone around the projection of a 3D curve extracted from the model. (a) projection of a 3D curve (blue) extracted from the main bifurcation (red dot) to one extremity of segmentation around which is drawn the 2D neighborhood (in orange), (b) graph edges in the neighborhood search zone (purple).

Implementation details: The previously described candidate selection assumes that the main bifurcation pairing is given as an initialization of the procedure. In practice this can either be obtained by a single click user interaction or an automated detection as in [Lacroix et al., 2012]. This assumption can also be overcome by launching multiple candidates selections given several main bifurcation pairing hypotheses or by symmetrizing the previous procedure. The latter case involves an additional neighborhood corresponding to the curve extremity $C[1]$ and the computation of the shortest path between each edge in the proximal neighborhood to each edge in the distal neighborhood. Regarding the radius $r(C)$ and its proportional coefficient, the previous main bifurcation point pairing gives a coarse translation alignment of proximal vessel parts, which is less and less precise as the 3D Euclidean distance with this bifurcation increases. The proportional coefficient has been determined by studying the range of displacement to retrieve during the registration, based on a 63 cases data base study.

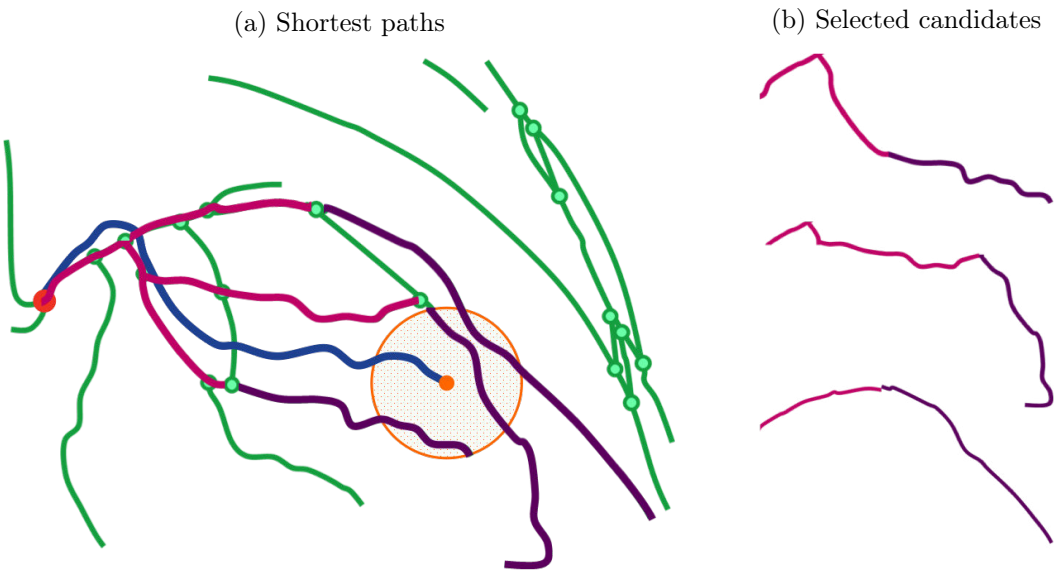

Figure 5.6: Candidates computed from each edge in the search zone. (a) shortest paths (pink) from each edge (purple) in the extremity neighborhood (orange), (b) set of pairing candidates for the 3D curve whose projection is represented in blue in (a).

5.2.3 Pairing Procedure

At this stage, we have described all the different elements necessary to build the first step of the ICC algorithm presented in Equation (5.16):

$$\Pi_i = \bigcup_{C \subset \mathcal{Y}} \Big(C, \text{Closest}_{\mathcal{X}}\big(T_{i-1}(C)\big) \Big) \tag{5.32}$$

in the case of 3D/2D vessel registration. Using Section 5.2.1 that defines the selection of curves to be matched, the previous equation can be re-written:

$$\Pi_i = \bigcup_{C \in \mathcal{C}_{\mathcal{Y}}} \Big(C, \text{Closest}_{\Gamma(T_{i-1}(C))}\big(T_{i-1}(C)\big) \Big) \tag{5.33}$$

where the operator $\text{Closest}_{\Gamma(T_{i-1}(C))}\big(T_{i-1}(C)\big)$ associates to $T_{i-1}(C)$ its closest in the set of candidates $\Gamma\left(T_{i-1}(C)\right)$. A small modification of the Closest(.) definition provided in Equation (5.15) is necessary due to the dimensionality difference between the model and the data:

$$\text{Closest}_{\mathcal{X}}\big(T(C)\big) = \underset{c \in \Gamma(T_{i-1}(C))}{\text{argmin}} \; \mathcal{F}\big(P \circ T(C), c\big) \tag{5.34}$$

The closeness between a model curve and a data curve is evaluated in the 2D space using the Fréchet distance $\mathcal{F}$.

As it was mentioned in the previous Section 5.2.2, the set of candidates $\Gamma\left(T_{i-1}(C)\right)$ can be restricted by imposing the main bifurcation point pairing (B, b). This assumption results in far less paths to consider and is justified by a simple initialization procedure consisting in identifying (coarsly) the main bifurcation in the image. However, one should note that we are not using this initial pairing as an anchor point, but as an hypothesis to justify the following main bifurcation pairing construction at each iteration i of the ICC algorithm:

$$\begin{aligned} b_i &= \text{Closest}_{\mathcal{X}}\big(P \circ T_{i-1}(B)\big) \\ b_i &= \underset{x \in \mathcal{X}}{\text{argmin}} \left\| x - P \circ T_{i-1}(B) \right\|^2 \end{aligned} \tag{5.35}$$

One can now compute the closest curve pairing of Equation (5.32) by replacing $\Gamma\left(C\right)$ by $\Gamma\left(C \mid (B, b_i)\right)$.

Experience showed that some particularly long curves may have empty candidates set because their extremities were too far from an existing edge in the graph. Such cases were often induced by a non-segmented distal part of the vessel in the 2D modality, due to lack of contrast in the image or even occlusion of the vessel distal part. By nature of the pairing procedure, this case will result into an empty pairing for the whole 3D vessel. We therefore added a shortening mechanism when no edge in the graph can be found in the search zone relative to a 3D curve C. This simple heuristic consists in considering the matching of $C_{3/4}$ instead of C, where $C_{3/4}$ is a sub-curve of C starting at $C[1]$ and ending at $3/4$ of the total length of C. If at least one candidate has been found the pairing procedure continues as described above, otherwise we consider a cut at $C_{1/2}$ then $C_{1/4}$.

Now that one is able to build a closest curve pairing, let us summarize the assumptions we made to build it:

- A curve extracted from the 3D must be matched to a curve in the 2D.
- The 2D curve matched to a 3D one should be close enough to the 3D curve extremities projection.
- The shortest path in the graph between two points, identified as potential extremities, is the candidate for matching.
- The best candidate among all is the one with the lowest Fréchet distance

While the two first points are hardly contestable, the two lasts can be challenged and will be discussed in 5.3.2.

5.2.4 Transformation Optimization

This section is dedicated to the second step of the Iterative Closest Curve (ICC) algorithm in the case of 3D/2D vasculature registration. Given a set of paired curves, we are looking for the optimal transformation minimizing the sum of the Fréchet distances. Since the Fréchet distance is based on an point pairing set that depends

on the transformation, we proposed in Section 5.1.3 an alternating optimization procedure that can be seen as an ICP algorithm where the closest point pairing is replaced by the Fréchet pairing of each paired curves. In this section, we adapt the transformation step of the general ICC algorithm to the 3D/2D case.

The goal is to find the optimal transformation T_i at a given set of curve pairings Π_i:

$$T_i = \underset{T\in\Omega}{\operatorname{argmin}} \sum_{(C,c)\in\Pi_i} \mathcal{F}\big(P \circ T(C), c\big) \tag{5.36}$$

where the Fréchet distance has been adapted to the 3D/2D case as it has been done in Section 5.2.3. The resolution of this problem involves to compute the point pairing set, induced by the Fréchet distance, between each pair of model curve and closest one in the data. To be used in our application, the Fréchet pairing defined in Equation (5.9) must be adapted to the 3D/2D case. The Fréchet pairing between a 3D curve C and a 2D curve c, denoted $\pi_{\mathcal{F}}(C, c)$, is built using the 2D Fréchet pairing:

$$\pi_{\mathcal{F}}(C, c) = \Big\{(Y, x) \in \mathcal{Y} \times \mathcal{X} \;\; \text{s.t.}\, (P(Y), x) \in \pi_{\mathcal{F}}\big(P(C), c\big)\Big\} \tag{5.37}$$

Using the previous equation one is now able to compute the sets of 3D/2D point pairings π_j corresponding at the first stage of the ICP-like procedure presented in Equation (5.19). This procedure iteratively refines the Fréchet pairing between curves (that depends on the transformation) and the optimal transformation itself. Multiple methods are provided in the literature to determine the optimal transformation that minimizes the least squares distance between paired points in π_j. Here we provide a solution where the set of admissible transformations Ω is the set of rigid transformations. In [Besl and McKay, 1992], a direct solution is provided to align two sets of paired points that belong to the same dimensional space. In order to retrieve a 3D transformation from the 3D/2D point pairing set π_j we create a 3D/3D point pairing set denoted $\overline{\pi}_j$ from π_j and apply the direct method depicted in [Besl and McKay, 1992].

To this aim, we define the back-projected line relative to the point x, denoted $P^{-1}(x)$, as the 3D line joining the point x in the image plane to the source. We define this 3D/3D point pairing set $\overline{\pi}_j$ by:

$$\overline{\pi}_j = \bigcup_{(Y,x)\in\pi_j} \left(Y \;,\; \underset{X\in P^{-1}(x)}{\operatorname{argmin}} \big\|{T'}_{j-1}(Y) - X\big\|^2\right) \tag{5.38}$$

which corresponds to transform a 3D/2D pairing (Y, x) to a 3D/3D pairing (Y, X) where X is the closest point to Y along the back-projected line. This point pairing set is substituted to π_j in the step-2a of the ICC algorithm (see end of Section 5.1.3).

Step-2b that consists in optimizing:

$${T'}_j = \underset{T\in\Omega}{\operatorname{argmin}} \sum_{(Y,X)\in\overline{\pi}_j} \big\|X - T(Y)\big\|^2 \tag{5.39}$$

can be solved in the space of rigid transformation Ω, by using the direct method provided in [Besl and McKay, 1992]. This method involves a quaternion representation of the 3D rotational part of the rigid displacement, which is retrieved by inverting a symmetric matrix built upon the cross-covariance matrix between paired points (see Appendix E). This update of the transformation is then re-injected into step-2a until convergence.

All previous details allow one to compute step-2 of the ICC algorithm and thus the whole registration process in the case of 3D/2D vessel registration. By replacing π_j, which refers to the Fréchet pairing between paired curves, by closest point pairings between $\mathcal{Y}$ and $\mathcal{X}$ (relaxing constraints on pairing belonging to the same curve and order preservation) one would obtain the ICP algorithm in the case of 3D/2D registration. This 3D/2D closest point pairing set ${\pi'}_j$ can be computed using:

$$ {\pi'}_j = \bigcup_{Y \in \mathcal{Y}} \left(Y \ , \ \underset{x \in \mathcal{X}}{\operatorname{argmin}} \left\| x - P \circ {T'}_{j-1}(Y) \right\| \right) \tag{5.40} $$

The definition of the 3D/2D ICP algorithm is important since sections of this thesis presenting results will often compare ICP and ICC approaches.

5.3 Experiments

The goal of this section is to give an example of applicability of the Iterative Closest Curve (ICC) algorithm and prove its potential with respect to the standard Iterative Closest Point method (ICP). By imposing pairing coherence along curves to be registered we will highlight that the ICC approach shows both more relevant pairings and better robustness regarding rotational displacement. To this end we use four clinical cases coming from three patients including one Chronic Total Occlusion (CTO) and one stenosis patient. Each case is composed of a 3D segmentation of the left coronary tree (as described in Section 4.1), a 2D segmentation obtained from a fluoroscopic image (as described in Section 4.2) and a manual pose estimation constituting the ground truth. Two cases were built from the CTO patient at different angulations. These different cases where chosen according to a hypothesis made in Section 5.2.3, which assumes that a vessel starting at the main bifurcation and ending at a segmentation extremity must correspond to the shortest path in the 2D graph.

5.3.1 Qualitative Results

N.B. This section is more a proof of concept of the ICC algorithm, on few cases in the scope of 3D/2D registration of vessels, than a study on a larger database demonstrating applicability during clinical procedure, which is the purpose of Chapter 8.

First, we want to highlight the structural coherence brought by the ICC methodology with respect to ICP. To this aim we computed point pairing sets relative to the ICC and the ICP algorithm at the same initial position. This position is given

by the system calibration, which determines coarse rotation initialization, and the in-plane translation initialization that is given by a single click user interaction. Pairings are computed using Equation (5.37) for the ICC pairings and using Equation (5.40) for the ICP pairings. These two pairing sets are presented in yellow in Figure 5.7. One can note that the multiple jumps highlighted in Figure 5.3 have completely disappeared in the pairing procedure involved by the ICC.

(a) ICP point pairings (b) ICC point pairings

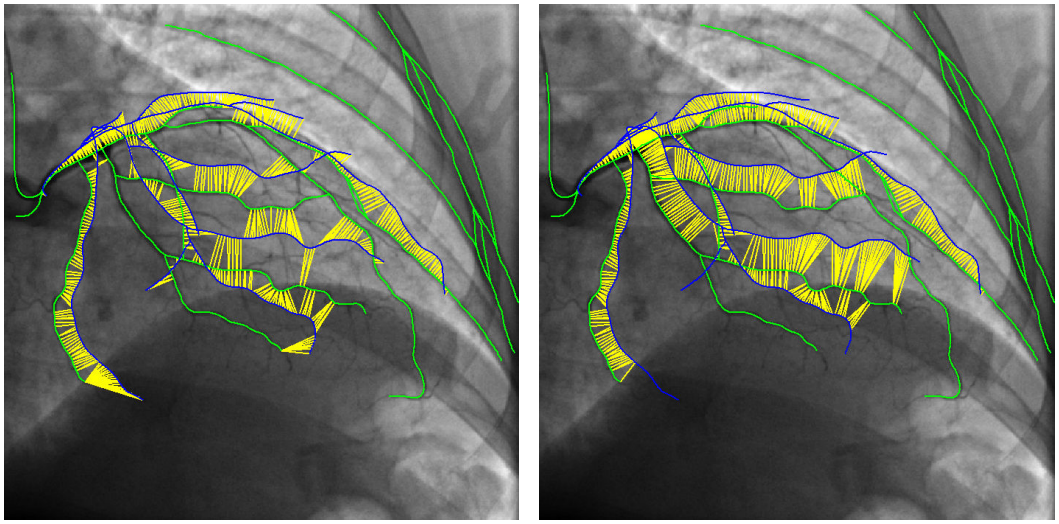

Figure 5.7: Comparison between the ICP and the ICC pairing at the same pose initialization (green: extracted 2D structure, blue: projected 3D structure on the image plane, yellow: pairing between structures). (a) point pairings given by the closest point pairing procedure of the ICP algorithm, (b) point pairings given by the closest curve pairing then the Fréchet distance of the ICC algorithm.

From this same initial position we launched both the ICP and the ICC algorithms. Results are presented in Figure 5.8, showing that the ICC was able to retrieve the correct registration position (see reference position in Figure 5.4b) unlike the ICP algorithm. Pairings have been assessed correct or incorrect using a ground-truth-based criterion properly described in Chapter 7. The majority of the pairings provided by the ICC algorithm are correct contrary to the ICP algorithm that falls into a local minimum because of the non-coherence of its pairing procedure. Thus, by imposing coherence in the registration we were able to build more relevant pairings reached convergence in that case while the ICP algorithm get stuck into a local minimum.

In order to confirm the robustness of the ICC framework with respect to the ICP one, we evaluate both registration algorithms on 100 random perturbation of the ground-truth pose (obtained manually). The random 3D displacement has been applied to the coronary tree followed by a step of alignment between the 3D main bifurcation and its detection in the 2D image, which constitutes the initialization

(a) ICP registered pose (b) ICC registered pose

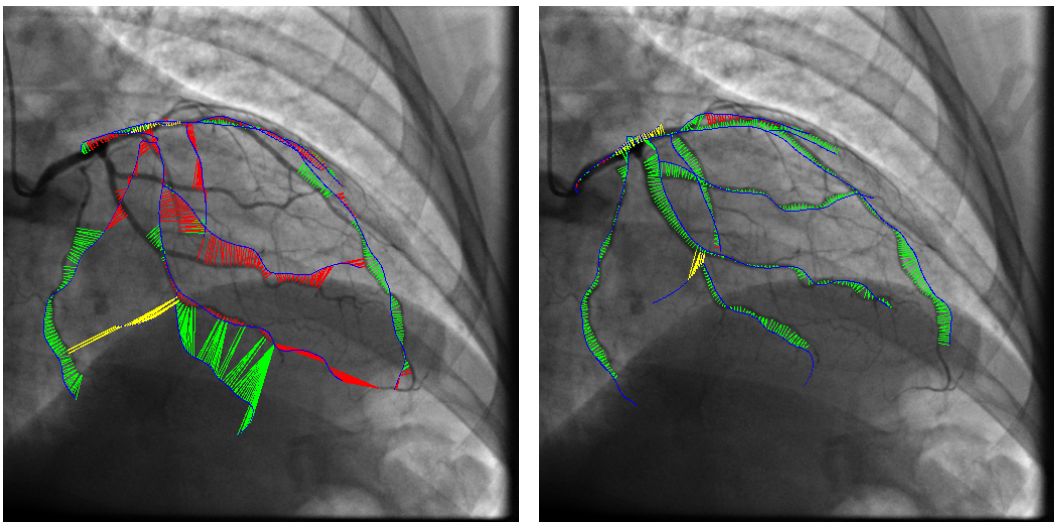

Figure 5.8: Comparison of the registered pose obtained at convergence of the ICP (a) and the ICC (b) algorithm. Thin blue line: the projection of the 3D structure at registration position, green: correct pairings, red: bad pairings, yellow: pairings relative to occluded vessels (non detectable in the projective image).

of the ICP and ICC algorithms. This later step has already been justified to be realistic either in a manual or automatic way. Since this alignment provides a coarse initialization in translation, we classify these perturbations by range of rotation angle. We conducted experiments on three ranges of angular perturbation: 5, 10 and 15 degrees.

We assessed the registration error computing the Mean Projective Distance (MPD) that is nicely defined in [van de Kraats et al., 2005]. The MPD is defined as the average distance between the projection of each point in the model at the registered position and the projection of the same point at the ground-truth position. To each perturbation is associated the MPD of the registered position. We computed the mean and the 90^{th} percentile of the MPD distribution for each range of perturbation. Table 5.1 shows that ICC presents lower indicators for every range in all the cases.

Here we provided evidence that one can benefit from working at the level of curves instead of the level of points. By introducing curve-to-curve pairing and distance, we showed that ICC algorithm overpassed the standard ICP algorithm and significantly improved the resulting pairings. The improvement in the pairings has been visually evaluated in test experiments. We also estimated the improvement by comparing the mean projection error obtained with our approach to the reference ICP method.

Table 5.1: Robustness comparative study between the ICP and the ICC algorithms. Statistics on Mean Projective Distance (MPD) at convergence of the registration procedure starting from a random perturbed position.

Case	MPD	5^o rotation		10^o rotation		15^o rotation	
		ICC	ICP	ICC	ICP	ICC	ICP
1	mean	1.4	2.1	3.2	5.0	6.9	9.3
	90%	3.0	3.7	7.4	10.3	15.6	18.8
2	mean	1.3	2.3	2.0	3.9	4.2	8.3
	90%	3.0	4.4	4.3	8.1	9.3	16.8
3	mean	1.7	3.4	4.6	6.9	7.1	10.6
	90%	3.9	6.6	8.7	13.9	12.4	21.2
4	mean	1.3	1.8	2.6	4.3	7.5	8.7
	90%	3.3	3.6	6.2	8.6	16.5	18.2

5.3.2 Limitations

The ICC algorithm proved that imposing coherence in the registration algorithm can greatly improve the robustness and the quality of the resulting pairings. However, we also identified several issues that should be addressed to provide an algorithm compatible with clinical expectations. These directions of improvement do not affect the ICC framework but refer to several choices of implementation made in the Section 5.2. Most choices were made for the sake of simplicity and aimed at giving an example that could be easily extended to different applications such as 2D/2D retinal fundus image registration, 3D/3D liver vasculature registration ...

First, regarding the choice of the curves to be matched, we considered curves from the main bifurcation to segmentation extremity. But in the case of the coronary tree vasculature, this representation leads to consider multiple times proximal part as it was highlighted in the Section 4.1.2. Thus 3D points that belong to proximal vessels are matched several times and contributes more in the computation of the optimal transformation than distal points. This problem can be handle by introducing weight attached to each pairing, taking into account the 3D point redundancy, and solve the associated weighted least squares problem. However, this leads to relax the one-to-one correspondence condition, as it is done in the Expectation Maximization (EM) ICP of [Granger and Pennec, 2002] where each model point is seen as a potential distribution of pairing. This constraint is only relaxed for proximal points that are considered several times but not for points that belong to distal parts. Treating differently proximal and distal points is not satisfying and should be addressed properly in the upcoming chapter 6.

Regarding the candidates selection (Section 5.2.2) two hypotheses have been pointed out to be less relevant than the others. First, the shortest path between two locations in the graph does not always correspond to a "real" vessel. This assumption can lead to take shortcuts in the 2D vasculature via noisy detections or taking a shorter path at a bifurcation created by vessel superimposition (which

does not exist in the patient's anatomy). The Figure 5.9 is composed of two clinical cases presenting several vessel superimpositions that create loops in the graph. By following the shortest path assumption, 2D candidate paths will always go through the shortest path to the main bifurcation without visiting some vessel parts in the orange regions. A smart approach will be designed to relax the shortest path hypothesis while avoiding a computational time explosion induced by evaluating all paths that can be extracted from the graph.

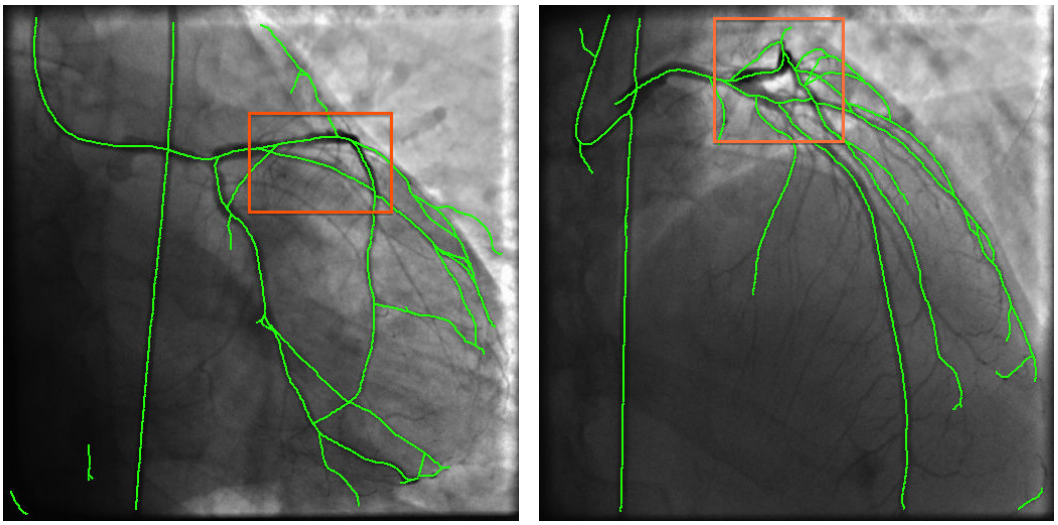

Figure 5.9: Cases where the shortest path assumption cannot be made. Orange regions highlight vessel portions that will never be consider in the candidates selection.

Secondly, the assumption "the closer, the better", made by choosing the closest candidate based on the Fréchet distance, has been pointed out by the literature to be non-sufficient in many cases. Several articles such as [Baka et al., 2013; Feldmar et al., 1997; Mitrović et al., 2013] demonstrate the importance of considering resemblance between matched elements. These approaches considered to enrich points by local information on vessel shape, such as the local tangent vector or the local curvature, in the matching procedure. The closest point pairing is not only determined by the Euclidean distance, but also by taking into account the local shape. It should be nice to extend this idea to entire curves.

In Section 4.1, we defined a sparse representation of the 3D vasculature by using a tree structure composed of curves and nodes respectively corresponding to vessel centerlines and bifurcations. This elegant representation avoids the redundancy of proximal vessels that are considered multiple times in the previous root-to-extremities set of curves representation. However, considering the matching of edges in the tree independently may induce irrelevant jumps at bifurcations. On the other side, imposing coherence at bifurcation locations leads to treat the pairing of edges simultaneously, which is a significantly more challenging task. This challenge

will be discussed more and addressed in the tree preserving pairing approach (in chapter 6).

Chapter 6

Tree-Topology Preserving Pairing

Contents

We have learned from the literature and from the work of chapter 5 that the pairing built between structures is the key of a successful registration algorithm. In the presentation of the Iterative Closest Curve (ICC) framework, we focused our efforts on describing a general algorithm that is applicable to any kind of registration problem where curves can be extracted from both sets. Guided by the work of [Liu and Bullitt, 1998] and [Duong et al., 2009], we considered the matching of model curves extracted from the main bifurcation of the tree and ending at segmentation extremities (leaves). But by doing so, common parts of these curves were matched multiple times without control on the coherence of created pairings. In this chapter, we describe a matching procedure that ensures a one-to-one correspondence between the model and the data structure, while preserving the particular topology of the vessel tree. This both consists in changing the type of curves (extracted from the model) to be matched and the pairing procedure itself. We will first define what a pairing that preserves the tree-topology is, and then give an intuition on how to build one of these.

The pairing procedure is expressed as an optimization of a pairing score over the set of possible tree preserving pairings. We propose a divide-and-conquer algorithm based on the optimal substructure of the problem, which is possible thank to a particular property of the pairing score. The resulting algorithm avoids the computational explosion of the direct approach (i.e. the evaluation of all possible tree

preserving pairings). This pairing procedure is then introduced into the ICC framework by replacing the previous pairing procedure described in Section 5.2 by the one described in this section. Designated by the term Tree Preserving Iterative Closest Curve (TP-ICC), this algorithm respects the tree-topology of the model without relying only on bifurcation matching as it is done in [Smeets and Bruyninckx, 2010; Serradell et al., 2015].

6.1 Definitions and Challenges

As it has been mentioned in the ICC framework (chapter 5), preserving topology during the pairing procedure conducts to more realistic and correct pairings. Here we want to go a step further in the preservation of the model structure by building a pairing set preserving the tree-topology. In Section 4.1.2, we have proposed a geometrical representation of the 3D vasculature under the form of a tree. It involves a set of edges $\mathbf{E}$, corresponding to vessel centerlines, that connect nodes in $\mathbf{N}$, corresponding either to anatomical bifurcations $\mathbf{B}$ or segmentation extremities $\mathbf{L}$, also called leaves. A tree structure $\mathcal{Y} = (\mathbf{E}, \{\mathbf{B}, \mathbf{L}\})$ counts two different types of connectivities: the connectivity between points along edges and the connectivity between edges at bifurcation nodes. We want to build a pairing set that preserves both types of connectivities.

One difficulty in the case of 3D/2D registration is that the 2D extracted structure is not a tree but a graph. Several articles have faced the problem of tree matching and graph matching, such as [Serradell et al., 2015] and [Smeets and Bruyninckx, 2010], by first building pairs of nodes between the two modalities and then identifying edge pairings using bifurcation matches. Despite the different types of registration applications shown in [Serradell et al., 2015] (covering neural trees in 3D electron microscopy, retinal fundus 2D images and coronary angiography 2D images) the authors only consider the registration of data of the same dimensions (3D/3D and 2D/2D but not 3D/2D). Actually, their method is based on the assumption that corresponding bifurcations can be identified in both structures to be registered, which is generally not the case in 3D/2D registration. First, locating precisely the point where one vessel splits into more than one (bifurcation) is quite easy in 3D but usually becomes tricky in the 2D projective image. In fact, connected vessels are often superimposed for a while around the bifurcation projection location, which complicates the precise identification of the splitting position.

Moreover, a one-to-one correspondence between bifurcations of the two modalities can not be guarantied. In the example of Figure 6.1, the orange region of interest of the 3D vasculature contains five different anatomical bifurcations that are superimposed onto the same detected vessel in the 2D fluoroscopic image. Bifurcations only detected in 2D can be also numerous because of vessel superimposition, which creates "fake" bifurcations, and bifurcation due to noisy detections. For the previous reasons, relying only on bifurcations to drive the pairing procedure is irrelevant in the case of 3D/2D vascular registration.

(a) Vascular tree (3D) (b) Projection on the image plane (2D)

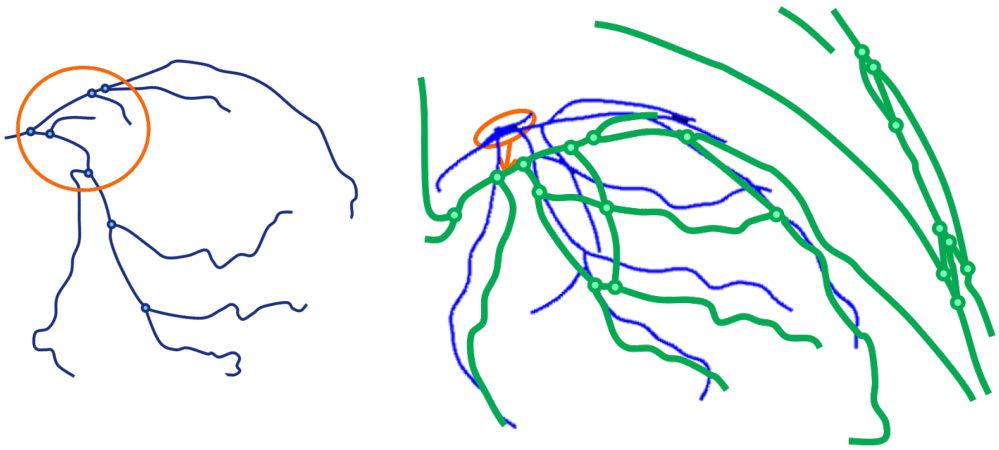

Figure 6.1: Non-correspondence between bifurcations in the 3D model and bifurcations in the 2D graph. The orange region of interest in (a) and (b) corresponds to the same part of the model. (a) 3D vascular tree with multiple proximal bifurcations circled in orange, (b) projection of the model into the image plane close to the registered position (The projection corresponds to the ground truth registration position slightly shifted to improve visualization).

Therefore, because techniques based on bifurcations cannot be used in our application, we directly match edges of the tree. A given edge E in the tree, can correspond to:

- An entire edge e in the graph. This occurs when 3D bifurcations linked by E exactly correspond to the 2D bifurcations linked by e (rare case since bifurcations are hard to locate precisely in 2D).
- A sub-curve of an edge e, when at least one bifurcation has been misdetected or even not detected.
- Several connected edges, in the case of bifurcation created by vessels superimposition or noisy detection.

Thus, an edge E of the tree $\mathcal{Y}$ is expected to be paired to a path p extracted from the graph $\mathcal{X}$ as it is defined in Equation (5.27) of Section 5.2. Moreover, if we want to preserve the tree-topology during the pairing procedure then we have to preserve the connectivity between edges at bifurcation nodes. If E and E' are connected by the bifurcation node B, then we expect that their respective paired paths p and p' are connected in the graph. Exactly as in Equation (5.24), we define the connexion between two edges E and E' of the vascular tree $\mathcal{Y}$, denoted $E \leftrightarrow E'$, by:

$$E \leftrightarrow E' \iff \exists B \in \mathbf{B}, \begin{cases} E[1] = B \text{ or } E[\#] = B \\ E'[1] = B \text{ or } E'[\#] = B \end{cases} \tag{6.1}$$

where $\mathbf{B}$ is the set of bifurcation nodes in the tree $\mathcal{Y}$. We also extend the definition of connectivity given in Equation (5.24) from edges to paths in the graph. Two paths p and p' extracted from the graph $\mathcal{X}$ are said to be connected if:

$$p \leftrightarrow p' \iff \exists x \in \mathcal{X}, \begin{cases} p[1] = x \text{ or } p[\#] = x \\ p'[1] = x \text{ or } p'[\#] = x \end{cases} \tag{6.2}$$

where x is a point in the graph $\mathcal{X}$ that is not necessarily a bifurcation node but may also belong to an edge.

A tree-topology preserving pairing Π, also called a **tree pairing**, must be composed of elements that satisfy:

$$(E, p) \in \Pi \iff \begin{cases} E \in \mathbf{E} \\ p \sqsubset \mathcal{X} \\ \forall \left(E', p'\right) \in \Pi,\ E \leftrightarrow E' \ \Rightarrow\ p \leftrightarrow p' \end{cases} \tag{6.3}$$

where $p \sqsubset \mathcal{X}$ denotes that p is a path extracted from the graph $\mathcal{X}$ as defined in equation (5.27). We denote $\Psi(\mathcal{Y}, \mathcal{X})$ the set of possible tree pairings that make correspondences from the 3D tree model $\mathcal{Y}$ to the 2D graph data $\mathcal{X}$. The upcoming tree pairing procedure is designed to find the best tree-topology preserving pairing $\hat{\Pi}$ in $\Psi(\mathcal{Y}, \mathcal{X})$, in a sense of a tree pairing score $\overline{S}$ that will be defined in Section 6.3. We thus need to solve the following problem:

$$\hat{\Pi} = \underset{\Pi \in \Psi(\mathcal{Y}, \mathcal{X})}{\operatorname{argmax}}\ \overline{S}(\Pi) \tag{6.4}$$

Before rushing into the algorithm that solves the previous equation (described in Section 6.4), let us first give an intuition to the reader on how to build one tree pairing.

6.2 Building a Tree Pairing

In the previous section we gave a definition of what a tree-topology preserving curve pairing set is, designated by the term tree pairing for the sake of simplicity. The definition given in Equation (6.3) allows to check if a given curve pairing set is a tree pairing or not but does not give the reader an intuition on how to build one. This definition involves the pairing of edges in the 3D tree to paths extracted from the 2D graph. We first present how we select candidate paths in the graph to be matched to a given edge of the tree[1]. Then, the construction of a tree pairing is explained to give the reader intuition on how to construct an element of $\Psi(\mathcal{Y}, \mathcal{X})$. The tree nature of the model encourages a recursive approach, starting at the root and progressively running the recursion with child edges and nodes. To illustrate the tree pairing building we will often rely on the toy example presented in Figure 6.2.

[1] We recall that we are building a non-symmetrical pairing from the model $\mathcal{Y}$ to the data $\mathcal{X}$.

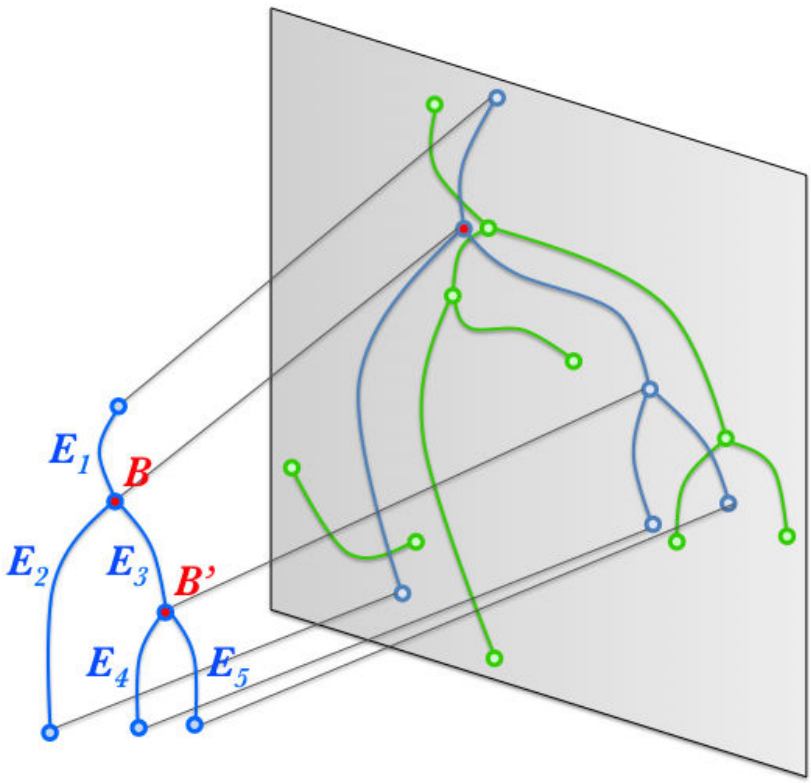

Figure 6.2: Toy example representing the 3D/2D registration problem. The blue tree on the left represents the 3D segmented vasculature and the gray plane on the right side corresponds to the image plane where the 2D segmentation is represented in green. The projection of the 3D structure onto the image is materialized by the black rays joining the tree to its 2D projection in dark blue. Red dots in 3D correspond to the two bifurcations of the tree (B and B'). The red dot in the projective plane corresponds to the 3D main bifurcation projection onto the manual click position provided by the user as an initial position.

6.2.1 Improved Candidates Selection

The goal of this section is to provide a set of paths extracted from the graph $\mathcal{X}$ that could be matched to a 3D model centerline E. These candidates must respect the connectivity constraint represented by a point pairing between the 3D bifurcation B (at an extremity of E) and a 2D point b that belongs to the graph (a node or a point along an edge). In the toy example presented in Figure 6.3a, the 3D curve E is projected onto the image plane to identify 2D compatible candidates for pairing. Since the bifurcation B is necessarily an extremity of the edge E, we will assume without loss of generality that $E[1] = B$. We start back from the definition of the set of pairing candidates $\Gamma\left(E \mid (B, b)\right)$ given in Equation (5.31) and re-written here:

$$p \in \Gamma\Big(E \mid (B,b)\Big) \Leftrightarrow \begin{cases} p \sqsubset \mathcal{X} \\ p[1] = b \\ p[\#] \in \mathcal{N}\left(P(E[\#]), r(E)\right) \end{cases} \tag{6.5}$$

where the first condition guarantees that p is a path extracted from the data graph, the second ensures the connectivity constraint and the last one restricts candidate paths to end in the neighborhood of the projected 3D extremity with a size controlled by a radius $r(E)$.

The first step of the candidate construction is thus to identify edges of the graph that are inside the search neighborhood. The disc $\mathcal{N}\left(P(E[\#]), r(E)\right)$ is circled in orange in Figure 6.3a and edges in the graph intersecting this region are presented in purple. A candidate must start at point b and must end along a purple curve. To restrict the number of potential candidates to test, we proposed earlier to consider the shortest path along the graph between each purple curves and the point b with respect to the geodesic distance. By adding this extra constraint during the construction of the set Γ we greatly limit the computational time by limiting the number of considered candidates. However, it has been pointed out in Section 5.3.2 that this assumption is not always admissible when vessel superimposition occurs.

We thus relax this implicit shortest path constraint imposed during the construction of $\Gamma\left(E \mid (B, b)\right)$ and add an additional constraint to the definition of the set of admissible candidates. Since exploring all paths between two given positions in the graph may become intractable in practice, we only consider paths that have a length compatible with the 3D projected one. All paths in the graph starting at b and ending along a purple curves are considered as potential candidates (see Figure 6.3b). Their lengths are going to be evaluated and candidates with non compatible one will be rejected. We recall that the length $\mathcal{L}(p)$ of a polygonal curve p is defined by:

$$\mathcal{L}(p) = \sum_{i}^{\#-1} \Big\| p[i+1] - p[i] \Big\| \tag{6.6}$$

It is expected that the difference between lengths of the projected 3D curve $P(E)$ and a candidate p is smaller than a certain threshold $\Delta L(E)$ depending on the model

curve to be matched:

$$\left|\mathcal{L}(P(E)) - \mathcal{L}(p)\right| < \Delta L(E) \tag{6.7}$$

This condition is added to Equation (6.5) to form the improved set of pairing candidates $\overline{\Gamma}\left(E \mid (B,b)\right)$:

$$p \in \overline{\Gamma}\Big(E \mid (B,b)\Big) \Leftrightarrow \begin{cases} p \sqsubset \mathcal{X} \\ p[1] = b \\ p[\#] \in \mathcal{N}\left(P(E[\#]), r(E)\right) \\ \left|\mathcal{L}(P(E)) - \mathcal{L}(p)\right| < \Delta L(E) \end{cases} \tag{6.8}$$

where, the threshold $\Delta L(E)$ represents the expected variation on the length of the projected curve $P(E)$

(a) Neighborhood search (b) Candidates construction

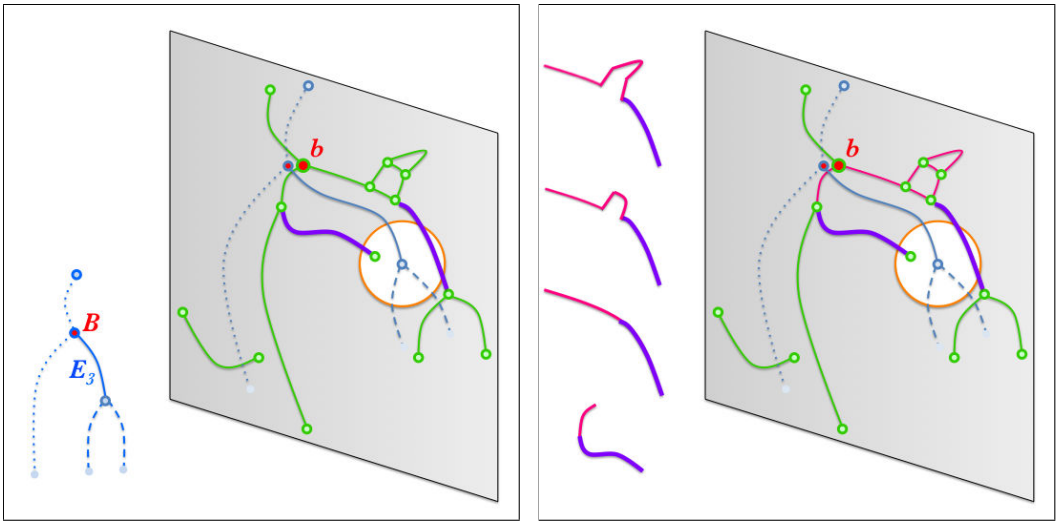

Figure 6.3: Improved candidates selection for the pairing of the edge E_3 of the toy example tree, knowing the bifurcation pairing (B,b). (a) represents the search zone neighborhood by an orange circle and the edges in the graph intersecting the search zone are drawn in purple. (b) shows on the left side paths from the point b and purple vessels built of edges in the graph highlighted in pink. Noisy detections on the right side of the image plane have been added to the toy example of Figure 6.2 to highlight that multiple paths can be extracted between a given departure and destination.

When a curve E is displaced in the 3D space its projection changes and so the length of its projection too. Therefore the tolerance on length difference depends on the maximum displacement of the curve E, which in our case corresponds to the expected displacement to compensate during the registration procedure[2]. But the

[2]The range of displacement to retrieve has been studied in our data base and has been set accordingly into the candidate selection procedure.

displacement to compensate is not the only factor impacting the expected length variation. The length of the projection of a 3D curve E tends to decrease when E gets closer to the projection axis. This phenomenon is called the projective foreshortening and often leads to self-superimposition in the case of vessels. An example of highly foreshortened vessel is provided in Figure 9.3. Under the condition that E is close to the optical axis $\overrightarrow{Opt}$ (relative to the projective operator P) and distant from the X-ray source of approximately the characteristic distance called Source-to-Object Distance (SOD), the length of the projected 3D curve can be approximated by:

$$\mathcal{L}\left(P(E)\right) \approx \frac{SID}{SOD} \cdot \sum_{i=1}^{M-1} \left\|E[i+1] - E[i]\right\| \sin(\theta_i) \tag{6.9}$$

where SID denotes the Source Image Distance (distance between the X-ray source and the detector), M denotes the number of points defining the polygonal curve E (number of points that define it: $E[M] = E[\#]$) and θ_i is the angle between the local vessel direction and the optical axis:

$$\theta_i = \text{angle}\left(\overrightarrow{E[i]E[i+1]}, \overrightarrow{Opt}\right) \tag{6.10}$$

Considering that the centerline E is uniformly sampled with a step δy such that:

$$\forall i \in [1 \dots M], \left\|E[i+1] - E[i]\right\| = \delta y \tag{6.11}$$

Equation (6.9) can be re-written:

$$\begin{aligned} \mathcal{L}\left(P(E)\right) &\approx \frac{SID}{SOD} \cdot \delta y \cdot \sum_{i=1}^{M-1} \sin(\theta_i) \\ &\approx \mathcal{L}\left(E\right) \cdot \frac{SID}{SOD} \cdot \frac{1}{M-1} \cdot \sum_{i=1}^{M-1} \sin(\theta_i) \end{aligned} \tag{6.12}$$

A 3D displacement will induce an angle variation $\Delta\theta$ for all θ_i, which will impact the length of the projected 3D curves. One can estimate the expected variation on the projected length $\Delta L(E)$ by computing the derivative of Equation (6.12) and using the Taylor approximation at the first order:

$$\Delta L(E) = \mathcal{L}(E) \cdot \frac{SID}{SOD} \cdot \frac{1}{M-1} \cdot \sum_{i} \cos(\theta_i)\Delta\theta \tag{6.13}$$

We are now able to build an algorithm that computes the set of admissible candidates $\overline{\Gamma}\left(E \mid (B, b)\right)$ defined in Equation (6.8). For all edges in the graph that have at least one point in the search neighborhood $\mathcal{N}\left(P(E[\#]), r(E)\right)$, we compute all paths starting from this edge and ending at point b that have a length compatible with the length of $P(E)$. This can be done with the recursive procedure described in Algorithm 2 starting with each edge in the search neighborhood as p. It involves

the use of the function $FrechetPairedPortion(E, p)$ that computes the sub-curve p' of p that is paired during the Fréchet pairing. This sub-curve p' satisfies:

$$\begin{cases} p' \subset p \\ (E[1], p'[1]) \in \pi_{\mathcal{F}}(E, p) \\ (E[\#], p'[\#]) \in \pi_{\mathcal{F}}(E, p) \end{cases} \tag{6.14}$$

where $\pi_{\mathcal{F}}(E, p)$ is the Fréchet pairing between E and p as defined in Equation (5.37). The reader can refer to Figure 6.4, where the paired portion of the curve is between the two red dots. This algorithm builds the set of compatible candidates to be matched to E. One of them has then to be selected.

Algorithm 2 Recursive compatible candidates building

INPUT: E : 3D edge of the tree $\mathcal{Y}$ to be matched,
INPUT: b : destination point in the graph $\mathcal{X}$,
INPUT: $\Delta L(E)$: length tolerance,
INPUT: p : path along the graph $\mathcal{Y}$ already built,
OUTPUT: $\overline{\Gamma}$: resulting set of compatible paths with the curve E.

```
1: function CompatiblePaths(E,b,ΔL(E),p)
2:     Γ̄ ← ∅
3:     if b ∈ p then
4:         p' ← FrechetPairedPortion(E,p)
5:         if |L(p') − L(P(E))| < ΔL(E) then
6:             Γ̄ ← {p'}
7:         end if
8:     else
9:         if L(p) < L(P(E)) + ΔL(E) then
10:            for all e connected to p in the graph do
11:                Γ̄ ← Γ̄ ∪ CompatiblePaths(E,b,ΔL(E),p ∪ e)
12:            end for
13:        end if
14:    end if
15:    return Γ̄
16: end function
```

To perform the recursive construction of the upcoming Section 6.2.2, it is necessary to provide a point pairing for the child bifurcation (at an extremity of E). In other words, we have to provide a pairing between the 3D bifurcation B' (represented as a blue point in the bottom of Figure 6.4) and a point along the 2D vessel, denoted b'. We use the Fréchet pairing procedure, defined in Equation (5.37), to construct this end point correspondence since it builds a set of relevant point pairings between two curves by preserving the point order along them. The child bifurcation point pairing (B', b') is thus defined by the last point pairing in the Fréchet pairing $\pi_{\mathcal{F}}$

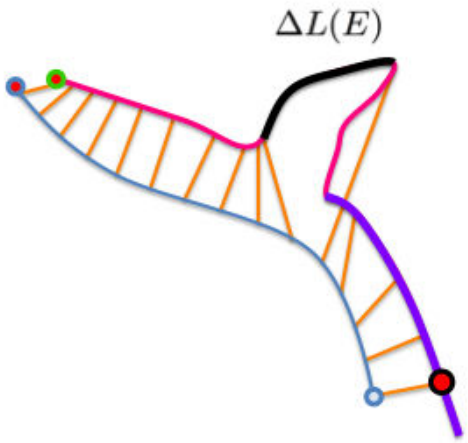

Figure 6.4: Fréchet pairing induced by the Fréchet distance computed using Algorithm 1. The starting pairing (given as input) corresponds to the red dots respectively circled in blue and green. The big red dot circled in black in the bottom right corner corresponds to the 2D point paired to the last point of the projected 3D curve (in blue).

between E and p:

$$\begin{cases} B' = E[\#] \\ (B', b') \in \pi_{\mathcal{F}} \end{cases} \tag{6.15}$$

In Figure 6.4, it corresponds to the point pairing between the bottom blue dot and the bottom red dot. This step completes the algorithms necessary to build a tree pairing from an initial main bifurcation pairing.

6.2.2 A Top-Down Approach

As for the pairing procedure depicted in Section 5.2.3, we assume that a coarse alignment in translation is given as initialization. This initialization is expected to be given by a single-click of the clinician on the 2D main bifurcation, or its automatic detection as it is performed in [Lacroix et al., 2012]. We assume that this initialization gave the state of the toy example represented in Figure 6.2. From this pose we assume that we are able to retrieve the main bifurcation point pairing denoted (B, b) between the main bifurcation in the 3D tree and a point that belongs to the 2D graph (node or point along an edge). This initial pairing bifurcation close to the root encourages a top-down pairing approach, starting from the tree root and progressively descending to the leaves. Moreover, while distal parts of 3D vessel may not appear in the image (because of occlusion or out-of-field-of-view reasons), proximal vessels should be present. In fact, proximal parts are close to the injection catheter, which should be visible in the image for safety reasons. We thus want to

build a tree pairing, under the constraint (B, b), that is an element of the set:

$$\Psi\big(\mathcal{Y}, \mathcal{X} \mid (B, b)\big) \tag{6.16}$$

This set corresponds to the different admissible tree pairings between $\mathcal{Y}$ and $\mathcal{X}$ such that the main bifurcation B in the model is paired to the point b in the data.

We initiate the top-down tree pairing procedure by matching the root to a candidate path extracted from the graph. Candidates for the root pairing are selected using the procedure depicted in the previous Section 6.2.1. In Figure 6.5a, we get only one candidate to be paired to the root: the centerline corresponding to the plain green curve. This candidate is chosen to be paired to E_1 and this curve pairing constitutes the first element of the future tree pairing. Now that the root is paired, the entire descending structure (dashed blue curves in Figure 6.5a) needs to be paired too, while taking into account the connectivity constraint. As defined in Section 6.1, the connectivity constraint is carried by the common bifurcation between a parent edge and child edges. In the particular case of the root, the common bifurcation pairing is already given by initialization. To pair the entire tree, the recursion is continued with each child sub-tree. A sub-tree of a tree $\mathcal{Y}$ starting at edge E, denoted $\mathcal{Y}_{|E}$, is composed of the edge E and all its descendant nodes and edges. By nature of the tree structure, any sub-tree extracted from a tree is also a tree. In the toy example of Figure 6.5a, the sub-tree $\mathcal{Y}_{|E_3}$ is composed of the edges E_3, E_4 and E_5 as well as the nodes in the tree connected by them[3].

In the example of Figure 6.5b, the left child sub-tree is only composed of one edge: E_2. As for the root pairing, only one path links b and the vicinity of the projected edge extremity. This curve pairing is added to the set of curve pairings, which builds the tree pairing, and no further recursion calling is needed for this side of the tree. Regarding the recursion relative to the right child sub-tree of the root, the sub-tree $\mathcal{Y}_{|E_3}$ still needs to be paired (see Figure 6.5c). As it was done for the entire tree, we start by pairing the root of this sub-tree (E_3) and will then pair each child sub-tree.

We identified two compatible paths p_1 and p_2 in the graph of Figure 6.5c to be paired to E_3. Because of the connectivity constraint, choosing one over the other will impact the potential pairing of the child edges (dashed blue curves). Pairing E_3 to p_1 will lead to have no potential pairing candidate for the child edges (E_4 and E_5). Contrary to p_1, the curve p_2 is not a "dead-end " and gives possible pairings for E_4 and E_5. For the purpose of this example, we chose to pair E_3 with p_2, add this pairing to the current tree pairing and continue the recursion with each child sub-tree. Again, to continue the recursion the point pairing of the child bifurcation B' must be determined using the Fréchet pairing procedure. This pairing gives the correspondence between B' and the point b' along the 2D structure[4] as presented in Figures 6.6a and 6.6b. Recursion continues with the left and right child sub-trees of

[3]It can be noted that the bifurcation B of the tree $\mathcal{Y}$ is also a node of $\mathcal{Y}_{|E_3}$. Yet, it is not any more a bifurcation of the sub-tree but a leaf node.

[4]Here the reader should note that the point b' is not a node of the graph but belongs to an edge.

(a) Root pairing

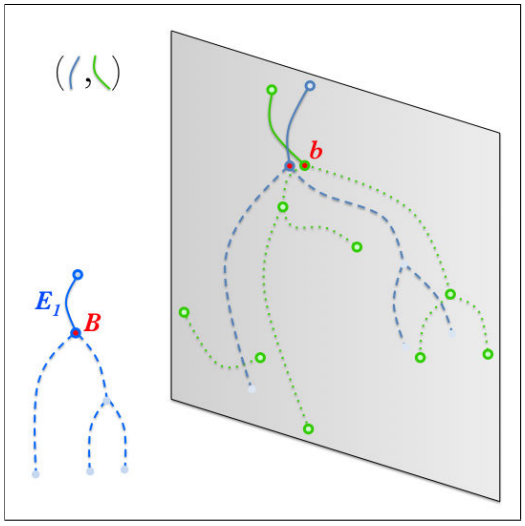

(b) Left son pairing

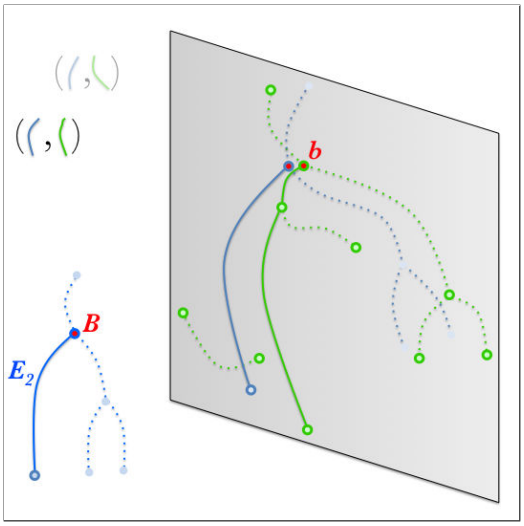

(c) Right son pairing

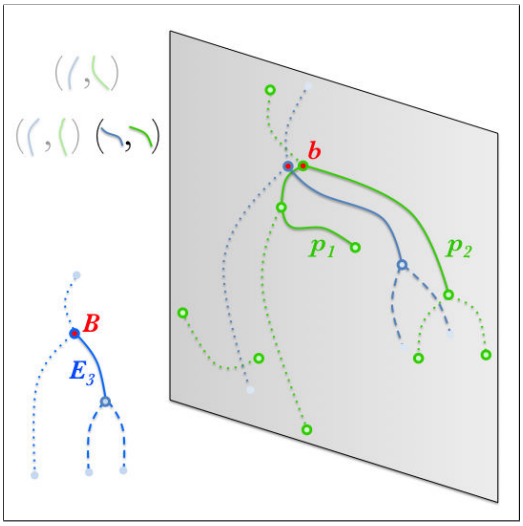

Figure 6.5: Top-down tree pairing construction by recursive curve pairings on a toy example. Pairings are submitted to the same connectivity constraint: the point pairing of the main bifurcation (B, b). The plain curves represent the edge paired at the current recursion, the dashed blue curves correspond to the descendants of the current edge that will be impacted by the current choice of pairing and the plain green curves are the potential candidates extracted from the 2D structure (dotted green curves). Curve pairings that will compose the resulting tree pairing are progressively revealed in the top left corner. (a) represents the pairing of the root edge E_1, (b) the curve pairing of its left child edge E_2 and (c) the curve pairing of its right child edge E_3. The latter involves to continue the recursion that is presented in Figure 6.6.

E_3 that are both composed of only one edge (E_4 and E_5). Knowing the bifurcation pairing (B', b'), E_4 and E_5 are respectively paired using the same procedure (see Figures 6.6a and 6.6b). No more edges of the tree need then to be paired and the recursion stops.

(a) Left grand son pairing (b) Right grand son pairing

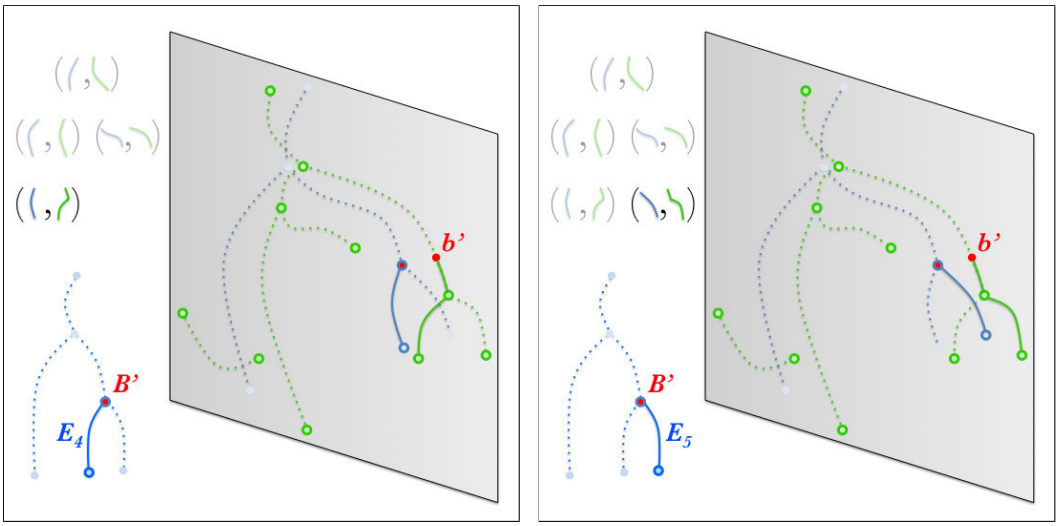

Figure 6.6: Top-down tree pairing construction (part 2). Child edges of E_3 are paired knowing the connectivity constraint (B', b') that have been obtained using the Fréchet distance between E_3 and p_2 of Figure 6.5c. (a) corresponds to the pairing of edge E_4 and (b) to the pairing of edge E_5. The latter finishes the recursion and the resulting curve pairing, which is a tree pairing, is presented in the top left corner of (b).

By this example of a top-down tree pairing construction, one is thus able to progressively build a curve-pairing set that preserves the connectivity constraint at each bifurcation of the tree. This recursive heuristic can be summarized as:

1 Choose a path p extracted from the graph $\mathcal{X}$ that will be paired to the root edge R of the current tree taken from a set of candidates compatible with the current bifurcation pairing (B, b).

2 Determine the child bifurcation pairing (B', b') given by the chosen curve pairing (R, p).

3 If the current root R is not a leaf then call step 1 for each child sub-tree of edge R given the child bifurcation pairing (B', b').

The connectivity constraint, materialized by a point pairing of a 3D bifurcation, influences the compatible paths in the graph that can be paired to a given edge in the tree. In the previous example we chose one of the path to be paired to E_3

based on our intuition. The goal of this chapter is to build the best tree pairing automatically. To do so, we first need to design a score to evaluate the quality of a given tree pairing.

6.3 Rating a Tree Pairing

We decided to address the tree pairing problem as the optimization of a tree pairing score $\overline{S}(.)$, which results into solving Equation (6.4). This approach is quite natural since it is not much different from the one used in the Iterative Closest Point (ICP) algorithm where the point pairing is made accordingly to the optimization of the sum of closest point distance. The score both takes into account the geometric distance and the resemblance between curves using a similar formulation based on the Fréchet distance. We first start by defining the curve pairing score in Section 6.3.1 and then use it to build the tree pairing score in Section 6.3.2.

6.3.1 Curve Pairing Score

The curve pairing score $S(.)$ is designed to assess the quality of pairing (C, c) relative to a 3D curve C and a 2D curve c. The problem of dimensionality difference between curves has already been raised in Section 5.2.3. Back then, this distance was assessed in the 2D image plane by the mean of the Fréchet distance between $P(C)$ and c. We denote by $F(C, c)$ the geometrical distance between C and c based on the very same principle:

$$F(C, c) = \mathcal{F}(P(C), c) \tag{6.17}$$

where P is the projective operator, given by calibration of the system, and $\mathcal{F}$ denotes the 2D Fréchet distance defined in Equation (5.8). One would have noticed that Equation (6.17) does not contain any transformation operator. Actually, the matching between curves does not necessarily involve a transformation of one of the two curves. But in practice, the ICC-framework considers the matching of curves at a given transformation T. This could be achieved either by applying the transformation to the model curve (here $T(C)$ would replace C), or by introducing it in the projective operator (here $P \circ T$ would replace P). From now on we consider that if such a transformation exists, it has already been applied to obtain the curve C.

This geometric distance, which preserves the curve topology, has been used in Section 5.2.3 to build the curve pairing set. It is important to take it into account since a good pairing candidate must be spatially close to the projection of the 3D curve extracted from the model. But the literature highlighted the importance of completing this geometric distance with shape information to increase correct pairing success rate. Instead of using some local shape descriptors, such as tangent vector or curvature as in Baka et al. [2014]; Lee and Won [2011]; Serradell et al. [2011], we propose to quantify the resemblance between two curves globally. As for the geometric distance $F(C, c)$, the resemblance between curves will be evaluated in the 2D image plane.

The major issue regarding local information such as tangent vectors and local curvature is their reliability in highly foreshortened portions. If we refer to Figure 6.1, especially the 3D proximal part circled in orange, defining a local curvature or vessel direction for the projected 3D structure seems really challenging. We thus designed a shape resemblance measure, which avoids approaches based on local shapes, by mimicking the human eye behavior: "Two curves have similar shapes if a rigid transformation can align them with a small registration error". Since we want to assess the resemblance between curves in the image plane, this sub-problem will be addressed as a 2D registration problem. We align the projected 3D model curve $P(C)$ with the 2D data curve c using a similar principle that the one involved to compute the transformation in the second step of the ICC algorithm (see Section 5.2.4). We propose an "ICP-like" procedure based on the pairing induced by the Fréchet distance between curves.

Given the 2D/2D curve pairing $(P(C), c)$, we run the following 2D rigid registration procedure:

a. Compute the Fréchet pairing $\pi_{\mathcal{F}}$ between $P(C)$ and c at a given 2D transformation.

b. Given the point pairing set $\pi_{\mathcal{F}}$, update the 2D rigid transformation $\hat{T}_{2D}$ that minimizes the sum of squared distance between paired points

c. Return to step a. until convergence.

At the end of this registration procedure, the transformation $\hat{T}_{2D}$ is assumed to correspond to the best 2D alignment between curves taking into account point order along them. As we said before, two curves have similar shapes if the distance between them at the registered position is small. We define the 2D resemblance $R(C, c)$ associated to a given 3D/2D curve pairing (C, c) by:

$$R(C, c) = \mathcal{F}\left(\hat{T}_{2D} \circ P(C), c\right) \tag{6.18}$$

where the Fréchet distance $\mathcal{F}$ (defined in Equation (5.8)) measures the resulting error after 2D registration. One should note that this resemblance constitutes a global[5] shape distance that tends to 0 for a perfect match.

Since it is assumed that a good pairing between curves corresponds to both a small distance and a good resemblance, we build the curve pairing score as a function of these two measures. To mix the 3D/2D Fréchet distance $F(C, c)$ and the resemblance $R(C, c)$ we first propose a normalization of each of these measures into a Fréchet score:

$$S_F(C, c) = e^{-\frac{F(C,c)^2}{2{\sigma_F}^2}} \tag{6.19}$$

and a resemblance score:

$$S_R(C, c) = e^{-\frac{R(C,c)^2}{2{\sigma_R}^2}} \tag{6.20}$$

[5]Global is used in contrast to methods using local shape estimators.

The normalization parameters σ_F and σ_R are respectively set to typical values[6] of the Fréchet distance and the resemblance criterion. We finally define the curve pairing score $S(C, c)$ by:

$$S(C, c) = \alpha \cdot S_F(C, c) + (1 - \alpha) \cdot S_R(C, c) \tag{6.21}$$

where $\alpha \in [0; 1]$ controls the relative importance between the geometric distance and the shape distance. All previous scores defined in equations 6.19, 6.20 and 6.21 assign a real value between 0 and 1 that quantifies the quality of a pairing. While 1 corresponds to a perfect match with respect to some criterion, the score progressively decreases to 0 as the pairing becomes less relevant.

The use of zero-asymptotic decreasing functions (as the inverse exponential) to build scores is important when several curve pairings are chosen simultaneously. Let us consider a toy example to illustrate this. Given two curves C_1 and C_2 with the same length, we assume that only two configurations can occur:

- C_1 is paired to c_1 and C_2 is paired to c_2. We assume that $\mathcal{F}(C_1, c_1) = 100mm$, which is a really bad pairing, and $\mathcal{F}(C_2, c_2) = 7mm$, which is a doubtful pairing.
- C_1 is paired to $c_1{}'$ and C_2 is paired to $c_2{}'$. Here we assume that $\mathcal{F}(C_1, c_1{}') = 200mm$, which is a really bad pairing too, and $\mathcal{F}(C_2, c_2{}') = 1mm$, which seems to be a good pairing.

Intuitively, while the pairing relative to C_1 seems always bad, one would favor the second case where the pairing of C_2 looks good. If we consider a linear normalization of the Fréchet distance as the score, the chosen couple will surely be the first one. On the contrary, exponential normalization allows to make small distinction between a "really-bad" and an "even-worse" pairing.

Generalization to other dimensions: The curve pairing score defined in Equation (6.21) allows to compute a curve-to-curve distance that takes into account their geometric distance and their shape resemblance. Contrary to state of the art methods, the shape resemblance measure does not involve to compute local descriptors that may not be well defined in several locations. Moreover, since both terms are based on the Fréchet distance the resulting score preserves the curve topology. This score can easily be extended outside the scope of 3D/2D matching by removing the projective operator P from the previous equations. Implementations of 3D/3D and 2D/2D Fréchet distance and ICP algorithm are sufficient to obtain a curve pairing score between curves of the same dimensional space.

6.3.2 Tree Pairing Score

Thank to the previous Section 6.3.1, we are able to quantify the quality of a given pairing between a 3D curve (extracted from the model $\mathcal{Y}$) and a 2D curve (extracted

[6] Typical values have been determined on a study of correct curve pairings at calibration position.

from the data $\mathcal{X}$). Since a tree-topology preserving pairing Π (also called a tree pairing) is composed of several curve pairings, we will define the tree pairing score $\overline{S}$ based on the score S of the curve pairings composing it. By looking at the optimized objective function of Equation (5.17), one would note that every point of the model have equal contribution in the optimization. Thus, a given curve pairing contributes accordingly to the number of points composing the model curve of this pairing. In our case the points constituting the polygonal curves are equally sampled, therefore the contribution of the pairing (C, c) to the resulting transformation is proportional to $\mathcal{L}(C)$, which is the length of the 3D curve C. Each curve pairing score is weighted accordingly to the contribution they will have in the transformation optimization. The tree pairing score is thus defined by:

$$\overline{S}(\Pi) = \sum_{(C,c)\in\Pi} \mathcal{L}(C) \cdot S\big(C, c\big) \tag{6.22}$$

where Π is a tree pairing that is composed of edges of the 3D tree paired to paths extracted from the 2D graph. One interesting property of this tree pairing score is that it is separable into independent scores relative to each curve pairing that compose it.

The goal of this score is to evaluate the quality of several tree pairings and choose the best among different possibilities. As mentioned in Section 6.2.2, different tree pairings can be built by a top-down approach that progressively pair edges of the tree while preserving the connectivity at bifurcation nodes. An evaluation of each constructed tree pairing can be performed and the pairing with the highest score is chosen. It can occur that the set of candidates for a given model edge E is empty, meaning that no admissible path in the graph has been found. The edge E will not contribute in the tree pairing score of Equation (6.22). Thus, an empty pairing $(E, \emptyset)$ is considered to have a zero score, which corresponds to a pairing between two curves infinitely distant from each other with respect to the Fréchet distance and that presents totally different shapes.

6.4 Tree Pairing Algorithm

Here we are looking for the best pairing among all possible tree-topology preserving curve pairings that realizes the maximum of a tree pairing measure: in other words solving Equation (6.4). Thank to Section 6.2 we know how to build an element of the set $\Psi(\mathcal{Y}, \mathcal{X})$ of tree pairings between the model $\mathcal{Y}$ and the data $\mathcal{X}$. Using Section 6.3 we are able to evaluate a given tree pairing Π, both taking into account a geometrical distance and a shape resemblance criteria. This section describes the algorithm designed to find the best pairing in a smart way.

On th one hand, the brute force approach consisting in evaluating each element of $\Psi(\mathcal{Y}, \mathcal{X})$ is intractable in practice. On the other hand, since the choice of a candidate for a given centerline impacts potential pairings of all of its children, following the top-down approach of Section 6.2.2 by choosing a candidate for a

given edge in the tree (based on the curve pairing score for example) without taking into account the descendants of E seems irrelevant. We build a pairing procedure that takes advantage of the optimal substructure of this optimization problem that can be recursively divided into simpler subproblems.

6.4.1 Optimal Substructure Formulation

Given the initial main bifurcation pairing (B, b), we aim at finding the best tree pairing $\hat{\Pi}$ by solving:

$$\hat{\Pi} = \underset{\Pi}{\operatorname{argmax}}\, \overline{S}(\Pi) \tag{6.23}$$

where Π is a tree pairing that belongs to the set of tree-topology preserving pairing between $\mathcal{Y}$ and $\mathcal{X}$ knowing the main bifurcation pairing:

$$\Pi \in \Psi\left(\mathcal{Y}, \mathcal{X} \mid (B, b)\right) \tag{6.24}$$

An element Π of the set of tree pairing possibilities (i.e. that satisfies Equation (6.24)) can be decomposed into:

$$\Pi = \{(R, p)\} \cup \Pi_{E_1} \cup \Pi_{E_2} \ldots \tag{6.25}$$

were (R, p) denotes the curve pairing of the root edge of the tree $\mathcal{Y}$ given by Π, $(E_1, E_2 \ldots)$ are child edges of the root R in the model tree and Π_{E_1} (respectively Π_{E_2}, ...) is the subset of curve pairings extracted from Π that are relative to the child sub-tree $\mathcal{Y}_{|E_1}$ (respectively $\mathcal{Y}_{|E_2}$ and other child sub-trees).

By definition of a tree preserving pairing, Π is composed of pairings between every edges in the tree $\mathcal{Y}$ that preserve connectivity at bifurcation nodes. Each set Π_{E_k} is composed of pairings making correspondences between all edges in the sub-tree $\mathcal{Y}_{|E_k}$ and paths extracted from $\mathcal{X}$ preserving connectivity at bifurcations, which is the definition of a tree pairing of $\mathcal{Y}_{|E_k}$. Moreover, if we denote by $(B', b_p{}')$ the point pairing relative to the child bifurcation of R [7] that is induced by the curve pairing (R, p) (using Equation (6.15)) then each subset relative a child sub-tree $\mathcal{Y}_{|E_k}$ satisfies:

$$\Pi_{E_k} \in \Psi\left(\mathcal{Y}_{|E_k}, \mathcal{X} \mid (B', b_p{}')\right) \tag{6.26}$$

In other words, a tree pairing Π can be decomposed into the union of a curve pairing relative to the root and tree pairings relative to each child sub-tree of the root. Each of these child sub-trees can be recursively decomposed in the same way.

Using the definition of the tree pairing score of Equation (6.22) and the decomposition of the tree pairing Π provided in Equation (6.25), we obtain:

$$\bar{S}\left(\Pi\right) = \mathcal{L}(R) \cdot S\left(R, p\right) + \bar{S}\left(\Pi_{E_1}\right) + \bar{S}\left(\Pi_{E_2}\right) \ldots \tag{6.27}$$

[7] One should note that for the particular case of the root R, the child bifurcation pairing is already given by initialization and we thus have $(B, b) = (B', b_p{}')$.

By replacing $\bar{S}(\Pi)$ by the previous score decomposition in Equation (6.23) we found that its maximum satisfies:

$$\max_{\Pi} \bar{S}(\Pi) = \max_{p} \left\{ \mathcal{L}(R) \cdot S(R,p) + \max_{\Pi_{E_1}} \bar{S}(\Pi_{E_1}) + \max_{\Pi_{E_2}} \bar{S}(\Pi_{E_2}) \dots \right\} \tag{6.28}$$

subject to:

$$\Pi \in \Omega(\mathcal{Y} \mid (B,b)) \ , \ p \in \overline{\Gamma}(R \mid (B,b)) \ , \ \Pi_{E_k} \in \Omega\left(\mathcal{Y}_{C_k} \mid (B', {b_p}')\right) \tag{6.29}$$

where k indexes the different children of R and $\overline{\Gamma}(.)$ denotes the set of admissible candidates to be paired with R defined in Equation (6.8)

The previous Equation (6.28) highlights that the problem of finding the best tree pairing for the entire tree $\mathcal{Y}$ can be expressed as finding the optimal paired path for the root with respect to some criterion. This criterion involves the resolution of subproblems (one for each child sub-tree) that follow the exact same formulation as the initial pairing problem but referring to the child sub-trees. These subproblems are "simpler" because trees to match are smaller than the parent one. Each of them can also be divided into more subproblems until leaf edges are reached and subproblems become equivalent to find the path in the set of candidates that realizes the maximum of the curve pairing score. This property of breaking down a problem into simpler subproblems is known in the literature as an *optimal substructure*[8] and can be directly implemented into a recursive algorithm.

6.4.2 Divide-and-Conquer Algorithm

A divide and conquer algorithm is a recursive implementation that solves a problem presenting an optimal substructure formulation. This denomination refers to the recursive nature of the tree pairing algorithm that progressively involves the pairing of "simpler" tree (sub-trees with less and less nodes and edges). Based on Equation (6.28) we designed a pairing optimization procedure presented in Algorithm 3. In order to build the pairing for the entire tree we call Algorithm 3 with the root (the sub-tree extracted from the root edge is the entire tree $\mathcal{Y}$) and the main bifurcation pairing given by initialization. This algorithm involves the computation of:

- **LengthTolerance**: the absolute length difference allowed between the projection of E and an admissible path. This difference depends on the projective foreshortening of E and is defined in Equation (6.13).

- $\mathcal{N}(P(E[\#]), r(E))$: denotes the neighborhood around the projection of the 3D extremity of E, which does not correspond to bifurcation B, s$P(E[\#])$. Its definition and its size $r(E)$ are discussed in Section 5.2.2 especially around Equation (5.29).

[8] A precise definition of the optimal substructure property can be found in chapter 15 of [Cormen et al., 2009].

Algorithm 3 Divide-and-conquer tree pairing algorithm

INPUT: E : 3D edge defining the sub-tree $\mathcal{Y}_{|E}$,
INPUT: (B, b) : parent bifurcation pairing of E,
OUTPUT: $\hat{\Pi}_E$: optimal tree pairing of the sub-tree $\mathcal{Y}_{|E}$.

function TreePairing(E,(B, b))
  $\overline{\Gamma} \leftarrow \emptyset$
  $\Delta L =$ LengthTolerance(E)
  for all $e \in \mathcal{N}\left(P(E[\#]), r(E)\right)$ **do**
    $\overline{\Gamma} \leftarrow \overline{\Gamma} \cup$ CompatiblePaths(E,b,ΔL,e,e)
  end for
  $S_{best} = -1$
  $\hat{\Pi}_E \leftarrow \emptyset$
  for all $p \in \overline{\Gamma}$ **do**
    $\Pi_{curr} \leftarrow \{(E, p)\}$
    $S_{curr} = \mathcal{L}(E) \cdot S(E, p)$
    $(B', b_p{}') \leftarrow$ ChildBifurcationPairing(E, p)
    for all $E_{child} \in$ Children(E) **do**
      $\Pi_{curr} \leftarrow \Pi_{curr} \cup$ TreePairing(E_{child},$(B', b_p{}')$)
      $S_{curr} = S_{curr} + \overline{S}(\Pi_{curr})$
    end for
    if $S_{best} < S_{curr}$ **then**
      $S_{best} = S_{curr}$
      $\hat{\Pi}_E \leftarrow \Pi_{curr}$
    end if
  end for
  return $\hat{\Pi}_E$
end function

- **CompatiblePaths**: refers to the selection of compatible candidates for the matching with E defined in Algorithm 2.

- **ChildBifurcationPairing**: given a curve pairing (E, p), the determination of the child bifurcation pairing is provided by using the Fréchet distance in Equation (6.15). One would note that for the particular case of the root R of $\mathcal{Y}$ the main bifurcation pairing is already provided by initialization and thus gives $(B, b) = (B', {b_p}')$.

- **Children**: designate the set of child edges of E in the tree $\mathcal{Y}$. If this set is empty the recursion has reached a leaf edge and thus stops.

By taking advantage of the optimal substructure of the problem, this divide-and-conquer algorithm saves a considerable amount of time with respect to its brute force counterpart. The optimal substructure formulation is often associated to dynamic programming. However, dynamic programming is concerned when a recurrent overlapping occurs between subproblems. In our case, the generated subproblems (given a child bifurcation pairing $(B', {b_p}')$) refer to sub-trees that are non-overlapping between each other and thus need not to compute twice the same thing. However, different candidate paths p may generate the same child bifurcation pairing that will lead to the computation of the same subproblems (that will return the exact same solution each time). Since the decision will be made accordingly to the pairing score between the current edge and these candidates, if several paths in $\overline{\Gamma}$ lead to the same child bifurcation we will only run the recursion with the one with the highest curve pairing score. This refinement suppresses many recursion steps in the case of noisy detection and parallel paths occur in the graph such as in Figure 6.7.

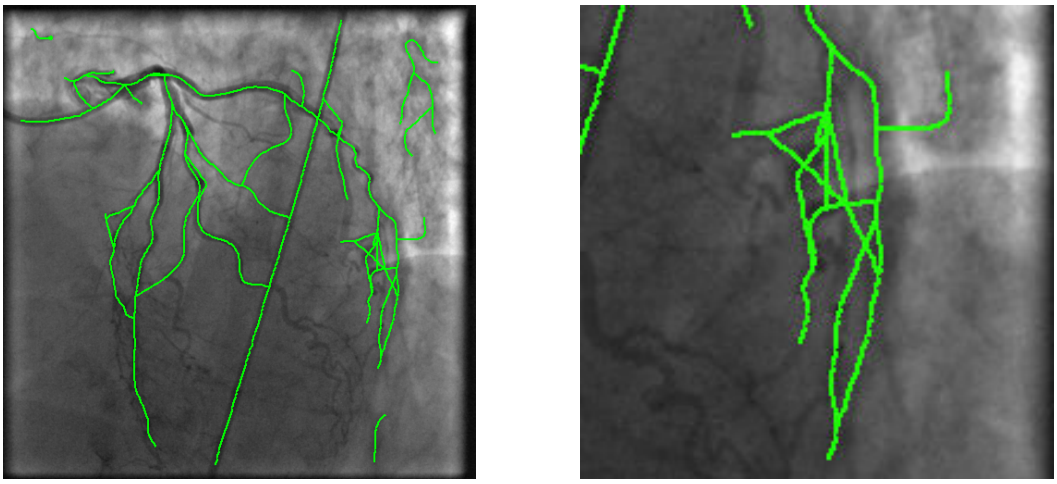

Figure 6.7: Noisy segmentation of the fluoroscopic image (right: zoom on the noisy part)

This noisy cluster of small edges and bifurcation can also occur in the search neighborhood $\mathcal{N}(P(E[\#]), r(E))$ itself. In this case, the previous pre-selection of

paths does not have a big impact because the child bifurcation generated by each of the noisy ending paths are generally different. The set $\overline{\Gamma}$ is thus composed of several similar curves that only differs from each other in a small area where the graph structure complexity increases due to fake centerline detection. Multiplicity impacts a lot the computation time but not much the resulting pairing. We therefore decided to restrict the set $\overline{\Gamma}$ to a limited number of elements, by progressively choosing the most relevant ones based on their elementary pairing score and their redundancy with respect to other candidates. The redundancy of a path $\tilde{p}$ with respect to already selected paths $\overline{\Gamma}'$ is defined as:

$$\frac{\text{size}\left(\bigcup_{p\in\overline{\Gamma}} p' \cap p\right)}{\text{size}\left(p'\right)} \tag{6.30}$$

This restriction $\overline{\Gamma}'$ of the set $\overline{\Gamma}$ can be seen as a stopping condition that is used to control computational time in all situations.

6.5 Tree-Topology Preserving Iterative Closest Curve

Now that we have defined a pairing procedure that endorses the tree-topology of the model, we introduce it in the ICC framework. The tree pairing procedure will replace of the pairing procedure described in Section 5.2.3 and thus will create the Tree-topology Preserving Iterative Closest Curve (TP-ICC) algorithm. Starting from Equation (5.15), we replace the undefined set of curves $C \subset \mathcal{X}$ by a sum over edges in the graph:

$$\hat{T} = \underset{T\in\Omega}{\text{argmin}} \sum_{E\in\mathbf{E}} \mathcal{F}\Big(T(E), \text{Closest}_{\mathcal{X}}\big(T(E)\big)\Big) \tag{6.31}$$

where $\mathbf{E}$ is the set of edges in the 3D tree. Contrary to the previous implementation described in Section 5.2.1, curves to be matched are not redundant with respect to each other and thus are not suffering from ambiguities in proximal parts.

To take into account the tree-topology of the model, pairing between edges cannot be built independently but simultaneously in a tree pairing procedure. Therefore the Closest(.) operator refers now to:

$$\text{Closest}_{\mathcal{X}}\big(T(E)\big) = p \sqsubset \mathcal{X} \;\text{ s.t. }\; (E,p) \in \hat{\Pi} = \underset{\Pi\in\Psi(T(\mathcal{Y}),\mathcal{X})}{\text{argmax}} \overline{S}(\Pi) \tag{6.32}$$

where $\Psi\left(T(\mathcal{Y}),\mathcal{X}\right)$ is the set of admissible tree pairings[9] between the tree $\mathcal{Y}$ transformed by T and the graph $\mathcal{X}$; and $\overline{S}$ is the tree pairing score defined in Equation (6.22) that assesses a tree pairing. Here, the score used to obtain the closest curve pairing is not used as the objective function to optimized. In fact, the purpose of this score is to provide the best pairing between the two structures while

[9]We recall that a tree pairing is a curve pairing set between the model tree and the data graph that preserves the tree-topology of the model.

the minimization of the objective function aims at finding the transformation that best align them.

The TP-ICC iterative scheme can be written as follow:

$$\begin{cases} \Pi_i = \underset{\Pi \in \Psi(T_{i-1}(\mathcal{Y}),\mathcal{X})}{\operatorname{argmax}} \overline{S}(\Pi) \\ T_i = \underset{T \in \Omega}{\operatorname{argmin}} \sum_{(C,c)\in\Pi_i} \mathcal{F}\big(T(C), c\big) \end{cases} \tag{6.33}$$

where the tree pairing step (first line of the previous equation) is computed using Algorithm 3. The second step that corresponds to the transformation optimization can be solved using the exact same approach as the one described in Section 5.2.4. From the set of curve pairings Π_i, the Fréchet pairing for each pair (E, p) is computed and stored in a point pairing set π_i:

$$\pi_i = \bigcup_{(E,p)\in\Pi_i} \pi_{\mathcal{F}}\big(T_{i-1}(E), p\big) \tag{6.34}$$

Contrary to the previous pairing procedure implementation of Section 5.2.3, the curves considered in the TP-ICC algorithm do not have any overlap between them and thus a point $Y \in \mathcal{Y}$ cannot be matched twice in π_i. Moreover, the use of the Fréchet distance together with the tree pairing ensures that the resulting point pairing set π_i preserves the two types of connectivities in the tree: connectivity (and order) along edges and connectivity at bifurcation nodes. This point pairing set is used to update the optimal transformation estimation and the two interlocked iterative procedures that constitute the ICC-framework are run.

From an objective function point of view, the TP-ICC approach optimizes the very same formulation as the ICP and the ICC presented in Equation (5.20). As discussed in Section 5.1.4, this sum of distances between paired points does not change but the constraints imposed to the pairing set does. While the previous ICC implementation enforces point pairings to be coherent along curves extracted from the model (curves are matched to curves and order along them are maintained), the TP-ICC algorithm ensures that:

- the resulting point pairing set constitutes a one-to-one pairing where each point of the model is only paired to one single point in the data;
- points that belongs to the same edge in the tree $\mathcal{Y}$ are paired to the same curve extracted from the graph $\mathcal{X}$;
- point pairings preserve point orders along curves that are matched;
- connectivities at bifurcation nodes in the tree are preserved during the matching.

Chapter 7

Registration Quality Evaluation

Contents

This chapter is dedicated to the evaluation of the quality of a registration algorithm via experiments based on "real" clinical data. The adjective "real" refers to a clinical data set that has been acquired during standard of care PCI procedures where no gold-standard is available. We will see in this chapter that evaluating a registration algorithm under this condition is both important and challenging. A 3D/2D registration algorithm is intended to find a transformation of the 3D model that best aligns it with its 2D corresponding structure after a step of projection. This alignment is often quantified by computing the residual distance between model points, projected at the registered position, and their closest point in the manually segmented 2D structure. However, this measure lacks of specificity since no distinction is made between a vessel close to the overall structure and a vessel close to its correct correspondent. From a clinical application point of view, building meaningful correspondences between structures is as much important as recovering the optimal alignment. Whereas an indicator on the pairing quality would be of great help to evaluate and design registration algorithms, it is rarely assessed in the literature. To define two error measures relative to the alignment and the pairing, we propose a manual procedure to build the Ground-Truth (GT) sets that identifies corresponding vessels in both sets. We validate these two error measures with respect to visual assessment and find out good correlation and nice discriminative properties.

7.1 Literature on Registration Errors

In our study of 3D/2D registration literature, we distinguish two classes of methods. The first class is based upon the correct registered position of the 3D volume regarding the current patient state. This gold-standard registration provides a transformation T_{gold} that is the basis of the registration error measure. The second class regroups methods involving the identification of correspondences between the two modalities to be registered. The distance between these ground-truth correspondences quantifies the quality of the registration and can be used as a registration error. Elements of these two classes are depicted in the two next sections.

7.1.1 Errors based on Gold-Standard Transformation

In the literature evaluating registration algorithms using a gold-standard transformation, the great work of [van de Kraats et al., 2005] describes a standardized methodology claimed to be applicable to any type of 3D/2D registration topic involving CT volume and projective X-ray image. Using the capability of the C-arm system to provide an intra-operative 3D reconstruction (cone-beam reconstruction), the gold-standard transformation T_{gold} is determined automatically by 3D/3D registration of pre-operative and intra-operative volumes. Because 3D/3D registration algorithms do not suffer from one missing dimension between the model and the data, they are able to achieve robust alignment with good accuracy (as it is done in [Nithiananthan et al., 2011]). Using this transformation T_{gold} the two following error measures, relative to a resulting alignment $\hat{T}$ of the volume, can be computed:

- Target Registration Error (TRE). The mean TRE is the average distance between points of interest[1] in the 3D model transformed by $\hat{T}$ and their target position given by the transformation T_{gold}. More intuitively, it corresponds to measuring the distance between two locations in space: where a point should be registered and where it is actually registered by the algorithm.

- Projective TRE (or 2D TRE). It is the exact same principle as the previous TRE but points and their targets are projected into the image plane before computing their distance. This 2D error seems more appropriate than the 3D one since the result of the alignment is often assessed in the image plane. In fact, the fusion between the live 2D image and the projected segmented volume[2] is the privileged visualization for the user to confirm the registered pose.

The authors of [van de Kraats et al., 2005] also depict a methodology to compare two registration algorithms using this ground-truth transformation. The major assumption made in this article is that the 3D intra-operative reconstruction is exactly linked to the 2D image that has to be registered.

[1] Points of interest can be manually defined or can correspond to a segmentation of the model.
[2] As the one presented in Figure 2.18 of Section 2.4.1.

For our coronary arteries application, the first difficulty is to obtain a 3D reconstruction of the heart anatomy using a C-arm system. We have stressed in Section 2.3 that 3D imaging of the beating heart is a challenge of its own and is possible mostly with fast acquisition times. By design, the C-arm system cannot rotate around the patient as fast as a CT-scan can (around 50 times slower[3]). C-arm coronary arteries reconstruction is still a research topic that has not yet found its way to clinical routine (see [Blondel et al., 2006; Prümmer, 2010; Rohkohl, 2011] for examples of solution). The deformations of the coronary artery tree also challenge the straightforward correspondence between the intra-operative reconstruction and the 2D live acquisition. Moreover, the rotational acquisition (that allows to reconstruct the intra-operative volume) is usually not a part of the standard interventional procedure and thus would complicate the data collection.

Providing an evaluation technique that does not impact the clinical procedure is of great interest since it facilitates the data collection. Actually most of the 3D/2D vascular registration articles presented in Chapter 3 propose quantitative results without involving any modification of the clinical routine. Some articles, such as [Liu and Bullitt, 1998; Duong et al., 2009], involve an expert determining the transformation T_{gold} to evaluate the registration error. This step can be highly time consuming since the expert have to tune the different parameters, whose together define the transformation, to obtain the best fit between the volume projection and the fluoroscopic image. In the case of rigid transformation, six degrees of freedom are manually optimized which constitutes a challenge of its own. According to [Liu and Bullitt, 1998], manual rigid registration of 3D/2D cerebral vessels takes approximately one hour to be accurate. Finding the optimal transformation can become tricky since inferring the projective displacement created by a 3D transformation is challenging. Obviously retrieving a non-rigid deformation following the same way should be even more time consuming. Regarding the error measure, [Duong et al., 2009] evaluate their algorithm using both versions of the mean TRE (3D and 2D) . In [Liu and Bullitt, 1998] the maximum version of the TRE, computed at each segmented centerline points of the segmented volume, is considered.

In order to speed up the manual definition of T_{gold}, [Groher et al., 2009; Baka et al., 2014] identify anatomical landmarks in both modalities and then to find the transformation T_{gold} that best aligns paired landmarks. This is usually achieved by minimizing the sum of squared distance (as presented in late Section 5.2.4). This technique can be used to define a non-rigid gold-standard as it is done in [Groher et al., 2009]. In vascular structure, the diversity of anatomical landmark is limited to bifurcations and particular tortuosities along the vessel. It has been stressed in Section 6.1 that identifying precisely bifurcations in 2D can be quite challenging because of superimpositions. Moreover, identifying corresponding points of tortuosity is hardly feasible in the projective image. Finally, the number of anatomical landmarks can vary greatly from one patient to the other. Some of the

[3] C-arm system usually achieve a reconstruction spin (200^o) in 5 seconds while the new generation of CT achieve their full 360^o acquisition in 0.2 seconds.

right coronary tree extracted from our CT-scan database only count two or three bifurcations, which limits the potential number of degrees of freedom that can be retrieved.

In addition of the difficulty to define T_{gold}, errors measures based on a gold-standard transformation are by nature dependent on the type of transformation considered. It is usually claimed that non-rigid registration allows better fitting between two modalities (see [Sotiras et al., 2013]). The need of non-rigid alignment can rise quite quickly in case of cardiac application because of the respiratory motion and the beating heart. Thus, to define a T_{gold}-based error measure, one has to chose a model of transformation among the huge variety of available ones (again see [Sotiras et al., 2013]). However, the resulting error measure could be biased in favor of registration algorithms using the same transformation family contrary to algorithms optimizing in a different set of admissible transformations.

7.1.2 Errors based on Ground-Truth Correspondences

In order to overcome issues raised in the previous Section 7.1.1, another type of registration evaluation is considered in the literature: methods based on correspondences between structures to be registered. Such correspondences can be made by a clinical expert or a trained observer and will constitute the ground-truth. Correspondences can be of different types, as it will be shown in the following, but the error measure always takes the form of a distance between corresponding structures. By this mean, a registration algorithm will be assessed on its capacity to align parts of the structure of both modalities that should be close.

Similarly to [Groher et al., 2009; Baka et al., 2014], the error measure used in [Gatta et al., 2011] is based on the identification of landmarks in 3D and 2D along the coronary arteries. But contrary to [Groher et al., 2009; Baka et al., 2014], these landmarks are directly used to compute a projective error and not to determine an optimal transformation (no T_{gold}). In this case, the registration error is not computed on the whole 3D segmented coronary tree but only at the landmark points identified in both modalities. The corresponding error measure is the distance (in the 2D projective plane) between each 3D landmark projection at the registered position and its ground-truth correspondent in the image. As it has been stressed in Section 7.1.1, landmark points are difficult to locate precisely and few may be identifiable. Moreover, the majority of the vasculature of interest is not taken into account in the error measure and may not involve the region of interest to the clinician at the current state of the procedure.

To avoid the problem of precise anatomical points identification, [Metz et al., 2009; Serradell et al., 2011; Hadida et al., 2012; Rivest-Henault et al., 2012] manually click the 2D vessel structures corresponding to the whole 3D segmented tree. A global ground-truth correspondence is thus made between the 3D segmented vasculature (which is assumed to be correct according to Section 4.1) and its 2D counterpart. Both corresponding structures are usually composed of a set of points, which sample vessel centerlines. At first sight, constructing the 2D ground-truth may ap-

pear time consuming. But actually, a trained observer can achieve the ground-truth construction in less than five minutes per case. This 2D structure, which constitutes a part of the ground-truth, is then used to compute the Mean Projective Distance (MPD). In this case, the MPD is the average of the closest point distance between the projection of the 3D vasculature at the registered position and the 2D manually identified vessels. It differs from the 2D Target Registration Error (TRE) mentioned in Section 7.1.1 by the fact that here point-to-point correspondences are unknown a priori.

In the TRE case, the distance is taken between the same 3D structure at two different positions (respectively given by T_{gold} and $\hat{T}$) and thus point correspondences are implicitly given. However, the global correspondence between set of points necessitates pairings between points to compute the distance between them. The MPD error is based on the closest point pairing between the 3D model and the 2D manually clicked ground-truth. Both vascular structures are considered as sets of points as it is done in the ICP algorithm, which leads to the same type of problems as highlighted in Sections 3.3.1 and 5.1.2. Figure 7.1 presents two registered cases with similar MPD. The first one has been obtained with an ICP algorithm that has reached a wrong registered pose. Since the overall structure is quite close to the ground-truth the MPD is quite low. However, the majority of point pairings made to compute the MPD are wrong[4].

In the second case, the registered position corresponds to a similar MPD, but in that case the registration is correct. The remaining distance between structures is mostly due to non-rigid deformations that have not been compensated by the algorithm. Thus the MPD lacks of discrimination because it does not take into account that a given vessel in 3D must be close to its corresponding vessel in the 2D and not only close to the overall structure.

7.1.3 Necessity of new Error Measures

To conclude, regarding the measures quantifying the quality of $\hat{T}$ (alignment error), multiple approaches presented above are available but non of them suit perfectly to the 3D/2D registration of vascular structures. These measures either involve to define a gold-standard transformation (difficult to obtain); require to identify point of interest correspondences (that may be too few and complicated to locate precisely); or lack of discrimination regarding correct and wrong registration. Moreover, to the best of our knowledge, no proposition has been made in the literature to address the problem of pairing quality (except for synthetic datasets). We thus worked on building two measures quantifying the two output of a registration algorithm ($\hat{T}$ and $\hat{\pi}$) that are in accordance with the following specifications:

- The measures shall be applicable to any clinical dataset (and not only synthetic cases) without involving any modification of the standard of care procedure.

[4]The way correct and wrong pairings is decided is depicted in Section 7.3.2.

(a) Wrong registered case (b) Correct registered case

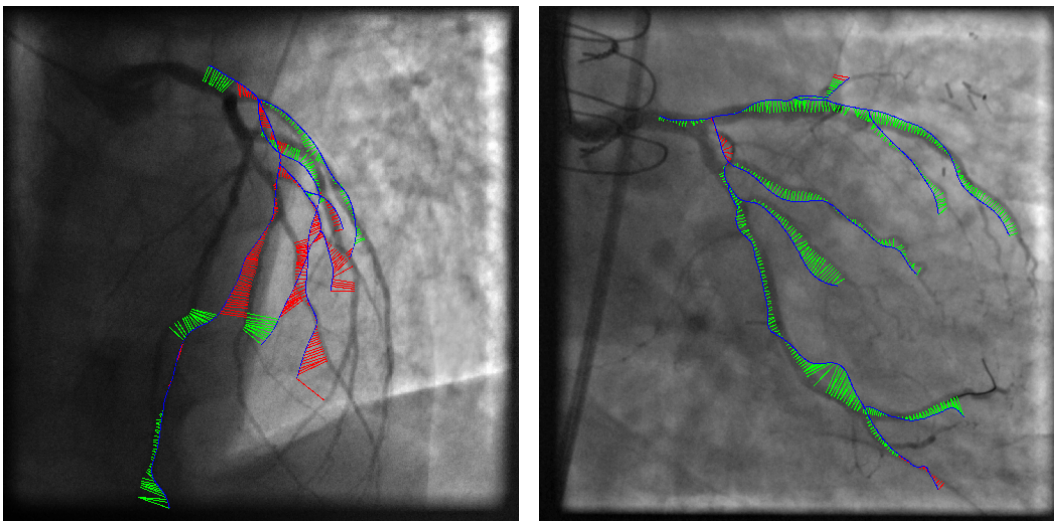

Figure 7.1: Registered positions of two cases with similar Mean Projective Distance (MPD). The thin blue lines are the projection of the 3D structure, green and red segments correspond to the closest point pairings between the 3D structure and the 2D ground truth and finally the color represents correct (green) and wrong (red) pairings. (a) registered position presenting a medium MPD where most of the vessels are mispaired, (b) registered position presenting a similar MPD as the previous but where a majority of vessels are well registered.

- The measures must be independent of the algorithm used or the type of admissible transformations considered in the optimization.
- Building both measures upon the same ground-truth is appreciable as well as considering a ground-truth that is not too time consuming to obtain.
- The measures shall be able to distinguish correct registration cases from the wrong ones (as in Figure 7.1).

7.2 Ground-Truth

In this section, we define the ground-truth upon which will be built the two error measures evaluating a registration algorithm. We chose not to consider measures based on a gold-standard transformation for the reasons highlighted in the previous section. Instead, we define this ground-truth as correspondences between the two modalities, that discriminate different vessels in the two modalities. Providing dense correspondences between the whole 3D vasculature and positions in the image space is hardly feasible except for synthetic experiments. Inspired from [Metz et al., 2009; Serradell et al., 2011; Hadida et al., 2012; Rivest-Henault et al., 2012], we consider the 3D segmented centerlines as a part of the ground-truth (GT) and identify the corresponding structure in the image. In clinical routine, the 3D vascular tree is validated and corrected if necessary by a clinical expert, which justifies its use in the GT. A more difficult part consists in defining the corresponding vasculature in the data, especially if we want to discriminate between vessels. We also propose in Section 7.3 to take advantage of this manually annotated structures to provide a reference transformation. This transformation will be obtained automatically from the ground-truth and can play the role of the gold-standard transformation used in several articles to provide a registered pose that will be perturbed in order to study robustness.

The ground-truth used in [Metz et al., 2009; Serradell et al., 2011; Hadida et al., 2012; Rivest-Henault et al., 2012] considers the vasculature as two sets of points and leads to errors that are based on non-coherent pairings (as highlighted in Figure 7.1a). We thus extend this GT to consider entire vessels instead of points. The main idea is that a trained observer establishes correspondences between vessels, taken one by one, in the two modalities. This constitutes a good compromise between the less precise global identification of the two vasculatures (as in [Metz et al., 2009; Serradell et al., 2011; Hadida et al., 2012; Rivest-Henault et al., 2012]) and the challenging strategy consisting in pairing each point along vessel centerline. Regarding the choice of curves to be manually matched, it has been highlighted in the previous section that identifying precisely the position of an anatomical bifurcation in 2D is a challenging task even for a trained observer. Therefore, identifying manually each 3D vessel portion between two bifurcations (an edge in the vascular tree) in the 2D image is hazardous. Instead, we chose the same type of curves as in Section 5.2.1 that avoids to precisely identify bifurcations by matching curves

extracted from the main bifurcation to extremities. We will take advantage of the redundancy induced in the proximal parts, that has been discussed in Section 5.3.2, in the definition of the two measures.

The first step to construct the ground-truth set $\mathcal{GT}$ is to extract from the model centerline curves linking the main bifurcation to extremities. This can be easily achieved by following the algorithm described in Section 5.2.1. For each vessel W_q extracted from the model, we identify its corresponding vessel in the 2D image denoted w_q. This 2D curve is built by several clicks along its center, starting from the main bifurcation identified in 2D. A toy-example, provided in Figure 7.2, represents the GT construction where the colored curves of the tree are the vessels W_q and the colored crosses are the manual clicks defining the curves w_q. To facilitate the work of the trained observer, we project the 3D vessel to be matched W_q onto the image plane at the position given by initialization (see Chapter 8 for more details on this initial pose estimation). This helps to identify the coarse location of the end of segmentation of the 3D vasculature. It can occur that the vessel W_q is not entirely visible in the image, because of occlusion, lack of contrast in the image or out of field of view reasons. In that case, the 3D vessel is cut at its last point identifiable in the 2D image.

The resulting ground-truth for a given case is thus defined by:

$$\mathcal{GT} = \left\{ \left(W_q, w_q\right), q \in [1 \dots M] \right\} \tag{7.1}$$

where M is the number of vessels extracted from the tree (also the number of leaves) and each pair (W_q, w_q) is a curve pairing between a 3D and 2D polygonal curves. Examples of 2D vessels manually identified are presented in Figure 7.3. Obtaining the 2D ground-truth part is quite simple and takes around five minutes for a trained observer. This ground-truth definition will allow us to define error measures taking into account the vessel structure of both modalities. It is also quite easy and fast to obtain for a trained observer and can be done without impacting any step of the clinical intervention. However, this definition of $\mathcal{GT}$ also induces redundancy in proximal vessel parts: a given point Y of the 3D model may belong to several curves W_q of the ground-truth and thus corresponding 2D portions will be clicked several times. This point will be addressed in the upcoming error measure by considering that the common part of multiple GT 3D vessels must be close to *every* corresponding GT 2D vessels.

7.3 Errors Definition

In this section, we define two complementary measures that evaluate the quality of the registration. The first one, called the **alignment error**, quantifies if the resulting transformation $\hat{T}$ provides a good fit between the projected 3D model and the 2D ground-truth. This error measure takes into account the vascular nature of registered structures as in the ground-truth definition. Regarding the resulting pairing set $\hat{\pi}$, we aim at judging which pairings are correct and which are wrong. The

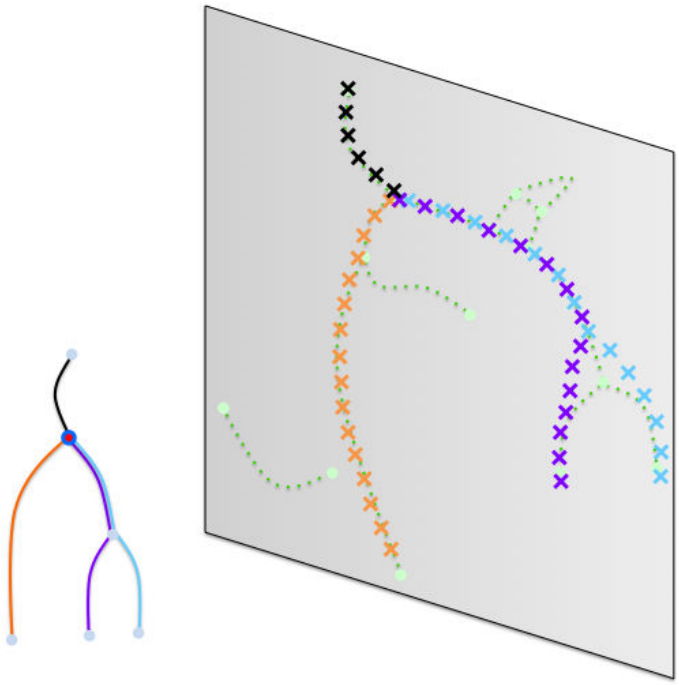

Figure 7.2: Toy example of the Ground-Truth construction. Colored curves in the tree represent vessels extracted from the main bifurcation (red point circled in blue) to segmentation extremities. Their paired correspondents in the 2D image plane are identified by manual clicks noted as crosses of same color as the 3D vessel one. One would note that these 2D marked centerlines may not exactly correspond to the 2D automatically segmented structure, especially around bifurcations.

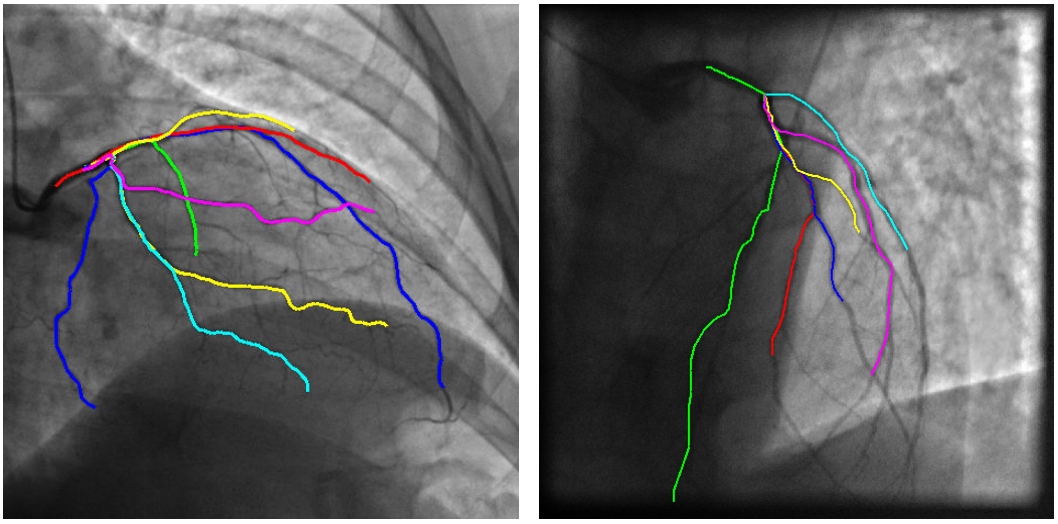

Figure 7.3: 2D ground-truth obtained by manual clicks along vessels in the image plane where each color corresponds to a different 3D vessel extracted from the main bifurcation to an extremity of the vascular tree. Proximal parts are identified multiple times, even if obviously a single artery is represented at these places.

corresponding **pairing error** is of great importance to quantify if the registration algorithm can be used in a roadmap application. Both measures are based on the same ground-truth defined in Section 7.2 and take into account the tree structure of the vasculature. In the following, we consider error measures built as the sum over the 3D structure $\mathcal{Y}$.

7.3.1 Alignment Error

The goal of the alignment error $\varepsilon_A(\hat{T})$ is to provide a quantitative measure of the fit between the 3D model $\mathcal{Y}$ transformed by $\hat{T}$ and the 2D locations where it should be projected. The ground-truth does not provide exact correspondence for each point Y in the model $\mathcal{Y}$ but for entire vessels from the main bifurcation to extremities. The Mean Projective Distance (MPD) is the most used measure to quantify the quality of a 3D/2D vessel registration algorithm. It is denoted $\varepsilon_{MPD}(\hat{T})$ and can be written:

$$\varepsilon_{MPD}\left(\hat{T}\right) = \frac{1}{\mathrm{card}(\mathcal{Y})} \sum_{Y \in \mathcal{Y}} \min_{q} \left\{ d\big(P \circ \hat{T}(Y), w_q\big) \right\} \tag{7.2}$$

where $\mathrm{card}(\mathcal{Y})$ denotes the number of points constituting the 3D model $\mathcal{Y}$, w_q are the 2D vessels manually clicked in the ground-truth $\mathcal{GT}$ and $d(., w_q)$ is the 2D distance to a curve w_q defined by:

$$d(x, w_q) = \min_{j} \left\| x - w_q[j] \right\| \tag{7.3}$$

The previous error definition does not takes into account that a 3D vessel W_q

shall be matched to a particular vessel w_q. We expect that a point Y belonging to a 3D GT vessel W_q must be projected close to the 2D GT vessel w_q. If the point Y belongs to several 3D GT vessels then we expect its projection to be close to *every* corresponding 2D GT curves. We propose thus to compute the distance between the projection of the transformed point Y and each vessel w_q to which it must be close (see Figure 7.4). The maximum of this distance above all w_q corresponds to the error of alignment associated to the point Y.

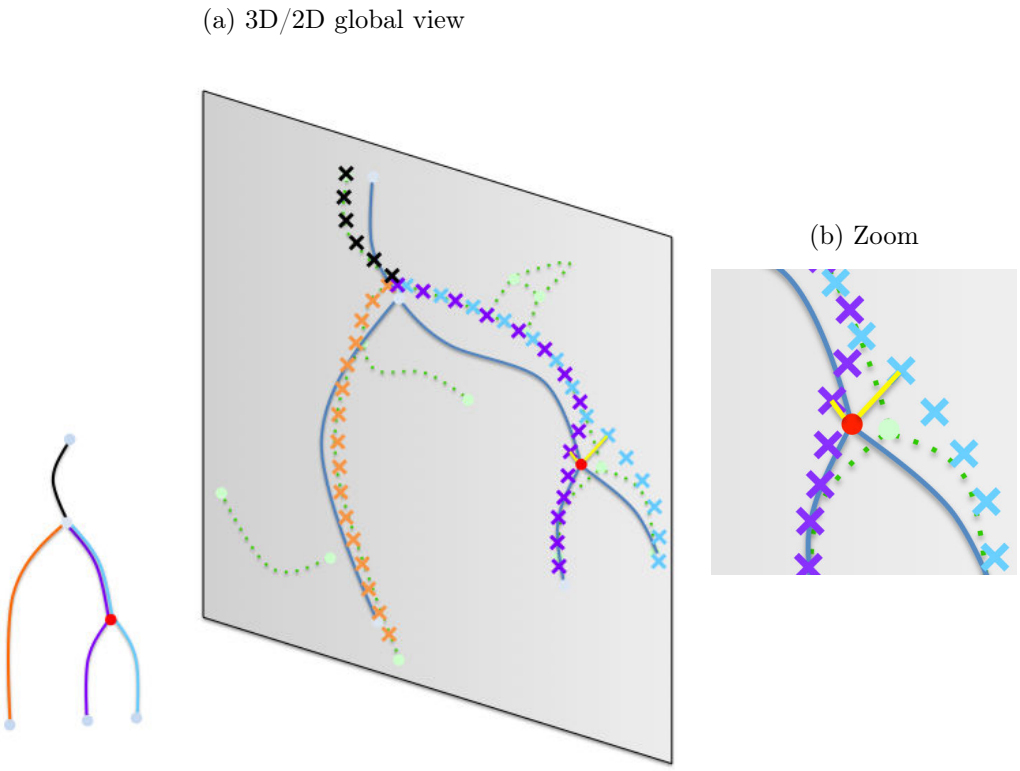

Figure 7.4: Toy example presenting the alignment error for a given point highlighted in red that belongs to two different ground-truth curves. (b) is a zoom of (a) around the point of interest projection onto the image plane (in red). The distance between this point projection and the 2D ground-truth corresponding curves that it must be close to are represented in yellow.

The alignment error $\varepsilon_A(\hat{T})$ can be defined by averaging[5] this maximal distance associated to each point of the model:

$$\varepsilon_A(\hat{T}) = \frac{1}{\mathrm{card}(\mathcal{Y})} \sum_{Y \in \mathcal{Y}} \max_q \left\{ d\big(P \circ \hat{T}(Y), w_q\big) \mathbb{1}_{W_q}(Y) \right\} \tag{7.4}$$

[5]We chose the average operator as it was chosen in the state of the art mean projective distance. In practice other versions such as maximum or n^{th} percentiles do not change the resulting correlation with visual evaluation (in Figure 7.7).

where $\mathbb{1}_{W_q}(Y)$ denotes the indicator function of the 3D GT curve W_q, which equals one if a point belongs to W_q and zero otherwise. One must note that this distance can be computed for any type of transformation. In the ground-truth definition of Section 7.2 it has been mentioned that several vessel parts present in the 3D model may not appear in the 2D image. In this case, 3D GT vessels W_p were cut at the last identifiable point in both modalities. Therefore it can occur that a point Y of the model $\mathcal{Y}$ may not appear in any curve of the ground-truth. The cardinal function used in Equations (7.2) and (7.4) is thus defined by:

$$\text{card}(\mathcal{Y}) = \sum_{Y \in \mathcal{Y}} \max_q \mathbb{1}_{W_q}(Y) \tag{7.5}$$

More intuitively, this function only counts points of the model that are present in at least one 3D GT curve.

As highlighted in Section 3.3, a distance between two feature sets is based on a point pairing set. One can take advantage of this pairing obtained from the ground-truth to build a GT-based registration algorithm. This algorithm alternates the construction of the point pairing set realizing Equation (7.4) and the computation of the optimal transformation in a least squares sense as defined in Section 5.2.4. The transformation T_{Ref} obtained at convergence can be compared to the gold-standard transformation often used in the literature. This reference transformation will be used in Chapter 8 to build several experiments.

7.3.2 Pairing Error

The alignment error of the previous sections quantifies the quality of the transformation $\hat{T}$ resulting from a registration algorithm. Yet, this transformation is not the only interesting output provided by a registration algorithm. The pairing set $\hat{\pi}$, obtained at convergence of the registration procedure, is of great interest to provide a guidance application to the clinician. We apply the same principle used in the alignment error: a point of the model should be paired to a point close to the corresponding 2D structure identified in the ground-truth. In other words, for a given point pairing (Y, x) of $\hat{\pi}$: if Y belongs to a 3D GT curve W_p then we expect that its paired point x is close to the corresponding 2D GT vessel w_p. In the toy example presented in Figure 7.5, the red point along the 3D structure is paired to the green point along the 2D segmentation. Since the red point belongs to two GT 3D vessels (the purple one and the blue one), the green point should be close to the purple and blue 2D GT manual clicks.

Similarly to the alignment error, the quality of a pairing depends on the following quantity:

$$\delta(Y, x) = \max_q \left\{ d\left(x, w_q\right) \mathbb{1}_{W_q}(Y) \right\} \tag{7.6}$$

We stress that this pairing distance is computed using the 2D paired point x; the point Y along the model is only used to define ground-truth vessels relative to the current pairing. By summing over all points in the model one is able to construct

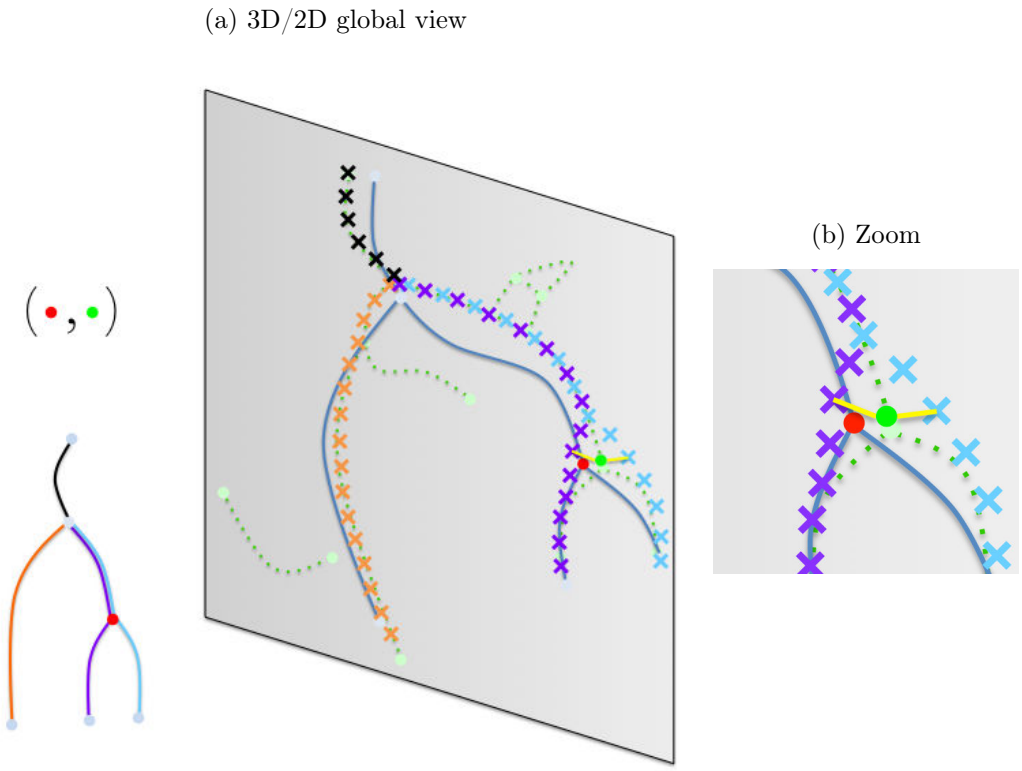

Figure 7.5: Toy example presenting the pairing error for a given point pairing between the 3D red point and the 2D green point. (b) is a zoom of (a) around the point of interest projection onto the image plane. As for the alignment error of Figure 7.4, the distance to each 2D ground-truth vessels of interest is evaluated. But contrary to the alignment error, the paired point along the 2D segmented structure (green dot) is used instead of the projected 3D point (in red).

a distance quantifying the average distance between paired point and the expected target. However, a pairing is more likely assessed as correct or wrong instead of close or far from the target. A pairing (Y, x) is considered as correct if x belongs to the vicinity of each curve w_p to which it should correspond. Thus we introduce a tolerance distance $r_{\mathcal{GT}}$ around each curve w_p that stands for the radius around the centerline constituting the vessel. We define a pairing as correct if the distance of Equation (7.6) is lower than $r_{\mathcal{GT}} = 3mm$. This tolerance threshold has been set to the typical diameter of the coronary arteries and corresponds to clinical expectation on the registration algorithm.

The pairing error is defined by:

$$\varepsilon_P(\hat{\pi}) = \frac{1}{\text{card}(\hat{\pi})} \sum_{(Y,x)\in\hat{\pi}} \mathbb{1}_{[r_{\mathcal{GT}};+\infty]}(\delta(Y,x)) \tag{7.7}$$

where $\mathbb{1}_{[r_{\mathcal{GT}};+\infty]}(.)$ is defined as:

$$\mathbb{1}_{[r_{\mathcal{GT}};+\infty]}(z) = \begin{cases} 1 \text{ if } z > r_{\mathcal{GT}} \\ 0 \text{ elsewhere} \end{cases} \tag{7.8}$$

The pairing error ε_P corresponds to the ratio of bad pairing among all pairings made by the algorithm. A pairing error of 0 means that the resulting pairing $\hat{\pi}$ contains only correct pairings and an error of 1 corresponds to the worst possible pairing set.

This way of assessing pairings is used to present pairing results in several figures of this thesis. Pairing assessed as correct will be presented in green and wrong ones would be red. One would have noticed in several figures the presence of yellow pairing. Similarly to the alignment error, the pairing error cannot quantify pairing relative to a point Y of the model that does not appear in the ground-truth. This type of pairings appears in yellow and will not contribute to the pairing error. The cardinal function is defined by:

$$\text{card}(\hat{\pi}) = \sum_{(Y,x)\in\hat{\pi}} \max_q \mathbb{1}_{W_q}(Y) \tag{7.9}$$

7.4 Validation

In the previous section we provided two different measures that quantify the outputs of a registration algorithm. But before we justify their use by conducting the following experiment. Different registration algorithms (ICP, ICC, TP-ICC) were run from various initial positions. Each of them resulted in an optimal transformation and an optimal pairing that have respectively been evaluated by the alignment error ε_A and the pairing error ε_P. Thus each registration configuration corresponds to a point in the plane $(\varepsilon_A, \varepsilon_P)$. We chose 200 points in this space that best pave it[6]

[6]The best pavement was obtained by iteratively choosing a point that is the farthest of the already chosen ones.

and asked a human observer to assess their quality by classifying them into three classes: good, acceptable and bad.

This manual evaluation was based on the following information provided to the trained observer:

- The native image without the segmented centerlines extracted to run the algorithm.
- The projection of the 3D model centerlines at the registered position, which is under evaluation.
- The evaluated pairings represented as straight lines between a 3D projected point and a 2D pixel.

Basically, it corresponds to the visualization presented in Figure 7.6, replacing pairings colors (obtained using the pairing error) by a neutral one. In this figure, an example of each class (good, acceptable and wrong) for a particular clinical case is provided. The resulting $(\varepsilon_A, \varepsilon_P)$-plane colored by the expert is provided in Figure 7.7. One would first note the good correlation between the visual evaluation of a trained observer and the couple of error measures presented. The lower both registration errors, the more likely the corresponding result is to be considered as correct.

It would be useful to define boundaries in the $(\varepsilon_A, \varepsilon_P)$-space in order to classify automatically the result of a registration algorithm in one of the three classes (good, acceptable and wrong). We define these regions manually as presented in Figure 7.8. The result of a registration algorithm (the transformation and the pairings) is qualified as wrong if more than 40% of the resulting pairings are incorrect or if the alignment error is more than $6mm$. If a given case presents both a resulting pairing error less than 20% and an alignment error smaller than $3mm$, the registration is considered as good. Results in between these two conditions are considered as acceptable. The goal of this classification is to provide an estimation of the success rate of a registration algorithm without involving a visual evaluation of an expert. One would note that manually defining boundaries in the $(\varepsilon_A, \varepsilon_P)$-space to separate different registration quality involves a condition on both measures. This shows the complementarity between the two measures.

Regarding the distribution of the points in the space, one would note that some registration configurations lead to a small pairing error but quite high alignment error. Based on the principle that correct pairings lead the registration procedure in the correct direction, we conclude that these cases would benefit from more degrees of freedom allowed by the transformation. Actually results shown here only consider rigid transformation and cases such as in Figure 7.1b could greatly benefit from non-rigid registration. On the other hand, configurations where the alignment error is low but the pairing error is high often mean that the registration procedure reached a local minimum that is not too far from the optimal rigid transformation. In such a case, starting a non-rigid registration procedure is questionable and can lead to clinically irrelevant deformations since many pairings have been evaluated as wrong.

(a) Inital pose estimate

(b) Wrong registration

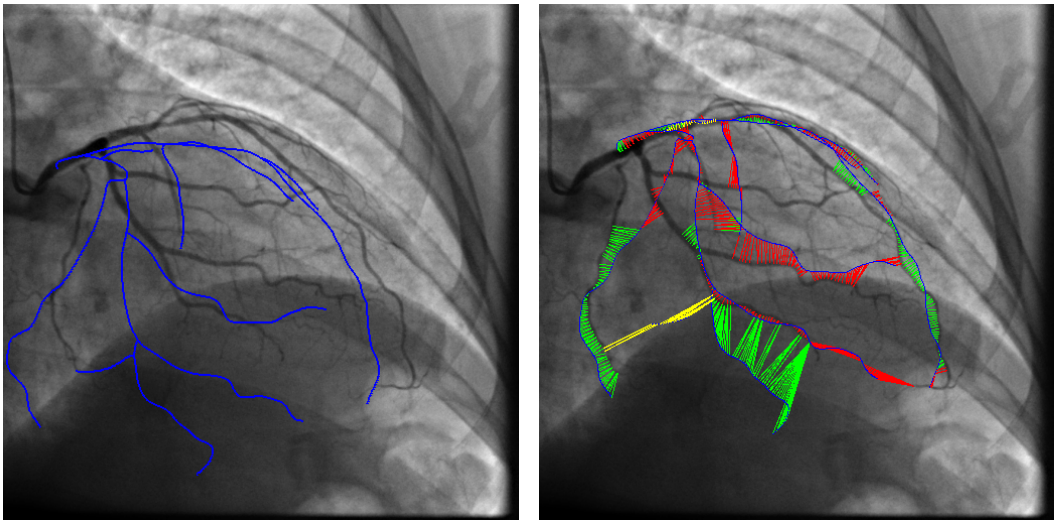

(c) Acceptable registration

(d) Good registration

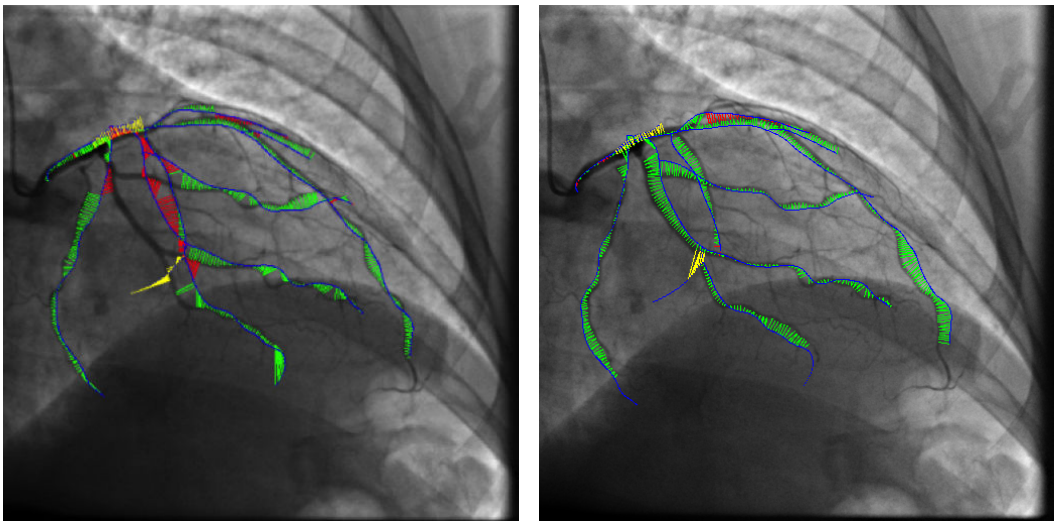

Figure 7.6: Three different registrations for the same clinical case presenting wrong, acceptable and good registration.

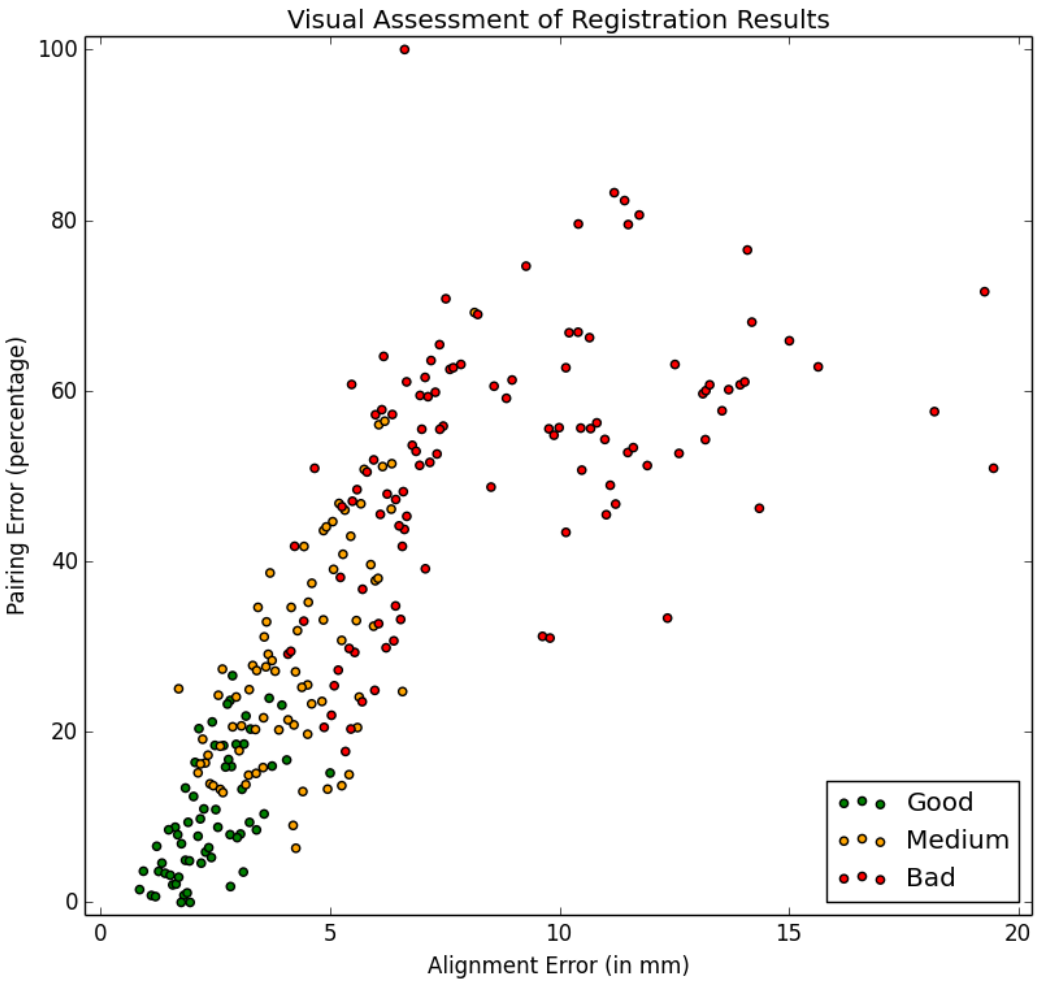

Figure 7.7: Alignment error function of the pairing error for 100 registration cases evaluated by a human observer. Each registered case has been evaluated as good, medium and bad based on the resulting pose and pairings.

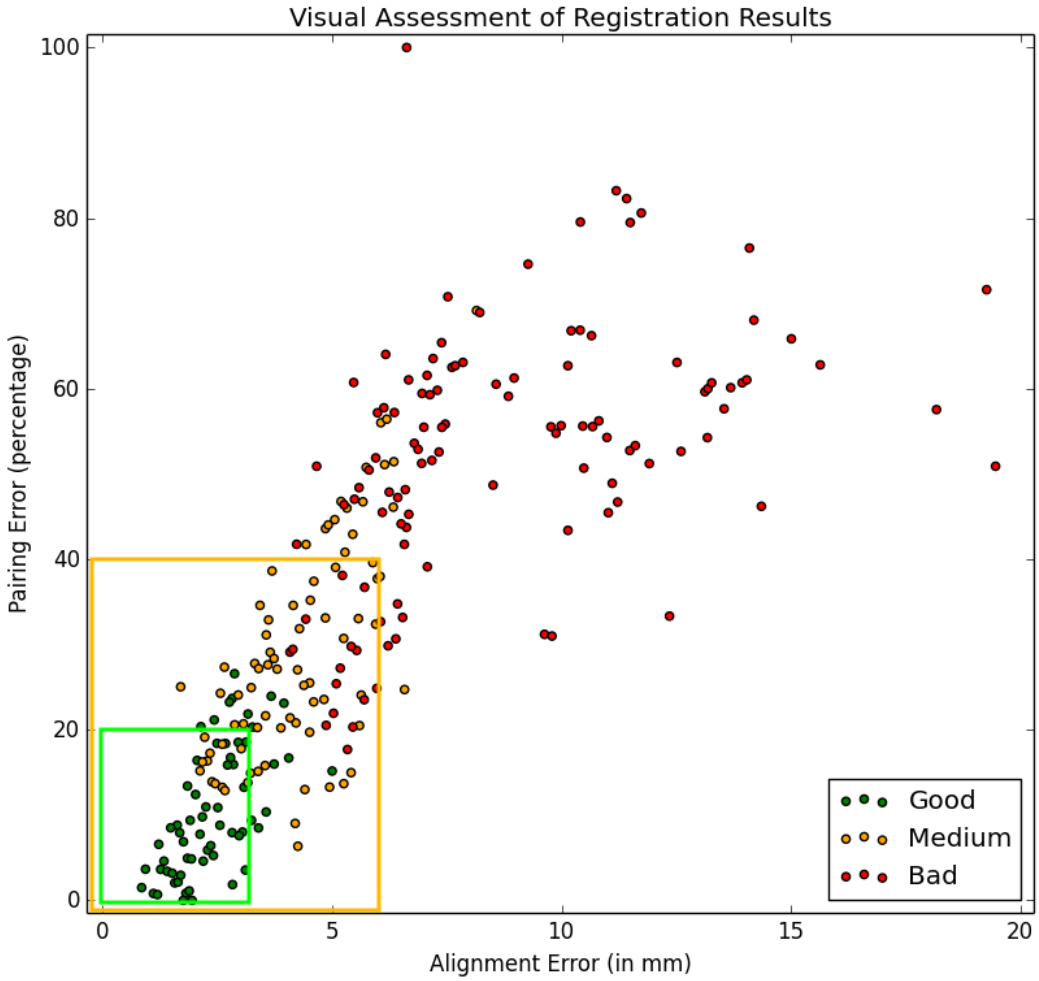

Figure 7.8: Regions in the $(\varepsilon_A, \varepsilon_P)$-space that define the success of a registration algorithm: good (inside the green rectangle), acceptable (outside the green region and inside the orange rectangle) and wrong (outside the orange rectangle).

These two complementary measures not only allow to assess the quality of the registration but can also provide to the developer of a registration algorithm where efforts should be made. If most of the cases present high pairing errors, then efforts should be made regarding the pairings: change pairing procedure or add an outlier rejection procedure (more discussed in Section 9.3.2). On the contrary, if most of the cases present low pairing errors, adding more degrees of freedom to the transformation makes sense.

Chapter 8

Experiments

Contents

In this section, we want to validate the main idea developed in this thesis: "Enforcing coherence allows to build better registration algorithms and more relevant outputs". We also provide evidences of the applicability of our approach regarding 3D/2D vessel registration for a clinical application. All the following results were obtained using patients data, making particular efforts to propose clinically realistic experiments. Regarding the different algorithms involved in this chapter, few variants of our approach depicted in Section 6.5, the Tree-topology Preserving Iterative Closest Curve (TP-ICC), are compared to the Iterative Closest Point (ICP) method.

A comparison with the ICC algorithm of chapter 5 will not be considered on the whole database. Actually, the described implementation assumes that the shortest path along the graph corresponds to the correct anatomic vessel between a given point and the main bifurcation. This assumption was made for the sake of simplicity and to prove a concept, but is not valid in most of the cases of the database. For this reason we decided not to include a comparison between ICC and TP-ICC.

8.1 Clinical Database Description

In order to run realistic experiments, we use a database composed of images collected at hospital sites in the context of standard of care procedures. Appropriate patient consents have been collected by physicians to include anonymized images in this research project. The database is built upon thirteen patients suffering from different kinds of pathology, such as stenosis or Chronic Total Occlusion (CTO), that impacts the left or right coronary tree. For each patient, a pre-operative Computed Tomography Angiography (CTA) scan has been acquired. In addition, several intra-operative X-ray sequences, where a contrast product injection fills the entire

vascular tree, are available for each patient. The set of registration cases forming the database has been extracted a posteriori from these acquisitions.

A case is composed of the following elements:

- **3D volume**: The vascular tree segmentation is automatically obtained from this reconstructed volume and is validated by a clinician in the clinical routine. This tree representation of the vasculature corresponds to the model, as described in Section 4.1. The CTA acquisition is synchronized with the cardiac cycle and is usually acquired during the diastolic phase. Most of the patients include the volume corresponding to a single phase.

- **2D image**: A frame is extracted from an intra-operative injected sequence, during which the electrocardiogram (ECG) is recorded. This frame is chosen to correspond to the same phase of the cardiac cycle where the CTA has been reconstructed (cardiac phase). In this situation, the amount of non-rigid deformation between the two modalities is expected to be limited. Actually, choosing the same phase shall minimize the remaining rigid registration error, even if there is no reason or practical experiment to prove out that this error can fall down to zero with any rigid transformation. The image is also chosen to contain as much vessels as possible in the image (injection phase). This step can be achieved automatically by injection detection techniques (such as [Chen et al., 2011; Matern et al., 2012]) or by manual selection of the frame of interest.

- **Projective Operator**: The matrix P allows to project a 3D point of the object onto the image plane at the current state of the X-ray source and detector. The projection matrix is derived from system parameters that describes the geometry of the image chain. These system parameters are stored together with the image pixels as defined in the DICOM[1] standard.

Since we address the registration problem using a single plane injected acquisition, several different cases can be extracted from the same patient. As it has been stressed in Section 2.2.2, the scope of our work is restricted to single plane acquisitions (registration of CT volume using only one projective image) because they are the most common in clinical practice. Two cases are considered different if: they are extracted from different patients; or if the type of coronary (left of right) is different; or if the current angulation of the system (given by P) is significantly different (system rotation of more than 10^o). From 13 patients, 63 registration cases were extracted to constitute the database.

For each case, features are extracted automatically from both modalities[2] aiming at sparsely representing the vasculature. The 3D vascular tree $\mathcal{Y}$, also called the model, is extracted using the procedure depicted in Section 4.1 and corrected if

[1] The DICOM protocol stands for Digital Imaging and COmmunications in Medicine. It became a standard regarding the medical data management.

[2] Actually, the pre-operative CT is rather considered as semi-automatic since it can be corrected by the clinician.

necessary by the clinician. The 2D vasculature $\mathcal{X}$, which is also called the data, is intended to be automatically segmented from the image during the intervention, as described in Section 4.2. The 2D graph representation of the data for all the 63 cases of the database has been presented in appendix Figures D.1, D.2 and D.3. Differences between $\mathcal{Y}$ and $\mathcal{X}$, highlighted in Section 4.3, constitute the major challenge to overcome by a registration algorithm. Because it seems difficult to simulate realistic 2D noisy graphs, we propose experiments based only on clinical inputs and not using a synthetic data set generation approach.

In order to provide quantitative evaluations using the two complementary error measures defined in Chapter 7, a ground-truth has been defined for every cases of the database. This ground-truth has also been used to define a reference transformation T_{Ref} for each case obtained by running an iterative procedure described in the end of Section 7.3.1. The transformation T_{Ref} can be seen as a gold-standard transformation, often used in registration evaluation, that corresponds to the correct transformation to retrieve by the registration algorithm. To ensure that this transformation is correct, a trained observer validation is performed on T_{ref} for each case. In this chapter, all the considered transformations are rigid.

Using the reference transformations T_{Ref}, we computed an average ground-truth transformation for each patient. The translational part of this rigid transformation is not meaningful since relative position of the table between acquisitions is not known[3]. Moreover, the initial alignment of the root bifurcation allows to obtain a constantly good estimation of the registration translation. Regarding the expected rotation to compensate, we assess its distribution by representing the rotation angle and axis respectively represented in Figure 8.1 and 8.2a. From this study on a limited number of patients, we conclude that no particular rotation axis seems to be privileged and that the angle of rotation seems quite uniformly distributed between zero and twenty degrees. These expectations will be used to construct a relevant range of perturbations in the upcoming robustness studies.

8.2 Pairings at Initial Position

In this section we illustrate that imposing coherence to the pairings between the two structures leads to correspondences that are more relevant from a clinical point of view. As highlighted in Section 3.3, feature-based registration algorithms involve the computation of a distance that relies on a set of pairings between structures to be matched. We thus study the pairings induced by different algorithms at the same position of the 3D model. Thanks to the pairing error ε_P, defined in Equation (7.7) of Section 7.3.2, we are able to assess the quality of a pairing based on the ground-truth defined for each case.

[3]In fact, the position of the table, which controls the translation of the patient, has no direct relationship with the C-arm system because they are two different machines.

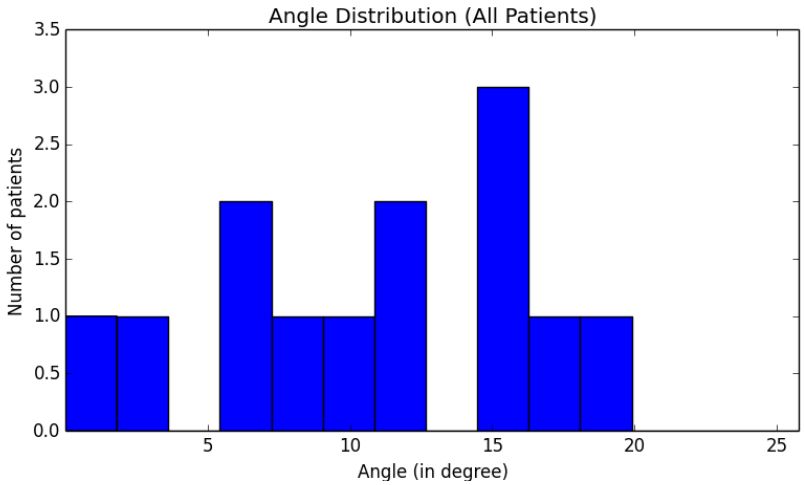

Figure 8.1: Histogram of the rotation angle computed from the rotational part of the reference transformation for each patient of the database.

(a) Axis distribution (view 1) (b) Axis distribution (view 2)

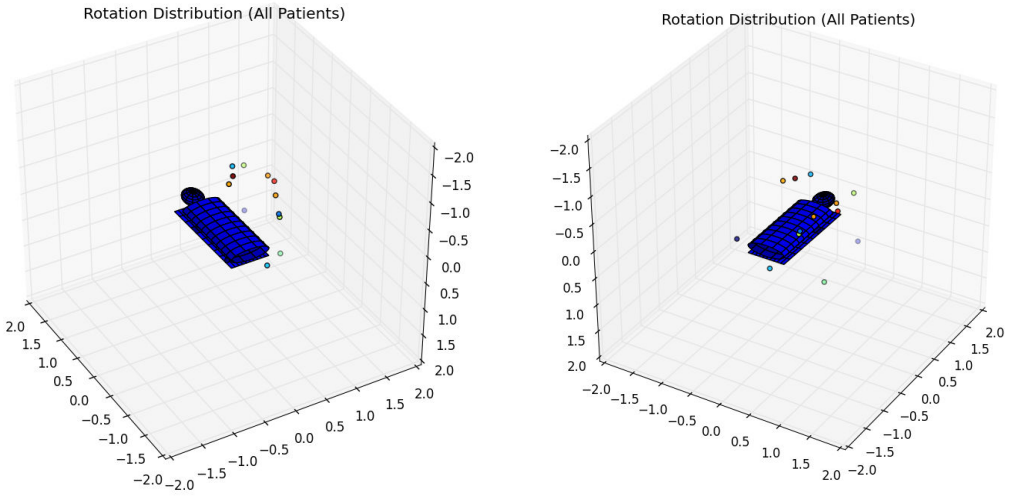

Figure 8.2: Distribution of the 3D rotation axis of the reference transformation computed for each patient of the database. Axis are computed such that the rotation angle belongs to $[0, \pi]$ and are normalized (axis of the figure have normalized unit and thus have no true meaning). They are represented in the 3D space as points on the unit sphere. The origin of the system is set to the center of the patient represented by the blue surface.

8.2.1 Imposing Coherence Improves Pairings

To highlight that imposing coherence allows to build better pairings, we compare the closest point pairing procedure of the Iterative Closest Point (ICP) algorithm to the point pairing set induced by the Tree-topology Preserving Iterative Closest Curve (TP-ICC) algorithm at the same position of the model. The ICP-pairings are computed by associating each point of the model to its closest in the data using Equation (5.40). No coherence constraint is imposed to these pairings and the decision criterion is only based on the Euclidean distance. Regarding the point pairing set relative to the TP-ICC algorithm, we first compute the curve pairing set using the tree-topology preserving pairing procedure summarized in Equation (6.23). This curve pairing set corresponds to the highest tree pairing score among all pairings preserving the tree-topology of the model. Point pairings are then obtained by computing the Fréchet pairing between each paired curves using Equation (6.34).

In Section 6.3, we evaluate the quality of a potential pairing using two criteria. The Fréchet distance quantifies the distance between curves while preserving the point order along them (contrary to the Hausdorff distance). The resemblance between curves is assessed in a global way without involving local shape descriptors. First, we want to demonstrate the contribution of the coherence imposed to the pairings. We set the parameter α of the score defined in Equation (6.21) to 1, which means that only the Fréchet distance contributes to this score and not the resemblance between curves. Pairings have been evaluated for each case of the dataset (all the 63), starting from an initial position given as follows. The 3D model structure is set at a distance SOD (Source Object Distance) of the X-ray source such that the 3D main bifurcation is projected onto the 2D main bifurcation[4].

In Figure 8.3, we compare the pairings induced by the ICP-algorithm and the pure geometrical version of the TP-ICC ($\alpha = 1$) at the same initial position. One would note that the pairing error relative to the TP-ICC algorithm is always lower or equivalent to the pairings produced by the ICP one. While 39.9% of the ICP-pairing are wrong in average, the average pairing error of the pure geometrical TP-ICC is of 28.6%. Therefore, by imposing to preserve the tree structure of the model along the pairings to the data, we were able to provide better correspondences. In Figure 8.4, we present the pairings at initial position of case 6 (see x-axis of Figure 8.3), which is a typical example of the great impact of the coherence constraint on the pairing error. Pairings induced by the ICP algorithm present "jumps" between different vessels, which also correspond to transitions from correct to wrong vessel portion pairing.

8.2.2 Resemblance between Curves is Crucial

By introducing a criterion on resemblance between curves ($\alpha < 1$) we are able to further decrease the pairing error on the same experiment (down to 22.5%). The good balance between the geometrical distance (computed by the Fréchet distance)

[4]The 2D bifurcation can be either manually or automatically identified.

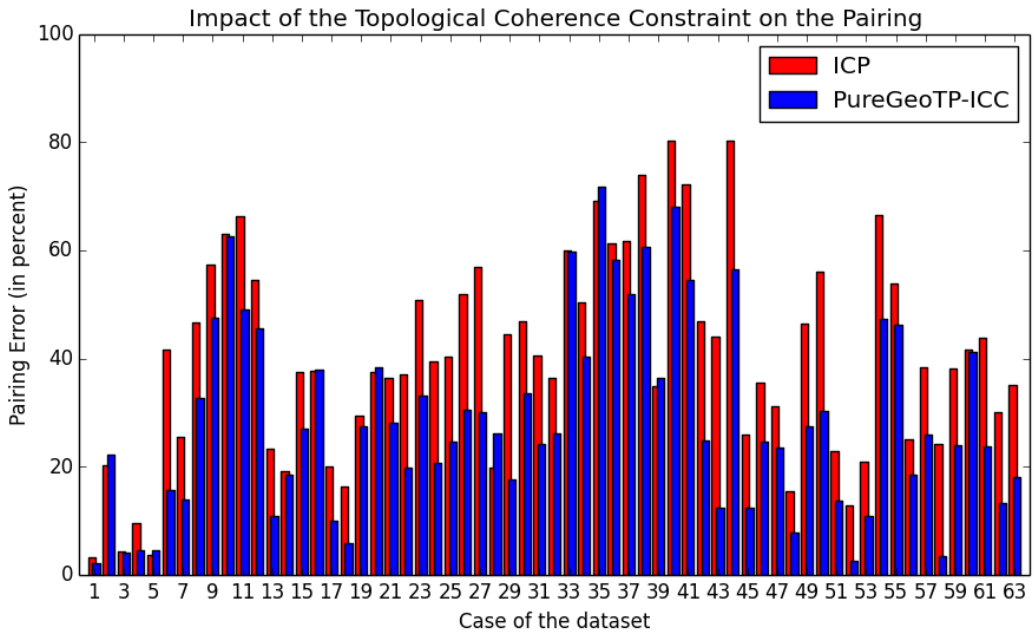

Figure 8.3: Comparison of the pairing built by the ICP and the pure geometrical TP-ICC algorithms at initial pose estimation. The pairing error for each algorithm is presented for each case of the dataset.

(a) ICP (b) Pure geometrical TP-ICC

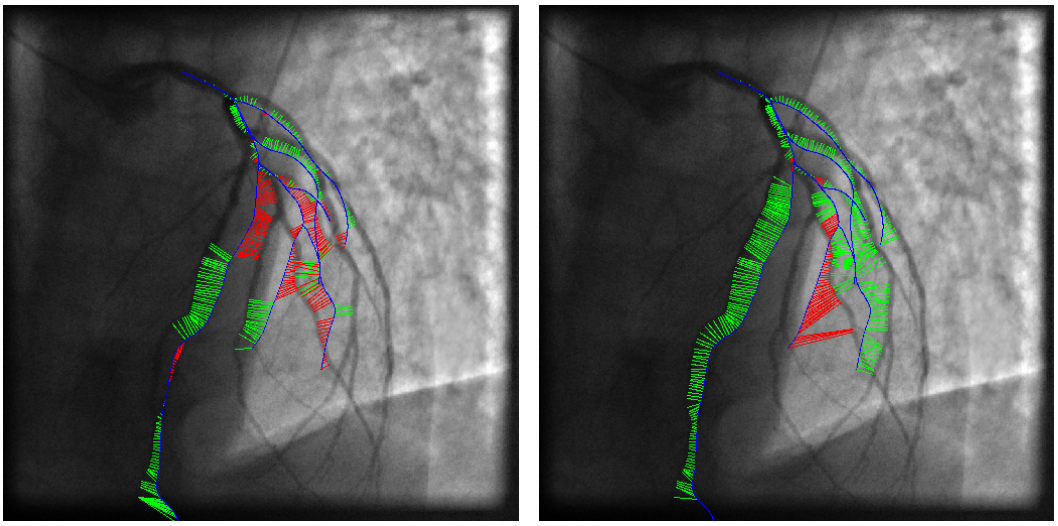

Figure 8.4: Example of pairings at the same initial position. These pairing sets correspond to the pairings made by the ICP algorithm (left) and the pure geometrical TP-ICC (right) at the first iteration. Correct pairings (green) and wrong pairings (red) are assessed based on the ground-truth using Equation (7.8)

and the shape distance (measured by the resemblance between curves) has been inferred by varying parameter α. For several values of α, we have run the pairing procedure at the same initial position as the previous experiment and evaluated the average pairing error for the whole database. Results are presented in Figure 8.5, showing that a good compromise exists around 0.25. One would note that the average pairing error above all cases in the dataset varies from 15% to 25%, which is a significant change.

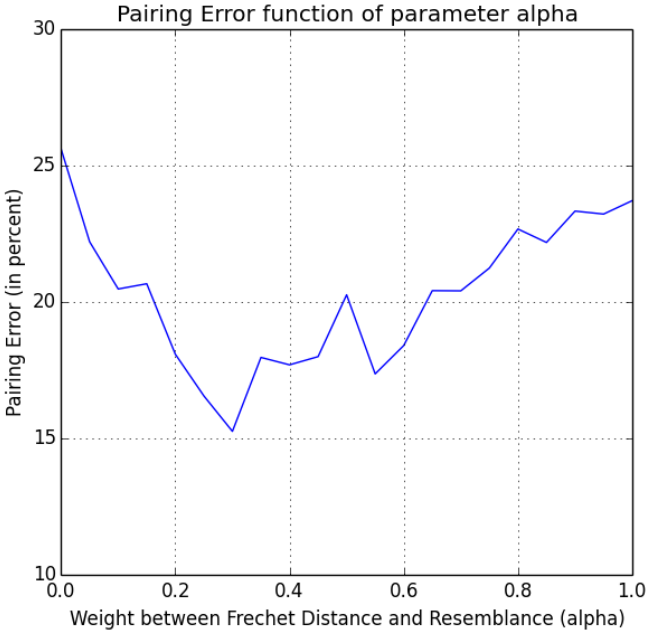

Figure 8.5: Evolution of the average pairing error (on the whole database) at calibration initial positions for different values of α. A balance around $\alpha = 0.25$ seems to be the best compromise between geometrical and shape distances.

By balancing the resemblance and the distance, we were able to retrieve correct pairings for a vessel in case 6 (see Figure 8.6) that was mispaired by the pure geometrical implementation (Figure 8.4b). The optimal value $\alpha = 0.25$ means that the best compromise over the whole database at initial position is obtained by giving 3 times more importance to the curve resemblance than their Fréchet distance. This is due to the fact that far from the registered solution the closest candidate is rarely the best and thus shape should be taken into account. One would note that only taking into account the curve resemblance ($\alpha = 0$) is worse than the optimal choice, which is in accordance with the intuition that a curve should be matched to a close and same shaped candidate.

Actually, this compromise between distance and shape is not only relevant far from registered pose. To prove it, we apply several perturbations to the registered position given by T_{Ref}. Each perturbation of the ground-truth pose will constitute

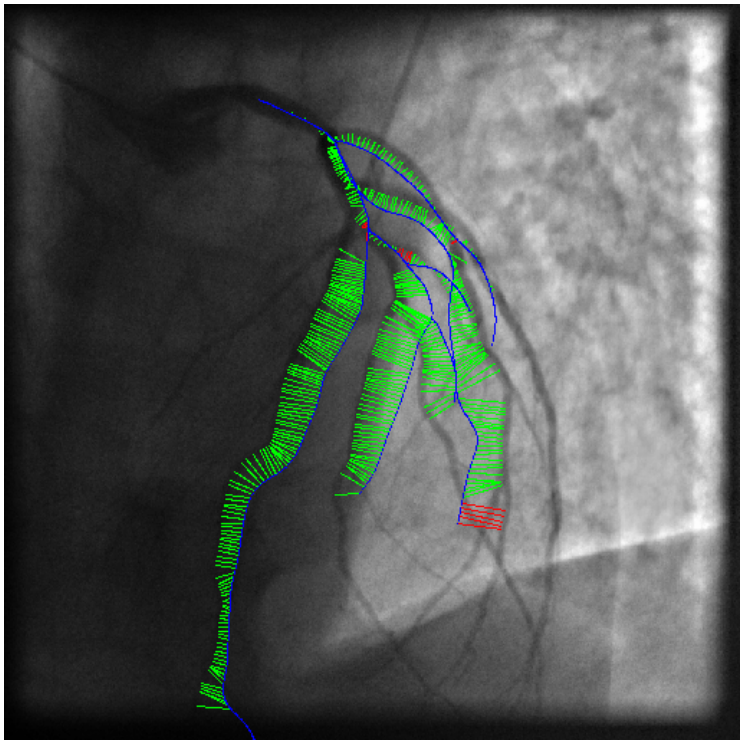

Figure 8.6: Pairings induced by the TP-ICC algorithm corresponding to the best compromise between geometrical and shape distance ($\alpha = 0.25$). This pairing set is obtained at the same initial position as in Figure 8.4.

an initial position for each case of the dataset from which we compute the point pairing set induced by the ICP and the TP-ICC algorithm. We generated 100 random rotations composed of uniform random axis and uniform angle distribution between 0 and 30 degrees, extending a little bit the study made on T_{Ref} in Section 8.1. Each perturbation was applied to the 63 cases from their respective ground-truth pose, leading to evaluate the pairing procedure of the ICP and the TP-ICC under 6300 registration conditions. Results on pairing errors are grouped regarding different ranges of perturbation and presented in Figure 8.7. No matter the range of perturbation, the TP-ICC provides better pairings at initial position than the ICP. In addition, our approach better behaves than the ICP algorithm as the rotation intensity increases.

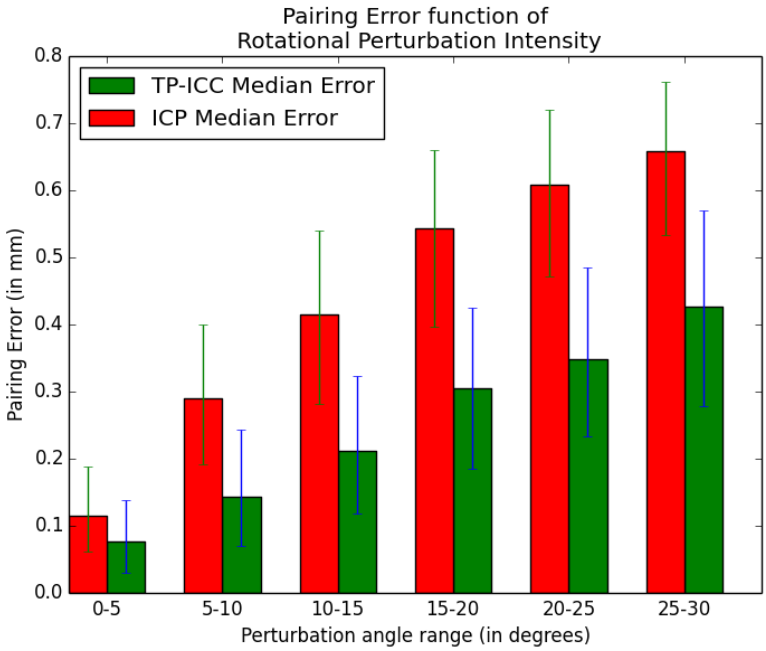

Figure 8.7: Evolution of the pairing error distribution at initial position function of the intensity of rotation to retrieve. The median value (bar) as well as the 75th percentile (top segment extremity) and the 25th percentile (botton segment extremity) is represented to compare the distribution of the error for the ICP (red) and the TP-ICC (green).

All previous experiments show that the proposed approach provides better correspondences than the one induced by the ICP algorithm. By imposing coherence along the tree and taking into account curve resemblance in a global way, the TP-ICC algorithm presents lower pairing error at initial position even for relatively big rotations (up to 30^o). Proving that the pairings induced by the TP-ICC are better than the ICP one, at the same position, is already an important result to stress. But these two algorithms are iterative and progressively refine pairings and opti-

mal transformation. Both the final transformation and pairing set should be now evaluated to prove the accuracy of our approach.

8.3 Accuracy Assessment

The previous section highlighted that the correspondences created by the TP-ICC are much more relevant than the closest point pairing induced by the ICP approach at various initial positions. Here, the initial pose was determined using the system parameters of the two imaging equipments and the 2D root position as it is depicted in Section 8.2. Starting from this position, defined for each case of the dataset, we launch the TP-ICC algorithm and measure the alignment error and pairing error associated to the resulting transformation $\hat{T}$ and pairing set $\hat{\pi}$ at convergence of the algorithm. These complementary error measures have been respectively defined in Sections 6.3.1 and 6.3.2. To provide a comparative basis, we ran the exactly same experiment with the ICP algorithm.

The alignment error and the pairing error distributions on the 63 cases are summarized by two box-plots comparisons in Figure 8.8. Box-plots allow to assess the error distribution of each algorithm without making much assumptions on their nature (Gaussian...). The median, the first quartile and the third quartile, all these indicators show that the TP-ICC has lower errors that the ICP approach. The lower pairing errors demonstrate that the pairings induced by the TP-ICC are not only better at the initial position but also at convergence of the iterative procedure. These more relevant pairings are an important factor to retrieve a more precise registration transformation, as shown by the alignment error that also decreases. By imposing coherence in the registration and using a global resemblance between curves, we were able to provide a more accurate registration algorithm both in terms of alignment and pairings.

The success rate found in this real condition experiment is provided in Table 8.1 for each of the previously described algorithm (ICP, pure geometrical TP-ICC and the TP-ICC). One will easily conclude from this table that the TP-ICC algorithm provides better results in terms of success than the ICP and the pure geometrical counterpart. If we define the success rate as the number of good and acceptable cases over the size of the dataset, the ICP algorithm presents a success rate of 68% and the TP-ICC is successful in 84% of the real conditions experiments. Failure cases and their reasons will be discussed in Section 8.5.

8.4 Robustness Study

In the previous section we have demonstrated the accuracy of the Tree-topology Preserving Iterative Closest Curve (TP-ICC) approach with respect to the Iterative Closest Point (ICP). The TP-ICC algorithm proved to have low alignment error and pairing error as well as an acceptable success rate on clinical data. Quantifying the accuracy is important, but to be used in a clinical environment a registration

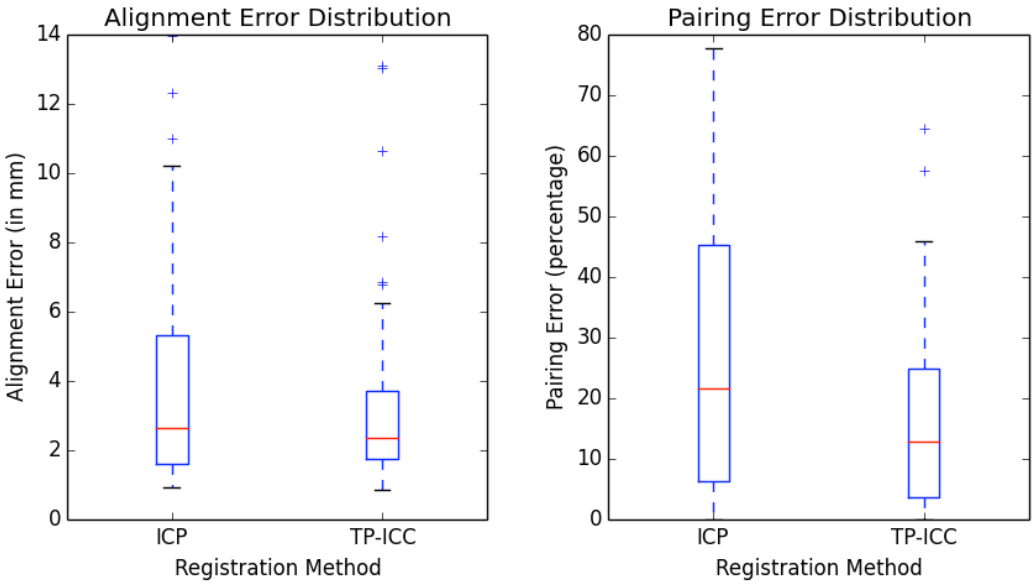

Figure 8.8: Error distributions at convergence of the ICP and the TP-ICC algorithm assessed by box-plot representation. Box-plots represent the median value (red) the first and third quartile (top and bottom blue rectange sides) and interquartile based outlier boundaries. The TP-ICC presents systematic lower indicators for the alignment error (left) and the pairing error (right).

Table 8.1: Results of different registration algorithms using the result classification provided in Section 7.4. The table contains the number of cases in each class for three algorithm run over the database of 63 cases in clinical initialization condition.

Registration method	**ICP**	**PureGeo TP-ICC**	**TP-ICC**
Good cases	31	29	36
Acceptable cases	12	19	17
Wrong cases	20	15	10

algorithm should also be robust. In order to measure the robustness, we apply random perturbations of the reference registration transformation T_{Ref} for each case. This reference transformation has been obtained automatically using the ground-truth of each case, as described in Section 8.1. Starting from this perturbed initial position we run the TP-ICC and the ICP algorithm to compare the robustness of a coherent and a non-coherent approach. Similarly to Section 8.3 we will compare the resulting alignment error, pairing error and success rate for both algorithms.

We explore the robustness with respect to the rotation around the reference position. By assuming that the main bifurcation has been identified in the image, one can assume that the translational part of the rigid transformation to retrieve is quite limited. Therefore we generate 150 different rotations (around the main bifurcation) distributed accordingly to the study on T_{Ref} provided in Section 8.1. This distribution of the rotational axis (uniform in space) and the rotational angle (uniform between 0 and 20^o) has been extended to the range $[0^o, 30^o]$ to study robustness on a full range of conditions. Each case of the dataset is registered starting from each of the 150 perturbed poses, which constitutes a set of 9450 registration results for each evaluated algorithm. The alignment error and the pairing error have been computed for each result and their distributions are presented in Figure 8.9.

For small rotation perturbations, lower than 10^o, the TP-ICC and the ICP perform quite similarly. As it has been highlighted in the literature, the ICP algorithm performs well if the starting pose estimate is close to the registered position. Under those conditions, the closest point assumption generally leads to correct pairings and thus results in a precise registration provided by the ICP approach. Since closest point pairing is justified in this case, it was not expected to see much difference with the TP-ICC algorithm that builds better pairing by imposing coherence. However, as the intensity of perturbation increases the difference between ICP and TP-ICC becomes more obvious. By imposing coherence along the registration and taking into account curve resemblance during the matching, the TP-ICC shows to be less sensitive to the increasing rotational perturbations than the ICP.

Showing a quantitative proofs of the robustness, in terms of alignment error and pairing error, between our approach and the ICP algorithm is an important result. But from a clinical point of view, it is more interesting to study how the increasing range of perturbation degrades the success rate. Using the previous definition of

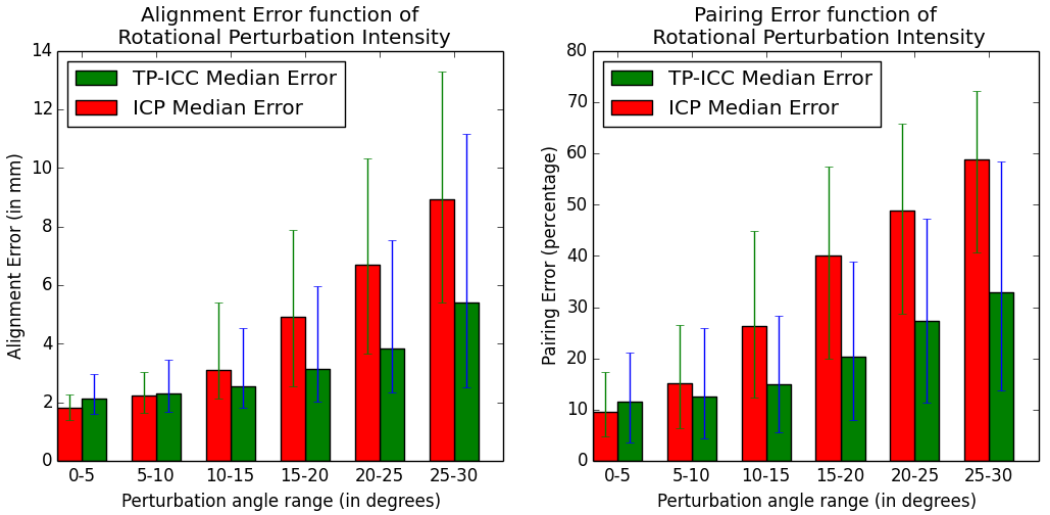

Figure 8.9: Robustness study regarding rotational perturbation. Distributions of the alignment error (left) and the pairing error (right) have been assessed for each range of perturbation using the median value (bar) and the 75^{th} percentile (top segment extremity) and the 25^{th} percentile (bottom segment extremity).

the success rate[5], we present in Figure 8.10 the evolution of the success rate with respect to the perturbation range. As it was expected, the success rate of the ICP algorithm decreases faster than the one of the TP-ICC. For rotational perturbations of more than 10^o, the TP-ICC performs significantly better than the ICP approach. By taking the example of rotations to compensate between 10^o and 15^o, the success rate associated to the ICP algorithm is about 66% while the TP-ICC reaches 82%. This particular range is important since it corresponds to most often observed range of perturbations on the Clinical expectations of the users in this field are above 80% if they can correct the failed cases and above 90% if not.

For small angular perturbations, the ICP seems to perform slightly better than the TP-ICC. This behavior is more deeply explained in Section 8.5. From now, we proved that the TP-ICC approach is nicely robust to the rotational displacement expected in clinical routine. This study on the rotational part of the rigid transformation was justified by the alignment of the main-bifurcation, which gives a coarse translation initialization. We investigate how the results depends on uncertainty in location of the main bifurcation.

Starting from the reference position (given by T_{Ref}) for each case, 50 random in-plane translations have been applied to the volume (leading to $63 \times 50 = 3150$ results for the success rate computation). The intensity of the perturbation (i.e. the norm of the in-plane translation vector) is uniformly distributed between 0 and $30mm$. It is intended to represent an imprecise identification of the main bifurcation, which generates an error on the initial alignment of the 3D volume

[5]Number of good and acceptable cases over the total number of registration cases.

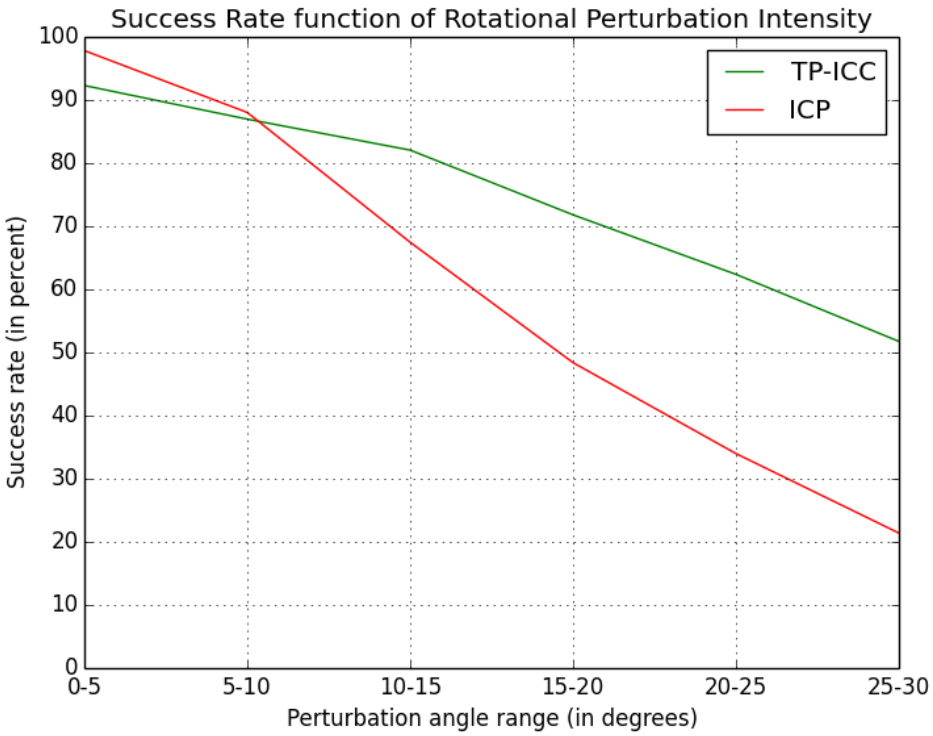

Figure 8.10: Evolution of the success rate with respect to the increasing range of rotational perturbations.

with respect to the image plane. We run two different experiments on the main bifurcation initialization. The pairing procedure of the TP-ICC approach assumes that the 3D main bifurcation is projected close to its corresponding one and thus explicitly depends on the in-plane translation initialization. First, we wanted to show that this type of initialization was not only necessary to the TP-ICC algorithm but also for the ICP one. In Figure 8.11a, we highlight that a large error on the 2D main bifurcation identification has disastrous impact on the success rate. Both the ICP and the TP-ICC algorithms are impacted a lot by large translations (more than $10mm$) showing that a coarse initialization in translation is mandatory to a successful registration.

(a) Extended study

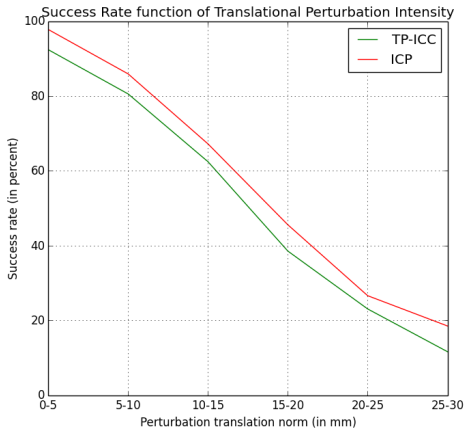

(b) Pragmatic study

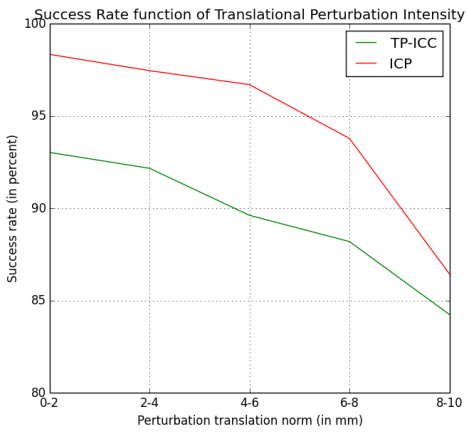

Figure 8.11: Robustness study regarding the location of the 2D main bifurcation. A study on large perturbation in translation is provided in (a) as well as a more realistic range of perturbation in (b).

While an error in translation up to $30mm$ could occur without initialization, one cannot expect it from the clinical user or a successful automatic initialization algorithm. In fact, $30mm$ in the image plane corresponds to approximately one fifth of the fluoroscopic image size. A more realistic upper bound for this main bifurcation identification error would be less than $10mm$. We thus propose to run the exactly same experiment on translational robustness but on the range $[0, 10]$ with 100 uniformly distributed in-plane translations (leading to $63 \times 100 = 6300$ experiments). Results are presented in Figure 8.11b. One would note that under this limited range of perturbations, the success rate of both algorithms decreases slowly and always stay above 80%.

The TP-ICC seems more impacted by this translational uncertainty compared to the ICP algorithm. This behavior is probably due to the assumption that the 3D main bifurcation pairing with its closest point in the 2D structure plays a key role in the first steps. Since all connectivity constraints imposed during the tree pairing

procedure start with the main bifurcation pairing, a mismatch may impact a lot the resulting pairings. In the example of Figure 8.12, noisy detected centerlines close to the root are not connected to the connected component in the graph that contains the vasculature. If the closest point to the 3D main bifurcation projection belongs to this centerline, the connectivity constraint will impose all edges in the tree to be matched to this isolated noisy part. It could result eventually into a failure of the algorithm[6].

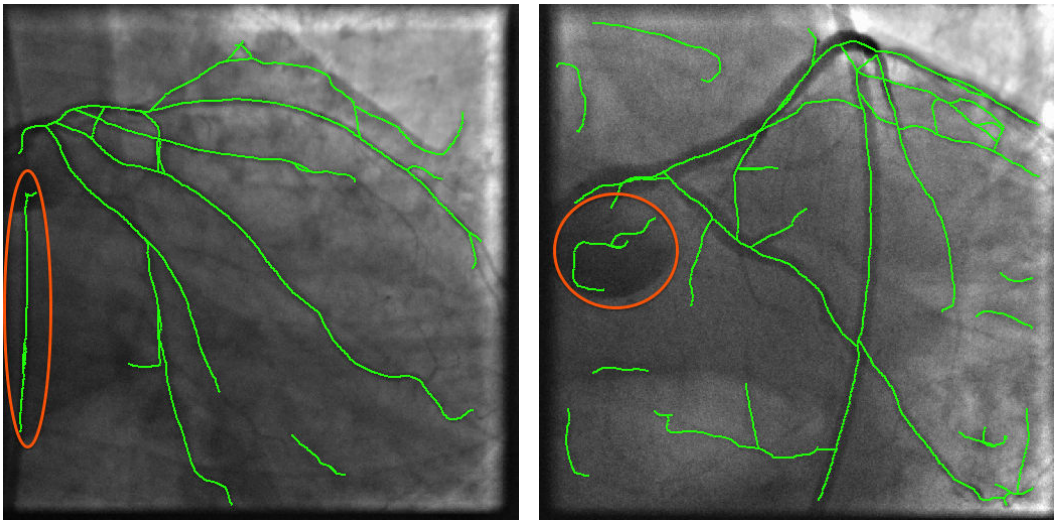

Figure 8.12: Two automatically segmented images presenting noisy detections (circled in orange) close to the main bifurcation.

8.5 Discussion

In this chapter, we have shown that by imposing coherence to the pairing set along the registration we were able to provide a more accurate and robust algorithm. We also highlighted the importance of considering the shape information during the matching in order to build better pairings. Success rate dependency regarding the main bifurcation initialization has been studied. We have concluded that if a coarse estimate of the translation is provided then our approach is robust enough to be used in clinical practice. In the light of these results, several questions raise.

First, how does our algorithm perform with respect to the closest state of the art algorithms. In [Baka et al., 2014] and [Rivest-Henault et al., 2012], the evaluation of their approaches was performed respectively on 12 and 5 clinical cases and claimed a success rate around 80% (81% for [Baka et al., 2014] and 1 patient over 5 remains with a high registration error no matter the optimizer used in [Rivest-Henault et al.,

[6]This issue could be addressed in further implementations by trying various possible pairings of the main bifurcation and evaluate them one by one. This evaluation can be performed without running the registration procedure (e.g. by computing the tree pairing and its score and choosing the best) or a posteriori by choosing the registered position according to some registration score.

2012]). So, our TP-ICC algorithm demonstrates a comparable success-rate of 84% but on a more representative database of 64 cases. Regarding accuracy of the registration, we highlighted in chapter 7.1 the lack of relevant registration error measure quantifying correctly the clinical expectations in case of percutaneous coronary interventions applications. We thus developed two error measures that showed a good correlation with respect to visual assessment of the registration quality. Thus, comparing directly the resulting registration error is complex, especially because [Baka et al., 2014] and [Rivest-Henault et al., 2012] involve non-rigid registration. Finally, a complete comparison between algorithms should also take into account computational time. The time of processing depends directly on the complexity of the extracted features. While our vessel extraction technique in the 2D projective image is fully automated, articles of [Baka et al., 2014] and [Rivest-Henault et al., 2012] involves manual segmentation, resulting into much less noise in the data-structure. Here again we can only claim that our approach has the same order of magnitude as the state of the art approaches (about three minute for the entire processing).

Second, one could have noticed several outliers highlighted by the box-plot representation from the accuracy study presented in Figure 8.8. Let us have a closer look to the alignment error and pairing error for each case of the dataset at the registered position. Results are presented in Figure 8.13 at convergence of the ICP and TP-ICC algorithm, both initialized at the same position. Besides cases showing good results for both algorithms, the TP-ICC algorithm outperforms the ICP approach in a significant number of cases for both the alignment error and pairing error. A typical example is provided in Figure 8.14, where one can see the great impact of pairing coherence in the registration. When the starting position is quite far from the registered one, the TP-ICC is able to recover the correct registration pose by imposing coherence to the pairings. On the contrary, the multiple pairing jumps along vessels created by the closest point assumption mislead the ICP registration.

However in few cases (27, 54 and 59) the ICP seems significantly better than our approach. All these cases have in common to present one long missing vessel in the 2D graph due to a total occlusion. An example is given in Figure 8.15. In this case, multiple incoherent pairings created by the ICP pairing procedure compensate themselves in the computation of the optimal transformation. However, by ensuring the connectivity constraint in the pairing procedure, the TP-ICC algorithm creates wrong (but topologically coherent) pairings that mislead the registration. This type of problem induced by differences between modalities is well known in the registration community. It is often addressed as an outlier detection problem and will be discussed in the upcoming Section 9.3.2.

Another question that has been raised in the previous section is about the behavior of the TP-ICC with respect to ICP for small angle perturbation. Under these conditions, the ICP and TP-ICC algorithms are successful in the majority of the cases since the initial pose is quite close to the registered one. Thus, such differences impact correctly registered cases in a range hardly noticeable by the user. An example is given in Figure 8.16. The small change between registration results comes from different pairings relative to a single vessel branch. While the closest

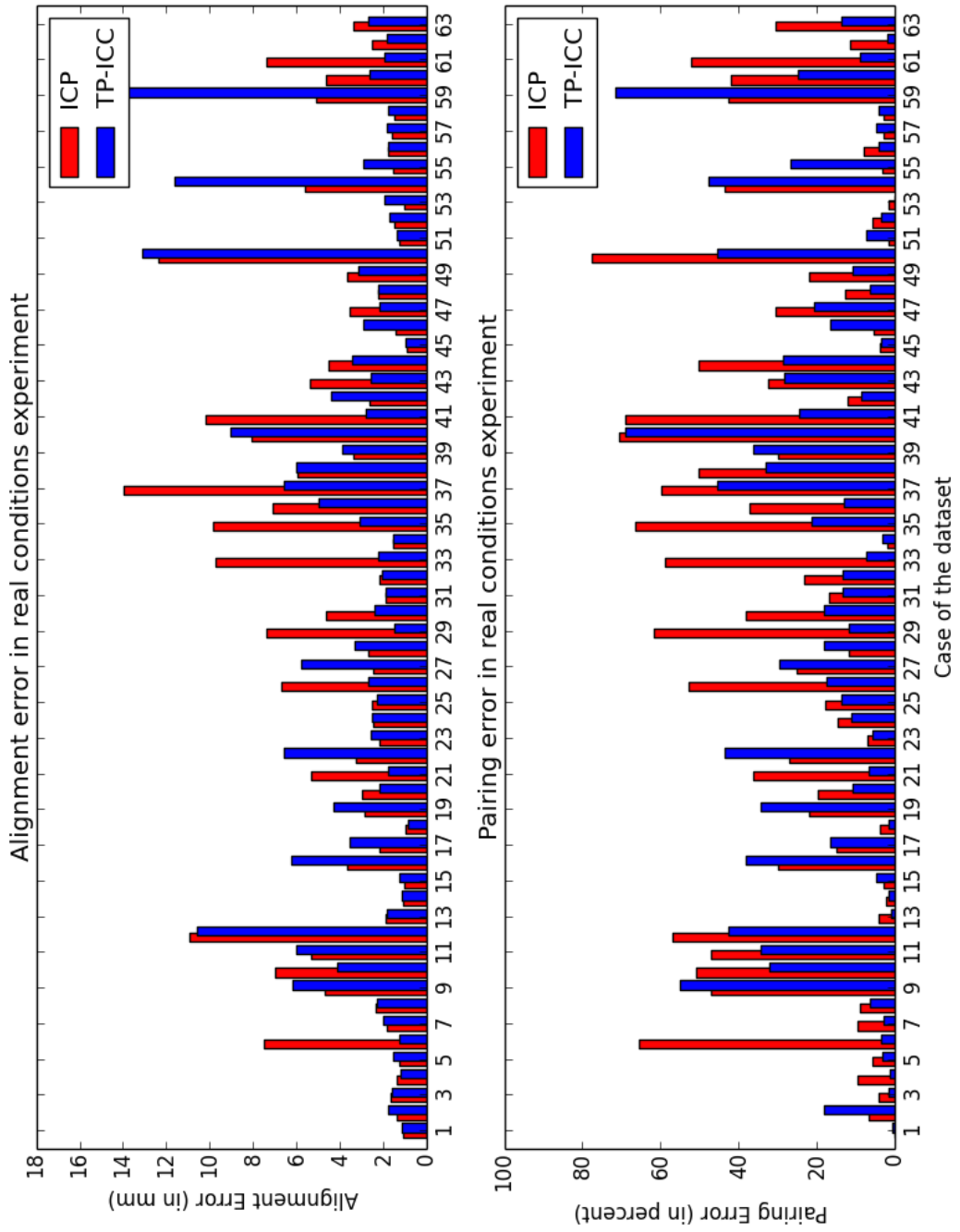

Figure 8.13: Errors on each case of the dataset under clinical condition registration. Figure is presented in landscape mode, showing the alignment error (top) and the pairing error (bottom) at convergence of the ICP (red) and TP-ICC (blue) algorithm.

(a) Detected 2D graph

(b) Initial 3D tree projection

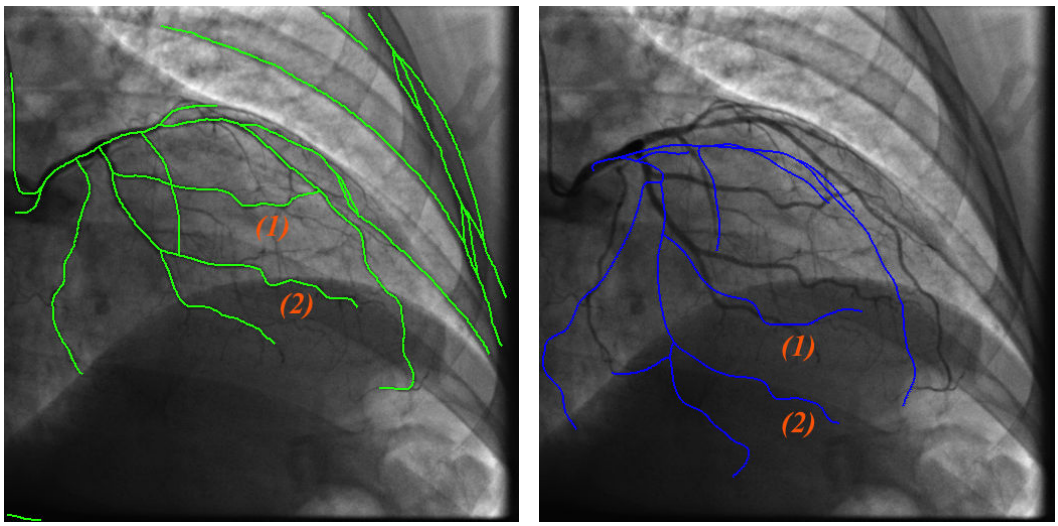

(c) ICP registration

(d) TP-ICC registration

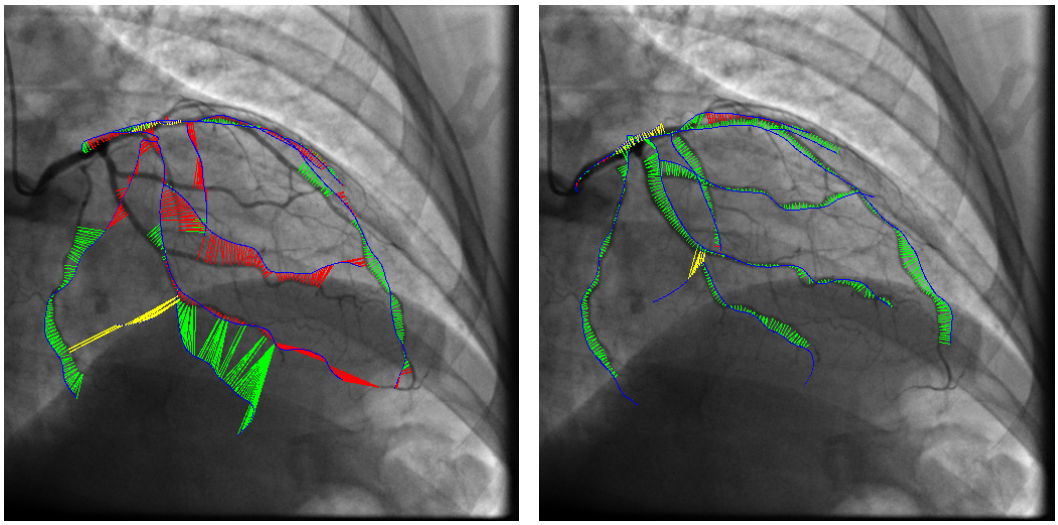

Figure 8.14: Case of the dataset in which TP-ICC outperforms the ICP algorithm. (a) is the automatic segmentation (in green). (a) present the 3D tree centerline projection (blue) at the initial pose estimate. To help understanding this difficult case, we annotated two corresponding vessels (1 and 2) in (a) and (a). Registration results of the ICP (c) and the TP-ICC (d) contain the projection of the registered 3D centerlines (thin blue line) and the resulting pairings evaluated as correct (green), wrong (red) or occluded (yellow).

(a) Detected 2D graph

(b) Initial 3D tree projection

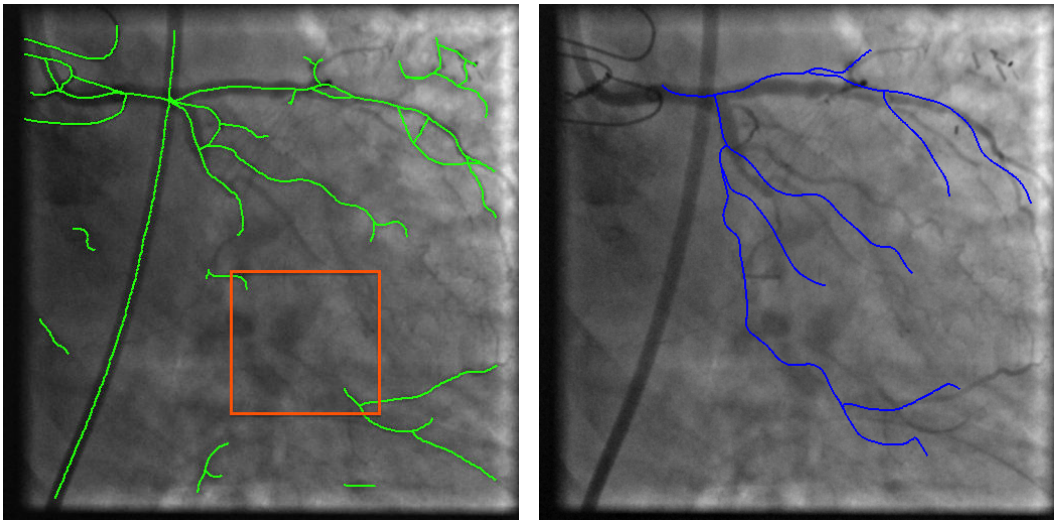

(c) ICP registration

(d) TP-ICC registration

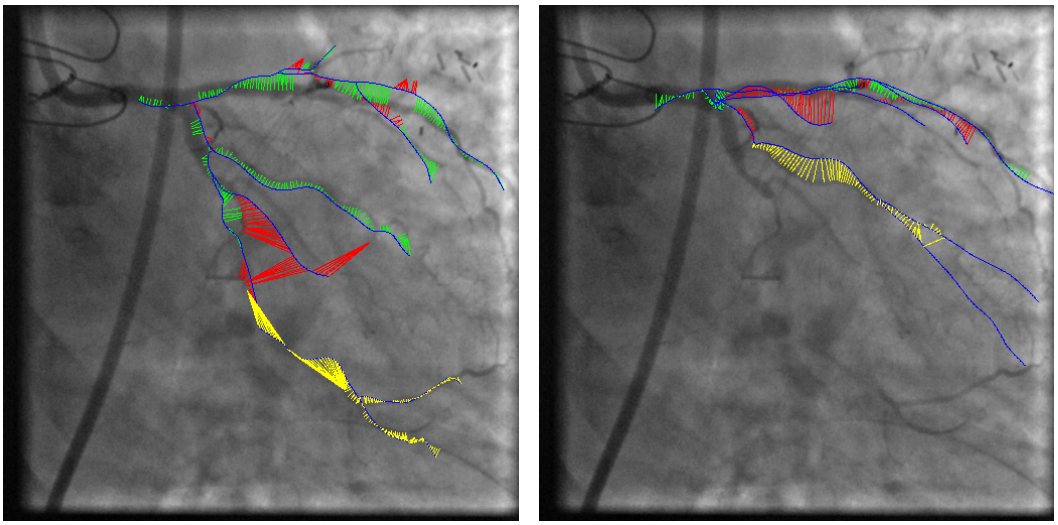

Figure 8.15: Case of the dataset that is better registered by the ICP than the TP-ICC algorithm. (a) is the automatic segmentation (in green) and the non-visible occluded vessel portion (inside the orange square). (b) present the 3D tree centerline projection (blue) at the initial pose estimate. Registration results of the ICP (c) and the TP-ICC (d) contain the projection of the registered 3D centerlines (thin blue line) and the resulting pairings evaluated as correct (green), wrong (red) or occluded (yellow).

point pairings created by the ICP algorithm are correct, the topologically coherent pairings of the TP-ICC algorithm are wrong. To investigate the reason of this mispairing, let us take a look at the corresponding 2D graph of Figure 8.17. This data graph has been automatically extracted from the fluorosopic image using the procedure depicted in Section 4.2. One would note that the corresponding 2D vessel branch of interest has not been connected correctly during the graph extraction. Because of this connexion error, the tree-topology preserving pairing procedure will not consider the 2D correct vessel as a potential candidate since it does not satisfies the connectivity constraint.

(a) ICP registration (b) TP-ICC registration

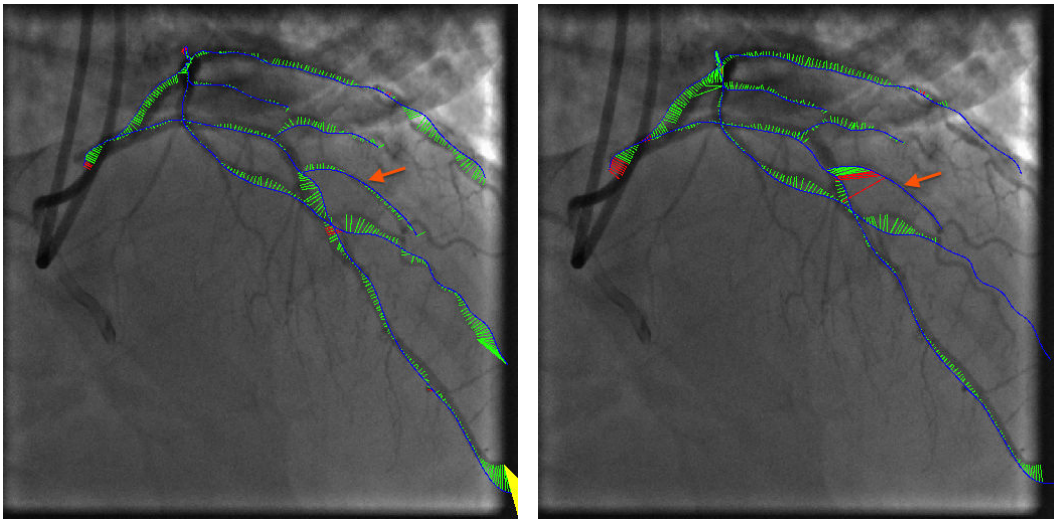

Figure 8.16: Registered pose corresponding to a small rotational perturbation where the ICP algorithm (a) performs slightly better than the TP-ICC (b). The main difference is relative to the pairing of the vessel pointed by the orange arrow.

This problem could be solved in an outlier rejection approach, by detecting mispairings and excluding them from the transformation optimization step. A more promising approach inspired from [Groher et al., 2007] can be introduced to improve the quality of the 2D segmentation. In their article, [Groher et al., 2007] proposed to use the current estimation of the registration pose in the segmentation procedure. The vessel enhancement filter (as the one described in Section 4.2.1) is enriched by the distance map of the 3D projected centerlines. Close to the registration pose, the closer a pixel is to the model tree projection, the more likely it belongs to a 2D vessel. By this mean, one is able to limit fake detection far from the projected model structure and segment less visible vessel close to the vasculature of interest.

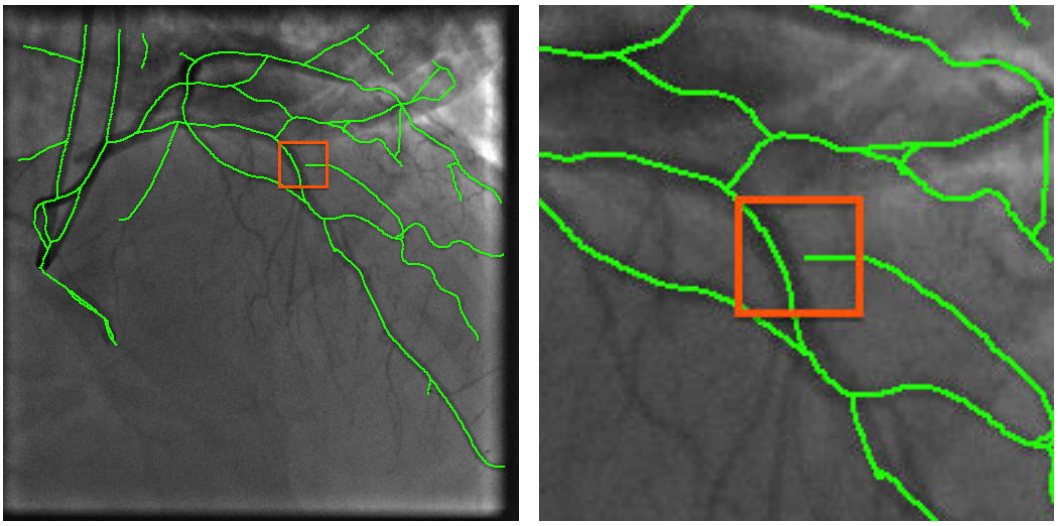

Figure 8.17: Vascular graph corresponding to the case of Figure 8.16. A connexion problem is highlighted inside the orange square in the entire image (left) and the zoomed part (right).

Chapter 9

Conclusion

Contents

9.1 Main Achievement

The main goal of this thesis was to address the problem of 3D/2D registration of the coronary arteries. On the one side, the live X-ray projective images provided by the interventional system are used to navigate dedicated tools inside the patient's vasculature. On the other side, the pre-operative Computed Tomography Angiography (CTA) highlights potential calcium deposits along the artery walls and the occluded channel in case of total occlusion. Both types of information are of interest to the clinician during the Percutaneous Coronary Intervention (PCI), but not visible in the live X-ray images. Bringing these two complementary modalities into correspondences can enrich the amount of information available during the clinical procedure. This necessitates a registration procedure that provides precise alignment and relevant pairings between the two vascular structures.

We have proposed an approach focused on building relevant correspondences between the vessel centerlines extracted from a 3D volume and a 2D image. To do so, we have designed a registration algorithm preserving the topology of the vasculature. By matching entire curves instead of points, the proposed Iterative Closest Curve (ICC) framework ensures the curvilinear structure preservation along the iterations. To take into account the particular topology of the vasculature, in which centerlines are connected with each other at bifurcation points, a tree-topology preserving pairing procedure has been developed. Centerline branches of the 3D tree are matched to curves extracted from the 2D image, while ensuring connectivity preservation at bifurcations. The resulting Tree-topology Preserving ICC (TP-ICC)

algorithm alternates the two following steps: 1) building a tree pairing; 2) finding the transformation minimizing the distance between paired curves.

The TP-ICC algorithm has been evaluated on a database of 63 cases collected after standard of care clinical procedures. A success rate of 84% has been obtained on this database under the expected clinical conditions. The registration success is judged based on two criteria: the projection of the 3D vasculature is close to its corresponding structure in the image; and the majority of the resulting pairings are correct. The proposed method also exhibits good results in term of robustness regarding the rotations to be compensated (up to 30^o). This high success rate demonstrates low sensitivity to an increasing range of initial pose angular perturbations. The TP-ICC also shows a low resulting pairing error that opens the way to a new step of performance assessment: the evaluation of the algorithm during live clinical procedure (under the form of a clinical study). Integration of this algorithm in the clinical workflow is still under discussion as well as the best way to fuse the two modalities (see Section 2.4.1). Several ways of improvements and extensions of the algorithm are discussed in 9.3.

9.2 Contributions

In this section we list some of the contributions of this Ph.D.

Iterative Closest Curve Framework Because of its general formulation and its high potential of re-usability, the ICC-framework may be the greatest contribution of this Ph.D. Yet, the ICC principle defined in Chapter 5 is based on a very simple idea: extend the well known Iterative Closest Point (ICP) algorithm to curves. It is composed of two steps that are iterated until convergence: construct pairings between curves extracted from both structures and find the transformation minimizing distance between paired curves. An example of pairing procedure is described, based on our 3D/2D application, and has been chosen to be as intuitive and as applicable as possible. The distance between curves is evaluated using the Fréchet distance, which relies on a point pairing set between curves preserving order along each of them. The sum of the Fréchet distance is optimized regarding a set of admissible transformations (rigid in our application). We have decided to take advantage of the underlying pairings induced by the Fréchet distance to determine the optimal transformation at a given curve pairing set. The transformation optimization step consists itself in an alternating optimization procedure, which is comparable to an "ICP-like" procedure where the closest point pairing procedure has been replaced by the Fréchet pairings built for each curve pairing.

Tree Pairing Procedure The challenge addressed in Chapter 6 is to obtain a one-to-one pairing procedure preserving the tree-topology of the vasculature while vessel superimpositions and few anatomical bifurcations in the 3D tree (down to 2 or 3) limits the use of approaches based on bifurcation matching. We have developed

a top down approach that pairs centerline edges of the tree. Starting from the root and progressively descending the tree, a connectivity constraint is imposed at every bifurcation nodes to preserve the tree-topology. Finding the best tree pairing is then addressed as an optimization of a dedicated tree pairing score. This score mixes geometrical distance and shape resemblance between paired curves composing the tree pairing, both criteria preserving the point order along curves. To quantify the resemblance between curves, we avoided computing local descriptors such as the tangent or the local curvature that are not well defined in highly foreshortened vessel portions. We have introduced a resemblance measure based on an intuitive idea: two curves look the same if one is able to align them with small error. The optimization of the resulting tree pairing score is performed by a divide-and-conquer algorithm. This type of algorithm is based on a property of the problem called optimal substructure, which has been demonstrated in Chapter 6. The computational explosion that would be induced by a naive test of all possible tree preserving pairings is avoided. Moreover, the resulting pairing procedure can be easily introduced into the ICC framework since a tree pairing is nothing but a set of curve pairings preserving the connectivity constraint at each bifurcation of the tree.

Registration error measures To evaluate this algorithm (called Tree-topology Preserving ICC or TP-ICC) and any other registration procedure, we created two error measures quantifying the quality of the two major outputs of a registration algorithm. The first one is the alignment error. It has already been addressed in the literature, but without distinguishing vessels close to the overall structure or close to their correct correspondent. Besides the alignment provided by the resulting registration transformation, another output is crucial to provide a roadmap application: the pairings between the two modalities. To the best of our knowledge, none of the articles about 3D/2D vessel registration has proposed a solution to evaluate the quality of the resulting pairings. We developed two complementary measures in Chapter 7, based on a single manually defined ground-truth, which does not impact the clinical procedure. The joint use of the alignment error and the pairing error has demonstrated good correlation with visual assessment of the registration quality performed by a trained observer.

9.3 Perspectives

In the course of our work, we have developed a registration approach that has been evaluated on numerous cases. Besides the encouraging results provided in Chapter 8, we identified additional possibilities of improvement applicable to our algorithm. They could lead to increase the level of automation, the robustness and the accuracy. We have also several examples of applicability of our method to other clinical fields. We have thought that describing in few lines these potential ideas could be important for futur investigators motivated by continuing our work. Given that only preliminary implementations of these ideas have been done, we will only show simple illustration of these results.

9.3.1 Automatic Initialization

Until now, it has been assumed that the main bifurcation is manually identified by the user in the 2D image. Since the main bifurcation is well defined in the 3D pre-operative structure, a single click interaction gives a coarse in-plane translation initialization to the registration algorithm. The out-plane translation is estimated by the Source-Object-Distance (SOD) and the initial rotation alignment is given by calibration of the system. We have seen in Chapter 8 that this type of initialization allows the TP-ICC algorithm to be accurate and robust under clinical conditions. This same chapter also gave us a range of accuracy expected in the localization of the 2D main bifurcation in order to maintain an acceptable success rate. Going one step further, this manual initialization could be replaced entirely by an algorithmic approach. Several proposals are described in the following.

First, one can identify the extremity of the catheter injecting the contrast medium in the arteries. In angioplasty procedure, the injection catheter is inserted at the entry of the main branch of the coronary tree, called the ostium, and its extremity should always be visible in the fluoroscopic image[1]. Usually, the main branch of the coronary tree (between the aorta and the main bifurcation) is quite short and thus the extremity of the catheter should be close to the main bifurcation. Since it is usually full of contrast product, the catheter can be easily identifiable, especially during non-injected phases. Figure 9.1 shows two frames of the same sequence taken before the injection and during the injection.

Several methods can be used to segment the catheter using a priori knowledge on this structure: dark contrasted object, curvilinear structure, approximately known diameter, touches one of the image borders... Since most of these characteristics are common to the vasculature (when contrast product is injected), it seems preferable to identify the catheter in the non injected phase. Automatically segmenting the catheter is still a challenge of its own, as highlighted in [Hernández-Vela et al., 2012], since multiple anatomical structures can present a similar look in the X-ray images. Moreover, identifying the extremity of the catheter may be tricky even from a correct segmentation.

[1] Both assumptions correspond to clinical recommendations for safety.

(a) Before injection (b) During injection

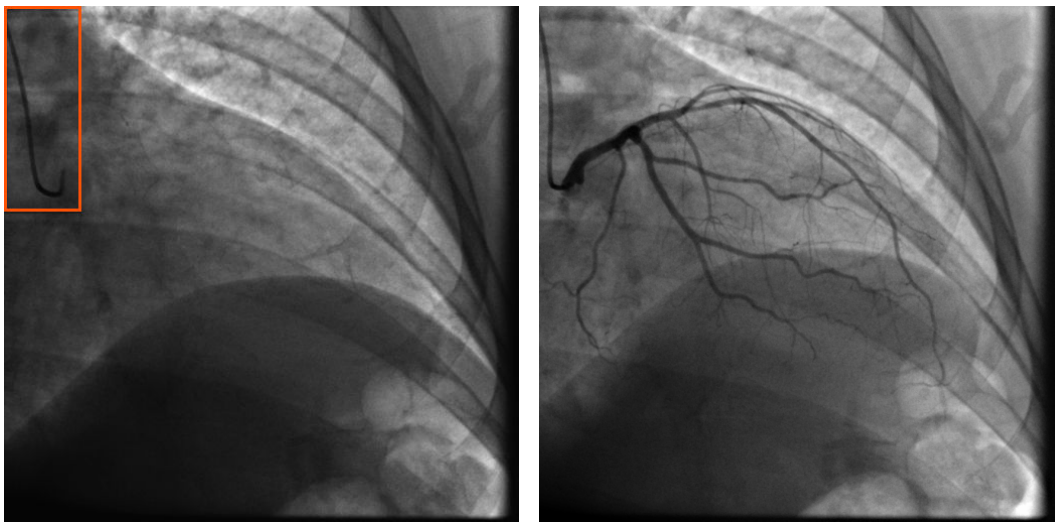

Figure 9.1: Two frames extracted from the same recorded injection. (a) highlights the injection catheter inside the orange rectangle before the beginning of the injection; (b) frame taken during the injection that corresponds to a case of the registration database.

Another ideas could be to identify the location of the proximal vasculature using the progressive propagation of the contrast medium. In Figure 9.2, we show different time-positions during the injection phase. If one is able to segment visible vessels in the phase t_1 (Figure 9.2a) then one can estimate quite precisely the main bifurcation position in the image. Similarly to the maximum of injection that can be obtained automatically (as discussed in Section 2.4.2), several methods can be used to isolate an early state of the injection phase. The segmentation of this image can be done by the Hessian based technique described in Section 4.2, but particular attention should be paid to limit fake detections.

The two previous propositions identify the main bifurcation in a frame that is not the one used to run the registration. Therefore a significant difference in position can occur due to the beating heart or a respiratory motion movement. We believe that an automatic initialization using only the graph structure extracted from the most injected image is the most promising solution. An exhaustive search can be run by trying all possible alignments between the 3D main bifurcation and each node of the 2D graph. Each pair gives a potential initial pose estimate. Each pose can be evaluated by a dedicated score such as the objective function optimized by the ICP or the ICC (detailed in Section 5.1.4). The initial pose can be selected a priori by choosing the main bifurcation pairing corresponding to the best score.

(a) Early phase t_1

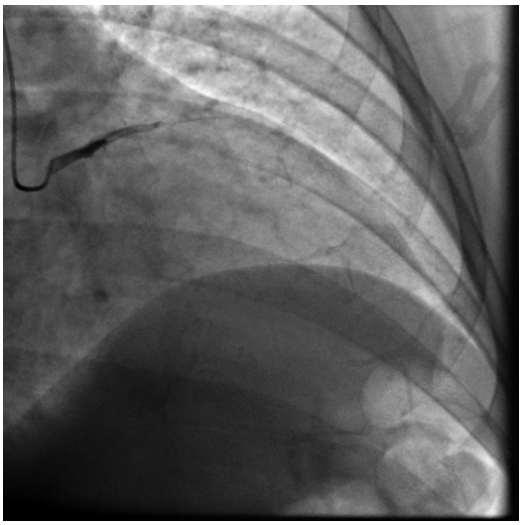

(b) Early phase t_2

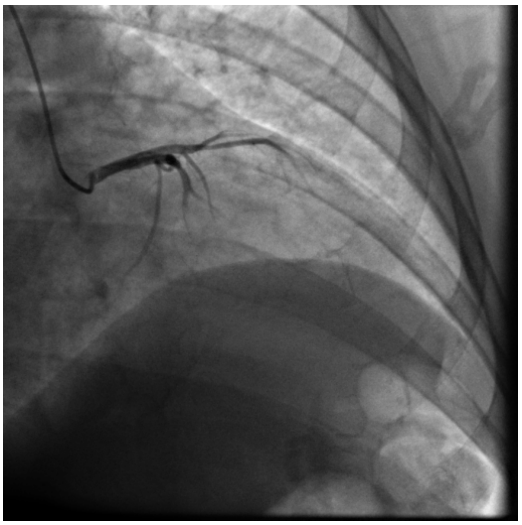

(c) Early phase t_3

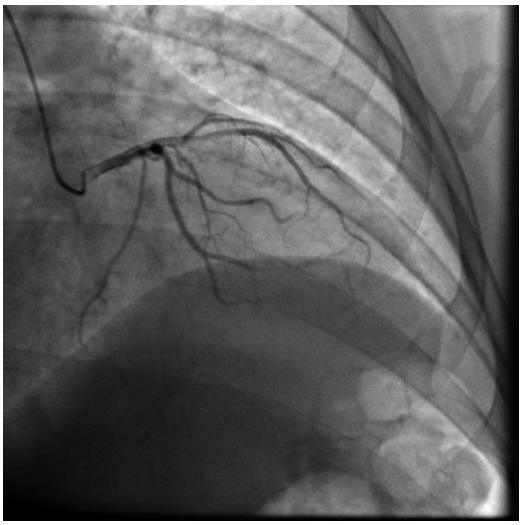

(d) Maximum phase t_M

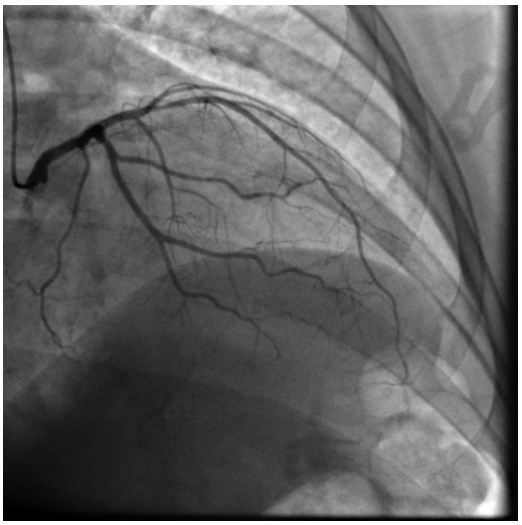

Figure 9.2: Frames of the same injected sequence taken at consecutive times ($t_1 < t_2 < t_3 < t_M$). The coronary tree is progressively filled of contrast medium and thus becomes progressively visible from the proximal part to the distal part in the X-ray image.

9.3.2 Outlier Rejection

One common difficulty in the registration topic is the impossibility to obtain a complete matching between the two datasets. This non-complete overlap in the anatomy can be due to the field of view, elements that are visible in one modality and not the other, and so on and so forth. So, it is very common that the two sets of features extracted from each modality are only partially overlapping. Therefore, matching the entire segmented vasculature necessarily leads to consider wrong pairings, which can mislead the registration. In order to robustify registration regarding such differences, it is often considered to reject some pairings before the transformation computation phase. Identifying automatically wrong pairings is addressed in the literature by outlier detection techniques, which refers to the statistical domain. Actually, registration can be seen as a data fitting problem as it is presented in [Tam et al., 2013] in an original way.

In the case of 3D/2D coronary arteries registration, multiple differences have been highlighted in Section 2.4 and Section 4.3. First, the automatic segmentation of the 2D image leads to multiple fake detections while the 3D pre-operative modality is corrected by the user. In order to limit the number of pairings relative to fake detections, we chose a model-to-data approach that matches points in the 3D model to points in the 2D data and not the other way round. Doing so, we limit the number of wrong pairings since points in the data are not obligatory paired, contrary to symmetrical approaches. Besides noise, these techniques also deal with differences at distal part of the vasculature. In fact, the intra-arterial injection used to obtain the 2D image allows to distinguish longer distal parts than in the pre-operative CTA scan, where the injection is done intra-venously. Such a difference in iodine injection generally leads to a deeper segmentation of the vasculature in 2D than in 3D and thus also constitutes a potential source of mispairing.

The previous paragraph highlighted that several parts of the data graph may not be present in the model tree. On the contrary, parts of the 3D segmented volume may not have been detected in the image. In case of occlusion in a coronary vessel, an entire portion of the segmented vascular tree is not visible in the 2D fluroscopic image, while the diffused contrast product and the calcifications reveal its presence in the CTA volume. A 3D vessel portion may also be outside the field of view imaged by the C-arm system and thus non-present in the data graph. To deal with these known differences between modalities and solve potential problems of mispairing, a step of outlier detection and rejection is often implemented. Since the Iterative Closest Curve (ICC) framework extends the Iterative Closest Point (ICP) principle to the level of curves, let us first depict outlier robust implementation of the ICP algorithm.

In [Rusinkiewicz and Levoy, 2001] are depicted several variants of the ICP algorithm, including approaches involving the rejection of pairings. In the original ICP algorithm, introduced in [Besl and McKay, 1992], pairings are made in the first step (see Section 5.1.2) using the closest point assumption. To each pairing is associated the distance between paired points that is called the residual error. The

distribution of the residual error is often analyzed to detect wrong pairings that are seen as statistical outliers. Different strategies are described in [Rusinkiewicz and Levoy, 2001] that involve:

- Cut the distribution at a maximum value defined a priori. It corresponds to reject pairings involving points too distant from each other that usually corresponds to "obvious" outliers.
- Reject the $n\%$ of pairings corresponding to the highest values in the Euclidean distance distribution. Here, a percentage of outlier is expected from the user that corresponds to the ratio of pairings expected to be wrong.
- The residual error is assumed to be Gaussian distributed and observations that do not respect this assumption are rejected. Average μ and standard deviation σ are computed from the pairings and only observations lower than $\mu + k\sigma$, where k controls the rejection tolerance, are kept.

Usually this rejection procedure is introduced as an extra step in the ICP procedure (presented in Section 5.1.2): 1) closest point pairing, 2) pairing rejection, 3) compute the transformation minimizing the distance between non-rejected paired points, 4) return to step-1 until convergence. This algorithm is known as the Trimmed Iterative Closest Point and has been presented initially in [Chetverikov et al., 2002]. Many different outlier rejection techniques exist in the literature (see [Chandola et al., 2009]), such as clustering approaches, and the reader should pay particular attention to identify assumptions made by each of them.

Outlier rejection can be seen as a weight assignment to each pair: 0 if a pair of points is rejected and 1 if not. Instead of hard thresholding, a weighted version of the ICP algorithm is presented in [Rusinkiewicz and Levoy, 2001] that involves a weighting depending on the Euclidean distance between paired points. This soft-rejection gives less importance to pairings with high Euclidean distance in the transformation computation than pairs between points close to each other and thus less likely to be outliers. The transformation optimization step of the ICP algorithm (see second line of equation (5.14)) can be re-written with weights:

$$T_i = \underset{T \in \Omega}{\operatorname{argmin}} \sum_{(Y,x) \in \pi_i} w(Y,x) \cdot \left\| x - T(Y) \right\|^2 \tag{9.1}$$

where $w(Y,x)$ is the weight associated to the point pairing (Y,x). Similarly to the ICP framework where they are introduced, both approaches consider to deal with outlier at the level of point without taking into account the vascular nature of structures to be matched.

But fortunately, these outlier robust implementations can be extended to the ICC framework. We recall that the ICC-algorithm, depicted in Section 5.1.3, is composed of two steps: the pairing between curves and the transformation computation. The second step is itself composed of two steps that can be seen as the ICP procedure where the pairing set construction is given by the Fréchet distance

between paired curves. A step of outlier rejection can be introduced in the ICC framework similarly to the ICP: between the curve pairing step and the transformation optimization step. Instead of computing the Euclidean distance between points, one can run the analysis of outliers at the level of curves based on the Fréchet distance. Even if the standard deviation based approach remains possible, the number of curves extracted from a coronary tree is limited (between 5 and 15), which can be insufficient to infer the distribution. Therefore, removing "obvious" outliers by defining an upper threshold on the Fréchet distance or weighting each curve pairing seem more promising solutions. The weighted transformation optimization step, which can replace the second line of Equation (5.16), is defined by:

$$T_i = \underset{T \in \Omega}{\operatorname{argmin}} \sum_{(C,c) \in \Pi_i} w(C,c) \cdot \mathcal{F}\big(T(C), c\big) \tag{9.2}$$

where $w(C, c)$ is the weight of the curve pairing (C, c).

Curve pairing weights can be compared to a score, as it is defined in Section 6.3.1. Examples of possible weights are:

- The normalized Fréchet distance as it is defined in Equation (6.19). Here it is assumed that curves close to each other are less likely to be outlier.
- The curve resemblance, defined in Equation (6.20), that quantifies the similarity of curve shapes globally and not using local descriptors.
- The vessel foreshortening, which is mentionned in Equation (6.9) and quantifies the degree of alignment between a vessel and the projection axis. Highly foreshortened vessels are usually submitted to strong changes in shape even for small rotations (see Figure 9.3), which increases their probability of being mispaired.

Any possible combination of these three scores can be imagined as well as adding other criteria. The iterative procedure minimizing the curve-to-curve distance, which can be seen as an "ICP-like" algorithm, is modified to add the curve to curve weight.

This ICP-like procedure based on the Fréchet pairings can also be robustified by rejecting several point pairings created by the Fréchet distance. While the curve pairing outlier rejection aimed at removing mispairing due to entire missing curves, a point level rejection procedure can handle problem of local noise and misdetection. Both levels of rejection can be handled in the ICC framework summarized in end of Section 5.1.3 by:

- Adding a curve pairing (soft) rejection step between step-1 and step-2, which creates a set of weights $w(C, c)$ for each curve pairing (C, c).
- Adding a point pairing (soft) rejection step between step-2a and step-2b, which created a set of weights $w(Y, x)$ for each point pairing (Y, x).

(a) Native image (b) Reference pose

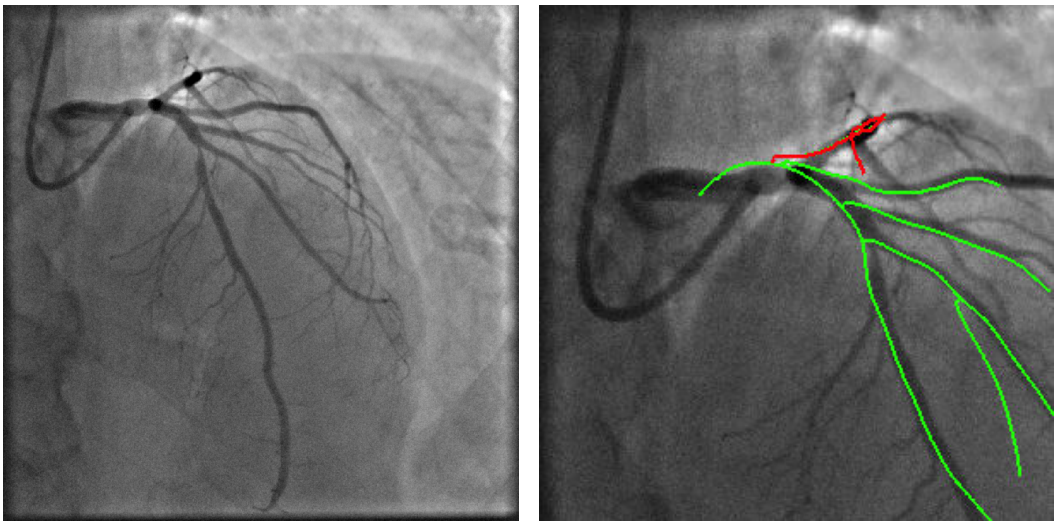

(c) Small rotation 1 (d) Small rotation 2

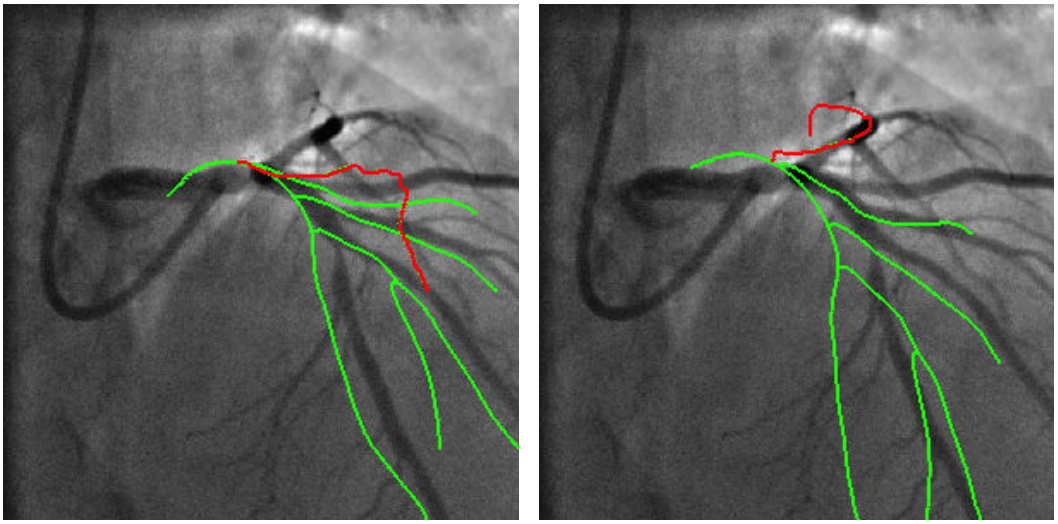

Figure 9.3: Change of shape of a highly foreshortened vessel (highlighted in red) submitted to small rotations (less that 5^o). The native entire image is presented in (a). Vascular tree projections (green) are presented at three different poses on a zoom of the native image: (b) at the references pose, (c) and (d) at two rotational perturbations of less than 5^o. The vessel presenting high foreshortening looks really different between views while the other vessels stay quite unchanged.

The transformation optimization of step-2b (second line of Equation (5.19)) can be re-written:

$$T'_j = \underset{T\in\Omega}{\operatorname{argmin}} \sum_{(Y,x)\in\pi_j} w(C,c)\cdot w(Y,x)\cdot \left\|x - T(Y)\right\|^2 \tag{9.3}$$

where the weights $w(C,c)$ and $w(Y,x)$ endorsing curve rejection and point rejection are mixed together.

The "obvious" pairing rejection has been implemented at the level of curve to solve the problem highlighted in Figure 8.15. A simple threshold is applied to the Fréchet distance, ignoring curve pairings corresponding to too distant curves. The implementation of an outlier robust TP-ICC algorithm allowed to improve cases where the ICP was better. An example is provided in Figure 9.4 in a patient suffering from Chronic Total Occlusion (CTO). In this case, an entire vessel portion is occluded and non visible in the X-ray image. Moreover another vessel branch is misdetected, which complicates even more the registration process. Even if this improvement seems promising, it will need further investigations regarding the cutting threshold and its robustness regarding perturbation of the reference pose. Weighted-based rejection is also a path to explore.

(a) Detected 2D graph (b) Outlier robust registration

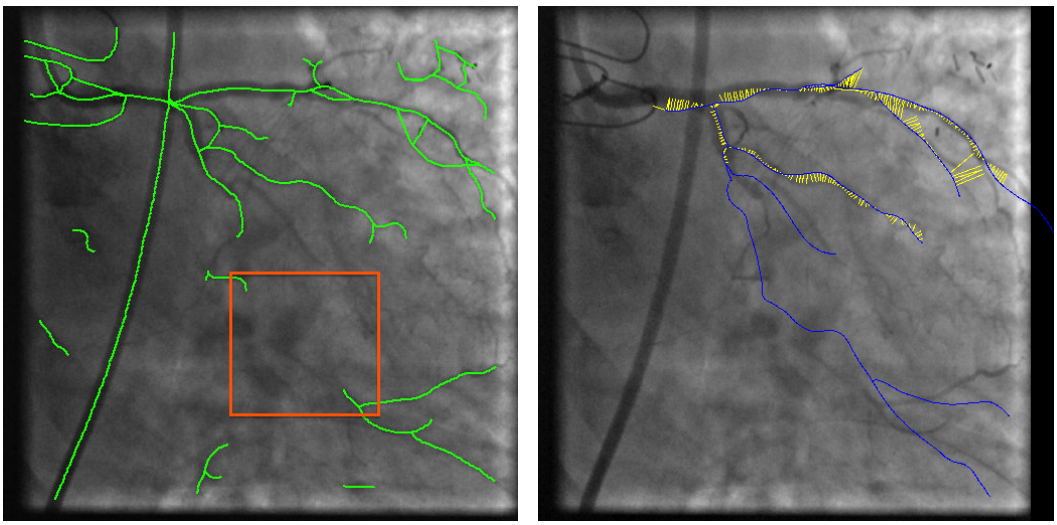

Figure 9.4: Outlier robust implementation of the TP-ICC algorithm applied to a CTO case. (a) shows the automatically detected vascular graph where the occluded vessel portion is missing in the orange rectangle; (b) registration position given at convergence of the TP-ICC algorithm (projection in blue and pairings in yellow).

9.3.3 Non-Rigid Registration

Results of Section 8.3 have shown that considering a rigid deformation was sufficient to attain an acceptable success rate in clinical practice. As highlighted in Section 2.4,

what is expected from a 3D/2D vascular registration algorithm is more to provide relevant correspondences than to show a "perfect" fit between structures. A rigid registration between the 3D volume and an injected frame, extracted from a sequence at the same cardiac cycle, allows to propose different types of fusion described in Section 2.4.1. However, a non-rigid deformation optimization can be necessary in order to further decrease the alignment error or to propose a temporal alignment along a whole cardiac cycle.

The Iterative Closest Curve (ICC) framework can easily handle non-rigid deformations in its scope. In fact, the only step that is impacted by the type of transformation considered is step-2b of the end Section 5.1.3, which consists in finding the transformation of the 3D model that minimizes the distance between paired points in a least squares sense. Given a finite set of paired points that belong to the same dimensional space, computing the optimal transformation is usually the most expected result from a transformation model. In our particular application, paired points belong to two different spaces linked by a projection operator. We have proposed in Section 5.2.4 a way to retrieve a 3D/3D point pairing set from a 3D/2D one.

A huge variety of non-rigid deformations are available in the literature and can be characterized by their number of Degrees of Freedom (DoF). The number of DoF corresponds to the minimum number of parameters necessary to define the transformation. In the 3D space it can vary from 3 for a translational only alignment, 6 for a rigid transformation and can increase up to (almost) $+\infty$. The more DoF are allowed, the better the transformation can represent local deformations. However, high number of DoF is synonymous of ill-posedness: the registration problem becomes under-constrained and the number of local minima in the cost function increases. To limit this phenomenon, a regularization term on the deformation is often added to the registration problem of Equation (5.1).

In the interesting review [Sotiras et al., 2013], many different non-rigid deformations are classified accordingly to how they were inspired:

- **Physics**: These mathematical models have been inspired from physics laws such as elastic body deformation, diffusion equation or the flows of diffeomorphisms.

- **Interpolation Theory**: The best known example is surely the spline-based interpolation that gave birth to the spline-based deformation field. All other radial basis functions (thin plate splines, Gaussian mixtures...) as well as the well known Free Form Deformation (FFD) infer the transformation of the whole space by interpolating the known displacement at particular points, called control points.

- **Prior Knowledge**: Some transformation models take advantage of the context where the registration will be applied. This type of transformations can model the biomechanic of the deformed structure or involve statistics on deformations learned from a rich database.

We chose a deformation model based on interpolation theory because they present generally low computational cost, do not involve modeling of the heart and are simple to understand.

Since coronary arteries (and linear structure in general) are sparse in the volume, it seems non-relevant to define a 3D dense deformation on the whole volume without any prior knowledge (model/anatomy). We thus decide to work with deformations applied only to centerlines that can be extrapolated to other part of the volume if necessary. We spread control points $\{p_i\}_{1...N_p}$ along the vessel tree centerlines and define a local transformation T_i in each of those points. Each control point will affect neighborhood points along the centerlines with a contribution decreasing with the distance. The contribution of a control point p_i at a given location in space is defined by a **basis function** ϕ_i [2].

Along the manuscript we have stressed the particular importance to take into account the topology of the structures involved. Therefore, we design the transformation model such that the influence of control points takes into account the two types of connectivities in the tree. Control points along the tree will not contribute accordingly to the 3D Euclidean distance but their influence will depend on the geodesic distance along the tree. We determine the transformation to apply to an arbitrary location y along the vessel structure, by a linear mixture of local transformations carried by control points and weighted by the basis-functions:

$$T(y) = \left[\sum_{i=1}^{N_p} \phi_i(y, p_i) T_i\right](y) \tag{9.4}$$

If we use linear transformation for each local transformation T_i, equation (9.4) can be re-written :

$$T(y) = \sum_{i=1}^{N_p} \phi_i(y, p_i) T_i(y) \tag{9.5}$$

We chose to represent the local transformation at each control points p_i by a translation vector $\mathbf{t_i}$, so that $T_i(y) = y + t_i$. The transformation at a point y (equation 9.5 can be re-written:

$$T(y) = \sum_{i=1}^{N_p} \phi_i(y, p_i)(y + \mathbf{t_i}) = \left(\sum_{i=1}^{N_p} \phi_i(y, p_i)\right) y + \sum_{i=1}^{N_p} \phi_i(y, p_i)\mathbf{t_i} \tag{9.6}$$

If we impose:

$$\sum_{i=1}^{N_p} \phi_i(y, p_i) = 1, \tag{9.7}$$

we can simplify equation 9.6 into

$$T(y) = y + \sum_{i=1}^{N_p} \phi_i(y, p_i)\mathbf{t_i} \tag{9.8}$$

[2] N.B. The index i under ϕ_i stress that basis function can be different between control points. In practice we will have $\phi_1 = \ldots = \phi_{N_p} := \phi$

Solving the optimal least squares alignment of two paired point sets can be achieved using the same technique as the spline resolution. Our model also exhibits a linear formulation and solving it becomes equivalent to compute the inverse of a particular matrix (details are provided in Appendix E).

Regarding the choice of basis functions, we consider a Gaussian function at each control point. In case of Gaussian basis function, the influence of a control point p_i on a point y in the structure can be expressed by

$$\phi(y, p_i) = \frac{1}{\sigma\sqrt{2\pi}} e^{-\left(\frac{d(y,p_i)}{\sigma}\right)^2} \tag{9.9}$$

where $d(.,.)$ is the geodesic distance along the tree structure. Parameter σ determines how fast the control point influence decreases.

Preliminary investigations on synthetic tree show promising results as presented in Figure 9.5 but a deeper study is expected before being able to show quantitative results.

Figure 9.5: Preliminary results on non-rigid registration. (a) Deformed synthetic case defined as target (green) and the initial structure (red). (b) Non-rigid registered transformation of the initial structure (red) aligned with target (green) using non-rigid implementation of the TP-ICC algorithm.

9.3.4 Applicability to Other Fields

In this thesis, we have built a registration algorithm designed to register a vascular tree segmentation in 3D and its X-ray projection acquired intra-operatively. Besides the proposed Percutaneous Coronary Intervention (PCI) application, other clinical fields can benefit from a 3D/2D registration algorithm imposing coherence along the matching procedure. During Trans-Arterial Chemo-Embolization (TACE), chemotherapeutic agents are injected directly into the arteries feeding a tumor[3]. This minimally invasive gesture also involves embolization (blockage) of these vessels in order to cut off blood supply to the tumor. It has been stressed in [Groher, 2008] that TACE can benefit from a fused visualization of the intra-interventional X-ray imaging modality (presented in Figure 9.6a) and a pre-operative 3D segmentation of the vasculature (presented in Figure 9.6b).

(a) Liver DSA (b) Liver 3D rendering

Figure 9.6: Modalities involved in the case of 3D/2D liver vasculature registration. (a) corresponds to a Digitally Subtracted Angiography (DSA) highlighting the liver vasculature, (b) presents a 3D rendering of a 3D X-ray reconstruction of the liver anatomy.

As for this thesis, liver fusion visualization necessitates a step of registration between the two modalities presented in Figure 9.6. An example of fusion is provided in Figure 9.7, which allows to visualize simultaneously the tumor (visible in the preoperative CT) with respect to the current state of the patient anatomy (thanks to the intra-operative imaging system). Assuming that the two segmentation techniques presented in Chapter 4 can be adapted to the liver application, one can directly apply the 3D/2D Tree-topology Preserving Iterative Closest Curve (TP-ICC) algorithm presented in Section 6.5.

[3]The reader can find a deeper description of the procedure in [Johns Hopkins Medicine, 2015b].

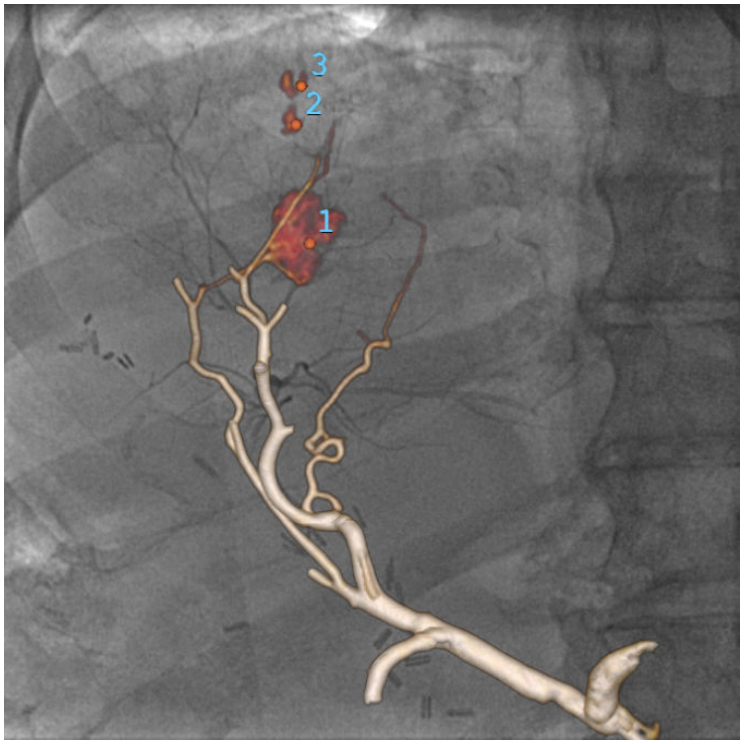

Figure 9.7: Example of fusion between intra-operative liver angiography and pre-operative CT scanner. Blue numbers denotes the principal tumor (1) and two secondary tumors (2 and 3) visible in the CT scan but not in the live guiding image.

A similar fusion application can be useful in neurology, where the brain vasculature is both rich an tortuous. Several clinical applications of the 3D/2D registration have been mentioned in the literature such as the improved guidance in intra-cranial aneurysm treatment [Hipwell et al., 2003] or ArterioVenous Malformations (AVM) as well as potential 4D DSA [Mitrović et al., 2013]. In case of AVM, the complexity of the pathologic vasculature constitutes a real challenge for the identification of vessels to treat (see Figure 9.8). Adding the pre-operative annotated feeding vessels could be of great interest during the embolization step of the procedure[4]. A fusion application similar to the one presented in Figure 9.7 can be imagined as well as a colorization of the vessel feeding the AVM as the one presented in Figure 9.9.

(a) AVM DSA (b) AVM 3D rendering

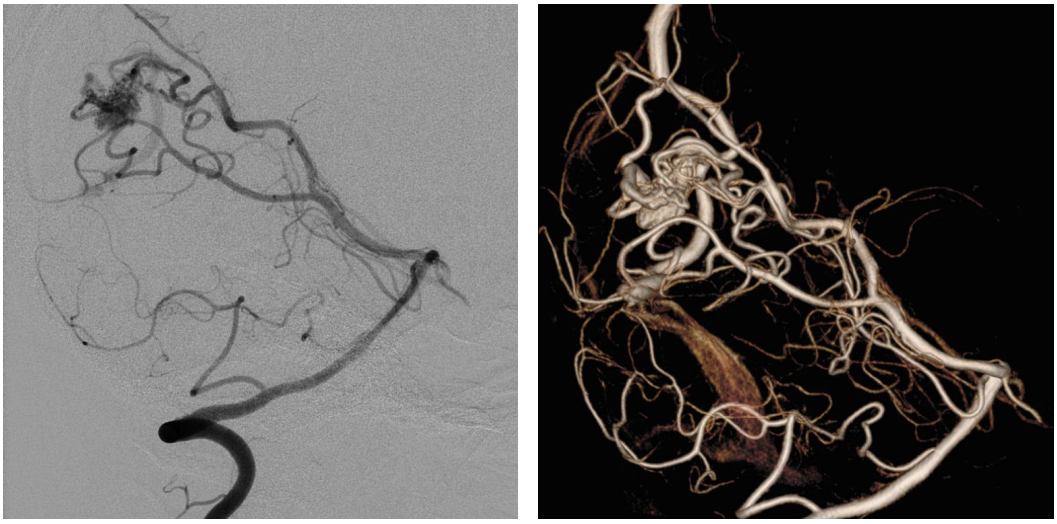

Figure 9.8: Modalities involved in the case of 3D/2D vessels registration for AVM. (a) 2D DSA used for intra-operative guidance, (b) pre-operative volume rendering of the CT scanner. One should note the extreme complexity of the vasculature.

All of the previous applications constitute immediate possible extension of the TP-ICC algorithm presented in this thesis. In fact, the 3D vasculature of the liver and the brain can be represented by a tree and its 2D projection as a graph. But in Chapter 5, we introduced a general framework that can be used to register any kind of structure from which curves can be extracted. Clinical contexts that come to mind are: retinal fundus 2D/2D registration [Serradell et al., 2015], pre-operative CT to intra-interventional cone-beam 3D/3D registration of the liver vasculature [Charnoz et al., 2005], 3D/3D registration of pulmonary structures [Smeets and Bruyninckx, 2010]. In addition of the ICC-framework, the two last applications can benefit from an extension of the tree-topology preserving pairing (presented in Chapter 6) since the two different structures to be matched can be represented as trees.

[4] A description of the standard procedure can be found in [Mayo Clinic, 2015].

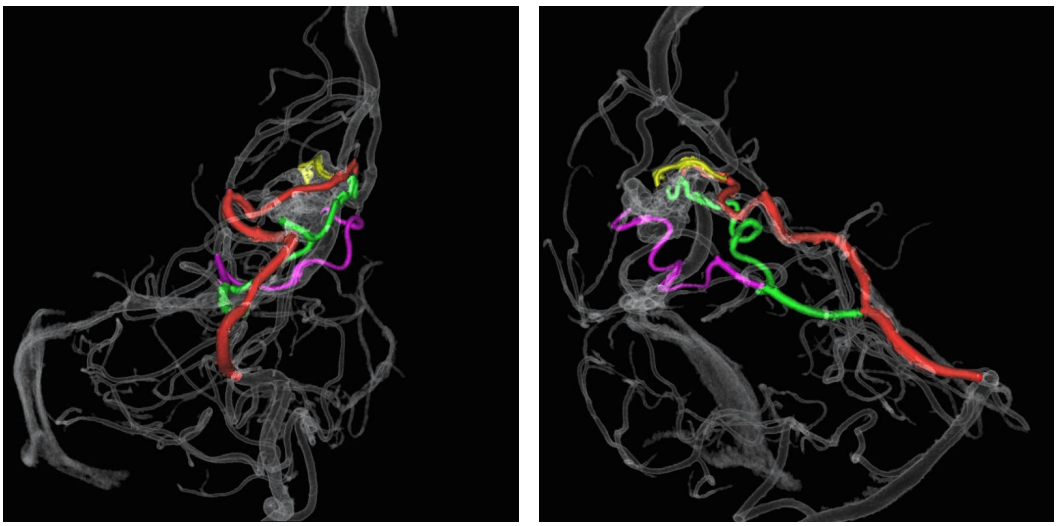

Figure 9.9: Feeders of the AVM colored differently in the brain vasculature (white).

Appendix A

List of Publications

A.1 Journal and Conference (with review committee)

- Benseghir, T., Malandain, G., and Vaillant, R. (2013). Iterative Closest Curve: a Framework for Curvilinear Structure Registration Application to 2D/3D Coronary Arteries Registration. In Medical Image Computing and Computer-Assisted Intervention - MICCAI 2013 (Vol. 8149, pp. 179-186)
- Benseghir, T., Malandain, G., and Vaillant, R. (2015). A Tree-Topology Preserving Pairing for 3D/2D Registration. In International Journal of Computer Assisted Radiology and Surgery - IJCARS 2015 (Vol. 10, Issue 5)

A.2 Supervised Master's Thesis

- Haouzi, D. (2013). Coronary Arteries Detection in 2D Angiography Sequences - French. ESME Sudria.
- Li, Z. (2013). Cardiac Motion Estimation in Interventional Cardiology - French. Sup'elec.
- Clemenceau, M. (2013). Rendering of X-ray Scanner Images for Fusion Application in Percutaneous Coronary Interventions - French. ISEP.
- This, A. (2014). Early Detection of Navigation Injection during Percutaneous Coronary Intervention - French. ECE Paris

Appendix B

Top-10 Causes of Death Globally

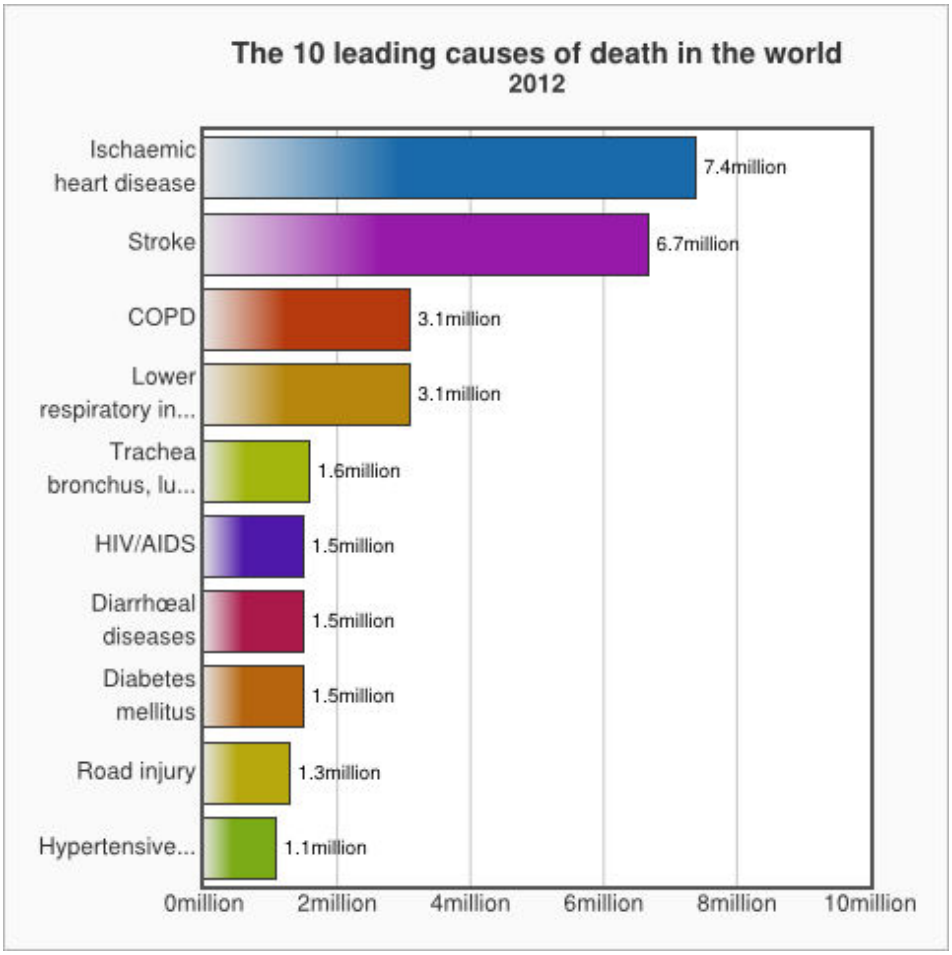

Figure B.1: Top-10 causes of deaths in 2012 taken from [World Health Organization, 2012]. Ischaemic heart disease is also known as coronary artery disease and constitute the clinical context of this thesis.

Appendix C

X-ray Image Formation and Background Removal

The intensity of the X-ray beam $I(x)$ reaching the detector at pixel x can be approximated by the Beer-Lambert law:

$$I(x) = I_0(x) \exp\left(-\int_{l=0}^{L} \mu(l) dl\right) \tag{C.1}$$

where $I_0(x)$ denotes the intensity of the X-ray beam leaving the source in the direction of the pixel x, l is a mute variable that describes the position along the ray line starting from the source ($l = 0$) to the detector ($l = L$) and $\mu(l)$ is called the linear attenuation coefficient and characterizes the material. The value of the attenuation coefficient mainly depends on the material density and mean atomic number. Soft-tissues are characterized by a low μ coefficient and thus do not much attenuate the X-ray beam, while bones greatly attenuate X-Rays. To opacify vessels in the X-ray modality a contrast medium is injected, resulting in an opacification of the lumen in the X-ray image. We denote μ_C the attenuation of the contrast medium that fills the arteries. The beam starting from the source to the pixel x will thus go through patient's arteries $\mathcal{L}'$ containing contrast product and the rest of the anatomy $\mathcal{L}$ that remains unchanged by the injection. Equation (C.1) can be re-written in that case:

$$\begin{aligned} I(x) &= I_0(x) \exp\left(-\int_{l\in\mathcal{L}} \mu(l) dl - \int_{l\in\mathcal{L}'} \mu_C dl\right) \\ I(x) &= \underbrace{I_0(x) \exp\left(-\int_{l\in\mathcal{L}} \mu(l) dl\right)}_{\tilde{I}(x)} \underbrace{\exp\left(-\int_{l\in\mathcal{L}'} \mu_C dl\right)}_{\Delta C(x)} \end{aligned} \tag{C.2}$$

where $\tilde{I}(x)$ denotes the intensity that would be observed at the detector if no contrast medium was injected and $\Delta C(x)$ represents the contrast of vessels in the injected image.

Regarding clinical application, only $\Delta C(x)$ is relevant in a live guidance context. In fact in neurology and liver minimally invasive procedures, a Digitally Subtracted Angiography (DSA) mode is used during the navigation phase. An image of the anatomy, called the mask I_M, is acquired without any contrast agent in order to estimate $\tilde{I}(x)$. When an injected image is then acquired, the mask is subtracted to it in the logarithmic domain (equivalent to a division in the image domain). Using

Equation (C.2) one is able to show that the resulting DSA image I_{DSA} characterize the contrast $\Delta C(x)$:

$$\begin{aligned} I_{DSA}(x) &= \log I(x) - \log I_M(x) \\ I_{DSA}(x) &\approx \log I(x) - \log \tilde{I}(x) \\ I_{DSA}(x) &\approx \log \frac{I(x)}{\tilde{I}(x)} \\ I_{DSA}(x) &\approx \log \Delta C(x) \end{aligned} \tag{C.3}$$

The final equality is not strict because the mask estimation of the background image is not perfect. Noise effects are limited by averaging multiple fluoroscopic images, but small relative motions can create artifacts in the resulting DSA. This technique is only applicable to particular anatomies where an estimation of the background anatomy at a time t is a relevant representation of the anatomy present in an injected image acquired at a time $t + \Delta t$. Thus, the DSA modality is only available for peripheral anatomy[1] such as brain or liver anatomy as presented in Figure C.1. Unfortunately, because of the beating heart and the respiratory motion, the DSA modality is not available in cardiac imaging.

[1] Basically all vessels except of heart vessels.

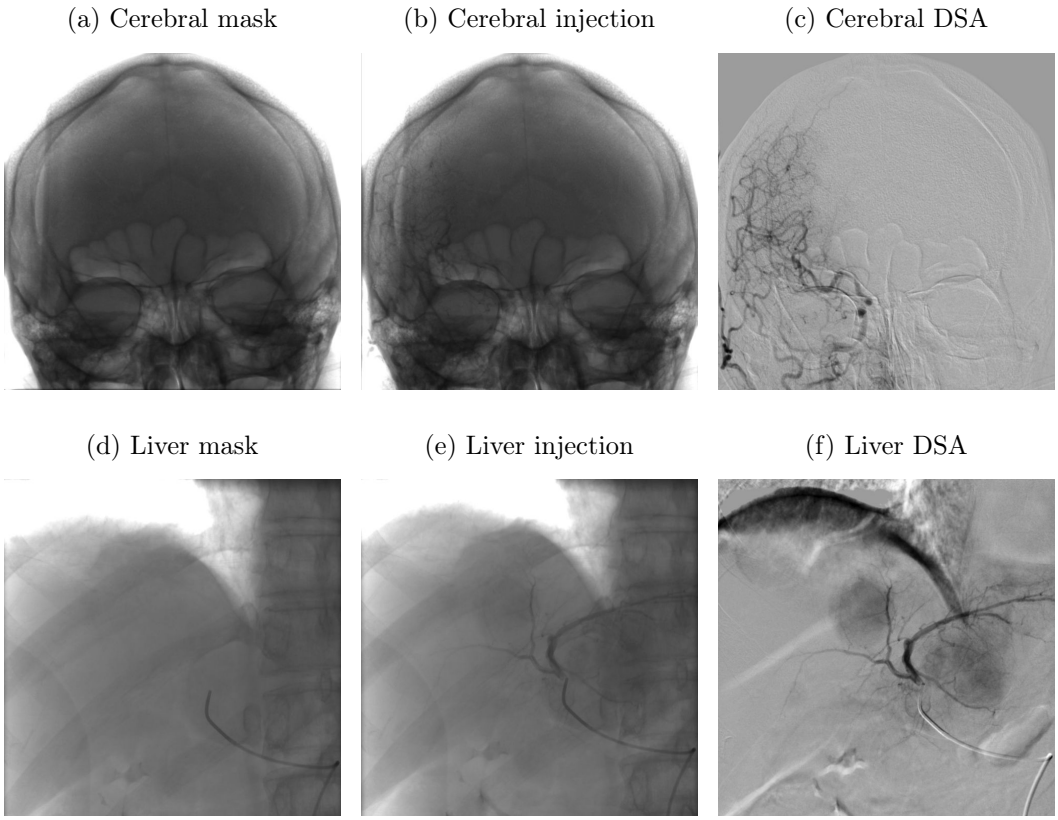

Figure C.1: Digitally Subtracted Angiography (DSA) of the brain vasculature (top row) and the liver (bottom row). Columns from left to right represent the mask estimating the background anatomy, the contrast medium injected image and the DSA resulting from the logarithmic subtraction of the injected image and the mask.

Appendix D

Vascular Graph Extraction

In this appendix we provide to the reader an overview of the whole 2D angiography database used to conduct the experiments of Chapter 8. From the following figures, one is able to assess visually the performance of the automatic vascular graph extraction described in Section 4.2.

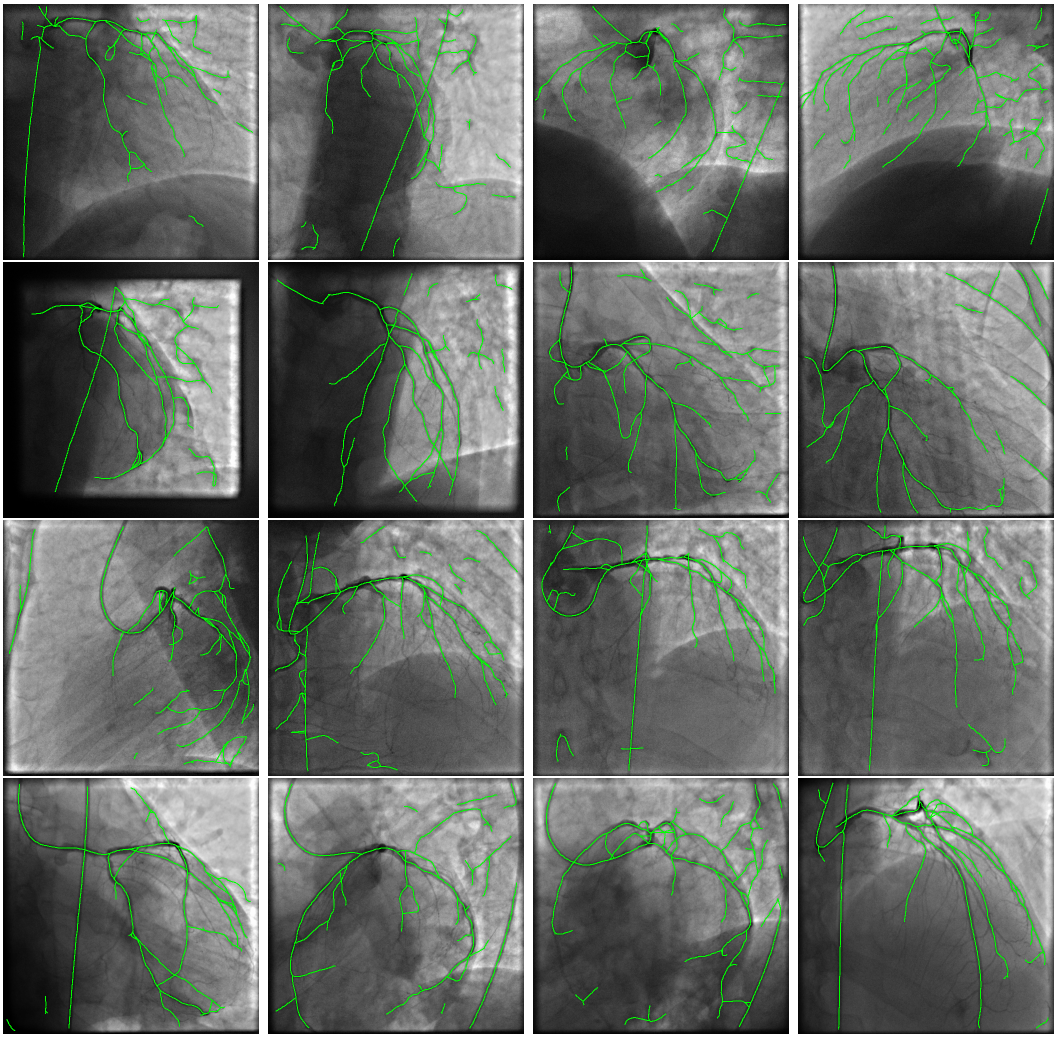

Figure D.1: Extracted 2D vascular graph (Part-1)

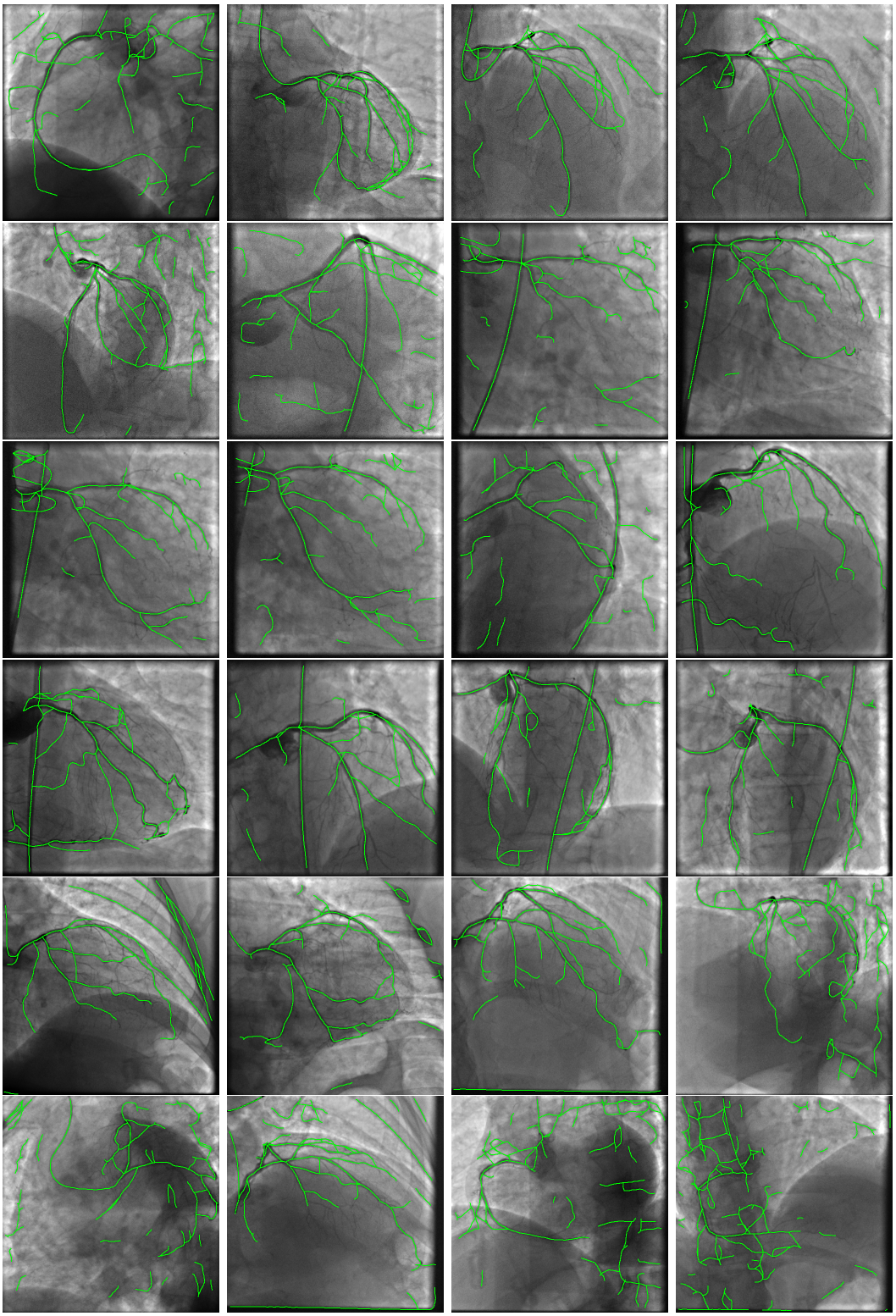

Figure D.2: Extracted 2D vascular graph (Part-2)

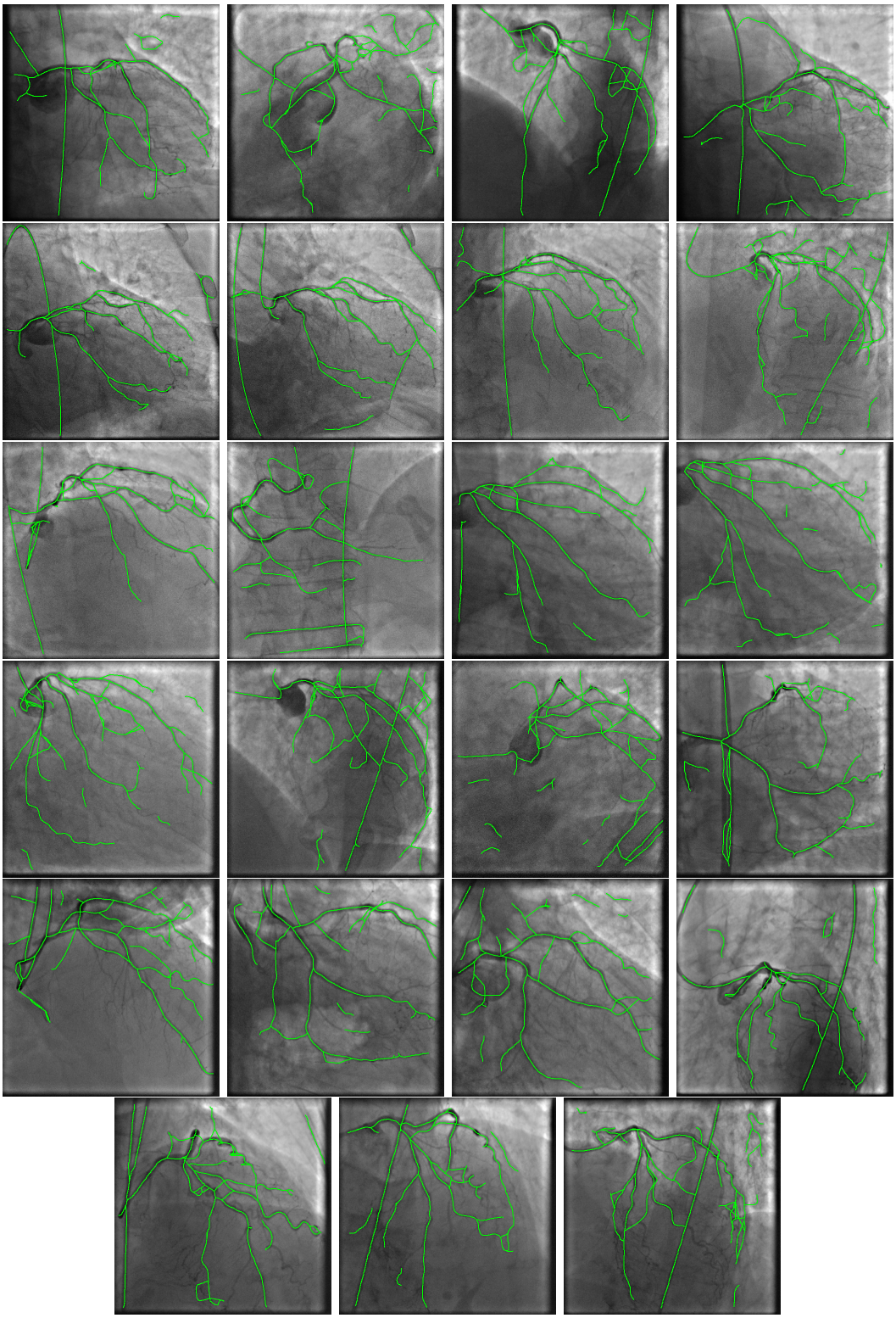

Figure D.3: Extracted 2D vascular graph (Part-3)

Appendix E

Compute Least Squares Non-Rigid Alignment

Given two sets of paired points under the form of a point pairing set π composed of point pairings (y, x). We aim at solving:

$$\hat{T} = \underset{T \in \Omega}{\operatorname{argmin}} \left\{ \sum_{(y,x)\in\pi} \|T(y) - x\|^2 \right\} \tag{E.1}$$

where the set of admissible transformation Ω is the one proposed in Section 9.3.3. The transformation T is defined as:

$$T(y) = y + \sum_{i=1}^{N_p} \phi_i(y, p_i)\mathbf{t_i} \tag{E.2}$$

where N_p is the number of control points, denoted p_i, spread along the vascular tree. ϕ_i corresponds to the contribution of the control point p_i at the location y. Each control point carries a transformation t_i that is a translation that define the resulting transformation T.

Equation (E.1) can be written:

$$\hat{T} = \underset{T=\{\mathbf{t_i}\}_{1\dots N_p}\in(\Omega)^{N_p}}{\operatorname{argmin}} \left\{ \underbrace{\sum_{(y,x)\in\pi} \left\| y - x + \sum_{i=1}^{N_p} \phi_i(y, p_i).\mathbf{t_i} \right\|^2}_{f(T)} \right\} \tag{E.3}$$

To determine the solution we derive with respect to each t_l, $l \in \{1 \dots N_p\}$ and set it equal to zero.

$$\frac{\partial f(T)}{\partial t_l} = \sum_{(y,x)\in\pi} 2 \times \left((\phi_l(y, p_l)) \left(y - x + \sum_{i=1}^{N_p} \phi_i(y, p_i).\mathbf{t_i} \right) \right) = 0 \tag{E.4}$$

$$\sum_{(y,x)\in\pi} \left(\phi_l(y, p_l) \left(\sum_{i=1}^{N_p} \phi_i(y, p_i).\mathbf{t_i} \right) \right) = \sum_{(y,x)\in\pi} \phi_l(y, p_l)(x - y) \tag{E.5}$$

$$\sum_{(y,x)\in\pi} \sum_{i=1}^{N_p} \phi_l(y, p_l)\phi_i(y, p_i).\mathbf{t_i} = \sum_{(y,x)\in\pi} (\phi_l(y, p_l)(x - y)) \tag{E.6}$$

$$\sum_{i=1}^{N_p} \left(\sum_{(y,x)\in\pi} \phi_l(y,p_l)\phi_i(y,p_i) \right) .\mathbf{t_i} = \sum_{(y,x)\in\pi} (\phi_l(y,p_l)(x-y)) \tag{E.7}$$

This equation is true for every $l \in \{1 \dots N_p\}$ and forms a system of N_p equations with N_p unknown translations. It can be rewritten in a matrix formulation $A.T = Z$ with $T = (t_1, t_2, \dots, t_{N_p})^t$,

$$Z = \begin{pmatrix} \sum_{(y,x)\in\pi} \phi_1(y,p_1)(x-y) \\ \sum_{(y,x)\in\pi} \phi_2(y,p_2)(x-y) \\ \vdots \\ \sum_{(y,x)\in\pi} \phi_{N_p}(y,p_{N_p})(x-y) \end{pmatrix}$$

and

$$A = \begin{pmatrix} \sum_{(y,x)\in\pi} \phi_1(y,p_1)\phi_1(y,p_1) & \cdots & \sum_{(y,x)\in\pi} \phi_1(y,p_1)\phi_{N_p}(y,p_{N_p}) \\ \vdots & \ddots & \vdots \\ \sum_{(y,x)\in\pi} \phi_{N_p}(y,p_{N_p})\phi_1(y,p_1) & \cdots & \sum_{(y,x)\in\pi} \phi_{N_p}(y,p_{N_p})\phi_{N_p}(y,p_{N_p}) \end{pmatrix} \tag{E.8}$$

If $\phi_1 = \phi_2 = \ldots = \phi_{N_p}$, we then define

$$B = \begin{pmatrix} B(y_1,p_1) & B(y_2,p_1) & \dots & B(y_{N_c},p_1) \\ B(y_1,p_2) & B(y_2,p_2) & \dots & B(y_{N_c},p_2) \\ \vdots & \vdots & \ddots & \vdots \\ B(y_1,p_{N_p}) & B(y_2,p_{N_p}) & \dots & B(y_{N_c},p_{N_p}) \end{pmatrix} \tag{E.9}$$

where we impose the sum of each column to be equal to 1 to satisfy equation 9.7.

The resolution of the registration problem is thus equivalent to the simple inverse problem $A.X = Z$, with $X = T$. If A has a non-zero determinant we can solve this system by computing the inverse matrix of A denoted A^{-1}.

Appendix F

The French Touch

F.1 Introduction

Cette thèse s'inscrit dans le cadre de l'imagerie interventionnelle. Dans ce domaine étendu, nous nous focalisons sur les procédures percutanées au sein du réseau artériel. Des systèmes d'imagerie sont utilisés afin d'aider le praticien (aussi appelé radiologue interventionnel) à délivrer le traitement via des outils dédiés qui sont insérés dans le réseau vasculaire du patient. Fournir des images adaptées au geste thérapeutique, en fonction du type d'intervention et du moment de celle-ci, constitue un véritable challenge. Le travail de recherche présenté dans ce manuscrit s'intéresse particulièrement aux interventions coronariennes percutanées. Les images sont acquises par un système de guidage interventionnel qui révèlent les outils manipulés par le clinicien par rapport à l'anatomie du patient. Elles sont acquises à une cadence maximale de 30 images par seconde avec une précision maximale de $0.2mm$. En général, ces caractéristiques satisfont la plupart des exigences cliniques. Cependant, certain cas particuliers appellent de nouvelles techniques de visualisation impliquant de plus en plus l'utilisation de modalités complémentaires d'imagerie. La combinaison de modalités est vue comme une voie potentielle d'amélioration visant à proposer une visualisation de l'ensemble des informations disponibles pendant l'intervention. Les images de guidage fournies par le système interventionel correspondent à la projection de l'anatomie du patient sur un plan. Elles sont produites grâce au principe d'atténuation des rayons-X par les tissus anatomiques et les autres objets présents dans le champs de vue. Dans de telles images les vaisseaux peuvent se superposer, ce qui ne facilte pas leur interprétation. De plus, dans le cas de vaisseaux totalement occlus, des difficultés additionnelles peuvent apparaitre.

Les parties occluses ne sont pas visibles dans l'image (2D) temps réel, parce que le coefficient d'atténuation du canal occlu ne peut être modifiée par l'injection d'agent de contraste. Fusioner une acquisition scanner pré-opératoire avec les images projectives pourrait améliorer le guidage per-opératoire. Le scanner tomodensitométrique angiographique (CTA) permet d'étudier le système vasculaire du patient en trois dimensions (3D). Ce type d'acquisition est le plus souvent effectué à des fins de diagnostic et permet de déterminer si le patient a besoin d'une procédure de revascularisation ou non. Le volume reconstruit comprend non seulement la lumière du vaisseau, mais également des informations supplémentaires telles que le type de matériau constituant la paroi de la vasculature. Une des caractéristiques de la présence d'une lésion est la présence de calcifications le long des artères. Celles-ci sont révélées par le CTA et permettent d'orienter le diagnostic ainsi que le type

de traitement à administrer. De plus, pour un patient souffrant d'une occlusion complète, le canal occlus est constitué d'un matériau spécifique qui peut être vu dans le volume 3D reconstruit. Ces deux types d'informations sont indispensables lors de la phase de navigation de l'intervention et le cardiologue pourrait bénéficier d'une visualisation condensée de ces éléments extraits du CTA pré-opératoire et les images per-opératoires. Mais ceci nécessite de les exprimer dans le même référentiel. La description de cette procédure et des besoins cliniques associés est l'objectif principal de chapitre 2.

Ces deux acquisitions représentent le patient à différents états (avant et pendant l'intervention), sur deux systèmes d'imagerie qui n'ont pas de lien pré-défini entre eux. Aligner deux modalités différentes, qui représentent une même réalité, au sein d'un même repère réfère au problème de recalage. Pour trouver la transformation qui permet d'aligner le volume CTA avec les images 2D de guidage, un algorithme de recalage optimise une fonction objectif qui quantifie la distance entre les deux structures d'intérêt. La majorité des méthodes de la littérature, dont la plupart sont présentées dans le chapitre 3, font appel à une étape de segmentation des vaisseaux. Les algorithmes de recalage basés caractéristiques (features) reposent sur l'établissement de correspondances entre les représentations géométriques extraites de chacune des deux modalités. Le succès de tels algorithmes repose sur la justesse des correspondances établies.

Créer des correspondances pertinentes est l'un des axes principaux de recherche concernant les algorithmes basés caractéristiques. Plusieurs articles de l'état de l'art améliorent la précision et la robustesse d'algorithmes de recalage en prenant en compte la structure particulière des objets à mettre en correspondance. La connaissance a priori de la vasculature permet d'utiliser une information locale (comme la direction de la tangente ou la courbure locale) afin d'améliorer la procédure d'appariement ou pénaliser des appariements non-cohérents le long de ces structures. Cependant, la plupart des articles de la littérature ne considère pas la structure vasculaire comme un tout. Nous expliquons en détails dans le chapitre 4 comment sont extraites les caractéristiques (features) qui correspondent au mieux à chacune des deux modalités. Nous définissons ensuite un cadre général dédié au recalage de courbes, qui assure la préservation des structures curvilinéaires tout au long des itérations. Cette méthode étend le principe du point le plus proche itéré (Iterative Closest Point, ICP) aux ensembles de courbes.

L'algorithme que nous proposons est appelé courbe la plus proche itérée (Iterative Closest Curve, ICC) et sa formulation générale est applicable aux situations où les courbes constituent les caractéristiques clefs d'une structure. L'algorithme ICC, qui est le sujet du chapitre 5, alterne deux étapes : la construction d'appariements entre courbes extraites des deux modalités et le calcul de la transformation minimisant la distance de Fréchet entre les courbes appariées. La distance de Fréchet est une distance courbe à courbe basée sur un ensemble d'appariements de points qui préserve l'ordre le long de chaque courbe (et préserve donc la topologie de celles-ci). En mettant en correspondances des courbes entières ainsi qu'en optimisant la distance de Fréchet, le principe de l'ICC permet de prendre en compte la structure

curviligne de manière globale. Dans une étape supplémentaire, nous considérons les artères coronaires comme un arbre dans lequel les vaisseaux sont connectés les uns aux autres à des points de bifurcation. Cet arrangement fait appel à deux formes de connectivités: celle des points le long d'une même courbe et celle entre les courbes aux points de bifurcation.

Dans le chapitre 6, nous décrivons une procédure d'appariement d'arbre qui préserve ces deux types de connectivités. Cette étape est rendue particulièrement difficile à cause de la nature projective de l'image 2D de guidage. Les méthodes concernant l'appariement d'arbres reposent majoritairement sur la mise en correspondance de noeud (dans notre cas les points de bifurcation) dans chaque modalité. Cette hypothèse est généralement non-satisfaite dans le cas du recalage 3D/2D à cause de la superposition de vaisseaux dans l'image projective (2D). Nous définissons alors ce que nous considérons comme un appariement préservant la structure d'arbre dans le cas 3D/2D et proposons une approche descendante (au sens de l'arbre) pour apparier la vasculature 3D. La récursion débute au niveau de la racine et les différents sous-arbres sont alors appariés en continuant la récursion jusqu'aux feuilles. Un possible appariement d'arbre est évalué par le biais d'un score qui prends en compte la distance spatiale entre les courbes appariées mais aussi leur ressemblance en terme de forme. Le processus d'appariement est formulé comme un problème d'optimisation de ce score. Il est résolu par un algorithme de diviser-pour-conquérir, ce qui évite l'explosion combinatoire qui serait générée en essayant tous les appariements possibles.

Cette procédure d'appariement peut facilement être introduite dans le cadre général de l'ICC, ce qui donne naissance à l'algorithme TP-ICC. Afin d'évaluer cette méthode de recalage, nous avons créé deux mesures d'erreur complémentaires, chacune relative à une des sorties attendue par un tel algorithme: l'alignement (pose de recalage) et l'appariement. Nous nous sommes efforcés dans le chapitre 7 de fournir des mesures intuitives, pertinentes d'un point de vue clinique et basées sur une véritée terrain (qui peut être obtenue sans impacter la procédure clinique standard). L'erreur d'alignement quantifie la distance entre la projection de la structure 3D, à la position de recalage, et la position où elle devrait se trouver selon la vérité terrain. La qualité des appariements quant à elle est quantifiée par l'erreur d'appariement. Ces deux mesures montrent de bonnes corrélations avec une évaluation visuelle du recalage et sont utilisées dans le chapitre 8 pour évaluer l'approche proposée.

F.2 Conclusion

F.2.1 Principaux aboutissements

Le but principal de cette thèse était d'adresser le problème du recalage 3D/2D des artères coronaires. D'un côté, les images projectives "temps-réel" fournies par le système interventionnel sont utilisées afin de naviguer les outils cliniques dans la vasculature du patient. De l'autre, le scanner tomodensitométrique angiographique

(CTA) met en évidence les dépots de calcium le long des parois des artères ainsi que le canal occlus (en cas d'occlusion chronique totale). Ces deux informations sont intéressantes pour le clinicien durant l'intervention, mais ne sont pas visibles dans les images rayon-X de guidage. Mettre en correspondance ces deux modalités complémentaires pourrait enrichir la quantité d'information disponible durant la procédure. Ceci nécessite une étape de recalage fournissant un alignement précis et des appariements pertinents entre les deux structures vasculaires.

Nous avons proposé une approche orientée sur la construction d'appariements plus pertinents entre les lignes centrales des vaisseaux extraites du volume 3D et d'une image 2D. Pour ce faire, nous avons proposé un algorithme qui préserve la topologie de la vasculature. En mettant en correspondance des courbes entières, le cadre général de la courbe la plus proche itérée (Iterative Closest Curve, ICC) assure la préservation de la structure de courbe tout au long des itérations. Afin de prendre en compte la topologie particulière de la vasculature (dans laquelle les lignes centrales des vaisseaux sont connectées à des points de bifurcation), nous avons mis en place une procédure d'appariement préservant la topologie d'arbre. Les branches de l'arbre 3D sont appariées à des courbes extraites de l'image 2D, en assurant la préservation de la connection aux points de bifurcation. L'algorithme TP-ICC qui en résulte alterne les deux étapes suivantes: 1) construire un appariement d'arbre; 2) trouver la transformation minimisant la distance entre les courbes appariées.

Cet algorithme a été évalué sur une base de données de 63 cas collectées à la suite de procédures cliniques standards. Sous des conditions d'utilisation clinique, nous avons obtenu un taux de succès de 84% sur cette base de données. Le succès d'un recalage est jugé sur la base de deux critères: la projection des vaisseaux 3D est proche de leur structures correspondantes dans la 2D; et la majorité des appariements résultants sont corrects. La méthode proposée montre aussi de bons résultats en terme de robustesse par rapport aux rotations à compenser (jusqu'à 30^o). Ce comportement montre une faible sensibilité à une perturbation croissante de la position initiale estimée. L'algorithme TP-ICC résulte aussi en une faible erreur d'appariement qui ouvre la voie vers une nouvelle façon de mesurer ses performances: son utilisation dans un contexte clinique. L'intégration d'un tel algorithme dans le milieu clinique (sous la forme d'une étude clinique par exemple) est toujours en discussion, tout comme la façon de présenter au mieux la fusion des informations des différentes modalités. Plusieurs voies d'amélioration et extensions de cet algorithme ont été identifiée au long de ce manuscrit, qui mériteraient d'être creusées.

F.2.2 Contributions

Dans cette partie, nous listons les contributions principales de cette thèse.

Le cadre de l'ICC Grâce à sa formulation générale et son haut degré de réutilisabilité, le cadre de l'ICC semble être notre plus forte contribution au domaine. Pourtant, le principe de l'ICC est très simple: étendre le principe de l'ICP aux courbes. Cet algorithme est composé de deux étapes qui sont itérées jusqu'à con-

vergence : construire un appariement entre courbes extraites de chaque structure et déterminer la transformation qui minimise la distance entre courbes appariées. Un exemple de procédure d'appariement a été décrit pour notre application 3D/2D. Nous l'avons choisi pour être à la fois intuitif et aussi largement applicable que possible. La distance entre courbes est évaluée par la distance de Fréchet qui est basée sur un appariement de points préservant l'ordre au long de chacune des courbes. La somme des distances de Fréchet est optimisée par rapport à l'ensemble des transformations admissibles (rigides dans notre cas). Nous avons proposé d'utiliser les appariements induits par la distance de Fréchet afin de determiner la transformation optimale pour un ensemble donné de courbes appariées. L'étape d'optimisation de la transformation consiste elle-même en une procédure d'optimisation alternée comparable à un algorithme ICP mais où l'appariement au plus proche voisin est remplacé par l'appariement de Fréchet.

Procédure d'appariement d'arbre L'un des défis de cette thèse était d'obtenir une procédure assurant une correspondance "un-un" qui préserve la topologie d'arbre de la vasculature alors que les vaisseaux se superposent dans l'image et que peu de points de repère anatomique sont disponibles. Nous avons développé une approche descendante qui apparie les branches de l'arbre récursivement. En partant de la racine et descendant progressivement l'arbre, une contrainte de connectivité est imposée à chaque bifurcation pour préserver la topologie d'arbre. Trouver le meilleur appariement d'arbre est résolu comme un problème d'optimisation d'un score d'appariement conçu spécialement. Ce score prend en compte la distance spatiale entre courbes appariées mais aussi la ressemblance entre leur forme, le tout en respectant l'ordre des points le long des deux courbes. Afin de quantifier la ressemblance de forme, nous avons évité de nous baser sur des descripteurs locaux (comme la tangente ou la courbure locale) car ils ne sont pas toujours bien définis au niveau des vaisseaux subissant un fort raccourcissement projectif. Nous avons introduit un critère de ressemblance s'appuyant sur l'idée suivante: deux courbes se ressemblent si l'on est capable de les recaler l'une sur l'autre avec une faible erreur résultante. Le score d'appariement d'arbre qui en résulte est optimisé par un algorithme de division-pour-conquérir basé sur une propriété de sous-structure optimale du problème. Ceci évite une approche directe qui engendrerait une explosion combinatoire. De plus, la procédure d'appariement qui en résulte peut être facilement introduite dans le cadre de l'ICC. En effet, un appariement d'arbre n'est autre qu'un ensemble de courbes appariées respectant les contraintes de connectivité supplémentaire à chaque bifurcation.

Les mesures d'erreur de recalage Afin d'évaluer l'algorithme TP-ICC, ou n'importe quel autre algorithme de recalage, nous avons créé deux mesures d'erreur qui quantifient chacune un des résultats attendus d'un algorithme de recalage. La première est l'erreur d'alignement. Celle-ci a déjà été abordée dans la littérature, mais jamais en faisant la distinction entre les vaisseaux composant le réseau vas-

culaire. Le second résultat attendu est un ensemble de correspondances correctes entre les deux modalités, qui servira à l'établissement d'une application de navigation. A notre connaissance aucun des articles de la littérature addresse le problème de l'évaluation de la qualité des appariements fournis par l'algorithme. Nous avons proposé deux mesures complémentaires basées sur une vérité-terrain qui n'impacte en aucun cas la procédure clinique standard. L'utilisation conjointe de l'erreur d'alignement et de l'erreur d'appariement démontre une bonne corrélation avec une évaluation visuelle du recalage par un observateur entrainé.

Bibliography

Alt, H. and Godau, M. (1992). Measuring the resemblance of polygonal curves. In *Eighth Annual Symposium on Computational Geometry*, pages 102–109. (Cited on pages 70 and 71.)

Baka, N., Metz, C., Schultz, C., Neefjes, L., van Geuns, R., Lelieveldt, B., Niessen, W., van Walsum, T., and de Bruijne, M. (2013). Statistical coronary motion models for 2D+t/3D registration of X-ray coronary angiography and CTA. *Medical Image Analysis*, 17(6):698–709. (Cited on pages 38, 39, 69 and 94.)

Baka, N., Metz, C., Schultz, C., van Geuns, R., Niessen, W., and van Walsum, T. (2014). Oriented gaussian mixture models for nonrigid 2D/3D coronary artery registration. *IEEE Transactions on Medical Imaging*, 33(5):1023–34. (Cited on pages 38, 39, 43, 69, 110, 123, 124, 156 and 157.)

Besl, P. and McKay, N. (1992). A method for registration of 3-D shapes. *IEEE Transactions on Pattern Analysis and Machine Intelligence*, 14(2):239–256. (Cited on pages 34, 39, 69, 70, 76, 77, 82, 89, 90 and 169.)

Blondel, C., Malandain, G., Vaillant, R., and Ayache, N. (2006). Reconstruction of coronary arteries from a single rotational X-ray projection sequence. *IEEE Transactions on Medical Imaging*, 25(5):653–663. (Cited on page 123.)

Borgefors, G. (1988). Hierarchical chamfer matching: A parametric edge matching algorithm. *IEEE Transactions on Pattern Analysis and Machine Intelligence*, 10(6):849–865. (Cited on page 35.)

Branislav, B., editor (2013). *What Should We Know About Prevented, Diagnostic, and Interventional Therapy in Coronary Artery Disease*. InTech. (Cited on page 7.)

Cardiovascular News (2004). Drug-eluting stent penetration in europe. http://www.cxvascular.com/cn-archives/cardiovascular-news-issue-9/drug-eluting-stent-penetration-in-europe. (Cited on page 11.)

Chan, H., Chung, A., Yu, S., and Wells, W. (2004). 2D-3D vascular registration between digital subtraction angiographic (DSA) and magnetic resonance angiographic (MRA) images. In *International Symposium on Biomedical Imaging*, pages 708–711. IEEE. (Cited on page 33.)

Chandola, V., Banerjee, A., and Kumar, V. (2009). Anomaly detection: A survey. *ACM Computing Surveys (CSUR)*, 41(3):15. (Cited on page 170.)

Charnoz, A., Agnus, V., Malandain, G., Soler, L., and Tajine, M. (2005). Design of robust vascular tree matching: validation on liver. In Christensen, G.

and Sonka, M., editors, *Proc. of Information Processing in Medical Imaging 2005 (IPMI'05)*, volume 3565 of *LNCS*, pages 443–455, Glenwood springs, Colorado, USA. Springer. (Cited on page 179.)

Chen, T., Funka-Lea, G., and Comaniciu, D. (2011). Robust and fast contrast inflow detection for 2D X-ray fluoroscopy. In Fichtinger, G., Martel, A., and Peters, T., editors, *Proc. of Medical Image Computing and Computer-Assisted Intervention (MICCAI 2011)*, volume 6891 of *LNCS*, pages 243–250, Toronto, Canada. Springer. (Cited on pages 52 and 142.)

Chetverikov, D., Svirko, D., Stepanov, D., and Krsek, P. (2002). The trimmed iterative closest point algorithm. In *16th International Conference on Pattern Recognition*, volume 3, pages 545–548. (Cited on page 170.)

Cormen, T. H., Leiserson, C. E., Rivest, R. L., and Stein, C. (2009). *Introduction to Algorithms*. The MIT Press, third edition. (Cited on page 115.)

Diagnostic and Interventional Cardiology (2014). FDA expands xience stents indication for coronary chronic total occlusions. http://www.dicardiology.com/article/fda-expands-xience-stentsE28099-indication-coronary-chronic-total-occlusions. (Cited on page 11.)

Diestel, R. (2012). *Graph Theory*, volume 173 of *Graduate texts in mathematics*. Springer, 4th edition. (Cited on page 45.)

Duong, L., Liao, R., Sundar, H., Tailhades, B., Meyer, A., and Xu, C. (2009). Curve-based 2D-3D registration of coronary vessels for image guided procedure. In *SPIE*, volume 7261. (Cited on pages 41, 70, 82, 97 and 123.)

Eiter, T. and Mannila, H. (1994). Computing discrete Fréchet distance. Technical report, Christian Doppler Laboratory for Expert Systems, TU Vienna, Austria. (Cited on pages 71 and 72.)

Escaned, J. (2015). MSCT: Where could it help for procedural planning. In *Chronic Total Occlusion Summit 2015*. (Cited on page 23.)

Feldmar, J., Ayache, N., and Betting, F. (1995). 3D-2D projective registration of free-form curves and surfaces. In *International Conference on Computer Vision (ICCV 95)*, pages 549–556. (Cited on page 39.)

Feldmar, J., Malandain, G., Ayache, N., Fernández-Vidal, S., Maurincomme, E., and Trousset, Y. (1997). Matching 3D MR angiography data and 2D X-ray angiograms. In *CVRMed-MRCAS'97*, volume 1205 of *LNCS*, pages 129–138, Grenoble, France. Springer. (Cited on pages 39, 42, 43, 69 and 94.)

Florin, C., Williams, J., Khamene, A., and Paragios, N. (2005). Registration of 3D angiographic and X-ray images using sequential Monte Carlo sampling. In

Computer Vision for Biomedical Image Applications, volume 3765 of *LNCS*, pages 427–436. Springer. (Cited on page 35.)

Frangi, A. F., Niessen, W. J., Vincken, K. L., and Viergever, M. A. (1998). Multiscale vessel enhancement filtering. In Wells, W. M., Colchester, A., and Delp, S., editors, *Medical image computing and computer-assisted intervention (MICCAI 1998)*, volume 1496 of *LNCS*, pages 130–137, Cambridge, UK. Springer. (Cited on pages 53, 56 and 58.)

Gatta, C., Balocco, S., Martin-Yuste, V., Leta, R., and Radeva, P. (2011). Non-rigid multi-modal registration of coronary arteries using SIFTflow. In *Pattern Recognition and Image Analysis*, volume 6669 of *LNCS*, pages 159–166. Springer. (Cited on pages 33, 42 and 124.)

Glowacki, P., Pinheiro, M. A., Türetken, E., Sznitman, R., Lebrecht, D., Kybic, J., Holtmaat, A., and Fua, P. (2014). Reconstructing Evolving Tree Structures in Time Lapse Sequences. In *Conference on Computer Vision and Pattern Recognition (CVPR)*, pages 3035–3042. (Cited on page 52.)

Granger, S. and Pennec, X. (2002). Multi-scale EM-ICP: A fast and robust approach for surface registration. In *European Conference on Computer Vision*, volume 2353 of *LNCS*, pages 418–432. Springer. (Cited on pages 37, 69 and 93.)

Groher, M. (2008). *2D-3D Registration of Vascular Images*. PhD thesis, Technische Universtät München. (Cited on page 177.)

Groher, M., Bender, F., Hoffmann, R.-T., and Navab, N. (2007). Segmentation-driven 2D-3D registration for abdominal catheter interventions. In *Medical Image Computing and Computer-Assisted Intervention - MICCAI 2007*, volume 4792 of *LNCS*, pages 527–535. Springer. (Cited on pages 35 and 161.)

Groher, M., Zikic, D., and Navab, N. (2009). Deformable 2D-3D registration of vascular structures in a one view scenario. *IEEE Transactions on Medical Imaging*, 28(6):847–860. (Cited on pages 37, 40, 41, 69, 70, 123 and 124.)

Hadida, J., Desrosiers, C., and Duong, L. (2012). Stochastic 3D motion compensation of coronary arteries from monoplane angiograms. In *Medical Image Computing and Computer-Assisted Intervention - MICCAI 2012*, volume 7510 of *LNCS*, pages 651–658. Springer. (Cited on pages 124 and 127.)

Hernández-Vela, A., Gatta, C., Escalera, S., Igual, L., Martin-Yuste, V., Sabaté, M., and Radeva, P. (2012). Accurate coronary centerline extraction, caliber estimation, and catheter detection in angiographies. *IEEE Transactions on Information Technology in Biomedicine*, 16(6):1332–1340. (Cited on page 166.)

Hipwell, J. H., Penney, G. P., McLaughlin, R. A., Rhode, K., Summers, P., Cox, T. C., Byrne, J. V., Noble, J. A., and Hawkes, D. J. (2003). Intensity-based 2-D-3-D registration of cerebral angiograms. *IEEE Transactions on Medical Imaging*, 22:1417–1426. (Cited on pages 31 and 179.)

Jian, B. and Vemuri, B. (2011). Robust point set registration using gaussian mixture models. *IEEE Transactions on Pattern Analysis and Machine Intelligence*, 33(8):1633–1645. (Cited on page 38.)

Johns Hopkins Medicine (2015a). Coronary artery bypass graft surgery (CABG). http://www.hopkinsmedicine.org/healthlibrary/test_procedures/cardiovascular/coronary_artery_bypass_graft_surgery_cabg_92,P07967/. (Cited on page 8.)

Johns Hopkins Medicine (2015b). Transarterial chemo embolization (TACE). http://www.hopkinsmedicine.org/liver_tumor_center/treatments/intraarterial_therapies/tace.html. (Cited on page 177.)

Kerrien, E., Berger, M., Maurincomme, E., Launay, L., Vaillant, R., and Picard, L. (1999). Fully automatic 3D/2D subtracted angiography registration. In *Medical Image Computing and Computer-Assisted Intervention - MICCAI 1999*, volume 1679 of *LNCS*, pages 664–671. Springer. (Cited on page 32.)

Kirbas, C. and Quek, F. (2003). Vessel extraction techniques and algorithms: a survey. In *Symposium on BioInformatics and BioEngineering*, pages 238–245. (Cited on page 52.)

Kita, Y., Wilson, D., and Noble, A. (1998). Real-time registration of 3D cerebral vessels to X-ray angiograms. In *Medical Image Computing and Computer-Assisted Interventation - MICCAI'98*, volume 1496 of *LNCS*, pages 1125–1133. Springer. (Cited on pages 34 and 36.)

Lacroix, R., Florent, R., and Auvray, V. (2012). Model-based segmentation of the left main coronary bifurcation from 2D angiograms. In *International Symposium on Biomedical Imaging (ISBI)*, pages 780–783. IEEE. (Cited on pages 86 and 106.)

Langet, H. (2013). *Sampling and Motion Reconstruction in Three-dimensional X-ray Interventional Imaging*. PhD thesis, Ecole Centrale Paris. (Cited on page 19.)

Lee, J.-H. and Won, C.-H. (2011). Topology preserving relaxation labeling for nonrigid point matching. *IEEE Transactions on Pattern Analysis and Machine Intelligence*, 33(2):427–432. (Cited on page 110.)

Liu, A. and Bullitt, E. (1998). 3D/2D registration via skeletal near projective invariance in tubular objects. In *Medical Image Computing and Computer-Assisted Interventation - MICCAI 98*, volume 1496 of *LNCS*, pages 780–787. Springer. (Cited on pages 40, 70, 97 and 123.)

Maintz, J. and Viergever, M. (1998). A survey of medical image registration. *Medical Image Analysis*, 2(1):1–36. (Cited on pages 27 and 28.)

Markelj, P., Tomaževič, D., Likar, B., and Pernuš, F. (2012). A review of 3D/2D registration methods for image-guided interventions. *Medical Image Analysis*, 16(3):642–661. (Cited on pages 27, 28, 30 and 31.)

Matern, D., Condurache, A. P., and Mertins, A. (2012). Event detection using log-linear models for coronary contrast agent injections. In *International Conference on Pattern Recognition Applications and Methods - ICPRAM 2012*, pages 172–179. (Cited on pages 52 and 142.)

Mayo Clinic (2015). Brain AVM (arteriovenous malformation). http://www.mayoclinic.org/diseases-conditions/brain-avm/diagnosis-treatment/treatment/txc-20130139. (Cited on page 179.)

Metz, C., Schaap, M., and Klein, S. (2009). GPU accelerated alignment of 3-D CTA with 2-D X-ray data for improved guidance in coronary interventions. In *International Symposium on Biomedical Imaging*, pages 959–962. IEEE. (Cited on pages 31, 32, 42, 124 and 127.)

Metz, C. T., Schaap, M., Klein, S., Baka, N., Neefjes, L. A., Schultz, C. J., Niessen, W. J., and van Walsum, T. (2013). Registration of 3D+t coronary CTA and monoplane 2D+t X-ray angiography. *IEEE Transactions on Medical Imaging*, 32(5):919–931. (Cited on page 36.)

Mitrović, U., Špiclin, Z., Likar, B., and Pernuš, F. (2013). Method for 3D-2D registration of vascular images : Application to 3D contrast agent flow visualization. In *Clinical Image-Based Procedures. From Planning to Intervention (MICCAI Work-Shop CLIP)*, volume 7761 of *LNCS*, pages 50–58. Springer. (Cited on pages 40, 69, 94 and 179.)

National Heart, Lung, and Blood Institute (2015a). Angioplasty intervention. http://www.nhlbi.nih.gov/health/health-topics/topics/angioplasty/during. (Cited on page 7.)

National Heart, Lung, and Blood Institute (2015b). Plaque buildup in an artery. http://www.nhlbi.nih.gov/health/health-topics/topics/angina. (Cited on page 6.)

Nithiananthan, S., Schafer, S., Uneri, A., Mirota, D. J., Stayman, J. W., Zbijewski, W., Brock, K. K., Daly, M. J., Chan, H., Irish, J. C., and Siewerdsen, J. H. (2011). Demons deformable registration of CT and cone-beam CT using an iterative intensity matching approach. *Medical Physics*, 38(4):1785–1798. (Cited on page 122.)

Penney, G. P., Weese, J., Little, J. A., Desmedt, P., Hill, D. L., and Hawkes, D. J. (1998). A comparison of similarity measures for use in 2-D-3-D medical image registration. *IEEE transactions on medical imaging*, 17(4):586–95. (Cited on page 31.)

Prümmer, M. (2010). *Cardiac C-Arm Computed Tomography: Motion Estimation and Dynamic Reconstruction*. PhD thesis, Friedrich-Alexander-Universität Erlangen-Nürnberg (FAU). (Cited on page 123.)

Rivest-Henault, D., Sundar, H., and Cheriet, M. (2012). Nonrigid 2D/3D registration of coronary artery models with live fluoroscopy for guidance of cardiac interventions. *IEEE Transactions on Medical Imaging*, 31(8):1557–1572. (Cited on pages 34, 35, 36, 43, 124, 127, 156 and 157.)

Rohkohl, C. (2011). *Motion Estimation and Compensation for Interventional Cardiovascular Image Reconstruction*. PhD thesis, University of Erlangen-Nuremberg. (Cited on page 123.)

Ruijters, D., ter Haar Romeny, B. M., and Suetens, P. (2009). Vesselness-based 2D-3D registration of the coronary arteries. *International Journal of Computer Assisted Radiology and Surgery*, 4(4):391–397. (Cited on pages 32 and 33.)

Rusinkiewicz, S. and Levoy, M. (2001). Efficient variants of the ICP algorithm. In *Third International Conference on 3-D Digital Imaging and Modeling*, pages 145–152. IEEE. (Cited on pages 34, 69, 77, 169 and 170.)

Serradell, E., Pinheiro, M., Sznitman, R., Kybic, J., Moreno-Noguer, F., and Fua, P. (2015). Non-rigid graph registration using active testing search. *IEEE Transactions on Pattern Analysis and Machine Intelligence*, 37(3):625–638. (Cited on pages 42, 98 and 179.)

Serradell, E., Romero, A., Leta, R., Gatta, C., and Moreno-Noguer, F. (2011). Simultaneous correspondence and non-rigid 3D reconstruction of the coronary tree from single X-ray images. In *International Conference on Computer Vision 2011*, pages 850–857. (Cited on pages 41, 43, 110, 124 and 127.)

Smeets, D. and Bruyninckx, P. (2010). Robust matching of 3D lung vessel trees. In *MICCAI Workshop on Pulmonary Image Analysis*, volume 2, pages 61–70. (Cited on pages 42, 98 and 179.)

Sotiras, A., Davatazikos, C., and Paragios, N. (2013). Deformable medical image registration: A survey. *IEEE Transactions on Medical Imaging*, 32:1153–1190. (Cited on pages 27, 28, 124 and 174.)

Sundar, H. (2006). A novel 2D-3D registration algorithm for aligning fluoro images with 3D pre-op CT/MR images. In *Proceedings of SPIE*, volume 6141. (Cited on pages 34 and 35.)

Tam, G. K. L., Cheng, Z.-q., Lai, Y.-k., Langbein, F. C., Liu, Y., Marshall, D., Martin, R. R., Sun, X.-f., and Rosin, P. L. (2013). Registration of 3D point clouds and meshes : A survey from rigid to non-rigid. *IEEE Transactions on Visualization and Computer Graphics*, 19(7):1199–1217. (Cited on page 169.)

Türetken, E., Benmansour, F., Andres, B., Pfister, H., and Fua, P. (2013). Reconstructing loopy curvilinear structures using integer programming. In *Conference on Computer Vision and Pattern Recognition (CVPR)*, pages 1822–1829. (Cited on page 52.)

Türetken, E., Benmansour, F., and Fua, P. (2012). Automated reconstruction of tree structures using path classifiers and mixed integer programming. In *Computer Vision and Pattern Recognition (CVPR), 2012 IEEE Conference on*, pages 566–573. (Cited on page 52.)

Turgeon, G.-A., Lehmann, G., Guiraudon, G., Drangova, M., Holdsworth, D., and Peters, T. (2005). 2D-3D registration of coronary angiograms for cardiac procedure planning and guidance. *Medical Physics*, 32(12):3737. (Cited on page 33.)

van de Kraats, E. B., Penney, G. P., Tomazevic, D., van Walsum, T., and Niessen, W. J. (2005). Standardized evaluation methodology for 2D-3D registration. *IEEE Transactions on Medical Imaging*, 24(9):1177–1189. (Cited on pages 92 and 122.)

World Health Organization (2012). Comparison of the top 10 causes of deaths across income groups. `http://www.who.int/mediacentre/factsheets/fs310/en/index3.html`. (Cited on page 183.)

Zhang, D. P. (2010). *Coronary Artery Segmentation And Motion Modelling*. PhD thesis, Imperial College London. (Cited on page 52.)

Zitová, B. and Flusser, J. (2003). Image registration methods: a survey. *Image and Vision Computing*, 21(11):977–1000. (Cited on pages 27 and 28.)

Recalage preservant la topologie des vaisseaux: application à la cardiologie interventionnelle

Résumé:

Cette thèse s'inscrit dans le cadre de la cardiologie interventionnelle. Intégrer des informations telles que la position des calcifications ainsi que la taille et forme d'une occlusion dans les images fluoroscopiques constituerait un bénéfice pour le praticien. Ces informations, invisibles dans les images rayons-X pendant la procédure, sont présentes au sein du scanner CT préopératoire. La fusion de cette modalité avec la fluoroscopie apporterait une aide précieuse au guidage temps réel des outils interventionnels en bénéficiant des informations fournies par le CT. Cette fusion requiert une étape de recalage qui vise à aligner au mieux les deux modalités et fournir des correspondances pertinentes entre elles. La plupart des algorithmes de recalage 3D/2D de vaisseaux rencontrent des difficultés à construire des appariements anatomiquement pertinents, essentiellement à cause du manque de cohérence topologique le long du réseau vasculaire.

Afin de résoudre ce problème, nous proposons dans cette thèse un cadre générique pour le recalage de structures curvilinéaires. L'algorithme qui en découle préserve la structure des courbes appariées. Les artères coronaires pouvant être représentées par un ensemble de courbes arrangées en arbre, nous proposons aussi une procédure d'appariement qui respecte cette structure. Le recalage d'un arbre 3D sur un graphe 2D est ainsi réalisé en assurant la préservation des connectivités aux bifurcations. Le choix de l'appariement est basé sur un critère prenant en compte la distance géométrique ainsi que la ressemblance entre courbes. Ce critère est évalué grâce à une forme modifiée de la distance de Fréchet.

Une base de données de 63 cas cliniques a été utilisée à travers différentes expériences afin de prouver la robustesse et la précision de notre approche. Nous avons proposé deux mesures complémentaires visant à quantifier la qualité de l'alignement d'une part et des appariements engendrés d'autre part. La méthode proposée se montre précise pour les alignements de la projection du modèle CT et des artères coronaires observées dans les images angiographiques. De plus, les appariements obtenus sont anatomiquement pertinents et lálgorithme a prouvé sa robustesse face aux perturbations de la position initiale. Nous attribuons cette robustesse à la qualité des appariements construits au fur et à mesure des itérations.

Mots Clefs: Recalage 3D/2D; Artères coronaires;

Topology Preserving Vascular Registration: Application to Percutaneous Coronary Intervention

Abstract:

In percutaneous coronary interventions, integrating into the live fluoroscopic image vessel calcifications and occlusion information that are revealed in the pre-operative Computed Tomography Angiography can greatly improve guidance of the clinician. Fusing pre- and intra-operative information into a single space aims at taking advantage of two complementary modalities and requires a step of registration that must provide good alignment and relevant correspondences between them. Most of the existing 3D/2D vessel registration algorithms do not take into account the particular topology of the vasculature to be matched, resulting into pairings that may be topologically inconsistent along the vasculature.

A first contribution consisted in a registration framework dedicated to curve matching, denoted the Iterative Closest Curve (ICC). Its main feature is to preserve the topological consistency along curves by taking advantage of the Frechet distance that not only computes the distance between two curves but also builds ordered pairings along them. A second contribution is a pairing procedure designed for the matching of a vascular tree structure that endorses its particular topology and that can easily take advantage of the ICC-framework. Centerlines of the 3D tree are matched to curves extracted from the 2D vascular graph while preserving the connectivity at 3D bifurcations. The matching criterion used to build the pairings takes into account the geometric distance and the resemblance between curves both based on a global formulation using the Frechet distance.

To evaluate our approach we run experiments on a database composed of 63 clinical cases, measuring accuracy on real conditions and robustness with respect to a simulated displacement. Quantitative results have been obtained using two complementary measures that aim at assessing the results both geometrically and topologically, and quantify the resulting alignment error as well as the pairing error. The proposed method exhibits good results both in terms of pairing and alignment and demonstrates to be low sensitive to the rotations to be compensated (up to 30 degrees).

Keywords: 3D/2D Registration; Coronary Arteries;